

NOTE TO USERS

Page(s) missing in number only; text follows. Page(s) were scanned as received.

247 - 248

This reproduction is the best copy available.

UMI[®]

Theoretical Studies of Seeded Water Clusters: Structure, Thermodynamics and Photochemistry

Denise Koch

A Thesis

in

The Department

of

Chemistry and Biochemistry

Presented in Partial Fulfillment of the Requirements
For the Degree of Doctorate of Philosophy at
Concordia University
Montreal, Quebec, Canada

January 2006



Library and
Archives Canada

Bibliothèque et
Archives Canada

Published Heritage
Branch

Direction du
Patrimoine de l'édition

395 Wellington Street
Ottawa ON K1A 0N4
Canada

395, rue Wellington
Ottawa ON K1A 0N4
Canada

Your file Votre référence

ISBN: 978-0-494-16266-8

Our file Notre référence

ISBN: 978-0-494-16266-8

NOTICE:

The author has granted a non-exclusive license allowing Library and Archives Canada to reproduce, publish, archive, preserve, conserve, communicate to the public by telecommunication or on the Internet, loan, distribute and sell theses worldwide, for commercial or non-commercial purposes, in microform, paper, electronic and/or any other formats.

The author retains copyright ownership and moral rights in this thesis. Neither the thesis nor substantial extracts from it may be printed or otherwise reproduced without the author's permission.

AVIS:

L'auteur a accordé une licence non exclusive permettant à la Bibliothèque et Archives Canada de reproduire, publier, archiver, sauvegarder, conserver, transmettre au public par télécommunication ou par l'Internet, prêter, distribuer et vendre des thèses partout dans le monde, à des fins commerciales ou autres, sur support microforme, papier, électronique et/ou autres formats.

L'auteur conserve la propriété du droit d'auteur et des droits moraux qui protègent cette thèse. Ni la thèse ni des extraits substantiels de celle-ci ne doivent être imprimés ou autrement reproduits sans son autorisation.

In compliance with the Canadian Privacy Act some supporting forms may have been removed from this thesis.

Conformément à la loi canadienne sur la protection de la vie privée, quelques formulaires secondaires ont été enlevés de cette thèse.

While these forms may be included in the document page count, their removal does not represent any loss of content from the thesis.

Bien que ces formulaires aient inclus dans la pagination, il n'y aura aucun contenu manquant.


Canada

Abstract

Theoretical Studies of Seeded Water Clusters: Structure, Thermodynamics and Photochemistry

This thesis provides a detailed and thorough theoretical investigation of the solvation structure of ions in water clusters and of solvation effects on photochemically-induced electron transfer processes occurring in seeded aqueous clusters. $\text{NaI}(\text{H}_2\text{O})_n$ clusters were chosen as a model system for the latter because the electronic structure of NaI is characterized by a curve crossing of ionic and covalent states, and the presence of solvent molecules can significantly affect the NaI electronic structure and photodissociation dynamics due to the differential solvation of these two states. Furthermore, the surface solvation state adopted by large halide ions determines to a great extent the solvation structure of alkali-metal halides in water clusters, and therefore significantly affect their photochemistry. The first-ever rigorous investigation of the solvation thermodynamics of halide-water clusters, presented here, reveals that entropy and polarization drive the ion from a surface to interior solvation structure by cluster size 20 for fluoride, and cluster size 60 for the heavier halides. The outcome of the simulations seems to depend strongly on the choice of model used to describe the system intermolecular interactions, and an array of first-principles simulation methodologies has been designed accordingly. Designing models that allow for solvent polarization and

computationally efficient semiempirical methods that can properly describe weak interactions is shown to be essential throughout the thesis. Nonadiabatic simulation techniques were developed, in combination with an hybrid quantum-mechanics/molecular mechanics (QM/MM) model to describe intermolecular interactions, in order to investigate the photodissociation dynamics of $\text{NaI}(\text{H}_2\text{O})_n$ clusters. Simulation results suggest that the addition of only a few water molecules is sufficient to completely quench the oscillatory NaI dynamics observed in the gas phase, but that the process is dominated by rapid water evaporation. As a result, electron transfer in $\text{NaI}(\text{H}_2\text{O})_n$ is largely governed by the NaI large-amplitude motion, like in the gas phase, and the solvent only influences the nonadiabatic dynamics by mediating the NaI internuclear separation at which curve crossing occurs. When embedded in an argon matrix, however, the $\text{NaI}(\text{H}_2\text{O})_n$ nonadiabatic dynamics appears to involve an activationless or activated inverted electron transfer process along the solvent coordinate analogous to what may occur in solution.

Dedication

To my son Jonathan

Acknowledgements

I wish to thank my supervisor, Dr. Gilles Peslherbe, for his guidance throughout the research presented here and all the members of my thesis committee, Drs. John Capobianco, Peter Bird and Heidi Muchall, for their critical evaluation of the work presented in this Thesis. I would also like to thank Dr. Ann English for her constructive advice. I also wish to thank the National Sciences and Engineering Research Council, the Fonds Québécois de Recherche sur la Nature et les Technologies and Concordia University for fellowships and scholarships that supported the research presented in this Thesis. Finally, I wish to acknowledge the generous allocation of computational resources from the Centre for Research in Molecular Modeling, the Western Canada Research Grid and the Réseau Québécois de Calcul Haute Performance, without which this research would not have been possible.

Contributions of the Authors

The research presented in this thesis has been, for the most part, conducted and written by myself, under the supervision of Dr. Gilles H. Peslherbe. Qadir K. Timerghazin performed high-level *ab initio* calculations to characterize the NaI excited state in the presence of water molecules described in Chapter 4, and our collaborators Drs. James T. Hynes and Branka M. Ladanyi, with whom this research was initiated, mainly contributed comments to the manuscript. The simulations reported in Chapter 6, employ model potentials built on earlier work (and computer routines) by Tao-Nhan Nguyen.

Table of Contents

Table of Contents	viii
List of Figures	xi
List of Tables.....	xiii
List of Abbreviations.....	xvi
Chapter 1	
Introduction	1
1.1 Preamble	2
1.2 Solvation of ion and ion pairs in aqueous environments	4
1.3 Reaction dynamics in aqueous ion pair clusters.....	7
1.4 Objectives.....	13
Chapter 2	
On the Transition From Surface to Interior Solvation in Iodide-Water Clusters	19
2.1 Introduction.....	20
2.2 Simulation Procedure	22
2.3 Results and Discussion.....	24
2.4 Concluding Remarks.....	33
Chapter 3	
Solvation Structure and Thermodynamics of Halides in Water Clusters	35
3.1 Introduction.....	36
3.2 Simulation Methodology.....	39
3.2.1 Interaction potentials.....	39
3.2.2 Evaluation of potential of mean force.....	43
3.3 Results	45
3.4 Discussion.....	57
3.5 Concluding Remarks.....	70
Chapter 4	
Nonadiabatic Trajectory Studies of NaI(H ₂ O) _n Photodissociation Dynamics.....	74
4.1 Introduction	75

4.2 Computational Methodology.....	80
4.2.1 QM/MM Potential Energy Surfaces.....	80
4.2.2 NaI Electronic Structure and Potentials	81
4.2.3 Solvation and Water Potentials	85
4.2.4 Molecular Dynamics with Quantum Transitions	88
4.2.5 Simulation of Experimental Data.....	91
4.3 Results and Discussion.....	94
4.3.1 Ground-State Structures – Initial Conditions	94
4.3.2 Nonadiabatic Dynamics	99
4.3.3 Water Evaporation Dynamics	103
4.3.4 NaI–H ₂ O Energy Transfer and Mechanistic Aspects.....	106
4.3.5 Connection with Experiment	108
4.4 Concluding Remarks.....	120
Chapter 5	
Photodissociation Dynamics of NaI(H₂O)_n Clusters with a Polarizable Model.....	125
5.1 Introduction	126
5.2 Computational Procedure	131
5.2.1 QM/MM Potentials	131
5.2.2 Constant-Temperature MD Simulations and Free Energy Calculations	136
5.2.3 Nonadiabatic Dynamics	138
5.2.4 Simulation of Probe Signals.....	140
5.3 Results and Discussion.....	141
5.3.1 Franck-Condon Energy Gaps.....	141
5.3.2 NaI(H ₂ O) _n Photodissociation Dynamics	145
5.3.3 Connection with Experiment	152
5.3.4 Electron Transfer Reaction in NaI(H ₂ O) _n Clusters	160
5.4 Concluding Remarks.....	166
Chapter 6	
On the Photoexcitation of NaI Ion Pairs in Water, Ammonia and Acetonitrile Clusters.....	171
6.1 Introduction.....	172
6.2 Computational Methodology.....	176
6.2.1 QM/MM Molecular Dynamics Simulations	176
5.3	183
6.2.2 Model Quantum Chemistry Calculations.....	183
6.3 Results and Discussion.....	186
6.4 Concluding Remarks.....	193
Chapter 7	
Outlook and Future Directions	196

7.1 Solvation Thermodynamics from First Principles	197
7.1.1 Introduction.....	197
7.1.2 PMFs Generated with Semiempirical Quantum Chemistry	199
7.1.2.1 Simulation Methodology	199
7.1.2.2 Preliminary Results	203
7.1.3 <i>Ab initio</i> Refinements of Model Ion-Water Cluster PMFs.....	206
7.1.3.1 Simulation Methodology	206
7.1.3.3 Conclusions	212
7.2 Quantum effects in halide-water clusters.....	213
7.2.1 Introduction.....	213
7.2.2 Simulation Methodology.....	215
7.2.3 Preliminary results	219
7.2.4 Conclusion	224
7.3 Vibrational excitation/relaxation of ion pairs in clusters and solvation control of reactivity.....	226
7.4 Photodissociation Dynamics of NaI(H₂O)_n Clusters in a Matrix.....	228
7.4.1 Introduction.....	228
7.4.2 Simulation Methodology.....	228
7.4.3 Preliminary Results	229
7.4.4 Conclusions.....	231
7.5 Concluding Remarks.....	232
Chapter 8	
General Conclusions	234
Bibliography	245

List of Figures

Figure 2.1 Potentials of mean force for $\Gamma(\text{H}_2\text{O})_n$	25
Figure 2.2 $P(r_{cm})$ distributions for $\Gamma(\text{H}_2\text{O})_n$	26
Figure 2.3 Representative OPLS structures for $\Gamma(\text{H}_2\text{O})_n$	28
Figure 2.4 $P(\theta)$ distributions for $\Gamma(\text{H}_2\text{O})_n$	29
Figure 2.5 H- Γ probability distributions for $\Gamma(\text{H}_2\text{O})_n$	31
Figure 3.1 $P(r_{cm})$ and $P(\theta)$ distributions for $\text{F}^-(\text{H}_2\text{O})_n$	46
Figure 3.2 $P(r_{cm})$ and $P(\theta)$ distributions for $\text{Cl}^-(\text{H}_2\text{O})_n$	52
Figure 3.3 $P(r_{cm})$ and $P(\theta)$ distributions for $\text{Br}^-(\text{H}_2\text{O})_n$	53
Figure 3.4 $P(r_{cm})$ and $P(\theta)$ distributions for $\Gamma(\text{H}_2\text{O})_n$	55
Figure 3.5 $P(r_{cm})$ and $P(\theta)$ distributions for $\text{Cl}^-(\text{H}_2\text{O})_{20}$	66
Figure 3.6 Comparison of MC and MD $P(r_{cm})$ distributions for $\text{Cl}^-(\text{H}_2\text{O})_n$ and $\Gamma(\text{H}_2\text{O})_n$	67
Figure 4.1 NaI adiabatic potential energy curves.....	77
Figure 4.2 Representative ground-state NaI($\text{H}_2\text{O})_n$	95
Figure 4.3 Thermal distribution of initial Na-H ₂ O distances	96
Figure 4.4 Distributions of ground-state NaI internuclear separations and Franck-Condon energy gap distributions	97
Figure 4.5 NaI($\text{H}_2\text{O})_n$ Excited-state population decay	100
Figure 4.6 Distributions of excited-state NaI vibrational periods	102
Figure 4.7 Average NaI dipole moment and average Na-H ₂ O force	104
Figure 4.8 Average weight of the ionic state in the NaI electronic structure.....	107
Figure 4.9 Two-photon probe signals for NaI($\text{H}_2\text{O})_n$ photodissociation on the X state .	111
Figure 4.10 Two-photon probe signals for NaI($\text{H}_2\text{O})_n$ photodissociation on the I state.	112
Figure 4.11 One-photon probe signals for NaI($\text{H}_2\text{O})_n$ photodissociation on the X state	114
Figure 4.12 One-photon probe signals for NaI($\text{H}_2\text{O})_n$ photodissociation on the I state..	115
Figure 4.13 Time-resolved photoelectron spectra for NaI($\text{H}_2\text{O})_n$	119
Figure 5.1 NaI adiabatic potential energy curves.....	127
Figure 5.2 Franck-Condon energy gap probability distributions and average shifts in the energy gaps relative to bare NaI as a function of cluster size.....	143
Figure 5.3 NaI($\text{H}_2\text{O})_n$ Excited-state population decay	146
Figure 5.4 Probability distributions of the water evaporation time.....	150
Figure 5.5 Two-photon probe signals for NaI($\text{H}_2\text{O})_n$ photodissociation on the X state .	154
Figure 5.6 Two-photon probe signals for NaI($\text{H}_2\text{O})_n$ photodissociation on the I state...	155

Figure 5.7 One-photon probe signals for $\text{NaI}(\text{H}_2\text{O})_n$ photodissociation	160
Figure 5.8 Change in free energy as a function of the solvent coordinate in solution....	162
Figure 5.9 Change in free energy as a function of the solvent coordinate for $\text{NaI}(\text{H}_2\text{O})_n$	163
Figure 5.10 Fit to the changes in free energy for $\text{NaI}(\text{H}_2\text{O})_n$	166
Figure 6.1 Franck-Condon energy gap probability distributions for H_2O , CH_3CN and NH_3	187
Figure 6.2 OPCS average shifts in the average Franck-Condon energy gaps relative to bare NaI	188
Figure 6.3 OPCS Franck-Condon energy gap probability distributions	189
Figure 6.4 in the average Franck-Condon energy gaps relative to bare NaI	190
Figure 7.1 OPLS, OPCS and PM3spc $P(r_{cm})$ distributions for $\text{Cl}^-(\text{H}_2\text{O})_{20}$	203
Figure 7.2 Representative $\text{Cl}^-(\text{H}_2\text{O})_{20}$ structure from PM3spc.....	204
Figure 7.3 DFT $P(r_{cm})$ distributions for $\text{Cl}^-(\text{H}_2\text{O})_{12}$	211
Figure 7.4 Average rotational and translational energies of NaI bound waters	228
Figure 7.5 Average NaI internuclear distance as a function of simulation time.....	231

List of Tables

Table 3.1 Parameters of the OPLS and OPCS model potentials.....	42
Table 3.2 Ionic radii and ion-water 0K binding enthalpies for the halide series	43
Table 3.3 Cluster enthalpies at 200 K	50
Table 3.4 Lennard-Jones parameters for varying chloride ion properties.....	64
Table 4.1 Model potential parameters for the NaI^+ probe states	92
Table 4.2 $\text{NaI}(\text{H}_2\text{O})_n$ properties	98
Table 4.3 Properties of the excited-state $\text{NaI-H}_2\text{O}$ forces	105
Table 5.1 Parameters of the OPCS model potential	135
Table 5.2 Features of $\text{NaI}(\text{H}_2\text{O})_n$ photodissociation dynamics	149
Table 5.3 Average excess Franck-Condon energies	157
Table 6.1 Properties of atom-solvent binary complexes	183
Table 6.2 Model potential parameters	186
Table 7.1 $\text{Cl}^-(\text{H}_2\text{O})_n$ and $(\text{H}_2\text{O})_n$ 300K binding enthalpies from PM3spc	200
Table 7.2 PM3 and PM3spc parameters.....	201
Table 7.3 $\text{Cl}^-(\text{H}_2\text{O})_n$ and $(\text{H}_2\text{O})_n$ 0K binding enthalpies from PM3spc	202
Table 7.4 $\text{Cl}^-(\text{H}_2\text{O})_n$ and $(\text{H}_2\text{O})_n$ 0K binding enthalpies from DFT	210
Table 7.5 PM3 and PM3spq parameters	220
Table 7.6 $\text{Cl}^-(\text{H}_2\text{O})_n$ and $(\text{H}_2\text{O})_n$ 0K binding enthalpies from PIMD.....	223
Table 7.7 Argon-solute and argon-solvent Lennard-Jones parameters.....	229

List of Abbreviations

AM1: Austin Model 1 semiempirical potential
CIP: Contact Ion Pair
CIS: Configuration Interaction with Singles excitations
CTTS: Charge Transfer To Solvent
DFT: Density Functional Theory
ET: Electron Transfer
FC: Frank-Condon energy
MC: Monte Carlo simulation method
MD: Molecular Dynamics simulation method
MDQT: Molecular Dynamics with Quantum Transitions method
MNDO: Modified Neglect of Differential Overlap
MO: Molecular Orbital
MP2: Möller-Plesset 2nd order perturbation theory
MRCI: Multi-Reference Configuration Interaction theory
NHC: Nose-Hoover Chain method
NNDO: Neglect of Differential Diatomic Overlap
OPCS: Optimized Parameters for Cluster Simulations
OPLS: Optimized Parameters for Liquid Simulations
PIMD: Path Integral Molecular Dynamics method
PM3: Parameter Method 3 semiempirical method
PM3spc: Parameter Method 3 with special parameters for classical simulations
PM3spq: Parameter Method 3 with special parameters for quantum simulations
PMF: Potential of Mean Force
QM/MM: Quantum Mechanics/Molecular Mechanics method
SSIP: Solvent-Separated Ion Pair
VB: Valence Bond theory
VDE: Vertical Detachment Energy
WHAM: Weighted Histogram Analysis Method

Theoretical Studies of Seeded Water Clusters: Structure, Thermodynamics and Photochemistry

Chapter 1

Introduction

1.1 Preamble

The solvation of ions and ion pairs in aqueous environments is of fundamental importance in biology, chemistry and environmental science. In biological systems, ions affect the conformations and activities of proteins and nucleic acids,¹⁻³ and the specificity of ion binding. For instance, ions regulate the electrostatic potentials, conductances, and permeability of cell membranes,^{4,5} the structure of micelles, and the hydrophobic (Hofmeister) effect, which drives partitioning, permeation, folding and binding processes.^{6,7} In chemistry, ions affect the rates of chemical reactions,^{8,9} and ion-exchange mechanisms, widely used for chemical separations.¹⁰ On the environmental side, heterogeneous chemistry involving sea salt aerosols is known to influence the chemical composition of the atmosphere.¹¹ Reactions involving halides, for example, at the interface between air and aerosol particles have been proposed to be responsible for the release of reactive halogen radicals into the atmosphere.¹² Since most of these biological and chemical processes occur in the presence of water molecules, water is a solvent of choice for fundamental and prototypical studies of ions and ion pairs.

It has been well established that the understanding of many biological and chemical processes involving ions and ion pairs in aqueous solution requires a deep knowledge of the molecular-level details of solute-solvent interactions. However, many properties of chemical species in the bulk phase are often different from the properties of the gas-phase species.^{13,14} As such, the bulk properties of a given solute result from collective interactions with the solvent and cannot be inferred from the properties of the

gas-phase species alone. Since the development of supersonic jets, clusters – an intermediate form of matter between the gas and bulk phases – have been used to probe the evolution of various properties from the gas to bulk phases. In particular, studies of clusters seeded with charged or neutral solutes provide means for detailed investigations of the role of individual solvent molecules in the solvation and reaction dynamics of these solutes.

As a matter of fact, the elucidation of the complex hydrogen bonding network within water clusters was ranked the eighth most significant scientific breakthrough of 2004 by Science Magazine. Moreover, the study of fundamental issues concerning ions and ion pairs in water clusters was underlined as being one of the significant aspects of this field of research.¹⁵ To cite the editor-in-chief of Science Magazine,

“Another dispute centers on where ions in a large body of water hang out. Do they reside at the surface or get sucked into the interior? Conventional wisdom says electrostatic forces at the water's surface repel ions that are abundant in seawater, forcing them to go deep. But researchers tracking sea salt particles in the air over Los Angeles say the particles are so rich in halides (chemical relatives of fluorine) that those ions must be present on the water's surface. This year, computer simulations supported the idea. If true, atmospheric scientists may have to ponder new types of chemical reactions occurring on the surface of aerosol particles.”¹⁵

The central focus of this thesis is to deepen our knowledge of surface vs. interior solvation of halides ions in water clusters, and to further our understanding of how solvation and the solvation structure around ions affect photochemically-induced reactions of alkali-metal halides, as could occur in sea-salt aerosols in our atmosphere. In this work, we develop and employ a variety of model, semiempirical, first-principles and

mixed model/first-principles techniques to address these fundamental aspects of ion and ion pair solvation.

1.2 Solvation of ion and ion pairs in aqueous environments

Salt ion-pair charge separation induced by solvent is one of the simplest and most fundamental processes in Nature. Nonetheless, the microscopic details of the charge separation process are yet to be fully understood. It is believed that charge separation in solution is related to different structural arrangements of solvent molecules around the individual ions forming the ion pair. In fact, ions are classified as kosmotropes (structure makers) or chaotropes (structure breakers) according to their relative abilities to induce the structuring or disordering of the water hydrogen-bonding network.¹⁶ As mentioned above, it has been observed both experimentally and theoretically that large halide ions (chaotropes) prefer to reside at the surface of small- to medium-sized water clusters, whereas alkali metal cations (kosmotropes) prefer to reside in the interior of the cluster. Detailed studies of this different solvation behavior could explain the charge separation reaction that occurs when alkali metal-halides are immersed in an aqueous solution, as well as the predominance of halide ions at the surface of sea salt aerosols. As such, many experimental and theoretical studies have been dedicated to elucidating the energetics and structure of ion-water clusters.

The first experimental technique applied to the study of ion solvation in clusters was high-pressure mass spectrometry. This technique provides thermodynamic data such as stepwise enthalpies, entropies, and free energies of ion solvation.¹⁷⁻²³ In cases where

the ion-solvent interaction is much stronger than the solvent-solvent interaction, structural information can be deduced from sharp changes in the evolution of the thermodynamic properties. The stepwise binding enthalpies of sodium in water clusters, for example, converges to the bulk limit with the addition of six water molecules, indicating that the formation of the first spherical solvation shell around the cation is sufficient to approach the bulk solvation.¹⁷ This experimental technique, however, is limited to cluster sizes of 10 or less water molecules, due to solvent condensation within the instrument.

Larger ion-solvent clusters can be studied with photoelectron spectroscopy. This technique measures the binding energy of the ion's outermost valence electrons. The solvated ion outer-shell electron binding energies are strongly dependent on the strength of the ion-solvent interactions and thereby, on the ion-solvent intermolecular distance. The cluster-size dependence of the electron vertical detachment energies (VDEs) and the electrostatic stabilization energies of the solvated ion – defined as the difference between the VDE and the electron affinity of the bare ion – are, therefore, sensitive to changes in the structural configuration of solvent molecules surrounding the ion.²⁴⁻⁴⁰ Photoelectron studies combined with simulations for iodide-water clusters containing up to 60 water molecules, for example, suggested that iodide ions reside at the surface, rather than in the interior, of clusters of even the largest sizes measured.^{29,41} The authors concluded that complementary theoretical and experimental information on these clusters, such as vibrational and charge transfer excitation spectra, would be required to reach final conclusions on the surface vs. interior solvation of iodide in water clusters.^{29,41}

Spectroscopic studies may provide much more detailed insight into the properties and structure of ion-solvent clusters. Vibrational spectroscopy can provide detailed information about aqueous solvation structures since the O-H stretching frequencies are very sensitive to the local environment around water molecules. In bulk water, the O-H stretching frequency is broad and featureless. However, in the presence of an ion, the observed O-H stretch involves a combination of a number of interwater hydrogen-bonded, ion-bound and nonbonded O-H stretches.⁴²⁻⁵⁰ The infrared spectra of cations in small water clusters thus display distinct splittings of the O-H stretching frequencies. However, the spectra of solvated halides normally show broadening, such that the splitting of the O-H stretching bands could only be observed for very small clusters.⁵¹ The recent development of argon predissociation spectroscopy, where mass-selected ion-water clusters are embedded in a cluster of Ar atoms,⁵¹⁻⁵⁶ has allowed the spectral resolution of the O-H stretching frequencies in anion-water clusters for a larger range of cluster sizes,⁵⁵ and the splitting of the O-H frequencies as a function of cluster size and the solvation structures could be inferred from the spectra.^{57,58}

Experimental studies of ion pairs in bulk solution have also provided insight into the solvation structure of the ions. On the grounds of salt solubilities, one would assume that at 300 K about nine water molecules per ion pair are necessary to dissolve NaCl in water and only about five for NaI.⁵⁹ Recent developments in surface-sensitive vibrational spectroscopy experiments have shown that large halide ions tend to lie at higher concentrations at the air/liquid interface of concentrated salt solutions, in contrast to their counter-ions which tend to remain deep within the bulk liquid.^{60,61} These results are

consistent with the surface solvation observed in halide-water clusters. In fact, the apparent hydrophobic character of the iodide ion has been shown to be responsible for the surface solvation structure of NaI ion pairs in small- to medium-sized water clusters, as iodide drags its sodium counterion to the surface of the water cluster. This has important implications for the photodissociation dynamics of $\text{NaI}(\text{H}_2\text{O})_n$ clusters.⁶²

In summary, understanding the microscopic details of ion solvation in water clusters is essential to elucidate complex chemical problems, such as the charge separation of salt ion pairs, the predominance of large halide ions at the surface of sea salt aerosols, and the effects of the solvation properties of solutes on chemical and biochemical processes occurring within the human body and in our environment. However, experimental techniques are limited in cluster size, and in the knowledge obtained about the microscopic details of ion solvation. The first objective of this thesis is to provide an in-depth theoretical analysis of the microsolvation of halides by rigorously investigating their structural and thermodynamic properties, in order to bridge the gap in available experimental data, and gain a more profound knowledge of the solute-solvent and solvent-solvent interactions governing the solvation properties of the ions.

1.3 Reaction dynamics in aqueous ion pair clusters

Solvent can affect elementary bond-forming and bond-breaking processes by either encaging reactive species and preventing them to escape from each other, or removing the excess excitation energy of the reactants through collisional cooling. Electron-transfer reactions are among the most elementary of all chemical processes and

they occur in many chemical and biological systems. Since electron-transfer reactions in natural environments are quite complex due to numerous interactions with the surrounding solvent matrix, studies of simplified model systems, such as photoinduced electron transfer in salt ion pairs, are required to understand the molecular details of this fundamental process. The advent of femtosecond spectroscopic techniques has provided an avenue to probe the real-time dynamics of electron transfer reactions in clusters and in the bulk.^{63,64}

Alkali-metal halides, and particularly NaI, have served as paradigm systems studies of photoinduced electron transfer reactions, because an avoided crossing region between the ground and excited electronic states, formed by the crossing of ionic and covalent states, occurs at relatively short internuclear distances in these ion pairs.^{63,64} Since electron-transfer dynamics in gas-phase NaI are well characterized, the system provides a solid foundation for comparative solvation studies in clusters and in the bulk. Of particular interest is the influence of individual solvent molecules on the branching ratio of the population of ground-state atomic ($\text{Na} + \text{I}$) products versus that of dissociated ($\text{Na}^+ + \text{I}^-$) ions and on long-lived excited-state ($\text{Na}^* + \text{I}$) species. Polar solvents are known to stabilize ionic species, and as such, polar solvents should have a more dramatic effect on photodissociation reactions of ionic species than nonpolar solvents. The ground NaI (ionic) state is highly stabilized by the presence of polar solvent molecules relative to the excited state, which is mostly covalent in the Franck-Condon region, leading to a large blue shift of the ground to excited state transition wavelength. Another consequence of the differential stabilization of the ionic and covalent states is that the curve-crossing

region will be shifted to larger internuclear distances than in the gas phase, where coupling between the two states is much weaker, leading to an increased production of atomic $\text{Na}(\text{solvent})_n + \text{I}(\text{solvent})_n$ products relative to the gas phase.

A further issue concerning the effects of polar solvent molecules on the photodissociation and electron transfer dynamics of ion pairs is the existence of a possible equilibrium between stable contact ion pair (CIP) and solvent-separated ion pair (SSIP) structures in the ground state, in contrast to the bulk behavior.⁶² The transition from the ground state to the first excited state mainly occurs from CIP conformations.⁶² For SSIP structures, the possibility of electron transfer occurring between the ground state Na^+ and I^- ions is expected to be smaller due to the presence of solvent molecules between the two ions. This suggests that vanishing excitation efficiency might be a good indicator of charge separation in clusters.⁶⁵

The additive solvation effects on photodissociation dynamics cannot yet be thoroughly characterized by experimental means, because neutral parent clusters cannot be mass-selected by time-of-flight mass spectroscopy prior to photoexcitation. Nonetheless, recent experimental studies have provided invaluable information concerning the dependence of the reaction dynamics on the degree of solvation of the solute species by polar solvent molecules.^{66,67} These studies have shown that the ground- to excited-state absorption threshold – which is proportional to the probability of undergoing excitation – shows a strong blue shift upon addition of the first solvent molecule, indicating an increase in the ground- to first excited-state Frank-Condon energy gap. However, beyond this first solvating molecule, the frequency of the

absorption threshold is barely affected. Furthermore, the Na + I atomic product probability was shown to increase dramatically with the addition of the first water molecule, and to decay monotonically with the addition of more water molecules reflecting the fact that the avoided crossing region between the electronic states is indeed moved towards larger NaI internuclear distances in the presence of polar molecules.

Finally, related multi-photon ionization studies of alkali-metal halides in polar solvent clusters may also provide evidence for ion-pair charge separation in the presence of polar molecules. In experimental multi-photon ionization studies of NaI ion pairs in polar solvent clusters of water, acetonitrile and ammonia,⁶⁸ a very clear solvent-selective behavior was observed in the distribution of the $\text{Na}^+(\text{solvent})_n$ product ions, detected by time-of-flight mass spectrometry. Product clusters of sizes up to 50 have been observed for NaI-water cluster multi-photon ionization, but no clusters larger than size 10 and 7 have been observed in the case of ammonia and acetonitrile clusters, respectively. The lack of large cluster products has been attributed to early ground-state charge separation for the latter two solvents, since photoexcitation to the first NaI excited state does not occur from SSIP configurations. However, other photochemical behavior, such as charge-transfer-to-solvent (CTTS) excitation might be possible in SSIPs. The absorption threshold wavelength for the CTTS transition, estimated from photoionization work on iodide-water clusters,⁶⁹ is quite similar to that for the ground to excited state transition of free NaI, around 300 nm. Thus, in clusters, CIPs and SSIPs may both absorb light with equivalent efficiencies, the former to the $\text{NaI}(\text{solvent})_n$ excited state akin to gas-phase NaI and the latter to a CTTS state.

Solvent molecules not only affect reaction dynamics through differential solvation of solute charge distributions and the electronic structure of reactive species, their presence can also enhance bond formation by encaging reactive species or by removing the excitation energy of reactants through collisional cooling. Solute-solvent vibrational energy transfer phenomena can thus strongly influence the overall dynamics of product formation in chemical reactions, and is a fundamental issue which needs to be addressed when considering solvation effects on reaction dynamics. It was found in a previous femtosecond pump-probe experiment of NaI in rare-gas clusters, for example, that the excited-state $[\text{Na}\dots\text{I}]^*$ transient species was stabilized through collisional vibrational energy relaxation with surrounding rare gas atoms, leading to long-lived probe signals. This is due mainly to the fact that the transient species relaxes to the electronically excited-state ground vibrational level through solute vibrational-to-solvent translational energy transfer. This $[\text{Na}\dots\text{I}]^*$ vibrational relaxation favors trapping of the excited state at short internuclear separations. Since probability of nonadiabatic transition to form atomic products is inversely proportional to the NaI internuclear separation in the curve-crossing region, a decrease in the amount of dissociated atoms was observed.

Vibrational energy transfer in polar solvents has an even greater effect on photodissociation reactions than non-polar solvents. In femtosecond pump-probe experiments of I_2^- in liquid water, an ultrafast vibrational energy relaxation of the excited-state transient species was observed on the picosecond timescale, leading to a radiative transition and recombination of the transient species in the ground state.^{70,71} In subsequent studies of the same system, the population evolution of a given excited

vibrational state was followed by femtosecond spectroscopy, and ultrafast vibrational energy relaxation processes were also observed.⁷² It is clear from these studies that Coulombic interactions play a central role in the vibrational energy transfer between a polar solute and a surrounding polar solvent.

Previous studies have shown that the product ratios of photoinduced electron transfer reactions can be influenced by the vibrational state of the excited species. It would therefore be interesting to be able to prepare and monitor species in a given vibrational state in order to understand the effects on the electron transfer dynamics. Microscopic control of the outcome of a chemical reaction is a long-standing dream of physical chemists.⁷³ Recently, femtosecond lasers have emerged as a particularly suitable tool for the so-called quantum control of reaction dynamics. Gerber and co-workers were pioneers in demonstrating the use of tailored femtosecond laser pulses from a computer-controlled pulse shaper to control the branching ratios of various photodissociation channels.⁷⁴ Further, Rabitz and co-workers recently suggested that high-intensity laser pulses allow control of dissociative rearrangement reactions in which chemical bonds are not only selectively broken, but also newly formed.⁷⁵ In the case of salt ion pairs, it was demonstrated that quantum control of the initial vibrational level in excited-state gas-phase NaI can lead to a 60% increase in the INa^+/Na^+ product ratios following excitation to the probe state.⁷⁶

Given the difficulties of performing experimental studies on neutral solute-solvent clusters, the second objective of this thesis is to perform theoretical simulations of the photodissociation dynamics of alkali-metal halides in the presence of an increasing

number of water molecules, in order to assess the stepwise solvation effects on the electron transfer dynamics, and to understand molecular-level solute-solvent interactions which govern solute to solvent energy transfer of ground-state and excited-state salt ion pairs in aqueous clusters. Of particular importance in solvated ion pairs is the possibility of CIP to SSIP solvation state interconversion following ground-state vibrational excitation, and the possibility of opening an alternate photochemical route (CTTS states) resulting from excitation of clusters in the SSIP solvation state.

1.4 Objectives

The primary objective of this thesis is to understand how the solvation structure of paradigm solutes in solvent clusters affects their reactivity. In this endeavor, the elementary electron transfer reaction occurring upon photoexcitation of alkali-metal halides is chosen as a model system to advance our knowledge of solvation effects on reaction dynamics, mainly because photodissociation of the gas-phase ion pairs has been well characterized.⁷⁷ The surface solvation state adopted by large halide ions in water clusters can have profound effects on the cluster photochemistry. A portion of this thesis is therefore dedicated to providing a detailed investigation of the solvation states adopted by halides in water clusters, before turning our attention to the effects of solvation on the photochemical behavior of NaI seeded solvent clusters. Various theoretical techniques are employed for these purposes, and are thoroughly detailed in each chapter.

In Chapters 2 and 3, a rigorous and quantitative investigation of the solvation structure and thermodynamics of halide-water clusters is reported, presented in order to

characterize the nature of the ion interior and surface solvation states, and to establish which properties govern the solvation structure of the ions in water clusters. Iodide is the first ion for which the existence of the surface solvation state in water clusters was hypothesized.²⁹ Accordingly, iodide has become a paradigm ion for investigations of microsolvation in clusters, and Chapter 2 is devoted to iodide-water clusters. The main objectives of this chapter are to determine in which range of cluster sizes the transition from surface to interior solvation occurs, and what factors finally drive iodide to preferentially adopt an interior solvation state like in the bulk. For these purposes, we evaluate the potentials of mean force (PMF), or the free energy change along the ion-to-water center-of-mass distance, which constitutes the most rigorous means to establish the thermodynamically favored solvation state of solutes in solvent clusters. In Chapter 3, the investigation is extended to the full halide series, providing for the first time a detailed comparison of the solvation structure and thermodynamics of these ions in water clusters across the halide series.

The main objective of Chapters 4 and 5 is to investigate the effects of solvation on photochemically-induced reactions of alkali-metal halides, NaI in particular. Chapter 4 centers on the investigation of photodissociation dynamics of $\text{NaI}(\text{H}_2\text{O})_n$ clusters as a function of increasing cluster size, in order to assess the gradual effects of solvation on the NaI electron transfer reaction. Femtosecond probe signals and time-resolved photoelectron spectra are simulated for connection with experiment, and to gain a better understanding of experimental observations concerning $\text{NaI}(\text{H}_2\text{O})_n$ cluster photodissociation dynamics. In Chapter 5, an improved methodological approach is

employed, which allows more quantitative simulations of the photodissociation dynamics of even larger clusters. The present findings about the NaI electron transfer process in clusters are then connected and contrasted with earlier theoretical predictions based on the theory of electron transfer in solution.

In Chapter 6, a different aspect of NaI photodissociation is explored. The previous two chapters concentrate on the details of the NaI excited-state dynamics following photoexcitation, and on the resulting electron transfer reaction, in the presence of an increasing number of solvent molecules. Chapter 6 focuses on the photoexcitation process itself, and on the solvent-selective behavior of multi-photon excitation of NaI in water, ammonia and acetonitrile clusters observed experimentally. As mentioned earlier, the disappearance of the multi-photon ionization product signal could be attributed to ground-state NaI charge separation within the cluster, to the predominance of photoexcitation to a charge-transfer-to-solvent (CTTS) state, or to massive solvent evaporation as was observed for $\text{NaI}(\text{H}_2\text{O})_n$ clusters in Chapters 4 and 5. Recent simulations have rendered the argument of ground-state charge separation questionable.^{62,78,79} Characterization of the CTTS states in large clusters is a colossal task that may not even be possible with currently available state-of-the-art computational resources, and before we engage into intensive simulations of the photodissociation dynamics akin to those performed in Chapters 4 and 5 for all solvents, we wish to confirm or rule out one last hypothesis that could explain the solvent-selective behavior of NaI multi-photon ionization in clusters, i.e. whether different extents of differential solvation of the ground and excited states could result in inhibition of photoexcitation for

some solvents at smaller cluster sizes than for others. Accordingly, the objective of Chapter 6 is to investigate the photochemical properties of NaI in ammonia, acetonitrile and water clusters.

The investigations performed in these chapters have lead to a number of new research avenues. Chapter 7 explores a few of these avenues, and presents preliminary results obtained from methodologies developed specifically for that purpose. The first section of the chapter is devoted to the development of first principles methodologies aimed at providing a highly accurate description of the solvation structure and thermodynamics of seeded clusters, as PMFs obtained with model potentials do not seem to yield definitive results. Since the generation of PMFs employing “on the fly” high-level quantum chemistry calculations would be computationally prohibitive, two first-principles methodologies are explored, one based on semiempirical quantum chemistry “on the fly”, and the other based on the refinement with a limited number of high-level quantum chemistry calculations of PMFs generated with model potentials or with lower-level quantum chemistry methods. Since seeded water clusters are only stable at low temperatures and are typically held together by weak interactions that involve light hydrogen atoms, they may be prone to quantum (nuclear) effects, and accordingly, the second section addresses the inclusion of quantum effects by means of path integral molecular dynamics. As mentioned earlier, ion pairs are known to exist as contact ion pairs (CIP) or solvent-separated ion pairs (SSIP) in clusters, both species with different photochemical behavior. While CIPs have optically accessible excited states akin to those of bare ion pairs, but modulated by the solvent field, SSIP photoexcitation presumably

gives rise to charge-transfer-to-solvent (CTTS) states with very different fate and dynamics. In the third section, we thus explore the CIP to SSIP interconversion following NaI vibrational excitation and subsequent relaxation, as a possible avenue for solvation control of NaI photochemistry in clusters. Controlling the outcome of chemical reactions has been a long-standing goal of physical chemists. Finally, our investigations of the $\text{NaI}(\text{H}_2\text{O})_n$ photodissociation dynamics revealed that solvent molecules influence the electron transfer process, but rapid solvent evaporation precludes the observation of an activated inverted electron transfer process akin to what happens in solution. By embedding these clusters in a rare gas matrix, solvent evaporation could be greatly reduced, and therefore the gradual effects of solvation on NaI photodissociation dynamics, as a function of increasing cluster size, could be observed more readily. Accordingly, preliminary results of the photodissociation dynamics of $\text{NaI}(\text{H}_2\text{O})_n \bullet \text{Ar}_m$ clusters are presented in the last section of Chapter 7.

To summarize, this thesis presents an array of simulation methodologies that were developed to provide valuable insight into the effects of solvation on the elementary electron transfer reaction occurring upon photoexcitation of paradigm NaI ion pairs, and advance our fundamental knowledge of the role of solvent in chemical reactions in general, with the hope that the newly gained knowledge for simple, prototypical systems can be applied to simulated and better understand electron transfer processes in more complex molecular systems. The solvation structure of NaI in solvent clusters greatly affects the cluster photochemistry. The surface solvation state adopted by large halide ions in water clusters is of particular interest because it may be responsible for a different

photochemical behavior, relative to other solvents, such as acetonitrile and ammonia, where the ions dwell in the cluster interior.^{78,79} The determination of the cluster size range at which the transition from surface to interior solvation occurs is also of fundamental importance since this transition could explain the change in alkali metal-halide cluster photochemistry as a function of cluster size. Moreover, the detailed investigation of the “hydrophobic” nature of large halide ions can advance our understanding of chemical reactions involving these ions in the atmosphere and in living organisms.

Theoretical Studies of Seeded Water Clusters: Structure,
Thermodynamics and Photochemistry

Chapter 2

On the Transition From Surface to Interior Solvation in Iodide-Water Clusters

Published as:

Denise M. Koch and Gilles H. Peslherbe
Chemical Physics Letters 359, 381 (2002)

2.1 Introduction

Ionic hydration has been the focus of numerous studies over the years, due to its fundamental importance in chemistry,⁸⁰ biology⁸¹ and environmental science.⁸² Despite this long-lasting interest, the molecular-level details of ionic hydration have yet to be fully understood. Recent developments in experimental and theoretical techniques pertaining to cluster studies offer new possibilities for probing these processes.⁸³ In particular, cluster studies provide means for detailed investigations of the role of individual solvent molecules in the solvation of ionic species. An important issue in ionic cluster studies is the hydration structure of halide ions. Numerous experimental^{21,29,46,84,85} and theoretical^{58,86-90} studies suggest that large halide ions preferentially sit at the surface of small-to-medium sized aqueous clusters, rather than being fully surrounded by water molecules, as they would be in the liquid phase.

Previous theoretical studies have made a connection between the solvation structure of ions and the competing ion-solvent and solvent-solvent interactions.⁹¹⁻⁹⁴ For large halides, since the ion-water binding energy is of a similar magnitude as the water-water binding energy, the water molecules tend to bind to each other rather than to the ion, and the ion-water interaction is not strong enough for the ion to disrupt the relatively stable water network. A key question that arises from the existence of surface solvation states for large halide ions in aqueous clusters concerns the cluster size at which the solvation behavior of these ions converge to bulk, *i.e.* at what cluster size does the ion adopt an interior, bulk-like, solvation structure? Markovich *et al.*²⁹ analyzed the $\text{I}^- (\text{H}_2\text{O})_n$

cluster ($n=1-60$) vertical detachment energies and solvent electrostatic stabilization energies resulting from photoelectron spectra, and could not conclude with certainty whether the clusters were in an interior or a surface solvation state. More recently, Coe⁹⁵ combined small cluster experimental solvation data,^{21,29,92} the results of simulations in model polar solvent clusters of intermediate size,⁹⁶ and limiting continuum dielectric trends for large clusters to determine the evolution of the ion solvation free energy from the smallest cluster size to bulk. This analysis predicts that a gradual transition from surface to interior solvation occurs over the range $n=1-60$, and the transition to bulk behavior occurs around $n \sim 60$.

In the present work, we perform a quantitative investigation of the thermodynamics of surface vs. interior solvation in $\Gamma^-(\text{H}_2\text{O})_n$ clusters in order to identify the possible transition from surface to bulk behavior. A convenient coordinate for discriminating between surface and interior solvation is the distance between the ion and the solvent center of mass, which would be close to zero for an ideally spherically solvated interior ion, and obviously deviates significantly from zero for a surface solvation state.⁶² We calculate the free energy change along this coordinate, *i.e.* as the ion is forced to move towards or away from the solvent cluster center of mass, by means of constrained Monte Carlo simulations with model potentials. These potentials of mean force (PMF), as well as cluster structural properties, are investigated for $\Gamma^-(\text{H}_2\text{O})_n$ clusters ($n=32, 64$) with both non-polarizable and polarizable model potentials in order to assess the importance of polarizability on the thermodynamics of the halide-water clusters.⁹⁷ A brief account of the model potentials and simulation procedure is given in the next

section. This is followed by a discussion of our simulation results, and by concluding remarks.

2.2 Simulation Procedure

The simulation procedure has been thoroughly described elsewhere,^{62,97} and only a brief summary is provided here. Canonical ensembles of cluster configurations are generated at a temperature of 200 K by the Metropolis Monte Carlo method.⁹⁸ Each new trial configuration is generated randomly by translating one water molecule in every Cartesian direction, and rotating it around its Euler angles. The range of displacements for each degree of freedom was chosen to ensure an overall configuration acceptance ratio of ca. 40%.⁶² The data is collected - after proper equilibration - in the form of successive Markov chains. This procedure allows us to a) account for evaporation of water molecules by discarding from data collection the chains in which evaporation of one or more water molecules has occurred, and b) to ensure that multiple local minima are sampled by gradually heating the clusters to 500 K and cooling them down in between each new chain. Overall, 2 to 4 million configurations are generated in a given simulation.

Two classical intermolecular model potentials are employed in order to describe the solvent-solvent and solute-solvent interactions. The first model, hereafter referred to as OPLS, consists of the TIP4P water model⁹⁹ supplemented by optimized parameters for liquid simulations (OPLS).^{97,100} The second model, hereafter referred to as OPCS,⁹⁷ involves a polarizable five-site water model and optimized parameters for cluster

simulations (OPCS). The latter model employs a water model with gas-phase experimental geometry, a three-dimensional point charge distribution, a polarizable site and distributed repulsion-dispersion sites, while the ion carries a point charge, a polarization site and a repulsion-dispersion site.^{62,97} The water-water and ion-water interactions are parameterized from experimental data supplemented by ab initio calculations for small clusters.⁹⁷

The potential of mean force $W(r_{cm})$, where r_{cm} denotes the distance between the ion and the solvent center of mass, is generated by means of statistical perturbation theory evaluation of free energy differences.¹⁰¹ The distance between the ion and the solvent center of mass is constrained to a given value r_{cm} in the course of Monte Carlo simulations via a Lagrange multiplier approach.⁹⁸ For each configuration in the ensemble, the ion is displaced so as to increase and/or decrease the distance between the ion and the solvent center of mass by an increment dr_{cm} of 0.2 Å, and the Helmholtz free energy or potential of mean force change is evaluated as

$$\Delta W(r_{cm}) = W(r_{cm} + dr_{cm}) - W(r_{cm}) = -k_B T \ln \left\langle e^{-[U(r_{cm} + dr_{cm}) - U(r_{cm})]/k_B T} \right\rangle_{r_{cm}}$$

where $\langle \dots \rangle$ denotes the canonical ensemble average. In practice, we make use of the results of forward perturbation for a simulation constrained at the value r_{cm} , and those of backward perturbation for a simulation constrained at the value $r_{cm} + dr_{cm}$, and evaluate the free energy change by the acceptance ratio method of Bennett.¹⁰² This procedure also allows us to estimate error bars in the potential of mean force from the two distinct ensemble averages obtained from the simulations.⁹⁷ In the present simulations, the total

error in the potentials of mean force is ± 0.2 kcal/mol over the range of r_{cm} values 0 to 7 Å.

2.3 Results and Discussion

The potential of mean force (PMF) profiles are shown in Fig. 2.1 for $\Gamma(\text{H}_2\text{O})_n$ clusters ($n=32,64$) with both model potentials. The curves for $\Gamma(\text{H}_2\text{O})_{32}$ are quite broad and shallow, as seen from Figs. 2.1a and 2.1b, with a minimum at a distance between the ion and the solvent center of mass r_{cm} of ~ 2 Å. Two minima appear in the PMF profiles of $\Gamma(\text{H}_2\text{O})_{64}$, shown in Figs. 2.1c and 2.1d, suggesting that two distinct solvation states may exist for this cluster size. Accordingly, the r_{cm} probability distribution $P(r_{cm})$, calculated from the PMF data as $P(r_{cm}) = 4\pi r_{cm}^2 e^{-W(r_{cm})/kT}$ and shown in Fig. 2.2, suggest that only one solvation state is present for $\Gamma(\text{H}_2\text{O})_{32}$, but two distinct states may exist for $\Gamma(\text{H}_2\text{O})_{64}$.

Let us first turn our attention to $\Gamma(\text{H}_2\text{O})_{32}$ for which only one solvation state seems to be inferred from the $P(r_{cm})$ distributions. The PMF curves shown in Figs. 2.1a and 2.1b exhibit a large range of r_{cm} values, between ca. 0.5 and 3.5 Å, for which the PMF profile appears flat, and representative structures corresponding to these r_{cm} values, which are displayed in Figs. 2.3a and 2.3b, suggest that $\Gamma(\text{H}_2\text{O})_{32}$ is in a surface solvation state over this full range of r_{cm} values. Besides r_{cm} , a rather convenient coordinate for rigorous investigations of the solvation structure around ions is the angle θ between individual solvent molecules, the ion and the aqueous cluster center of mass, as depicted in Fig. 2.4.⁶² Large deviations from the isotropic angular probability

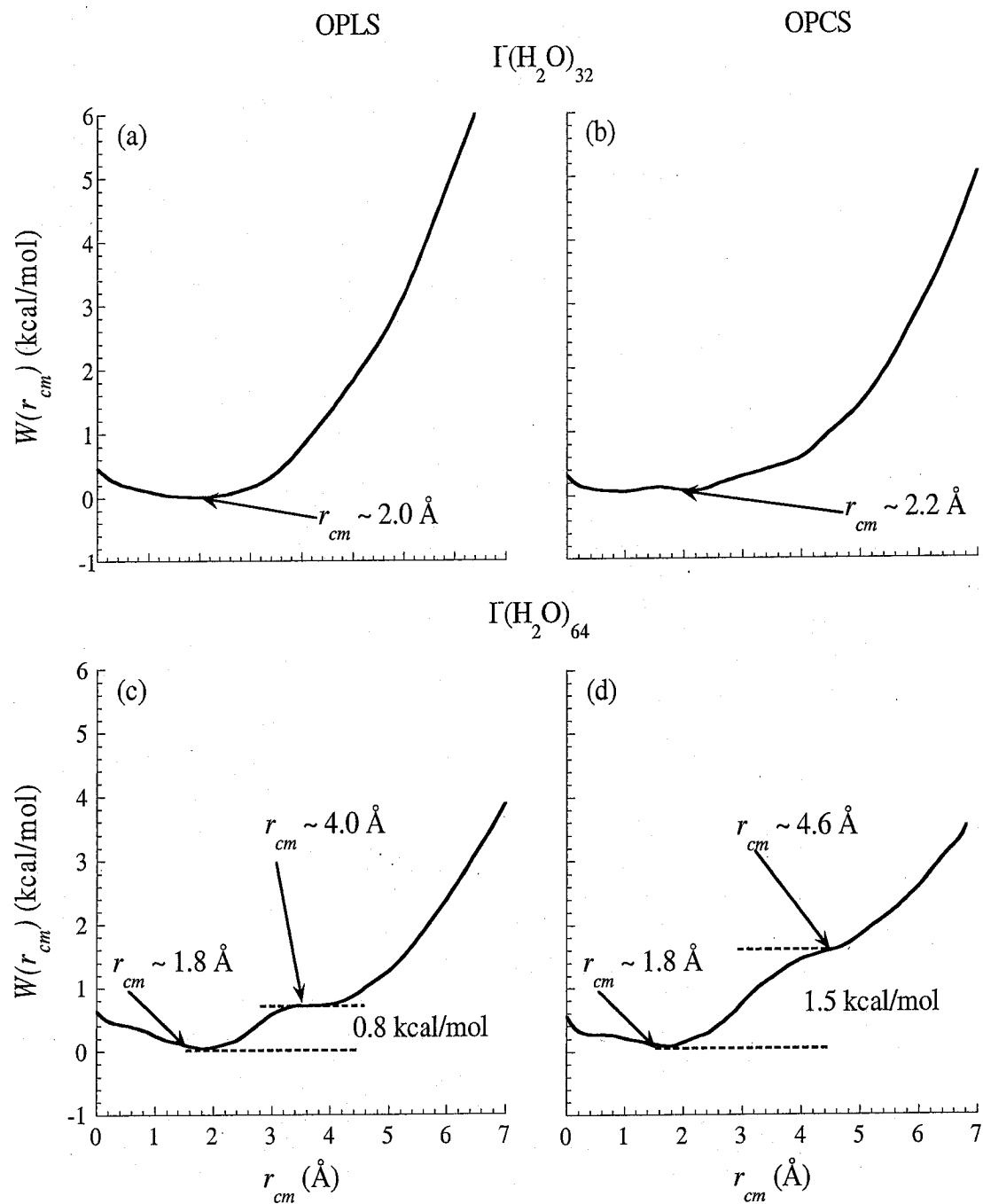


Figure 2.1 Potentials of mean force $W(r_{cm})$ generated with the OPLS (left panel) and OPCS (right panel) model potentials for (a) and (b) $\Gamma(\text{H}_2\text{O})_{32}$, and (c) and (d) $\Gamma(\text{H}_2\text{O})_{64}$.

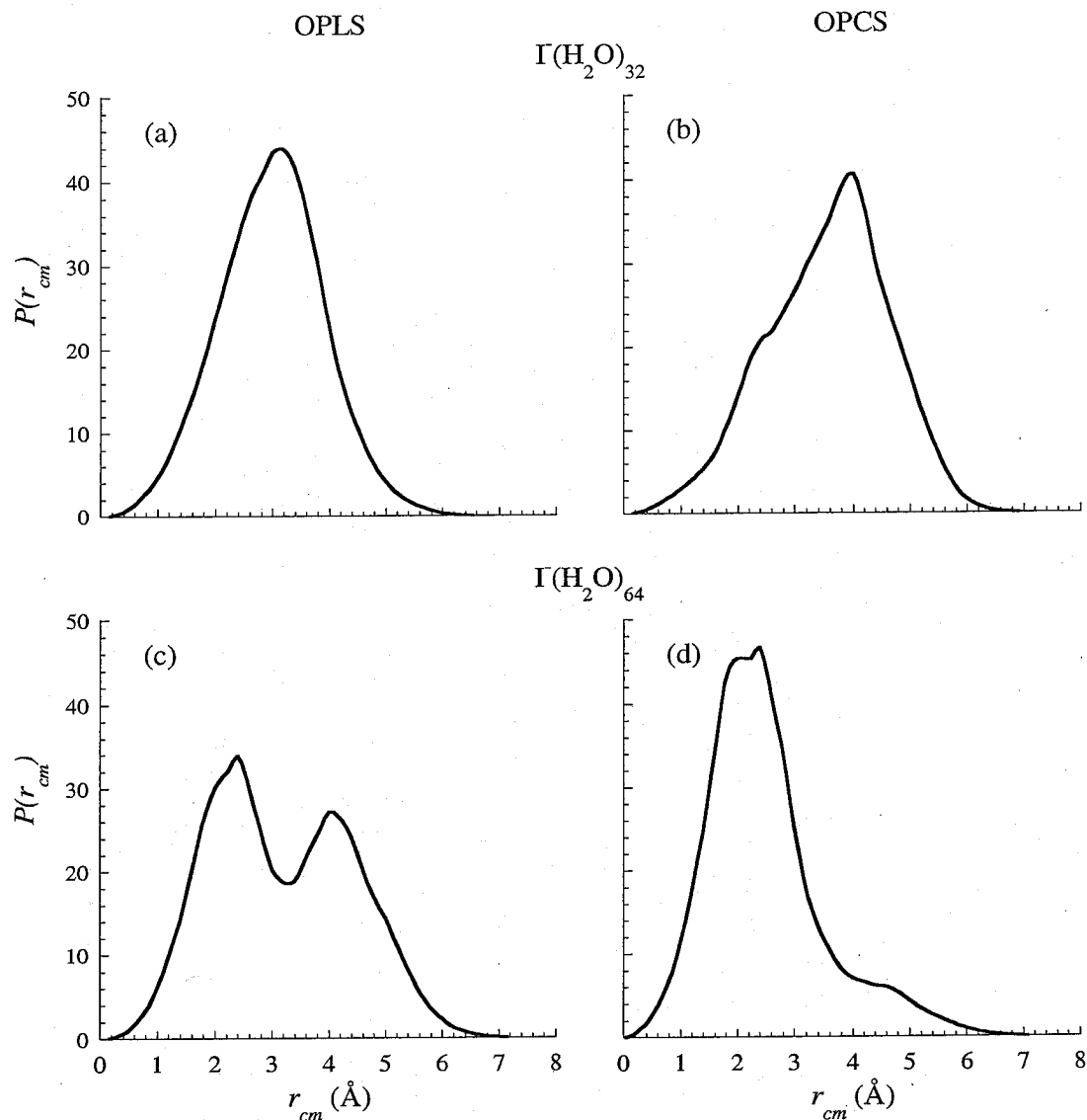


Figure 2.2 Probability distributions of the distance between the ion and the solvent center of mass $P(r_{cm})$ for (a) and (b) $\Gamma(\text{H}_2\text{O})_{32}$, and (c) and (d) $\Gamma(\text{H}_2\text{O})_{64}$ with both the OPLS (left panel) and OPCS (right panel) model potentials.

distribution $P(\theta)=\sin\theta$ are an indication of surface solvation.⁶² The angular probability distribution $P(\theta)$, displayed in Fig. 2.4a, are very similar for both $r_{cm} = 0.8$ and 3.6 Å. In both cases, a few water molecules are found on the side of the ion opposite to the solvent center of mass, suggesting that the cluster is in a surface solvation state over this wide

range of r_{cm} values. It must be noted that these clusters are not always spherical, as shown in Fig. 2.3a, such that the ion can still be on the surface of the cluster while having a small r_{cm} value.

As mentioned earlier, two minima appear in the PMF curves for $\Gamma^-(\text{H}_2\text{O})_{64}$, shown in Figs. 2.1c and 2.1d. The resulting $P(r_{cm})$ distribution for the OPLS model potential, which is shown in Fig. 2.2c, peaks at distances between the ion and the solvent center of mass of ca. 2.2 and 4.4 Å, clearly indicating the existence of two distinct solvation states. Representative structures shown in Figs. 2.3c and 2.3d for the clusters at these two r_{cm} values obviously correspond to interior and surface solvation structures, respectively. The angular probability distributions shown in Fig. 2.4b also demonstrate that the water molecules are more or less isotropically distributed around the iodide at $r_{cm} = 2.2$ Å, whereas a few molecules are found on the side of the ion opposite to the solvent center of mass for $r_{cm} = 4.4$ Å. The latter distributions actually resemble those for $\Gamma^-(\text{H}_2\text{O})_{32}$ in Fig. 2.4a, which we have shown to possess a surface solvation structure. Therefore, for a cluster size of 64, two distinct solvation states are present, and the angular probability distributions confirm that these states correspond to interior and surface solvation of iodide.

The equilibrium constant between the interior and surface states K_{IS} can be evaluated as

$$K_{IS} = \frac{[Interior]}{[Surface]} = \frac{\int_{Int} r_{cm}^2 e^{-W(r_{cm})/kT} dr_{cm}}{\int_{Surf} r_{cm}^2 e^{-W(r_{cm})/kT} dr_{cm}} = \frac{\int_{Int} P(r_{cm}) dr_{cm}}{\int_{Surf} P(r_{cm}) dr_{cm}}$$

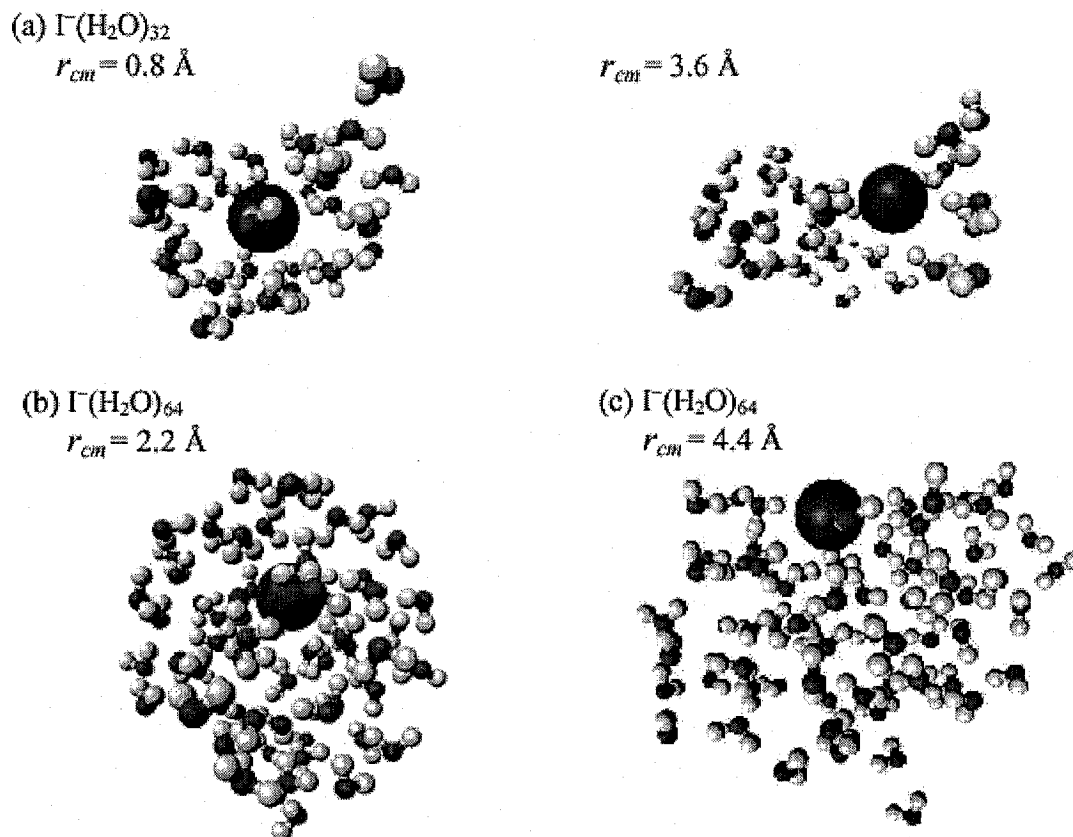


Figure 2.3 Representative OPLS structures for (a) $\Gamma(\text{H}_2\text{O})_{32}$ at $r_{cm} = 0.8$ and 3.6 \AA , (b) the interior solvation state of $\Gamma(\text{H}_2\text{O})_{64}$ at $r_{cm} = 1.8 \text{ \AA}$, and (c) the surface solvation state of $\Gamma(\text{H}_2\text{O})_{64}$ at $r_{cm} = 4.6 \text{ \AA}$.

where the integrals run over the appropriate r_{cm} values for the interior and surface solvation states, and the boundary between the two states is chosen at the minimum between the two peaks in the $P(r_{cm})$ distribution.⁹⁷ The resulting equilibrium constant is 1.6 ± 0.4 for the OPLS distribution of Fig. 2.2c, which indicates that the interior and surface states are almost equally likely for $\Gamma(\text{H}_2\text{O})_{64}$.

The effect of employing an explicitly polarizable model potential such as OPCS is to increase the free energy difference between the interior and surface solvation states of

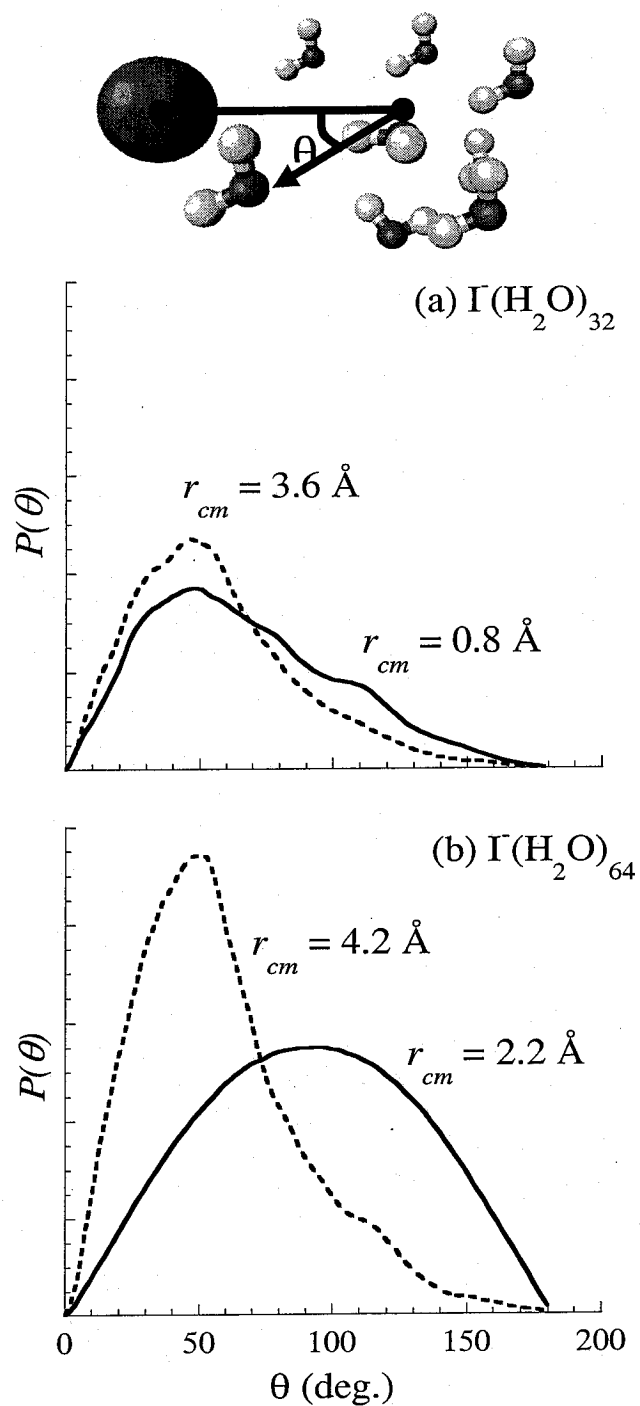


Figure 2.4 Angular probability distributions $P(\theta)$ for (a) $\Gamma(\text{H}_2\text{O})_{32}$ and (b) $\Gamma(\text{H}_2\text{O})_{64}$ predicted by the OPLS model. As shown in the inset, θ is defined as the angle between an individual solvent molecule, the ion and the solvent center of mass.

$\Gamma(\text{H}_2\text{O})_{64}$ from 0.8 kcal/mol to 1.5 kcal/mol (*cf.* Figs. 2.1c and 2.1d), which largely increases the predominance of the interior state over the surface state, as seen from the $P(r_{cm})$ distributions shown in Figs. 2.2c and 2.2d. With the OPCS model, the interior to surface equilibrium constant K_{IS} is 14.6 ± 0.8 , which represents a ten-fold increase in the population of the interior state relative to that of the surface state when compared to the OPLS predictions. We should point out that, in a theoretical investigation of the ion coordination number for $\text{Cl}^-(\text{H}_2\text{O})_n$ clusters, Stuart and Berne¹⁰³ found that polarizability favors surface solvation (up to a cluster size of 500), in contrast to our results for $\Gamma(\text{H}_2\text{O})_n$. We note that our own simulation results for $\text{Cl}^-(\text{H}_2\text{O})_n$ yield results similar to those of Stuart and Berne, even though different forms of polarizable models are employed, and we are presently investigating the differences between chloride-water and iodide-water clusters.¹⁰⁴

To further our understanding of surface vs. interior solvation as a function of cluster size, we consider the $P(r_{HI-})$ probability distributions for $\Gamma(\text{H}_2\text{O})_{32}$ and both solvation states of $\Gamma(\text{H}_2\text{O})_{64}$ in Fig. 2.5.¹⁰⁵ The most prominent feature of the $P(r_{HI-})$ probability distributions is the striking resemblance between all curves. The only difference between the $\Gamma(\text{H}_2\text{O})_{64}$ interior and surface states is found in the $P(r_{HI-})$ probability of finding a water molecule further away than 8 Å from the ion, which is close to the average globular radius of the interior state cluster of ca. 7 Å. Obviously, more waters are found further away from the ion in the surface state. In turn, the probability of finding water molecules, within 4 and 8 Å is higher for the interior state than for the surface state because the iodide is fully surrounded by water molecules, as

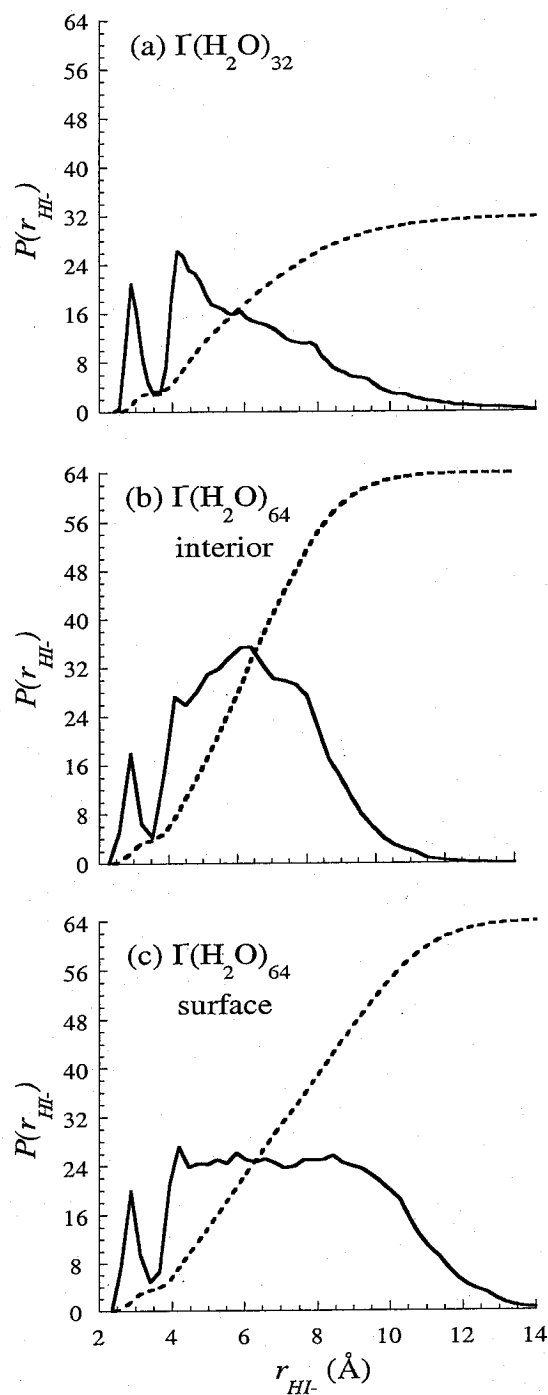


Figure 2.5 H-I⁻ probability distributions functions for (a) $\Gamma(H_2O)_{32}$, (b) the interior state of $\Gamma(H_2O)_{64}$, and (c) the surface state of $\Gamma(H_2O)_{64}$ predicted by the OPLS model.

seen in

seen in Figs. 2.3b and 2.3c. The fact that the $P(r_{HI-})$ distributions are very similar for short distances is rather surprising however. In principle, one would expect the solvation shell structure around iodide in the interior state to be better defined, and that the first solvation shell would contain more water molecules than in the surface solvation state (by first solvation shell, one actually refers to the first peak in the probability distribution functions and means the first few water molecules directly coordinated to the ions). However, the HI^- probability distributions displayed in Fig. 2.5 indicate that iodide is directly coordinated with 4 water molecules in the first solvation shell in all cases considered, and do not show evidence of a secondary shell structure for the cluster sizes investigated. Previous studies have suggested that the first solvation shell around large halide ions is often dynamic.¹⁰⁶ In other words, the molecules in the first solvation shell may dynamically exchange with molecules in outlying shells, resulting in a $4 + n$ type first shell structure. The $P(r_{HI-})$ distributions suggest that this type of dynamical exchange is present for $I^- (H_2O)_{32}$ and both solvation states of $I^- (H_2O)_{64}$, since the first minima in the $P(r_{HI-})$ distributions do not go to exactly zero.

Since the r_{HI-} probability distributions of $I^- (H_2O)_{64}$ are almost identical for the interior and surface states, let us now turn our attention to cluster enthalpies for both solvation states of the ion. Enthalpies can be obtained from our simulations as $\Delta H = \langle \Delta V \rangle + nRT$, where $\langle \Delta V \rangle$ is the ensemble average of the cluster potential energy. The enthalpies for the interior and surface solvation states are -647 and -646 kcal/mol for the OPLS model, and -636 and -634 kcal/mol for the OPCS model, respectively. The enthalpy difference between the two solvation states for both model potentials is not

significant within the error bar of 2 kcal/mol that we simply evaluated by varying the number of configurations employed to evaluate the ensemble averages. We note however that the surface state always seems to be energetically lower, even though we know from the interior to surface equilibrium constants that it is not thermodynamically favored, a finding that is even more pronounced for OPCS. Therefore, the free energy difference between both states must be due the difference in entropy between the interior and surface solvation structures. Furthermore, the larger free energy difference obtained with the OPCS model must be caused by a larger increase in the systems entropy due to polarization. As was suggested previously by Stuart and Berne,¹⁰³ polarization allows for fluctuating dipoles such that the water molecules may remain more mobile, and thereby increase the entropy of the system.

2.4 Concluding Remarks

We performed a quantitative investigation of surface vs. interior solvation in iodide-water clusters in order to better identify the possible transition from surface solvation to bulk behavior. We evaluated the free energy change as a function of the distance between the ion and the solvent center of mass r_{cm} for $\Gamma(\text{H}_2\text{O})_n$ clusters ($n=32$ and 64) by means of constrained Monte Carlo simulations, using both OPLS and OPCS model potentials. The resulting potentials of mean force (PMF) and r_{cm} probability distributions $P(r_{cm})$ indicate that one solvation state is present for $\Gamma(\text{H}_2\text{O})_{32}$ clusters, and two solvation states are present for $\Gamma(\text{H}_2\text{O})_{64}$ clusters. For $\Gamma(\text{H}_2\text{O})_{32}$, the angular probability distributions $P(\theta)$, where θ is the angle between individual solvent molecules,

the ion and the aqueous cluster center of mass, clearly demonstrate that the ion resides at the surface of the cluster over the full range of r_{cm} values considered. The $P(\theta)$ distributions also indicate that the two solvation states observed for the $\text{I}^-(\text{H}_2\text{O})_{64}$ cluster correspond to distinct solvation states, an interior state and a surface state, with peaks in the probability distributions at $r_{cm} \sim 2.2$ and 4.4 \AA , respectively. This clearly indicates a transition from surface to interior solvation around a cluster size of 64, which is consistent with a detailed analysis of experimental and model data performed by Coe.⁹⁵

The effect of explicit polarization can be simply inferred by a direct comparison of the OPLS and OPCS simulation results. Including explicit polarization causes a significant increase in the free energy difference between the surface and interior solvation states of $\text{I}^-(\text{H}_2\text{O})_{64}$, which results in a large increase in the interior to surface equilibrium constants, from 1.6 ± 0.4 for the OPLS model to 14.6 ± 0.8 for the OPCS model. Although the enthalpy difference between the two solvation states for both model potentials is not significant, the surface state tends to be slightly energetically favored, even though it is not thermodynamically favored, a finding that is even more pronounced for OPCS. This suggests that entropy and polarization effects, not too surprisingly, drive the ion towards the interior of the cluster around a cluster size of 64. A more comprehensive investigation of the thermodynamic and structural properties of halide-water clusters is underway.

Theoretical Studies of Seeded Water Clusters: Structure,
Thermodynamics and Photochemistry

Chapter 3

Solvation Structure and Thermodynamics of Halides in Water Clusters

To be submitted:

Denise M. Koch and Gilles H. Peslherbe,
Canadian Journal of Chemistry (2006)

3.1 Introduction

Investigation of the distribution of ions at air-liquid interfaces has drawn much attention in many fields of research in recent years, and has prompted hundreds of publications in the last five years alone, due to its relevance to in a multitude of biochemical and chemical processes. In biochemistry for example, solvation of ions at the interfaces between water and biomolecules affects the structure and stability of proteins, nucleic acids, and cell membranes.¹⁰⁷ In atmospheric chemistry, it was recently discovered that large halides are present at in higher concentrations at the surface of sea salt aerosols than other ions,^{12,60,61,108-110} a feature that may play an important role in the depletion of the ozone layer^{12,111,112} because of the resulting enhancement of reactions between gases such as ozone and halides at the surface of aerosols in the atmosphere.¹¹³⁻

119

In order to understand the increased concentration of halides at the air-water interface, and its consequences on chemical and biochemical reactions, it is essential to understand the microscopic details of the solvation of the ions. Since the advent of molecular beam techniques,¹²⁰ cluster studies have become an increasingly popular means to investigate solvation processes. In fact, one can observe the gradual build-up of solvation layers as a function of increasing cluster size, providing fundamental knowledge of the forces and interactions guiding the behavior of ions and solvent molecules. Many experimental studies have been dedicated to the study of ionic solvation.¹²¹ The various techniques employed are limited, however, in the range of cluster sizes that can be investigated, and detailed structural details of the clusters are

often difficult to infer unambiguously from experimental observables. Theoretical studies are therefore crucial to our understanding of ionic solvation, since they provide means to investigate the structure and dynamics of ionic clusters, which are difficult to infer from experimental data.

For this reason, a multitude of theoretical studies have been performed on ionic clusters,¹²¹ and much knowledge of the microscopic details of ionic solvation has already been obtained. Theoretical studies have allowed to establish, in conjunction with experimental data, that large halide ions prefer to sit at the surface of small-to-medium sized water clusters.^{58,86-90} In fact, Coe⁹⁵ concluded, through the analysis of small cluster experimental solvation data,^{21,29,92} the results of simulations in model polar solvent clusters of intermediate size,⁹⁶ and limiting continuum dielectric trends for large clusters, that a gradual transition from surface to interior solvation occurs over the range $n=1-60$, and the transition to bulk behavior occurs around cluster size 60.

Iodide has served as a paradigm for the investigation of surface vs. interior solvation in solvent clusters. For this reason, we recently performed a quantitative investigation of surface vs. interior solvation in iodide-water clusters by evaluating the potentials of mean force along the ion-to-water center-of-mass coordinate and the structural properties of $\text{I}^-(\text{H}_2\text{O})_n$ clusters [$n = 32, 64$] from Monte Carlo (MC) simulations with both non-polarizable and polarizable model potentials.¹²² Simulation results clearly indicated that the iodide ion tends to reside at the surface of a water cluster of size 32, whereas entropy and polarization effects make the interior solvation state more likely for a cluster size of 64.

More recently, Herce et al. investigated via molecular dynamics (MD) simulations the solvation thermodynamics of chloride in a cluster containing more than 200 water molecules, by evaluating the potential of mean force as the ion is pushed from the interior of the cluster towards the surface.¹²³ They determined that the free energy decreases as the ion reaches the surface of the cluster, and that the entropic contribution to the free energy was of the same order as the enthalpic contribution. Furthermore, they established that Coulombic and repulsion-dispersion interactions alone were not sufficient to explain the thermodynamically favored surface solvation state of chloride, and that subtle chloride-water and water-water many-body interactions play an important role in the solvation behavior of the ion.

Since most previous theoretical studies concentrated mainly on one or two ions in the halide series, we wish to perform a comprehensive investigation of the full halide series, in order to obtain a more profound understanding of the solvation characteristics of the ions, as they increase in size and polarizability. In the present work, we perform a quantitative investigation of the thermodynamics of surface vs. interior solvation for $X^-(H_2O)_n$ ($X=F, Cl, Br, I$) clusters in order to identify the possible transition from surface to bulk behavior. As in our previous work,¹²² a convenient coordinate for discriminating between surface and interior solvation is the distance between the ion and the solvent center of mass, which would be close to zero for an ideally spherically solvated interior ion, and obviously deviates significantly from zero for a surface solvation state.⁶² The potentials of mean force (PMF), *i.e.* the free energy change along this coordinate, as the ion is forced to move towards or away from the solvent cluster center of mass, as well as

cluster structural properties, are investigated for $X^-(H_2O)_n$ clusters with both non-polarizable and polarizable model potentials in order to assess the importance of polarizability on the thermodynamics of the halide-water clusters.^{62,97}

The outline of the article is as follows. In Section 3.2, we describe the intermolecular model potentials employed, the details of the molecular dynamics methodology and the theory for evaluating the potentials of mean force. We then report simulations results in Section 3.3, followed by a discussion of the results, in connection with previous studies performed on these ionic clusters in Section 3.4. We end with concluding remarks in Section 3.5.

3.2 Simulation Methodology

3.2.1 Interaction potentials

As in our previous investigation of the structure and thermodynamics of iodide-water clusters,¹²² we compute potentials of mean force obtained from simulations with two different intermolecular model potentials. The first model consists of the nonpolarizable TIP4P water model⁹⁹ supplemented by optimized parameters for liquid simulations (OPLS), hereafter referred to as the OPLS model potential.^{97,100,124} This model potential employs a rigid water molecule with experimental gas-phase geometry, and Coulombic and repulsion-dispersion terms to describe the ion-solvent and solvent-solvent interactions,

$$V = V_{Coul} + V_{rep-disp} \quad (3.1)$$

where the Coulombic part of the model potential

$$V_{Coul} = \sum_k \sum_{l < k} \frac{q_k \cdot q_l}{|\mathbf{r}_k - \mathbf{r}_l|} = \sum_k \sum_{l < k} \frac{q_k \cdot q_l}{r_{kl}} \quad (3.2)$$

represents the interactions between the fractional charges q_k on each atomic or ionic site (at position \mathbf{r}_k) of the monomers, and repulsion-dispersion interactions are modeled by Lennard-Jones potentials

$$V_{rep-disp} = \sum_{k,l} 4\epsilon_{kl} \left[\left(\frac{\sigma_{kl}}{r_{kl}} \right)^{12} - \left(\frac{\sigma_{kl}}{r_{kl}} \right)^6 \right] \quad (3.3)$$

The TIP4P water model employs 3 charge sites, 2 on the hydrogen atoms, and one at 0.15 Å from the oxygen atom on the bisector of the H-O-H angle. The parameters for the Lennard-Jones repulsion-dispersion parameters were adjusted to reproduce liquid-phase properties. All model potential parameters are listed in Table 3.1.

The second model potential, referred to as OPCS for optimized potentials for cluster simulations in our previous work and hereafter,⁹⁷ also employs a rigid water molecule with experimental gas-phase geometry. Its functional form, which has been described in detail elsewhere,⁹⁷ includes Coulombic, many-body polarization and Lennard-Jones repulsion-dispersion terms,

$$V = V_{Coul} + V_{pol} + V_{rep-disp} \quad (3.4)$$

where the Coulombic and repulsion-dispersion terms are described by Eqs. (3.2) and (3.3) as for OPLS, and the polarization energy is given by

$$V_{pol} = -\frac{1}{2} \sum_k \mathbf{E}_k^0 \cdot \boldsymbol{\mu}_k \quad (3.5)$$

where the electric field \mathbf{E}_k^0 due to the permanent charges of other monomers is given by

$$\mathbf{E}_k^0 = \sum_l q_l \cdot \frac{(\mathbf{r}_k - \mathbf{r}_l)}{|\mathbf{r}_k - \mathbf{r}_l|^3} \quad (3.6)$$

and the induced dipole moments are evaluated from

$$\boldsymbol{\mu}_k = \alpha_k \cdot \mathbf{E}_k = \alpha_k \cdot [\mathbf{E}_k^0 + \sum_{l \neq k} T_{kl} \cdot \boldsymbol{\mu}_l] \quad (3.7)$$

where T is the dipole tensor. Because of mutual polarization, the set of induced dipoles $\boldsymbol{\mu}_k$ is obtained in a self-consistent fashion by solving the linear equations of Eq. (3.7) in matrix form with LU decomposition and backsubstitution.¹²⁵

The OPCS water molecule bears 4 charge sites, 2 of which are the hydrogen atoms (H) while the other 2 (oxygen) sites (M) are located on the bisector of the H-O-H angle off the water plane, in order to reproduce the gas-phase water dipole and quadrupole moments. The oxygen atom carries one polarizable site with a polarizability taken from experiment,¹²⁶ and one repulsion-dispersion Lennard-Jones site. The model potential also includes H-H repulsion terms of the Born-Mayer form. The parameters for the solvent-solvent interactions were fitted to reproduce the experimentally-determined water-water binding energy,¹²⁷ and the gas-phase water-dimer geometry obtained from electronic structure theory calculations.⁹⁷ The ions all carry a polarizable site with polarizability taken from experiment,¹²⁶ and listed in Table 3.1. The ion-water Lennard-Jones ϵ and σ parameters were fitted with a nonlinear least squares algorithm¹²⁵ to reproduce the experimentally-determined ion-water 0 K binding enthalpies (D_0), as listed in Table 3.2, and $X^-(H_2O)$ geometries obtained from high-level electronic structure theory calculations.¹²⁸⁻¹³² The resulting parameters are listed in Table 3.1. We note that since OPLS was primarily developed for liquid-phase simulations and OPCS was

developed for cluster simulations (and based on small cluster data), simulations of intermediate-size clusters with both models yield limiting cases.

Table 3.1 Parameters of the OPLS and OPCS model potentials

Water		
OPLS		
$r_{\text{O-H}} = 0.9572 \text{ \AA}^b$		$\theta_{\text{H-O-H}} = 104.52^\circ{}^b$
$r_{\text{O-M}} = 0.15 \text{ \AA}$	$q_{\text{H}}/e = 0.52$	
	$\epsilon_{\text{O-O}} = 0.16 \text{ kcal/mol}$	$\sigma_{\text{O-O}} = 3.15 \text{ \AA}$
OPCS		
$r_{\text{O-H}} = 0.9572 \text{ \AA}^b$		$\theta_{\text{H-O-H}} = 104.52^\circ{}^b$
$r_{\text{O-M}} = 0.342 \text{ \AA}$	$q_{\text{H}}/e = 0.569$	$\theta_{\text{H}_2\text{O-M}} = \pm 43.4^\circ$
	$\alpha_{\text{W}} = 1.45 \text{ \AA}^3{}^c$	
	$\epsilon_{\text{O-O}}^d = 0.25 \text{ kcal/mol}$	$\sigma_{\text{O-O}}^d = 3.20 \text{ \AA}$
	$A_{\text{H-H}} = 10^5 \text{ kcal/mol}$	$B_{\text{H-H}} = 5.5 \text{ \AA}^{-1}$
Halides		
OPLS		
F^-	$\epsilon_{\text{O-F}} = 0.33 \text{ kcal/mol}$	$\sigma_{\text{O-F}} = 2.94 \text{ \AA}$
Cl^-	$\epsilon_{\text{O-Cl}} = 0.14 \text{ kcal/mol}$	$\sigma_{\text{O-Cl}} = 3.79 \text{ \AA}$
Br^-	$\epsilon_{\text{O-Br}} = 0.12 \text{ kcal/mol}$	$\sigma_{\text{O-Br}} = 3.89 \text{ \AA}$
I^-	$\epsilon_{\text{O-I}} = 0.22 \text{ kcal/mol}$	$\sigma_{\text{O-I}} = 3.98 \text{ \AA}$
OPCS		
F^-	$\epsilon_{\text{O-F}} = 0.08 \text{ kcal/mol}$	$\sigma_{\text{O-F}} = 3.39 \text{ \AA}$
$\alpha_{\text{F}} = 1.0 \text{ \AA}^3{}^c$		
Cl^-	$\epsilon_{\text{O-Cl}} = 0.16 \text{ kcal/mol}$	$\sigma_{\text{O-Cl}} = 3.85 \text{ \AA}$
$\alpha_{\text{Cl}} = 3.4 \text{ \AA}^3{}^c$		
Br^-	$\epsilon_{\text{O-Br}} = 0.80 \text{ kcal/mol}$	$\sigma_{\text{O-Br}} = 3.59 \text{ \AA}$
$\alpha_{\text{Br}} = 4.7 \text{ \AA}^3{}^c$		
I^-	$\epsilon_{\text{O-I}} = 0.85 \text{ kcal/mol}$	$\sigma_{\text{O-I}} = 3.81 \text{ \AA}$
$\alpha_{\text{I}} = 7.0 \text{ \AA}^3{}^c$		

^a r is the interatomic distance, θ is the angle, q is the atomic charge ($q = -1.0 e$ for all the halides), α is the polarizability, ϵ and σ are Lennard-Jones parameters and A and B are Born-Mayer potential parameters. ^b From reference 133. ^c From reference 126. ^d From reference 97. ^e From reference 100. ^f From reference 134.

Table 3.2 Ionic radii r_i and ion-water OK binding enthalpies for the halide series^a

	r_i (Å)	D_0 (kcal/mol)
F ⁻	1.2	23.3
Cl ⁻	1.7	13.1
Br ⁻	1.8	12.6
I ⁻	2.1	10.4

^a From Reference 126

3.2.2 Evaluation of potential of mean force

In our previous investigation of iodide-water clusters,¹²² we computed the potentials of mean force using Monte Carlo simulations with statistical perturbation theory evaluation of free energy differences¹⁰¹ along the distance between the ion and the center of mass of the water cluster r_{cm} . This approach requires statistical averages over a large number of configurations for each r_{cm} value to which the system is constrained, in order to obtain properly converged statistical averages, especially in regions of configurational space that are highly unfavorable energetically. Furthermore, the system must be constrained at short intervals along the coordinate of interest in order to involve only small energy differences in applying statistical perturbation theory. For these reasons, the generation of PMFs using this approach, while rigorous, can be computationally very intensive for systems with a large number of degrees of freedom, such as the ion-water clusters investigated herein. The umbrella sampling technique developed by Torrie and Valleau¹³⁵ has recently been used to evaluate potentials of mean force by Roux and co-workers, and has proven to be more computationally efficient for

this purpose than statistical perturbation theory.^{136,137} Briefly, umbrella sampling involves a biasing window potential, called the umbrella potential, which is introduced in the Hamiltonian in order to confine the system to a given region, or window, of configurational space. A harmonic potential of the form,

$$V^{umb} = \frac{1}{2}k(r_{cm} - r_{cm}^e)^2, \quad (3.8)$$

where k is a harmonic force constant, is employed to constrain the coordinate of interest to an equilibrium value r_{cm}^e for each window. Histograms of r_{cm} values, which are centered around r_{cm}^e , are then obtained for each successive window along the coordinate of interest. In order to obtain the potential of mean force from ensembles of configurations generated along the coordinate r_{cm} with umbrella sampling and to remove the artifacts introduced by the imposed constraints, we employ the weighted histogram analysis method (WHAM) developed by Kumar *et al.*¹³⁸ This method is explained in detail elsewhere,^{137,139} such that only the main features are outlined here. The WHAM technique combines the results from the biased simulation windows by determining an optimal estimate of the unbiased distribution $P(r_{cm})$ as a weighted sum over the biased distributions, and evaluating the weighting factors by minimization of the statistical error. The final potential of mean force $W(r_{cm})$ is obtained as

$$W(r_{cm}) = -k_B T \ln[P(r_{cm})] \quad (3.9)$$

where k_B is the Boltzmann constant and T the simulation temperature.

Umbrella sampling coupled with the weighted histogram analysis method can be employed with both Monte Carlo (MC) and molecular dynamics (MD) simulation

methodologies. We have chosen to employ MD simulations to evaluate the potential of mean force along the r_{cm} coordinate for halide-water clusters for efficiency. Even though MD simulations require evaluation of the force, the gradient of the energy with respect to all atomic coordinates, they may be better suited to simulate large systems where the collective motion of molecules is important, and usually yield converged results at a computational cost equivalent to or lower than that of MC simulations.¹⁴⁰ Nosé-Hoover MD simulations,^{141,142} thermostated at 200 K with a modified version of the velocity Verlet algorithm,¹⁴³ were used to generate configurational ensembles. A harmonic umbrella potential, as described above, was used with a force constant of 15 kcal/mol/Å². The latter value was found to ensure proper overlap between the distributions of ion-water center-of-mass distances $P(r_{cm})$ of successive windows, which were generated at intervals of 0.5 Å, along the r_{cm} coordinate.

3.3 Results

The left panel of Fig. 3.1 displays the ion-to-water center-of-mass distance distribution $P(r_{cm})$ for $F^-(H_2O)_n$, [$n = 12, 20$]. In order to ascertain whether peaks in the $P(r_{cm})$ distributions correspond to an interior or a surface solvation state, we also evaluate the angular probability distributions $P(\theta)$ for the angle θ between each water molecule, the ion and the water cluster center of mass. As was discussed in more detail elsewhere,¹²² the angular probability distribution is isotropic ($P(\theta) = \sin \theta$) if the ion is fully surrounded by solvent molecules, and characterized by a depletion of population at large angles ($< 150^\circ$), i.e. opposite to the ion-water cluster center-of-mass vector, if the ion resides at the surface of the cluster. For $F^-(H_2O)_{12}$, as shown in Fig. 3.1a, the $P(r_{cm})$

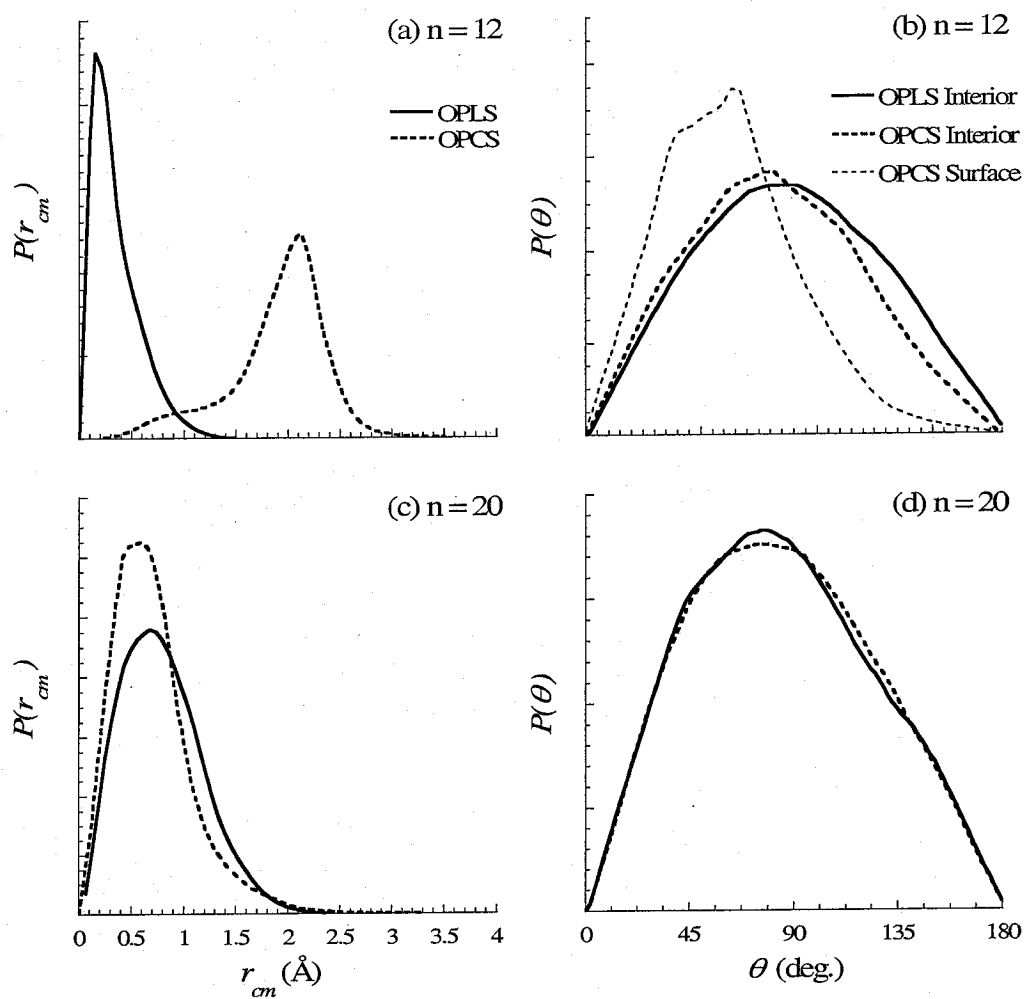


Figure 3.1 $F^-(H_2O)_n$, [$n = 12, 20$], ion-to-water center-of-mass distance probability distributions $P(r_{cm})$ (left panel) and angular probability distributions $P(\theta)$ (right panel), where θ is defined as the angle between each water molecule, the ion and the water center of mass, generated with the OPLS (line) and OPCS (dashed line) model potentials.

distribution exhibits one peak centered at 0.2 Å for the distribution predicted by OPLS. In

Fig. 3.1b, the $P(\theta)$ distribution, which was obtained from the ensemble of configurations

centered at an r_{cm}^e value of 0.5 Å, where the population of configurations with r_{cm} values close to the peak in the $P(r_{cm})$ distribution is relatively high, is clearly isotropic. Therefore, the OPLS model predicts that an interior solvation structure is thermodynamically favored for $F^-(H_2O)_{12}$. The $P(r_{cm})$ generated with the OPCS model potential has a broad feature centered at ~1.0 Å, and a more prominent peak at ~2.4 Å. The $P(\theta)$ distribution generated from the ensemble of configurations at $r_{cm}^e = 1.0$ Å is isotropic, thus corresponding to an interior solvation structure, whereas that at 2.5 Å is anisotropic with a depletion of water population opposite to the ion-to-water center-of-mass vector, thereby suggesting a surface solvation structure. Therefore, the OPCS model potential, in contrast to the OPLS model, predicts the coexistence of both interior and surface states, with the surface state being more thermodynamically favored for a cluster size of 12.

As described in detail elsewhere,^{62,122} the equilibrium constant between the interior and surface states K_{IS} can be evaluated as

$$K_{IS} = \frac{[\text{Interior}]}{[\text{Surface}]} = \frac{\int_{Int} P(r_{cm}) dr_{cm}}{\int_{Surf} P(r_{cm}) dr_{cm}}. \quad (3.10)$$

where the integrals are evaluated over the proper ranges of r_{cm} coordinates. For $F^-(H_2O)_{12}$, the equilibrium constant evaluated from the $P(r_{cm})$ distribution generated with OPCS is 0.14, indicating a ten-fold predominance of the surface state relative to the interior state in these clusters. In Table 3.3 are listed the cluster enthalpies at 200 K, which are evaluated as $\Delta H = \langle \Delta V \rangle + nRT$, where $\langle \Delta V \rangle$ is the average cluster potential

energy over the ensemble of configurations generated from the r_{cm}^e window closest to the peaks in the $P(r_{cm})$ distributions. If a peak does not show in the $P(r_{cm})$ distribution, for a given solvation state, the cluster enthalpy was evaluated from a window which corresponds to either a surface or an interior state, according to the angular probability distributions. For $F^-(H_2O)_{12}$, the cluster enthalpy obtained from simulations with OPLS for the interior state is 11 kcal/mol lower than that of the surface state, however, the enthalpies of the interior and surface solvation states are almost equal with OPCS. These results indicate that enthalpy drives fluoride to the interior of the cluster for OPLS, but that entropy favors surface solvation for OPCS.

In the case of $F^-(H_2O)_{20}$, the $P(\theta)$ distributions for both OPLS and OPCS display one major peak centered at ~ 0.5 Å, as shown in Fig. 3.1c. The $P(\theta)$ distributions, shown in Fig. 3.1d, are clearly isotropic, indicating that an interior solvation state predominates for both model potentials. For OPLS, the cluster enthalpy of the interior state is 7 kcal/mol lower than that corresponding to an hypothetical situation where the ion resides at the surface of the cluster. For OPCS, on the other hand, there is no significant difference between the cluster enthalpies obtained from ensembles of configurations where the ion dwells into the interior of the cluster and those where the ion resides at the surface. Therefore, both model potentials agree in predicting that fluoride prefers to adopt an interior solvation structure to a surface structure for cluster size 20. However, results of simulations with both model potentials paint a different picture, as to whether enthalpy or entropy drives the ion towards the interior of the cluster.

Inspection of the ion properties of the halides in Tables 3.1 and 3.2, makes it obvious that chloride and bromide have relatively similar properties, compared to fluoride, which has a significantly smaller polarizability and much higher ion-water binding energy. We can therefore expect that the cluster size dependence of the hydration thermodynamics for chloride and bromide will show similar features. The $P(r_{cm})$ distributions and $P(\theta)$ distributions for chloride and bromide in aqueous clusters of size 20, 32 and 64 are displayed in Figs. 3.2 and 3.3. For cluster size 20, the $P(r_{cm})$ distributions for both ions exhibit a single predominant peak, centered at ~ 1.8 Å for OPLS, and ~ 3.2 Å for OPCS, as shown in Figs 3.2a and 3.3a. The angular probability distributions, shown in Figs. 3.2b and 3.3b, indicate that OPLS predicts an interior solvation structure, whereas surface solvation is favored for OPCS. In the case of fluoride, there was a significant difference in the cluster enthalpy between interior and surface states with OPLS, but not for OPCS. For chloride and bromide, neither model potential predicts a significant difference in enthalpy between the two solvation states. Therefore, entropy must be the main factor that determines the preferred solvation state for bromide and chloride at a cluster size of 20. The simulation results with both models, however, disagree as to whether entropy favors an interior or surface solvation structure.

For cluster size 32, the $P(r_{cm})$ and $P(\theta)$ distributions evaluated with OPLS, shown in Figs. 3.2c, 3.2d, 3.3c and 3.3d, indicate that the interior state is thermodynamically favored for chloride, whereas both interior and surface solvation states coexist for bromide, with the peak in the $P(r_{cm})$ distribution corresponding to the interior state largely predominant over that corresponding to the surface solvation state. The

Table 3.3 Cluster enthalpies at 200 K, in kcal/mol.^a

n	12		20		32		64	
Solvation structure	Interior	Surface	Interior	Surface	Interior	Surface	Interior	Surface
F ⁻								
OPLS	202 ± 4	191 ± 4	287 ± 4	279 ± 5				
OPCS	177 ± 5	180 ± 4	269 ± 5	270 ± 5				
Cl ⁻								
OPLS			224 ± 5	222 ± 5	350 ± 7	347 ± 6	674 ± 8	675 ± 8
OPCS			227 ± 5	223 ± 5	358 ± 7	360 ± 7	715 ± 8	717 ± 10
Br ⁻								
OPLS			220 ± 5	218 ± 5	343 ± 7	340 ± 6	669 ± 8	675 ± 8
OPCS			225 ± 5	227 ± 5	354 ± 6	358 ± 6	714 ± 9	718 ± 9
I ⁻								
OPLS					345 ± 7	343 ± 6	658 ± 9	656 ± 9
OPCS					354 ± 6	350 ± 6	707 ± 8	712 ± 9

a. The listed errors are standard deviations of the cluster potential energy from its average value for the ensemble of cluster configurations.

equilibrium constant K_{IS} for the interior to surface solvation states of $\text{Br}^-(\text{H}_2\text{O})_{32}$ for OPLS is 16.7, indicating a predominance of the interior vs. surface state populations by one order of magnitude. As for OPCS, the $P(r_{cm})$ distributions, shown in Figs. 3.2c, and 3.3c, show the coexistence of both solvation states for chloride and bromide in a cluster of 32 water molecules. The $P(\theta)$ distributions evaluated over the window of configurations closest to the peaks in the $P(r_{cm})$ distributions confirm the coexistence of both interior and surface states, as shown in Figs. 3.2d and 3.2c. The equilibrium constant between the interior and surface states for bromide, $K_{IS} = 0.04$, is an order of magnitude smaller than that for chloride, $K_{IS} = 0.11$, indicating that surface solvation is more favored for bromide than for chloride for cluster size 32 with OPCS. Since chloride has a slightly higher ion-water binding energy, and smaller ionic radius than bromide, (*cf.* Table 3.2) it is not surprising that K_{IS} is larger for chloride than for bromide. As was the case for cluster size 20, there is no significant difference between the cluster enthalpies of the interior and surface states for both model potentials. Thus, we can conclude that entropy must be the major factor determining the preferred solvation structure for both chloride and bromide for cluster size 32. However, there is a discrepancy in the OPLS and OPCS results, as to which solvation structure is thermodynamically favored.

The ion-to-water center-of-mass distance distributions and angular distributions for chloride and bromide for cluster size 64 are shown in Figs. 3.2e, 3.2f, 3.3e and 3.3f. Once again, the $P(r_{cm})$ distributions generated with OPLS are very different from those generated with OPCS. For cluster size 32, OPLS predicts the existence of only the interior solvation state for chloride, and the coexistence of both states for bromide with a

predominance of the interior state. The equilibrium constant for interior vs. surface

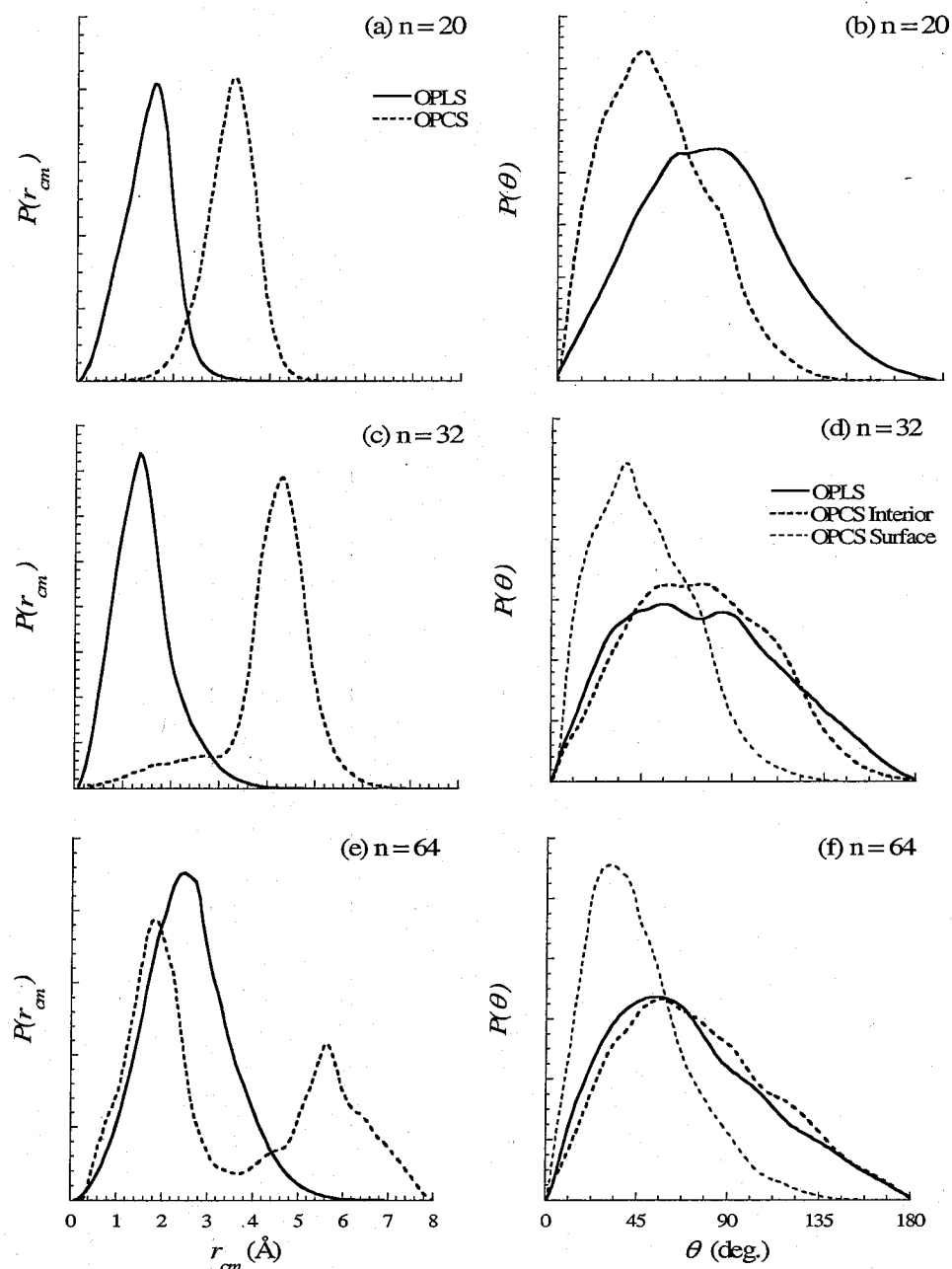


Figure 3.2 $\text{Cl}^-(\text{H}_2\text{O})_n$, [$n = 20, 32, 64$], ion-to-water center-of-mass distance probability distributions $P(r_{cm})$ (left panel) and angular probability distributions $P(\theta)$ (right panel), where θ is defined as the angle between each water molecule, the ion and the water center of mass, generated with the OPLS (line) and OPCS (dashed line) model potentials..

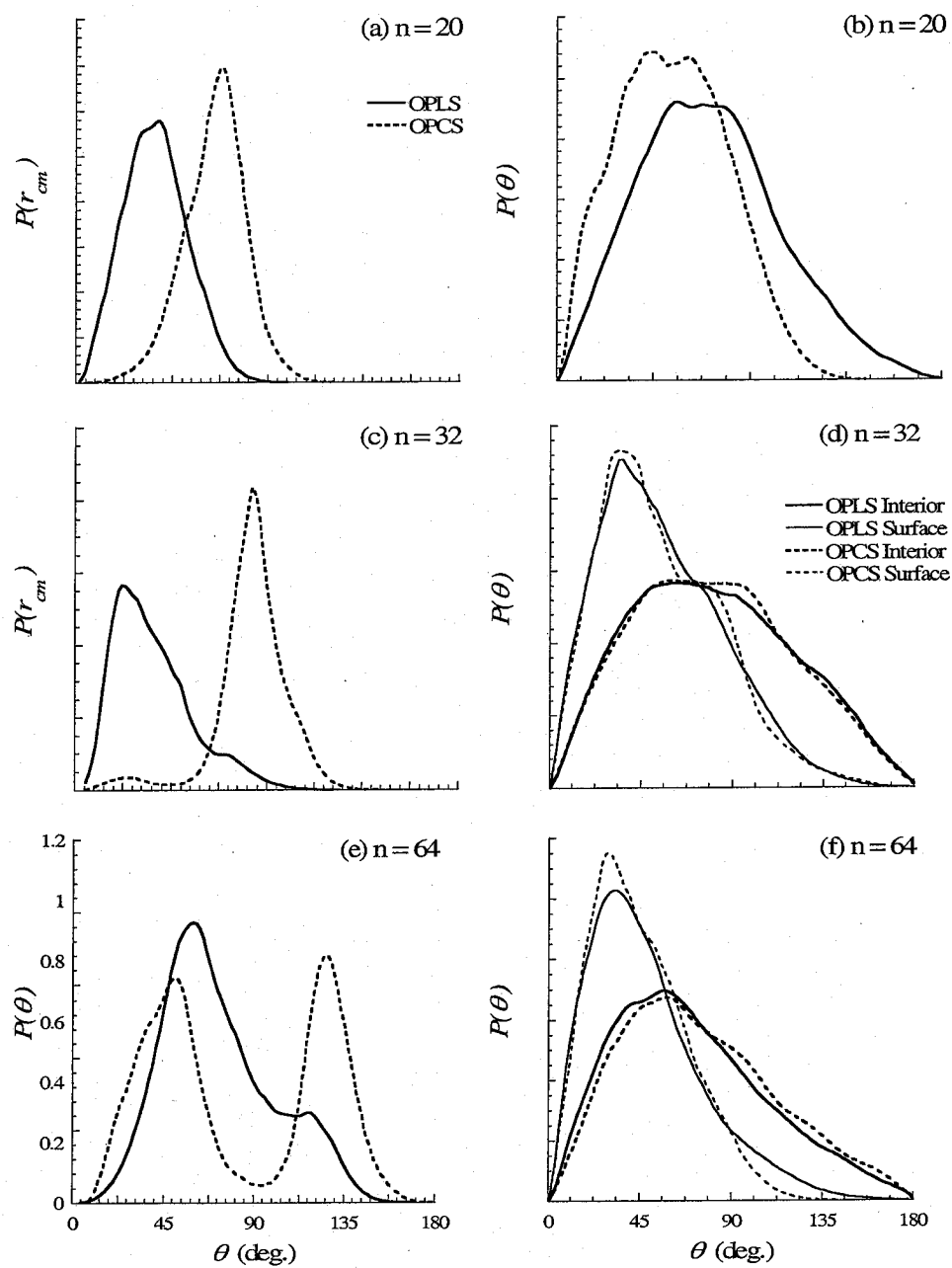


Figure 3.3 $\text{Br}^-(\text{H}_2\text{O})_n$, [$n = 20, 32, 64$], ion-to-water center-of-mass distance probability distributions $P(r_{cm})$ (left panel) and angular probability distributions $P(\theta)$ (right panel).

solvation is 5.5 in the case of bromide, indicating that the interior state is favored more than 5 times over the surface state in a cluster of 64 water molecules. With OPCS, the $P(r_{cm})$ distributions indicate the coexistence of interior and surface solvation states for both chloride and bromide. The interior-to-surface equilibrium constants are 1.4 and 0.97 for chloride and bromide, respectively, indicating an almost equal population of interior and surface states for both ions. Once again, the cluster enthalpies, listed in Table 3.3, are almost equal for the interior and surface solvation states for both model potentials, indicating that entropy rather than enthalpy determines the preferred solvation state of the ions.

The $P(r_{cm})$ and $P(\theta)$ distributions for $\Gamma(\text{H}_2\text{O})_n$, [$n = 32, 64$], are shown in Fig. 3.4. For iodide, both OPLS and OPCS predict a predominant surface solvation state for cluster size 32. For OPCS, the $P(r_{cm})$ distribution, shown in Fig. 3.4a, exhibit a small population of structures with r_{cm} in the range 0 to 2 Å, which corresponds to an interior solvation state, a shoulder at $r_{cm} \sim 3.5$ Å, which reflects the existence of an intermediate state where the ion is situated just below the surface of the cluster, and a pronounced peak at $r_{cm} \sim 5.0$ Å, which evidently corresponds to a surface state. For cluster size 64, both models predict an equilibrium between interior and surface states, with $K_{IS} = 0.5$ and 0.6 for OPLS and OPCS, respectively. Therefore, both model potentials predict a nearly equal probability of the interior and surface solvation states, with the surface state being slightly favored. Once again, the cluster enthalpies for the interior and surface states, listed in Table 3.3, are very similar, indicating that entropy must determine the

favorable solvation state of iodide for both cluster sizes. These results will be compared to those from previous work in the following Section.

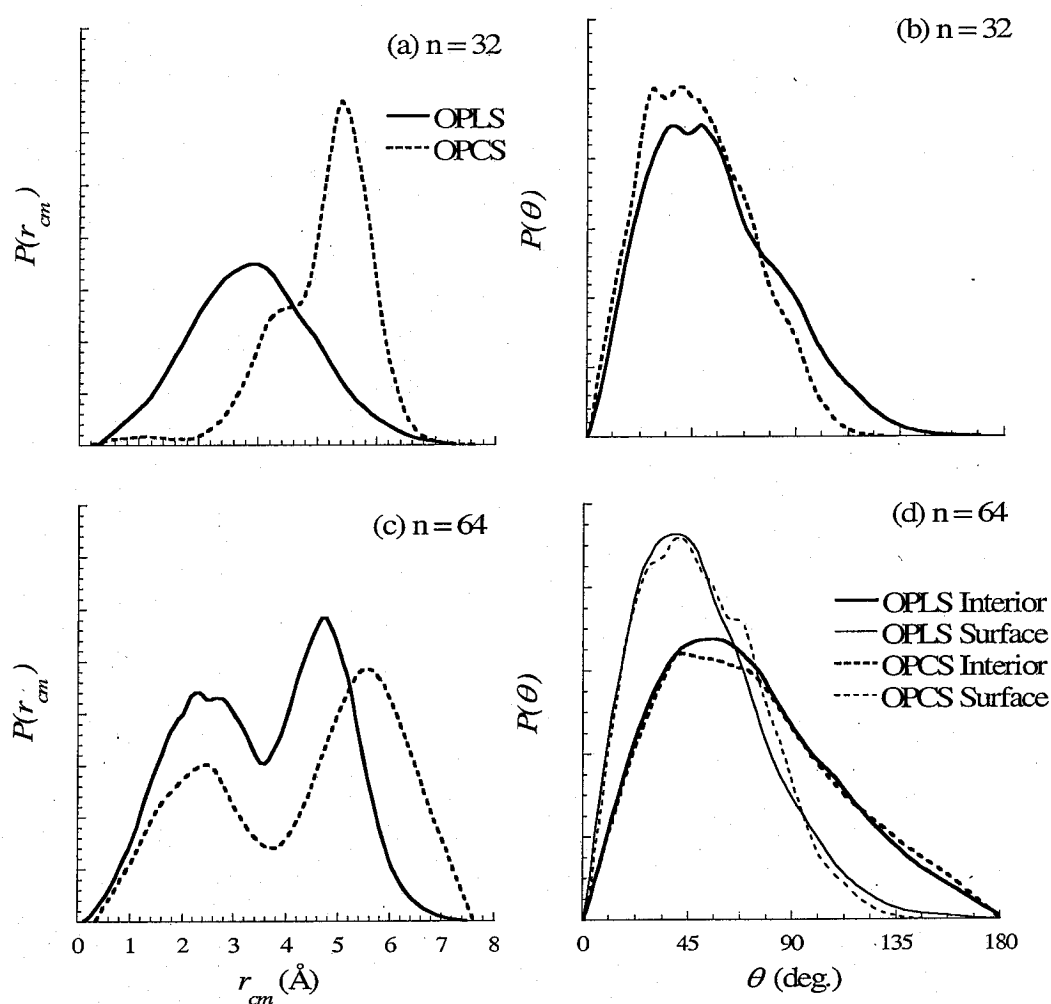


Figure 3.4 $\Gamma(\text{H}_2\text{O})_n$, [$n = 32, 64$], ion-to-water center-of-mass distance probability distributions $P(r_{cm})$ (left panel) and angular probability distributions $P(\theta)$ (right panel), where θ is defined as the angle between each water molecule, the ion and the water center of mass, generated with the OPLS (line) and OPCS (dashed line) model potentials.

In summary, simulations with both OPLS and OPCS model potentials support that entropy alone determines which solvation state is thermodynamically favored for chloride, bromide and iodide over the full range of cluster sizes investigated. In the case of fluoride, on the other hand, the model potentials yield conflicting results, as to whether enthalpy or entropy may govern the thermodynamically favored solvation structure. The OPLS model predicts that enthalpy favors interior solvation for cluster sizes 12 and 20, whereas the OPCS model predicts that entropy is the main factor contributing to the thermodynamically favored solvation state. Furthermore, there is a discrepancy in the simulation results with both model potentials as to which solvation state is preferred for a given cluster size. The OPLS model predicts that the interior state is thermodynamically favored over the whole range of cluster sizes, for fluoride, chloride and bromide. For iodide, on the other hand, OPLS predicts a surface solvation state at cluster size 32. The OPCS model seems more sensitive to cluster size effects, and to the properties of the ions. For OPCS, surface solvation is thermodynamically favored for the smaller cluster sizes, and interior solvation becomes increasingly more important with increasing cluster size. For fluoride, OPCS predicts that interior solvation is preferred at cluster size 20. For chloride, bromide and iodide, which have similar radii, polarizabilities, and ion-water binding enthalpies, the interior state is almost equally likely as the surface state at cluster size 64. Since OPLS predicts interior solvation, independently of cluster size or the detailed properties of the halides for most of the halides, we conclude that this model does not properly describe the thermodynamics of interior vs. surface solvation of halide-

ions in water clusters. In the following section, we will explore the various reasons behind the discrepancies between both model potentials in more detail.

3.4 Discussion

The preferred surface solvation structure of some ions in small- to medium-sized water clusters has been mainly attributed to their large ionic radius, as large ions significantly perturb the hydrogen-bonded network within the cluster, and to ion-water binding enthalpies similar to that of the binding enthalpy between water molecules within the cluster. As such, the water molecules tend to bind to themselves rather than to the ion, thus forcing the ion towards the surface of the cluster. The ionic radii r_i and the ion-water 0 K binding enthalpies (D_o) for the halides investigated in this work are listed in Table 3.2, and the ion polarizabilities α are listed in Table 3.1. The radii and polarizabilities increase from fluoride to iodide, whereas the ion-water binding enthalpies decrease. Since smaller ions will tend to infiltrate the hydrogen-bonded network of the water cluster more easily, and water molecules will preferentially bind to ions with ion-water binding enthalpies larger than the water-water interaction enthalpy within the cluster, we could expect that the interior state will become thermodynamically favored over the surface state at increasingly larger cluster sizes as we progress from fluoride to iodide down the halide series. Our simulation results suggest that equilibrium between interior and surface states, with a nearly equal probability of either state, exists for chloride, bromide and iodide at cluster size 64, but the fluoride ion prefers interior solvation by cluster size 20.

In the case of fluoride, previous simulations using model potentials, for cluster sizes 1 to 15, suggest that interior solvation states are favored over surface states at cluster size 4 and larger,^{144,145} consistent with experimental data and high-level electronic structure calculations of minimum energy cluster structures.^{42,90,130,146,147} The simulations reported here with OPLS also support this finding. In contrast, OPCS predicts that interior solvation states become thermodynamically favored over surface states for clusters containing more than 12 water molecules. Kim and co-workers performed high-level electronic structure calculations of small fluoride-water clusters, $n = 1-6$.¹²⁸ These calculations showed that interior and surface solvation states are nearly isoenergetic at 0 K for cluster size 6, and that entropy favors interior-solvated structures at higher temperatures. Consequently, at cluster size 6, entropy becomes the main factor which determines the thermodynamically favored solvation state, in agreement with the predictions of OPCS in the present simulations. On the other hand, OPCS predicts that entropy favors surface solvation for a cluster size of 12, rather than interior solvation, as would be expected from previous experimental and theoretical studies. As will be explained in more detail shortly, the choice of the model potential employed in simulations of halide-water clusters significantly affects the preferred solvation state of the ion. The fact that OPCS may provide a more realistic description of water-water and ion-water interactions may account for the discrepancies between the present simulations, and those performed with simpler model potentials.¹⁴⁵

The stability of clusters is known to vary significantly with cluster size, and cluster sizes with exceptionally high stabilities, called “magic number structures”,

exist.¹⁴⁸ Dreyman and Wachman found exceptionally stable structures for water clusters containing up to 21 water molecules.¹⁴⁹ The varying stability of water clusters as a function of cluster size may significantly affect the solvation behavior of ion-water clusters. It is therefore not unreasonable to assume that interior solvation states could be favored at small cluster sizes where the ion significantly affects a loose water network, whereas surface solvation states may predominate for larger cluster sizes where the water molecules adopt highly stable structures. This is an issue that could be resolved by generating potentials of mean force for intermediate cluster sizes, between 6 and 20 water molecules, and merits further investigation. It should be noted that the aforementioned electronic structure calculations predict thermodynamic properties from calculations on a limited number of local minimum energy structures, such that the floppiness of the cluster structure is underestimated, under the harmonic oscillator approximation, so that the water librational modes are improperly treated as harmonic vibrations. Therefore, such calculations do not properly account for the entropy of the clusters, and only calculations of ensembles of cluster configurations can yield reliable thermodynamics.

Many previous theoretical studies have noted discrepancies between simulation results with polarizable and nonpolarizable model potentials for the larger halides in the series.^{103,123,145,150-153} Stuart and Berne performed MD simulations with both OPLS and a polarizable fluctuating-charge water model to investigate the interior vs. surface solvation of $\text{Cl}^-(\text{H}_2\text{O})_n$ clusters, for $n \leq 255$.¹⁰³ Over the full range of cluster sizes, they observed that Cl^- is situated in the interior of the cluster with the nonpolarizable (OPLS) model, whereas the ion is situated near the surface with the polarizable model. More recently,

Yoo and Zeng performed a similar investigation of Cl^- and Br^- in water clusters, comparing once again the results obtained with OPLS and those with the Dang-Chang polarizable water model and polarizable ions.¹⁵⁰ They found that Cl^- is fully solvated for $n = 60$, and Br^- is partially solvated with the nonpolarizable (OPLS) model, but both ions reside at the surface up to cluster size 500 with the polarizable model. As mentioned earlier, Hecce et al. evaluated the PMF for a chloride moving from the interior to the surface of a cluster of 238 water molecules.¹²³ They also found that interior solvation is favored with a nonpolarizable 3-charge site water model, and surface solvation with a polarizable water model. Our simulations agree with previous work, in that OPLS favors interior solvation up to cluster sizes of 64 for chloride and bromide. However, in contrast to simulations performed with other polarizable model potentials, the present simulations with OPCS predict a nearly equal probability of the interior and surface solvation states for the larger halides at cluster size 64.

It is worth pointing out that this investigation and our previous work on iodide-water clusters are the first rigorous investigations of the surface-to-interior state transition in halide-water clusters as a function of cluster size. Most previous theoretical studies have concentrated on chloride and bromide, and to the best of our knowledge, this work and our previous investigation are the first to address the case of $\Gamma(\text{H}_2\text{O})_n$ by means of simulations. Except for the work of Hecce et al., no previous studies have resorted to the evaluation of potentials of mean force in order to distinguish the thermodynamically favored solvation structure of the halides as a function of cluster size. The evaluation of ion-to-water center-of-mass distance distributions not extracted from potentials of mean

force spanning a wide range of the r_{cm} coordinate, does not constitute a rigorous approach to determine the predominant solvation state of an ion. For instance, standard (equilibrium) MD simulations may simply sample configurations around a local free energy minimum if the latter is separated from a global minimum by a significant free energy barrier. Such simulations may also sample configurations along a single local free energy minimum and ignore other possible solvation states, unlike the present MD simulations with umbrella sampling.

The discrepancy between simulation results with different model potentials was attributed by Stuart and Berne to the fact that polarizable water molecules have a larger effective dipole moment than nonpolarizable water molecules, due to the added induced-dipole interaction inherent in polarizable water models. They argued that dipole-induced dipole interactions strengthen the hydrogen bonding network between neighboring waters, thus favoring surface solvation of the ions in water clusters.¹⁰³ The polarizable TIP4P fluctuating-charge model developed by Stuart and Berne was derived to reproduce liquid-phase properties of the solvent and the ion. Their model predicts an average water dipole moment of 2.62 D, which is consistent with the estimated liquid phase value of around 3 D.¹⁵⁴ For comparison, the nonpolarizable TIP4P model has a fixed dipole of 2.18 D, which is smaller than that of the liquid phase but larger than the gas phase value 1.8 D.¹⁵⁵ In contrast, the polarizable model, employed by Yoo and Zeng and parameterized to the gas-phase dipole and quadrupole moments of water and to electronic structure theory binding energies and dimer geometries, predicts an average dipole of 2.5 and 2.75 D for waters molecules at the surface and in the interior of the cluster,

respectively. The OPCS model employed herein, which was also derived from gas-phase and small cluster data, predicts a dipole moment ranging from 2.4D at the cluster surface to 2.75D in the cluster interior, as for the Dang-Chang water model. Therefore, the fact that OPCS predicts the coexistence of interior and surface states for the larger halides at cluster size 64, whereas the other polarizable models discussed above predict surface solvation for cluster sizes larger than 200, cannot be attributed to the water dipole moment, or effective polarizability, because all the water models described above have similar average water dipole moments in clusters. Furthermore, the discrepancy between the results of simulations with polarizable model potentials cannot be ascribed to the properties used to parameterize the models, since both the fluctuating charge model, which was parameterized to reproduce bulk properties, the Dang-Chang water model and OPCS, which were both parameterized to reproduce gas-phase and small cluster data, predict different solvation states, depending on cluster size, for chloride and bromide.

The main difference between the polarizable models used in previous studies and OPCS lies in the description of the charge distribution of the water molecules. As mentioned in the methodology section, OPCS employs 4 charge sites, with two sites that serve to mimic the oxygen lone pairs on the water molecules, whereas the other polarizable water models discussed employ 3 charge sites (and only one oxygen site). Thus, the charge distribution of the water molecules could be an important factor in properly describing the solvation behavior of halides in water clusters. Since the OPCS water model has more charge sites, each water molecule has more flexibility in forming hydrogen bonds with neighboring water molecules, which could favor the water-water

interactions within the cluster. Moreover, the charge distribution is planar for water models containing three charge sites. In contrast, the two oxygen charge sites of the OPCS model are situated off the plane of the water molecule, such that the charge distribution of the water molecules is more isotropic, and more realistic than models employing only three charge sites. The increased possibility of forming hydrogen bonds, and the nonplanar charge distribution of the OPCS water model may result in an increased entropic contribution, due to favorable ordering of the water molecules within the clusters. Consequently, we can conclude that an accurate description of the water charge distribution is also an important factor to obtain a proper description of the thermodynamics of interior vs. surface solvation in halide-water clusters

We have just established that a realistic description of the polarization and charge distribution of the water molecules is essential in the study of ionic solvation. Another important issue deals with how the inherent properties of the ion influence its solvation behavior in water clusters, and in particular, how the ion-water binding enthalpy and/or the ion polarizability influence the solvation structure and thermodynamics of the ion. In order to address this issue, we have performed simulations of $\text{Cl}^-(\text{H}_2\text{O})_{20}$ using an OPCS model potential where the ion-water binding enthalpy is varied at constant ionic polarizability, and the ion polarizability is varied at constant binding enthalpy, and new Lennard-Jones parameters were derived to account for the changes in the chloride-water potential energy surface following the variation in the aforementioned ion properties. The resulting Lennard-Jones parameters for each binding enthalpy and ion polarizability explored are listed in Table 3.4. The chloride-water binding enthalpy and the

polarizability of the chloride ion were varied to a point where the Lennard-Jones parameters remained within physically realistic limits. Simulations with these model potentials will also help assess the sensitivity and robustness of the model potential with respect to parameterization.

Figure 3.5 shows the r_{cm} probability distributions obtained by varying the chloride-water binding enthalpy and the ion polarizability. As shown in Fig. 3.5a, the change in the chloride-water binding enthalpy does not significantly affect the $P(r_{cm})$

Table 3.4 Lennard-Jones parameters for varying chloride polarizabilities (α) and 0 K chloride-water binding enthalpies (D_o)

α (\AA^3)	D_o (kcal/mol)	ϵ (kcal/mol)	σ (\AA)
1.0	13.1	0.2548	3.6014
2.0	13.1	0.2044	3.6781
4.0	13.1	0.1690	3.7746
5.0	13.1	0.2344	3.7170
3.4	12.0	0.0543	4.2610
3.4	14.0	0.0809	4.0094
3.4	15.0	0.2466	3.6568
3.4	16.0	0.6262	3.4135

distributions, since the distributions peak at ~ 3 \AA , regardless of the binding enthalpy.

The $P(r_{cm})$ distributions, however, vary significantly with the ion polarizability, as shown in Fig. 3.5b. In fact, interior solvation is favored for polarizabilities of 1.0 and 2.0 \AA^3 , and

surface solvation is favored for polarizabilities of 4.0 and 5.0 Å³. Consequently, our simulation results suggest that the polarizability of the ion affects the thermodynamics of interior vs. surface solvation much more drastically than the ion-water binding enthalpy. This observation supports the proposal that the entropic contribution to the free energy determines the solvation structure of the ion, rather than the enthalpy of the cluster, as was found in many previous studies,^{28,29,86,103,145,151,152,156-158} because polarization favors the mobility of the ion and the water molecules in the cluster. As mentioned earlier, entropy determines the solvation structure and thermodynamics even in small water clusters containing fluoride,¹²⁸ which has the highest ion-water binding enthalpy of the halide series, and for which we would expect the ion-water enthalpic contributions to dominate the free energy of the cluster.

In our previous investigation of the transition from surface to interior solvation in $\Gamma(\text{H}_2\text{O})_n$ clusters, a different methodology was employed, based on Monte Carlo (MC) simulations and free energy perturbation theory, with the same model potentials. Figure 3.6 shows the $P(r_{cm})$ distributions obtained with the MD procedure employed herein and the MC procedure employed previously, for $\text{Cl}^-(\text{H}_2\text{O})_n$ and $\Gamma(\text{H}_2\text{O})_n$, [$n = 32, 64$]. For $\text{Cl}^-(\text{H}_2\text{O})_{32}$, both the MC and MD simulations predict a predominant interior solvation state with OPLS, and a preference for surface solvation state with OPCS. For $\text{Cl}^-(\text{H}_2\text{O})_{64}$, the $P(r_{cm})$ distributions obtained with both simulation methods are also consistent: once again, OPLS predicts an interior solvation state, whereas OPCS predicts an equilibrium between interior and surface solvation states. Furthermore, both MC and MD simulations with OPCS predict a nearly equal probability of either solvation state, with $K_{IS} = 1.1$ and

$K_{IS} = 1.4$, respectively. For $\Gamma(\text{H}_2\text{O})_{32}$, the distributions obtained with both simulation methods also predict similar solvation thermodynamics with OPLS and OPCS. For

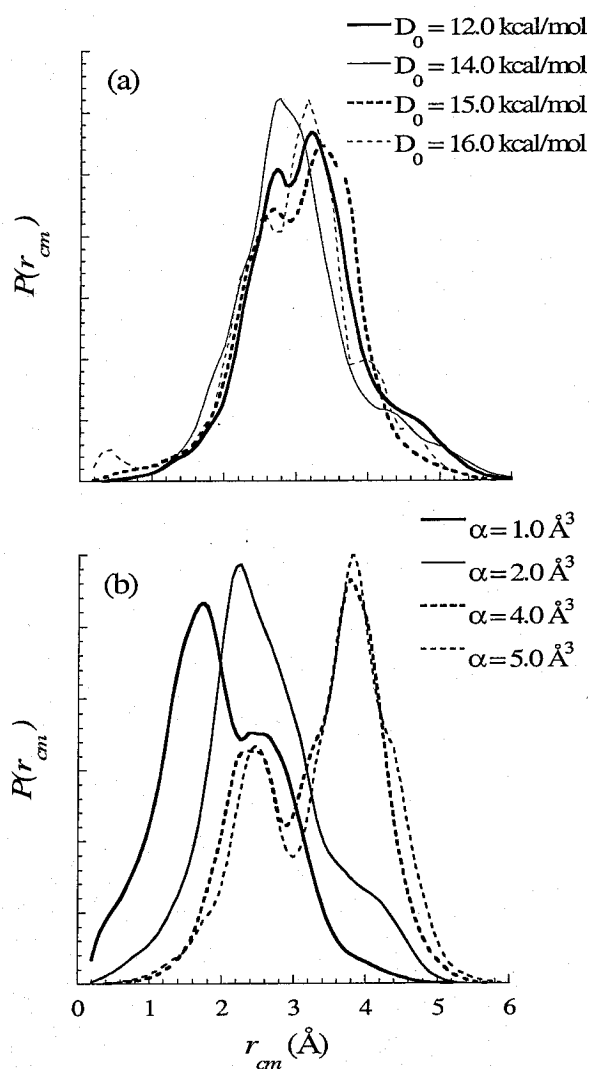


Figure 3.5 $\text{Cl}^-(\text{H}_2\text{O})_{20}$ ion-to-water center-of-mass distance probability distributions $P(r_{cm})$ obtained with an OPCS model where the ion-water binding enthalpy (D_0) is varied at constant ionic polarizability (Fig. 3.5a), and the ion polarizability (α) is varied at constant binding enthalpy (Fig. 3.5b).

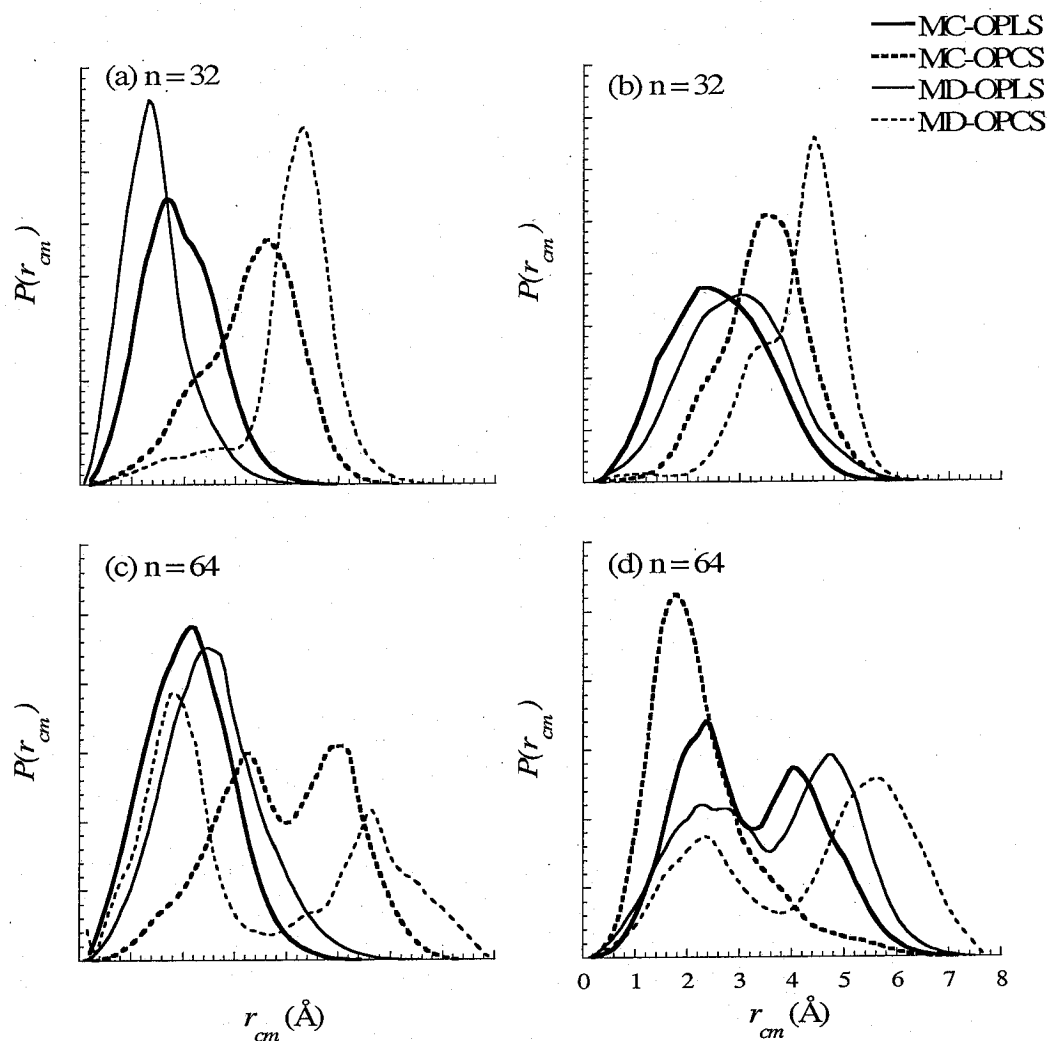


Figure 3.6 $\text{Cl}^-(\text{H}_2\text{O})_n$ (left panel) and $\text{I}^-(\text{H}_2\text{O})_n$ (right panel) ion-to-water center-of-mass distance probability distributions $P(r_{cm})$, for cluster sizes 32 (Fig. 3.6a) and 64 (Fig. 3.6b), comparing simulations from Monte Carlo (MC) simulations using free energy perturbation theory, and molecular dynamics simulations (MD) employing umbrella sampling coupled with the weighted histogram analysis method.

$\text{I}^-(\text{H}_2\text{O})_{64}$, on the other hand, the $P(r_{cm})$ distributions obtained from MC and MD simulations yield quite different results. With OPLS, the interior-to-surface equilibrium

constants obtained from the MC and MD simulations are 1.6 and 0.5, respectively, suggesting a preferred interior state according to MC simulations and a surface solvation state according to MD simulations. The inconsistency between the results from both simulation methodologies is even more pronounced for OPCS, in which case the $P(r_{cm})$ distributions obtained from MC and MD simulations yield equilibrium constants of 14.6 and 0.6, respectively, in serious disagreement with one another. Therefore, the $P(r_{cm})$ distributions obtained from MC and MD simulations are in fair agreement for chloride at cluster sizes 32 and 64 and for iodide at cluster size 32, but are inconsistent for $\Gamma(\text{H}_2\text{O})_{64}$.

Souaille and Roux compared the ensemble-averaged free energies, evaluated with the WHAM technique and with free energy perturbation theory, for a charge-dipole system consisting of a point charge and one water molecule.¹³⁶ They found that both techniques yielded similar average free energies, but that the WHAM technique greatly reduced the statistical error on the averages. To the best of our knowledge, however, these various techniques have never been compared for the evaluation of potentials of mean force. The $P(r_{cm})$ distributions obtained from the MC simulations, where the potential of mean force are evaluated with free energy perturbation theory,¹²² are calculated from the PMF as $P(r_{cm}) = 4\pi r_{cm}^2 e^{-W(r_{cm})/kT}$, thus biasing the distribution by a factor $4\pi r_{cm}^2$. Furthermore, the bias introduced by constraining the system to a given r_{cm} value is not removed in evaluating the potentials of mean force with this methodology. With the WHAM technique, on the other hand, the $P(r_{cm})$ distributions are obtained directly and the bias imposed on the system due to the introduction of an umbrella potential is removed. Therefore, it appears that not only accurate potentials are required

to obtain quantitative results concerning the solvation structure and thermodynamics of halide-water clusters, but the methodologies employed to evaluate the potential of mean force can also yield significantly different results. The aforementioned MC and MD methodologies differ in the treatment of the bias potential and the $P(r_{cm})$ distributions, as mentioned above, but also in the approach for configuration sampling. While in principle equivalent, MD and MC simulations explore the configurational space differently: the collective motion of molecules is correlated with MD, while ensembles of structures are generated by a set of uncorrelated molecular moves in MC. However, a detailed comparison of configuration sampling for ionic clusters with MC and MD simulations, and of the procedure to evaluate PMFs, is beyond the scope of the present work and is left for future study.

Finally, our investigation strongly suggests that an accurate description of the subtle ion-water and water-water interactions is essential to properly describe the solvation behavior of halides in water clusters. We mentioned earlier that OPLS is parameterized for liquid simulations, whereas OPCS is parameterized for cluster simulations. As such, we expected that the simulations with both models would yield results somewhat in between liquid-phase and gas-phase behavior. Accordingly, OPLS predicts interior solvation, independently of the ion or the cluster size, as would be expected from the bulk solvation behavior of the ions. OPCS, on the other hand, was shown to be much more sensitive to the properties of the ions and to cluster size. Nonetheless, one cannot conclude with absolute certainty that these simulations yield realistic solvation structures and thermodynamics, due to the sensitivity of the solvation

behavior on the model potential employed. Consequently, only simulations based on first-principles intermolecular interactions could yield a definitive answer concerning the cluster size dependence of interior vs. surface solvation in halide-water clusters. We are presently performing more definitive simulations employing both semiempirical and first-principles approaches in order to provide a definitive, quantitative and rigorous investigation of the solvation structure and thermodynamics of halide-water clusters.

3.5 Concluding Remarks

We performed a quantitative investigation of surface vs. interior solvation in halide-water clusters in order to identify the possible transition from surface solvation to interior solvation as a function of cluster size. We evaluated the free energy change as a function of the distance between the ion and the solvent center of mass r_{cm} in halide-water clusters by means of Nose-Hoover molecular dynamics simulations thermostated at 200 K with umbrella sampling, together with the weighted histogram analysis method, using both OPLS and OPCS model potentials. The resulting potentials of mean force (PMF) and r_{cm} probability distributions $P(r_{cm})$ indicate that interior solvation is thermodynamically favored with OPLS for all cluster sizes investigated and for the whole halide series, except for iodide, for which the surface solvation state is predominant at cluster size 32 and 64. With OPCS, on the other hand, our results indicate that fluoride favors interior solvation at cluster size 20, and, according to the interior-to-surface equilibrium constants, the interior and surface solvation states are nearly equally populated for chloride, bromide and iodide at cluster size 64, with the surface state becoming increasingly more favored as the ionic radii and polarizabilities increase down

the halide series. These findings are consistent with the variation in ionic properties, such as polarizability and ion-water binding enthalpy, along the halide series. Fluoride is much less polarizable, and the ion-water binding energy much larger than that of the other halides. It is therefore expected that fluoride will favor interior solvation at a lower cluster size than other halides. Chloride and bromide have very similar polarizabilities and ion-water binding enthalpies. Consistently, our results demonstrate very similar solvation behaviors as a function of increasing cluster size for the ions.

As mentioned above, with OPCS, fluoride favors a surface solvation for cluster sizes larger than 12, in contradiction with previous high-level electronic structure calculations that predict a transition from surface to interior solvation at cluster sizes 5 and 6.¹⁴⁷ The discrepancy with previous calculations may be due to the fact that water clusters form structures with exceptionally high stability at some cluster sizes,¹⁴⁹ which could explain why fluoride prefers to adopt an interior or surface solvation structure depending on cluster size. Furthermore, electronic structure calculations rely on the harmonic oscillator approximation to evaluate thermodynamic properties and are based on a few cluster structures, and therefore do not account for the floppiness of the cluster structures and may not yield a proper description of the entropy of these systems.

For the larger halides in the series, a discrepancy between the predictions of the OPLS and OPCS model potentials is also observed, consistent with what was found in previous work.^{103,123,145,150} This has been attributed to the fact that OPLS does not account for ion-water and water-water polarization, which has proven to be an essential factor in determining the solvation structure of ions in water clusters. Simulations of $\text{Cl}^-(\text{H}_2\text{O})_{20}$

clusters with varying ion-water binding enthalpies and polarizabilities reveal that the polarizability alone drives the ion to the surface or towards the interior of the cluster, and as such, the OPLS model cannot provide reliable thermodynamics of ionic solvation.

Various polarizable model potentials have been employed in the past to investigate the solvation structure of halides in water clusters,^{103,123,145,150} but these models predict that chloride and bromide ions reside at the surface of clusters containing up to 200 water molecules. The OPCS model, on the other hand, predicts an almost equal probability for interior and surface solvation states at cluster size 64 for both ions. All previous models, however, employ a 3-charge planar charge distribution for the water molecules. In contrast, OPCS uses a 4-charge site water model, where 2 of the charge sites are situated off the plane of the water molecule, which yields a 3-dimensional charge distribution that better reproduces the water multipole moments. Therefore, the polarizability of water and the ions may not be the only important factor in determining the solvation structure of halides in water clusters, and the details of the charge distribution may also play an important role. Since our simulation results suggest that the entropic contribution to the free energy is mainly responsible for the solvation structure of the ions, in accordance with previous studies, we believe that the 3-dimensional charge distribution of the OPCS water model may help capture the subtle interactions involved in a proper assessment of the cluster entropy.

In summary, our predictions with the OPCS model suggest that chloride, bromide and iodide undergo a transition from surface to interior solvation at around the same cluster size, whereas fluoride favors interior solvation at a much smaller cluster size,

consistent with the ion properties along the halide series. Furthermore, we have determined that entropy, rather than enthalpy, governs the solvation thermodynamics of halide-water clusters. The discrepancy between model potentials reveals that subtle polarization effects and the precise shape of the charge distribution of water significantly affects the cluster entropy and, thus, the solvation structure of ions in water clusters. Hence, further simulations, based on first-principles intermolecular interactions, need to be performed to eventually obtain a quantitative and definitive description of the transition from surface to interior solvation in halide-water clusters.

Theoretical Studies of Seeded Water Clusters: Structure,
Thermodynamics and Photochemistry

Chapter 4

Nonadiabatic Trajectory Studies of NaI(H₂O)_n Photodissociation Dynamics

Submitted as:

Denise M. Koch, Qadir K. Timerghazin, Gilles H. Peslherbe
Branka M. Ladanyi and James T. Hynes
Journal of Physical Chemistry A (2005)

4.1 Introduction

The electronic structure of alkali halides is characterized by a crossing of covalent and ionic curves, or equivalently an avoided crossing between ground and excited state adiabatic curves which change their electronic character in the neighborhood of the avoided crossing.¹⁵⁹ This characteristic leads to interesting effects in their dissociation dynamics and has prompted a number of experimental and theoretical studies of their gas-phase photodissociation dynamics, especially for NaI.^{63,64,159-167} The latter has attracted much attention because it is one of the alkali halides with the smallest internuclear separation at which the ionic and covalent curves cross.¹⁵⁹ At small internuclear separations, the electronic coupling between the diabatic states is large enough to enable the resulting adiabatic potentials to govern, at least in part, the nuclear motion. At large separations, this coupling is exponentially small and the dissociation proceeds nonadiabatically, as if there were no mixing of the covalent and ionic configurations.¹⁶⁸

The gas-phase photodissociation of NaI has been extensively investigated with femtosecond transition state spectroscopy,^{63,64,169} and experimental results have been successfully compared to quantum mechanical, semiclassical and classical calculations.^{63,163,166} In typical experiments, excitation from the ground (ionic) $^1\Sigma^+$ state to both the excited adiabatic $\Omega=1$ and $\Omega=0^+$ states – which are essentially covalent in the Franck-Condon region – are possible, and ionic products are not energetically accessible.¹⁶³ Due to symmetry considerations, the $\Omega=1$ state has no ionic character at any separation and, since it is purely repulsive and does not predissociate,¹⁷⁰ the NaI

molecules excited to this state produce free atoms on a very short time scale. On the other hand, the NaI molecules excited to the $\Omega=0^+$ state – whose character is covalent in the Franck-Condon region but ionic at larger separations – exhibit more interesting dynamics: they may be transiently trapped in a well formed by the avoided crossing of the covalent 0^+ and ionic surfaces, and then undergo a nonadiabatic transition to form atomic products.^{63,64} The excited-state population evolution can be followed in time by promoting the freshly excited NaI to a probe state, as depicted in Fig. 4.1, whose population can in turn be monitored by laser-induced fluorescence of the sodium D line^{63,64} or by collection of sodium ions by mass spectrometry.¹⁷¹ These detection schemes give rise to oscillatory signals – because of the transient trapping of the NaI population in the excited-state well – with decreasing amplitude, because of the leakage of excited-state population to form atoms via nonadiabatic transitions.

Our own interest in NaI has centered on the photodissociation dynamics for this system in solution⁶⁵ and in clusters.¹²⁴ Polar solvent molecules preferentially stabilize molecular species with a localized charge character, and ionic products of alkali halide photodissociation may become more favorable in solution or in small clusters. More generally, polar and/or polarizable solvents are known to modify solute electronic structures and influence the dynamics of chemical reactions, and we are particularly interested in the influence of solvation on the curve crossing dynamics of the NaI paradigm molecule. Our earlier theoretical work on NaI in solution,⁶⁵ which employed a combination of semiempirical valence bond theory in solution developed by Hynes and co-workers^{130,172} and transition state theory,¹⁷³ showed that activated electron transfer

(ET) would occur on the ms timescale. Remarkably, NaI was predicted to undergo electron transfer in the inverted regime.¹⁷⁴ Unfortunately, radiative deactivation of the freshly excited NaI followed by recombination of the ions on the ground state surface occurs on the ns timescale, and would short-circuit any electron transfer process. This work also suggested that activated ET might occur in small clusters, which are sufficiently large to involve significant solvation and “solvent” reorganization, but sufficiently small so that the associated ET barrier would be low enough to allow competition with radiative decay to an environmentally stabilized ground ionic state.

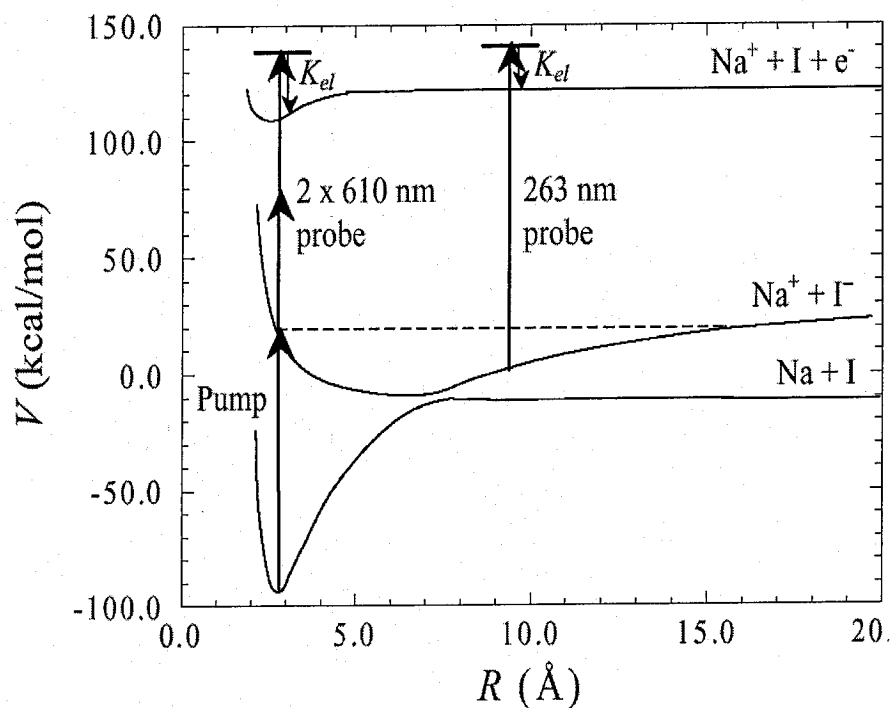


Figure 4.1 NaI adiabatic potential energy curves illustrating the two detection schemes (two-photon and one-photon probes) and the electron kinetic energy K_{el} employed to generate the time-resolved photoelectron spectra.

Cluster studies are also of independent fundamental interest, and have been the subject of recent experiments^{66,67,175} motivated in part by our earlier theoretical work,¹²⁴ which showed how the presence of a single solvent molecule affects the nonadiabatic dynamics of NaI photodissociation. In experimental studies of NaI ion pairs in polar solvent clusters of water, acetonitrile and ammonia,^{66,67,175} a very clear solvent-selective behavior was observed in the distribution of the detected Na⁺(solvent)_n product ions.¹⁷⁵ For instance, clusters of size up to n~50 have been observed experimentally with water, but no clusters larger than size 10 and 7 have been observed with ammonia and acetonitrile, respectively.¹⁷⁵ In previous theoretical work, we also investigated the structure and thermodynamics of NaI ion pairs in aqueous clusters.^{62,97} We found that NaI ion pairs are actually stable with respect to complete ground-state dissociation, even in very large water clusters, but that solvent-separated ion pairs (SSIP) become rapidly predominant over contact ion pairs (CIP) with increasing cluster size. Model electronic structure calculations showed that SSIP have a much reduced oscillator strength and may not possess optically accessible excited states akin to that of gas-phase NaI.⁹⁷ Our findings are consistent with the fact that products of NaI(H₂O)_n cluster photodissociation of size n>50 were not observed experimentally, as the larger SSIP parent clusters may just not be photochemically active. Interestingly enough, we also found that the structure of ion pairs in water clusters could be relatively simply related to that of the individual ions in water clusters.⁶² Of particular importance in this case is the now well-known hydration structure of the iodide ion in aqueous clusters,^{122,176,177} in which iodide preferentially sits at the surface of small- to medium-sized clusters, a solvation character

which may explain why NaI ion pairs are “dragged” to the surface of small water clusters.⁹⁷ Recently, Jungwirth and Tobias demonstrated that large halide ions tend to accumulate at the surface of the air/water interface of alkali-halide solutions for similar reasons, a finding which is of great importance for heterogeneous atmospheric chemistry.¹¹⁰

A striking finding in our earlier theoretical work¹²⁴ was the importance of solvent evaporation in the NaI(H₂O) photodissociation dynamics. Since it obviously significantly decreases the size of the cluster being investigated in the course of the reaction, one needs to pay attention to larger parent clusters in order to attempt a connection with experimental results, which have been primarily reported for the (product) cluster size range $n=1-8$.⁶⁷ One objective of the present work is to assess the importance of solvent evaporation in the photodissociation dynamics of NaI(H₂O)_n [$n>1$] clusters in order to make a more thorough connection with experimental findings. Another equally important objective is to investigate the nonadiabatic dynamics of photodissociation (and electron transfer) in NaI(H₂O)_n clusters as a function of cluster size and to simulate femtosecond probe signals and time-resolved photoelectron spectra for possible connection with experiment. As the differential solvation between the ionic and covalent NaI states increases with cluster size, one might expect different nonadiabatic transition dynamics as the ionic state becomes increasingly more stabilized upon addition of water molecules.

The outline of this article is as follows. The semiempirical valence-bond theory employed to describe the NaI electronic structure, the interaction potentials and the simulation methodology are presented in Section 4.2. The results of the simulations are

presented in Section 4.3, where particular attention is paid to water evaporation, nonadiabatic dynamics and possible connection with experiment. Concluding remarks follow in Section 4.4.

4.2 Computational Methodology

4.2.1 QM/MM Potential Energy Surfaces

In this work, we adopt a quantum mechanical/molecular mechanical (QM/MM) description of the NaI(H₂O)_n system, where the NaI solute is treated with semiempirical valence-bond (VB) theory and the water solvent molecules are described by classical model potentials. The total system Hamiltonian is

$$\hat{H}_T = \hat{K}_R + \hat{K}_{R^s} + \hat{H}(\mathbf{R}, \mathbf{r}, \mathbf{R}^s) + \hat{V}(\mathbf{R}, \mathbf{R}^s) \quad (4.1)$$

where \mathbf{R} and \mathbf{R}^s represent the nuclear degrees of freedom of the NaI solute and the solvent molecules, respectively, and \mathbf{r} the NaI solute electronic degrees of freedom. The first two terms in the Hamiltonian of Eq. (1) are the nuclear kinetic energies, the third term is the Hamiltonian for the NaI electronic structure and the last term represents the classical potential of the solvent molecules, including interactions with the solute nuclei. The solute Hamiltonian can be written as

$$\hat{H}(\mathbf{R}, \mathbf{r}, \mathbf{R}^s) = \hat{H}^0(\mathbf{R}, \mathbf{r}) + \hat{V}^C(\mathbf{R}, \mathbf{r}, \mathbf{R}^s) \quad (4.2)$$

where $\hat{H}^0(\mathbf{R}, \mathbf{r})$ is the solute gas-phase Hamiltonian and $\hat{V}^C(\mathbf{R}, \mathbf{r}, \mathbf{R}^s)$ represents the Coulombic interaction between the solvent molecule charge distribution and the solute electronic degrees of freedom. With this ansatz, it is obvious that the solvent is allowed to

affect the electronic structure of the solute via electrostatic interactions. Finally, the last term of the Hamiltonian in Eq. (1) is expressed as

$$\hat{V}(\mathbf{R}, \mathbf{R}^s) = \hat{V}_{ss}^C(\mathbf{R}^s) + \hat{V}_{ss}^{r-d}(\mathbf{R}^s) + \hat{V}^{r-d}(\mathbf{R}, \mathbf{R}^s) \quad (4.3)$$

where the first two terms are the solvent-solvent Coulombic and repulsion-dispersion interactions and the last term represents the repulsion-dispersion interaction between the nuclei of the solute and those of the solvent molecules.

4.2.2 NaI Electronic Structure and Potentials

The NaI electronic structure is expressed as a linear combination of *ionic* and *covalent* charge-localized VB (or diabatic) states

$$\psi = \sum c_i \Phi_i \quad (4.4)$$

and the wavefunction is solved for in the framework of semiempirical VB theory.^{65,178,179}

In this theory, some or all of the valence electrons are treated explicitly, while all other solute electronic and nuclear energy contributions are embedded in a core-core potential H^{cc} . One-electron and two-electron integrals for the electrons treated explicitly are evaluated using semiempirical expressions, based on the point charge, Pariser and Mulliken approximations,¹⁸⁰ resulting in analytical expressions for all diabatic matrix elements.

For alkali-metal halides MX, only two electrons need to be considered explicitly⁶⁵ and the charge-localized VB states are expressed as the normalized Slater determinants $\Phi_1 = N_1 |\bar{X}X|$ and $\Phi_2 = N_2 (|\bar{M}X| - |MX\bar{M}|)$ for the ionic and covalent states, respectively, where the core electrons have been omitted, X represents the halogen valence p orbital

lying along the bond axis, and M represents the alkali metal valence s orbital. The corresponding vacuum electronic Hamiltonian matrix elements, which represent the diabatic ionic and covalent curves, are given by⁶⁵

$$H_{11}^0(R) = \langle \Phi_1 | \hat{H}^0 | \Phi_1 \rangle = H^{cc}(R) - IP(X) - EA(X) - \frac{2e^2}{R}; \quad (4.5)$$

$$H_{22}^0(R) = \langle \Phi_2 | \hat{H}^0 | \Phi_2 \rangle = \frac{1}{2[1 + S_{MX}^2(R)]} \left\{ H^{cc}(R) - 2IP(X) - 2IP(M) - \frac{2e^2}{R} \right. \\ \left. - \frac{S_{MX}^2(R)}{1 + S_{MX}^2(R)} \left\{ 3IP(X) + 3IP(M) + EA(X) + EA(M) + \frac{2e^2}{R} + 2\rho(X) + 2\rho(M) \right\} \right\} \quad (4.6)$$

with the electronic coupling

$$H_{12}^0(R) = \langle \Phi_1 | \hat{H}^0 | \Phi_2 \rangle \\ = \frac{S_{MX}(R)}{\sqrt{2[1 + S_{MX}^2(R)]}} \left\{ 2H^{cc}(R) - 2IP(X) - IP(M) - EA(X) - \frac{2e^2}{R} - \frac{1}{2}\rho(X) - \frac{1}{2}\rho(M) \right\}, \quad (4.7)$$

while the diabatic state overlap is

$$S_{12}(R) = \langle \Phi_1 | \Phi_2 \rangle = \frac{S_{MX}(R)}{\sqrt{2[1 + S_{MX}^2(R)]}}, \quad (4.8)$$

where R is the internuclear separation, IP and EA are the ionization potential and electron affinity, $\rho(\chi)$ is a one-electron integral of the form $\langle \chi | 1/r | \chi \rangle$ and S_{MX} is the overlap between the metal s and halogen p orbital. For Slater orbitals,^{181,182} ρ is just the Slater exponent ξ divided by the principal quantum number n and the overlap S_{MX} can be calculated analytically in terms of auxiliary functions.¹⁸³ The 5p Slater orbital with

exponent $\xi=1.9$ and the 3s Slater orbital with exponent $\xi=0.7333$ are used here for iodine and sodium, respectively.^{181,182} The ionization potentials for sodium and iodine are 5.14 and 10.45 eV, respectively, while the electron affinity of sodium and iodine is 0.55 and 3.06 eV, respectively.¹²⁶

In the present work and in contrast to our earlier work,⁶⁵ we slightly depart from the original semiempirical theory and adjust the core-core potential parameters *separately* for both VB states in order to better reproduce experimentally derived potentials and experimental Franck-Condon (FC) energy gaps. $H_{11}^{cc}(R)$ is chosen so as to match the ionic diabatic state energy $H_{11}^0(R)$ with the widely accepted ionic potential due to Levine and coworkers,¹⁶² whose functional form is a slightly modified form of the Rittner potential,¹⁸⁴ i.e.

$$H_{11}^{cc}(R) = IP(X) + IP(M) + \left[A_{ion} + \left(\frac{B_{ion}}{R} \right)^8 \right] e^{-R/R_{ion}} + \frac{e^2}{R} + E_{vdw/pol}(R) \quad (4.9)$$

where the van der Waals attraction and polarization energy term is expressed as

$$E_{vdw/pol}(R) = -\frac{C_{vdw}}{R^6} - \frac{(\alpha_{M^+} + \alpha_{X^-}) \cdot e^2}{2R^4} - \frac{(2\alpha_{M^+}\alpha_{X^-}) \cdot e^2}{R^7}, \quad (4.10)$$

with $A_{ion} = 2760$ eV, $B_{ion} = 2.398$ eV^{1/8}Å, $R_{ion} = 0.3489$ Å, $C_{vdw} = 11.3$ eV·Å⁶, $\alpha_{M^+} = 0.408$ Å³ and $\alpha_{X^-} = 6.431$ Å³.^{162,185} There have been a number of experimental studies aimed at characterizing the covalent state.^{170,185-188} With a core-core potential of the form

$$H_{22}^{cc}(R) = IP(X) + IP(M) + A_{cov} e^{-B_{cov}(R-R_{cov})}, \quad (4.11)$$

where $A_{cov} = 0.8$ eV, $B_{cov} = 2.5$ Å⁻¹ and $R_{cov} = 2.65$ Å, the covalent state potential matches covalent curves derived from total absorption spectra¹⁷⁰ and is very similar to

potentials recently derived from various experiments.^{186,189} The position of the covalent repulsive wall that we have determined coincides with the one used by Zewail and coworkers for their classical and quantum mechanical calculations.^{63,163}

With the latter parameterization of the core-core potentials, the position of the covalent and ionic curve crossing determined here, $R_c \sim 7$ Å, is in good agreement with the commonly accepted value 6.93 Å.¹⁵⁹ The diabatic state electronic resonance coupling $H_{12}^0(R)$, obtained from the semiempirical VB calculations appears to have a more reasonable behavior than that of Zewail and coworkers,^{63,163} in that it is exponential in the internuclear separation range $R > 2.7$ Å, in agreement with electronic structure calculations.¹⁶⁷ The semiempirical VB theory value -0.06 eV of $H_{12}^0(R)$ at the crossing point is in rather good agreement with the accepted value -0.055 eV, for which there is a wide consensus, both theoretically and experimentally.^{63,168,185,186}

The secular equation is solved next for the two-state problem to yield the NaI adiabatic electronic ground ($X^1\Sigma^+$) and first excited ($A^1\Sigma^+$) states. The potential energy curves for both adiabatic states (*cf.* Fig. 4.1) are in good agreement with Multi-Reference singly and doubly excited Configuration Interaction (MRCI) electronic structure calculations by Sakai *et al.*,¹⁶⁵ and more recent ones by Alekseyev *et al.* that include spin-orbit coupling.¹⁶⁷ As expected, the first excited state exhibits a shallow well resulting from the avoided crossing of the ionic and covalent states. The gas-phase NaI Franck-Condon (FC) excitation energy predicted by our semiempirical VB model corresponds to a wavelength of 296 nm, which lies at the lower end of the experimental range of excitation wavelengths.^{63,64} For instance, the calculated FC excess energy in the excited

adiabatic state is 4 to 8 kcal/mol larger than its experimental counterpart for typical experiments carried out at 300 and 312 nm, respectively.^{63,64,171} Overall, the NaI potentials are in reasonable agreement, not only with experiment, but also with high-level electronic structure calculations.^{165,167}

4.2.3 Solvation and Water Potentials

The ionic-covalent electronic coupling is small in the neighborhood of the diabatic curve crossing (less than 2 kcal/mol), which is indicative of the Born-Oppenheimer regime of solvation,⁶⁵ where the solvent electrons move much faster than the solute electrons, so that the solvent effectively “feels” charge-localized solute state charge distributions. As a result, following our earlier work,^{65,190} the instantaneous solvation energy for the solute VB state charge distributions is computed and incorporated in the individual Hamiltonian matrix elements, i.e.

$$H_{ij} = H_{ij}^0 + V_{ij}^C \quad (4.12)$$

before solving for adiabatic energies. By using the point-charge approximation embedded in semiempirical VB theory, the diagonal Coulombic interaction matrix elements become

$$V_{ii}^C = \sum_j \frac{q_{Na}^i q_j^s}{|R_{Na} - R_j^s|} + \sum_j \frac{q_I^i q_j^s}{|R_I - R_j^s|} \quad (4.13)$$

where j labels the charge sites of solvent molecules (the s superscript refers to solvent molecules), and q_{Na}^i and q_I^i represent the sodium and iodine charges in the i^{th} diabatic state, respectively. Finally, the Coulomb-matrix off-diagonal elements are estimated via the Mulliken approximation

$$V_{ij}^C = \frac{S_{ij}}{2} (V_{ii}^C + V_{jj}^C). \quad (4.14)$$

This level of description of the solute-solvent electrostatic interactions in terms of point charges is in complete agreement with the spirit of the semiempirical VB theory used to describe the NaI electronic structure.

The sodium and iodine charges are obtained from a fit of the MRCI ground and first excited-state NaI dipole moments as a function NaI internuclear separation.¹⁶⁵ We note that, even though fixed gas-phase charge distributions are employed for the NaI diabatic states, the solvent polarizes NaI by modifying the contribution of each VB state to the NaI electronic structure. A very interesting feature of the dipole moment curves is that the first excited state is polarized in the Franck-Condon region, but with a reverse polarity, compared to that of the ionic ground state. For example, the apparent partial charges of Na^{+δ}I^{-δ} are 0.75 and -0.35 for the ground and excited adiabatic NaI states in the FC region, respectively. This finding, which appears to be characteristic of alkali halides, can be interpreted in light of semiempirical VB theory and the classical model of polarization that is embedded in the core-core potential in order to correct for the minimum basis set deficiency of semiempirical theory, as discussed earlier.¹²⁴ The latter finding, as we shall see shortly, has a dramatic impact on the NaI(H₂O)_n photodissociation mechanism and dynamics, just as was found previously for NaI(H₂O).⁶⁵

The water is described by the rigid TIP4P model,⁹⁹ which consists of Coulombic potentials for electrostatic interactions [$\hat{V}_{ss}^C(\mathbf{R}^s)$ in Eq. (3)], using point charges of 0.52e on the hydrogen atoms and -1.04e on an interaction site situated on the bisector of the H-

O-H angle at 0.15 Å from the oxygen atom, and parameterized Lennard-Jones functions for repulsion-dispersion interactions [$\hat{V}_{ss}^{r-d}(\mathbf{R}^s)$ in Eq. (3)] with parameters $\epsilon_{O-O} = 0.155$ kcal/mol and $\sigma_{O-O} = 3.154$ Å. The nonelectrostatic part of the NaI-water interactions [$\hat{V}^{r-d}(\mathbf{R}, \mathbf{R}^s)$ in Eq. (3)] is described by Lennard-Jones terms like for OPLS potentials.⁸⁶ The parameters for Na⁺-H₂O interactions ($\epsilon_{O-Na} = 0.499$ kcal/mol and $\sigma_{O-Na} = 2.446$ Å) are taken from the early work of Jorgensen and co-workers,¹⁰⁰ while the parameters for I⁻-H₂O interactions ($\epsilon_{O-I} = 0.225$ kcal/mol and $\sigma_{O-I} = 3.970$ Å), which have not been reported to our knowledge, were derived in the very same fashion as for other halide-water interactions.¹²⁴ The same Lennard-Jones parameters are used for both ion-water and atom-water interactions for simplicity. Simulations of the photoexcited NaI(H₂O) dynamics performed with a flexible water model,¹⁹¹ showed that energy transfer to water vibrations in the course of trajectories was negligible, indicating that the rigid water model is adequate for the present simulations. Furthermore, we note that with these model potentials, the electronic polarizability of the solvent molecules is kept frozen, instead of being instantaneously equilibrated to the solute charge distribution, in contrast to our earlier solution work.⁶⁵ According to high level MRCI electronic structure calculations,¹⁹² the water charge distribution does not change significantly between the NaI(H₂O) ground and excited states, such that the static charge distribution of the TIP4P water model is a sensible approximation for small clusters. Overall, we expect our QM/MM potentials to yield reasonably realistic dynamics for this system. As a matter of fact, successful comparison of our simulation results with experiment in Section III suggests that this is the case.

4.2.4 Molecular Dynamics with Quantum Transitions

Many methods have been developed to simulate non-Born-Oppenheimer dynamics. In this work, we employ a “surface hopping” trajectory method known as the “molecular dynamics with quantum transitions” (MDQT) method, developed by Tully and coworkers,¹⁹³ to follow the dynamics in the excited electronic state and the decay to the ground state. Surface hopping methods are known to describe well nonadiabatic dynamics involving rapid transitions, and we thus believe the MDQT method is best suited for our purpose. In this method, the classical particles (nuclei) are constrained to evolve on an individual adiabatic (electronic) potential energy surface with the quantum (electronic) degrees of freedom propagated simultaneously, and, at each trajectory timestep, the quantum subsystem time evolution dictates the choice of which adiabatic potential energy surface the dynamics will be propagated on in the following timestep.

The time-dependent wavefunction of the system is expanded in terms of the electronic adiabatic states

$$\Psi(\mathbf{Q}, \mathbf{r}, t) = \sum_j C_j(t) \psi_j(\mathbf{Q}, \mathbf{r}), \quad (4.15)$$

where $\mathbf{Q} = (\mathbf{R}, \mathbf{R}')$ represents all the nuclear degrees of freedom, i.e. both those of the solute and the solvent molecules. The wavefunction $\Psi(\mathbf{Q}, \mathbf{r}, t)$ is propagated together with the classical nuclear motion, using the “classical path” equations of motion¹⁹³

$$i\hbar \dot{C}_k = \sum_j C_j (V_{kj} - i\hbar \dot{\mathbf{Q}} \cdot \mathbf{d}_{kj}) \quad (4.16)$$

where

$$V_{kj} = \langle \psi_k | \hat{H} | \psi_j \rangle \quad (4.17)$$

are the Hamiltonian matrix elements over the adiabatic electronic states and

$$d_{kj} = \langle \psi_k | \nabla_Q \psi_j \rangle \quad (4.18)$$

is the nonadiabatic coupling vector between the electronic states, a key ingredient in the equations of motion for the quantum degrees of freedom. In contrast to earlier applications of the MDQT method,¹⁹³ where the propagation of the time-dependent wavefunction relied on a number of numerical approximations, the present mixed semiempirical VB/classical potential representation allows one to compute the elements of the nonadiabatic coupling vector – and thus the right-hand side of the quantum equations of motion, Eq. (16) – analytically, so that the propagation of the quantum degrees of freedom reduces to a two-point boundary value problem, which is solved efficiently and accurately by a second-order finite-difference-equation numerical method.¹²⁵

With the MDQT method, transitions can occur anywhere along trajectories, not just at localized avoided crossings. At each trajectory time step, the probability to undergo a transition is calculated from the time-dependent wavefunction expansion coefficients as¹⁹³

$$g_{kj} = \frac{f_{jk} \Delta t}{\rho_{kk}}; f_{jk} = 2\hbar^{-1} \text{Im}(\rho_{jk}^* V_{jk} - 2\text{Re}(\rho_{jk}^* Q \cdot d_{jk})), \quad (4.19)$$

where Δt is the time step, and ρ is the density matrix, i.e. $\rho_{kj} = C_k C_j^*$. A stochastic “fewest switches” algorithm is used to decide whether a hop to another adiabatic state should occur or not.¹⁹³ If a switch between states is performed, the energy difference

between the states is distributed among the various classical degrees of freedom along the nonadiabatic coupling vector as¹⁹³

$$\dot{Q}'_i = \dot{Q}_i - \frac{\gamma_{kk'} d_{kk'}^i}{m_i} \quad (4.20)$$

where m_i is the mass of the atom i , and

$$\gamma_{kk'} = \frac{b_{kk'} \pm \sqrt{b_{kk'}^2 - 4a_{kk'}[V_{kk}(Q) - V_{k'k'}(Q)]}}{2a_{kk'}}; a_{kk'} = \frac{1}{2} \sum_i |d_{kk'}^i|^2; b_{kk'} = \sum_i \dot{Q}_i \cdot d_{kk'}^i \quad (4.21)$$

In the MDQT method, each trajectory is propagated completely coherently, i.e. values of the coefficients of the time-dependent wavefunction are retained throughout the propagation, so that in order to account for quantum decoherence, one needs to propagate a swarm of trajectories for a given single classical initial condition. Each swarm trajectory follows its own path, and the resulting spreading of trajectories leads to a loss of phase coherence when summing the results over all trajectories.¹⁹⁴ Test calculations showed that a swarm of 100 trajectories was sufficient to obtain converged results for the NaI curve crossing dynamics, and we shall use this swarm size thereafter. Finally, in simulations^{195,196} where all or part of the system is described by quantum chemistry/mechanics and the remaining part is described with classical potentials, the “quantum” forces on the nuclei are customarily computed via the Hellmann-Feynman theorem.¹⁹⁷ However, Hellmann-Feynman forces are grossly in error in the small, incomplete basis set representation of semiempirical VB theory employed here, and analytical expressions for the forces with the aforementioned mixed semiempirical VB theory/classical potentials were derived. The nuclear motion is propagated classically

with the “velocity” version¹⁹⁸ of the Verlet algorithm,¹⁹⁹ and a stepsize of 0.2 fs, which ensures excellent energy conservation.

4.2.5 Simulation of Experimental Data

We apply essentially the same detection schemes as those reported by Jouvét *et al.* to obtain femtosecond probe signals and photoelectron spectra,^{67,171} in which excitation is made to a probe state which asymptotically correlates to Na⁺ + I + e. Recent electronic structure calculations,²⁰⁰ using Multi-Reference Configuration Interaction with Davidson correction and complete basis set extrapolation (MRCI+Q/CBS), suggest that the Na⁺...I complex has two energetically accessible electronic states within the range of experimental probe laser wavelengths employed for the study of bare NaI and NaI(H₂O)_n. Spin-orbit coupling of NaI⁺ electronic states yields the X ($\Omega = 1/2$) state, with pure Π character, and the I ($\Omega = 3/2$) state, which is a mixture of $^2\Pi$ and $^2\Sigma$ states, as shown in Fig. 4.1. Following selection rules for the photoionization of diatomic molecules proposed by Xie and Zare,²⁰¹ transition from the first excited NaI state to both the X and I NaI⁺ states are allowed, and promotion to both of these states is considered in our simulations. Accurate analytical potentials for the $^2\Pi$ and $^2\Sigma$ states of the NaI⁺ complex have been derived in previous work.²⁰⁰ The potentials consist of Born-Mayer repulsion terms and London dispersion terms for short-range interactions, and ion-induced dipole and ion-quadrupole terms for long-range interactions, *i.e.*:

$$V_{^2\Pi,^2\Sigma}(R) = Ae^{-Br} - \frac{C}{R^6} - \frac{\alpha \cdot e^2}{2R^4} + \frac{Q \cdot e}{R^3} \quad (4.22)$$

and the parameters, listed in Table 4.1, were obtained from a standard nonlinear least-square fit of the MRCI+Q/CBS potential energy curves. A semiempirical approach is used within our simulation procedure to obtain the spin-orbit coupled X and I state potential energy curves from the ²Π and ²Σ state analytical potentials.²⁰⁰ The resulting X and I states are given by

$$X_{\Omega=3/2}(R) = {}^2\Pi(R) - \lambda \quad (4.23)$$

and

$$I_{\Omega=1/2}(R) = \frac{1}{2} \left\{ {}^2\Sigma(R) + {}^2\Pi(R) + \lambda + \sqrt{[{}^2\Pi(R) - {}^2\Sigma(R)]^2 + 2\lambda[{}^2\Pi(R) - {}^2\Sigma(R)] + 9\lambda^2} \right\}, \quad (4.24)$$

respectively. The coupling constant λ is calculated from the experimental spin-orbit coupling of the free iodine atom $\xi = 7.25$ kcal/mol as $\lambda = \xi/2$. Finally, the diabatic probe states are not included when solving for the first two adiabatic states of NaI, as they lie very high in energy, and thus do not mix with the ionic and covalent NaI diabatic states.

Table 4.1 Model potential parameters for the ²Π and ²Σ NaI⁺ probe states of Eq. (4.22)

	² Π state	² Σ state
A (kcal/mol)	83340	71547
B (Å ⁻¹)	2.881	3.064
C (kcal/mol/Å ⁶)	7531	3728
α (Å ³)	5.02	4.53
Q (e·Å ²)	-0.34	0.72

Two different detection schemes (illustrated in Fig. 4.1) that were employed in previous experimental femtosecond studies of bare NaI and NaI(H₂O)_n clusters have been considered. Because of the dynamic stabilization of the ionic portion of the first NaI excited state by surrounding water molecules, a 2×610 nm probe scheme was used for cluster studies,⁶⁷ where ionization from the covalent branch of the first excited state was found to be efficient in solvent clusters. For reasons that will become obvious shortly, a second detection scheme was considered in this study, involving a 263 nm probe excitation from the ionic branch of the first excited state, as was used for studies of bare NaI.¹⁷¹ Essentially, for each excitation-detection (pump-probe) time delay, the species trapped in the first excited-state well, and only those for which the NaI excited state is predominantly covalent, undergo a vertical 2×610 nm excitation in the two-photon detection scheme, while only those for which the excited state is predominantly ionic undergo a vertical 263 nm excitation in the one-photon detection scheme. If the total energy of the freshly excited species exceeds that of the X and/or I probe state, the species are promoted to the given NaI⁺ probe state. As shown in Fig. 4.1, upon promotion to the NaI⁺ state, an electron is ejected with a kinetic energy K_{el} corresponding to the excess energy of the ionizing probe photon energy relative to the probe state (while the NaI nuclear kinetic energy remains unaffected by the ejection of the electron). The Na⁺(H₂O)_p and the NaI⁺(H₂O)_p probe signals, where p represents the detected product cluster size, were evaluated after propagating the NaI⁺(H₂O)_n dynamics on the probe state for 4 ps. This time was chosen to account for the long time delay between the probe pulse and detection by time-of-flight mass spectrometry. As done previously,¹⁷¹ the newly NaI⁺

ionized species is considered dissociated if the internal energy exceeds the binding energy of 10.4 and 4.2 kcal/mol for the X state for the I state, respectively.²⁰⁰ Water molecules are considered evaporated from the NaI excited state or probe state complex if their energy exceeds that of the Na⁽⁺⁾-H₂O or I⁽⁻⁾-H₂O binding energies. Finally, the resulting histogram distributions of the Na⁺(H₂O)_p and the NaI⁺(H₂O)_p species are convoluted with a gaussian function, with variance of 100 fs to 250 fs, in order to account for the presumably Gaussian experimental pump and probe pulse envelopes.

4.3 Results and Discussion

In this section, we first discuss the thermal distributions of NaI(H₂O)_n ground-state structures that serve as initial conditions in the MDQT simulations. The effect of solvation and water evaporation on the simulated excited-state population decay are then discussed. We also examine the water evaporation dynamics and the mechanistic details of the evaporative process, and finally, we connect our simulated probe signals with available experimental data, and propose various spectroscopic schemes to further explore the photodissociation dynamics of NaI(H₂O)_n clusters.

4.3.1 Ground-State Structures – Initial Conditions

Canonical ensembles of (20 x n) ground-state NaI(H₂O)_n [n=1-4] structures, *e.g.* 60 initial structures for NaI(H₂O)₃, were sampled from Nosé molecular dynamics²⁰² runs performed at 300 K with a modified version of the velocity Verlet algorithm.¹⁴³ Since the model potential employs rigid water molecules, there are only six degrees of freedom per water molecule, and thus 20 initial conditions per water molecule represents adequate

sampling. Representative structures for each cluster size are shown in Fig. 4.2, and the distributions of Na–H₂O intermolecular distances $P(R_{\text{Na-H}_2\text{O}})$ as a function of cluster size are displayed in Fig. 4.3. Since the room-temperature binding energy of Na⁺ to water (24 kcal/mol) is much higher than that of I[−] to water (~ 10 kcal/mol),^{17,21,203} the water molecules will tend to bind to the sodium end of NaI in the ground ionic state, as illustrated in Fig. 4.2. For all cluster sizes, a peak in the $R_{\text{Na-H}_2\text{O}}$ distribution, shown in Fig. 4.3, occurs at *ca.* 2.3 Å, which is approximately the equilibrium Na⁺–H₂O distance predicted by electronic structure calculations for small Na⁺(H₂O)_n clusters.⁶² For larger NaI(H₂O)_n [n=3,4] clusters a broad, second peak centered at $R_{\text{Na-H}_2\text{O}} \sim 4.0$ Å appears in

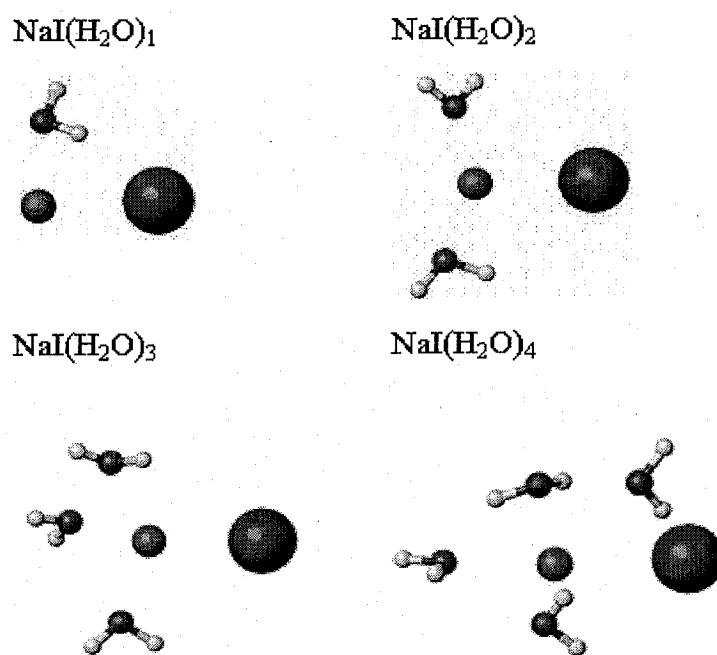


Figure 4.2 Representative ground-state NaI(H₂O)_n [n=1–4] cluster structures at 300 K.

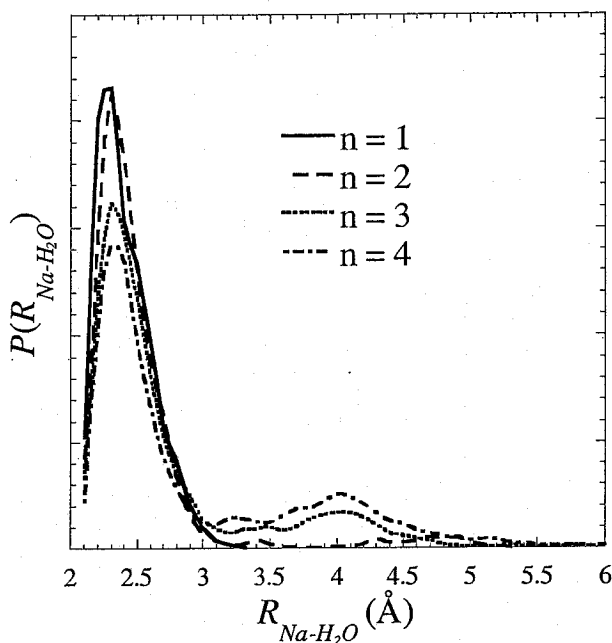


Figure 4.3 Thermal distribution of initial Na-H₂O distances $P(R_{\text{Na-H}_2\text{O}})$ obtained from Nosé molecular dynamics simulations of ground-state NaI(H₂O)_n clusters of size 1 (dash), 2 (dot), 3 (dash-dot), and 4 (thin solid).

the distributions. This broad peak corresponds to $\sim 2\%$ of the whole population of water molecules, which transiently dwell on the iodide end of ground-state NaI.

The canonical ensembles of configurations provide initial cluster structures for the MDQT simulations. In contrast to our previous NaI(H₂O) photodissociation dynamics study where a 296 nm pump pulse was used,¹²⁴ NaI(H₂O)_n clusters undergo a simple vertical Franck-Condon excitation with an energy corresponding to the difference between the ground and first excited-state potential energies ΔE_{FC} . Due to thermal excitation and the dynamically changing solvent environment, the ground-state NaI internuclear distance R varies significantly with cluster size, as evidenced by the distributions $P(R)$ shown in Fig. 4.4a. Accordingly, the initial FC excitation energy

differs for each starting NaI(H₂O)_n cluster configuration, resulting in FC energy gap

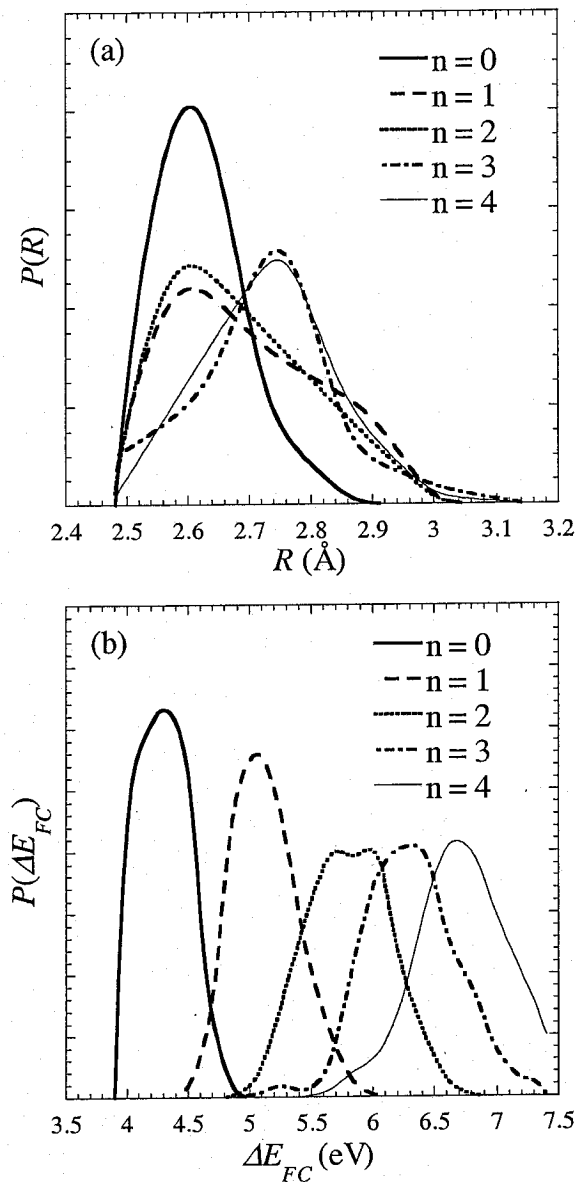


Figure 4.4 Distributions of (a) ground-state NaI internuclear separations $P(R)$, and (b) ground-to-excited state Franck-Condon (FC) energy gaps $P(\Delta E_{FC})$, for NaI(H₂O)_n clusters of size 0 (solid), 1 (dash), 2 (dot), 3 (dash-dot), and 4 (thin solid). Data has been smoothed to remove slight numerical noise.

distributions, which are shown in Fig. 4.4b. The average ΔE_{FC} , listed in Table 4.2, increases as a function of cluster size, which results in an overall increase of 2.3 eV for NaI(H₂O)₄, compared to that of bare NaI. The recent pump-probe experiment of Grégoire *et al.* suggests that the maximum in the absorption efficiency as a function of laser wavelength for NaI(H₂O)₂ is blue-shifted by 1.1 eV relative to that of bare NaI, and by 1.3 eV for NaI(H₂O)₁₆.⁶⁷ Electronic structure MRCI calculations using a double-zeta basis set predict excitation energies for NaI(H₂O)₂ and NaI(H₂O)₄ 1.1 eV and 1.2 eV larger than for bare NaI, respectively,¹⁹² in good agreement with experimental findings. Due to the discrepancy between our simulated ΔE_{FC} and the experimental and electronic structure theory results, we limit our simulations to small cluster sizes where the discrepancy in FC energy gap is not too large. As will be discussed later, this discrepancy is not a major concern and is of no consequence for the actual excited-state dynamics.

Table 4.2. NaI(H₂O)_n properties^a.

n	0	1	2	3	4
$\langle \Delta E_{FC} \rangle$ (eV)	4.2 ± 0.1	5.0 ± 0.2	5.7 ± 0.3	6.2 ± 0.3	6.7 ± 0.4
$\langle t_c \rangle$ (fs)	156 ± 10	168 ± 22	178 ± 22	182 ± 33	183 ± 40
$\langle V_{1,1c}^C \rangle$ (kcal/mol)		-1 ± 2	-3 ± 4	-4 ± 4	-5 ± 4
$\langle R_c \rangle$ (Å)	6.6 ± 1.3	7.1 ± 1.3	7.7 ± 1.3	8.1 ± 1.3	8.3 ± 1.3
$\langle T \rangle$ (fs)	1600 ± 300	1400 ± 400	1300 ± 500	1200 ± 700	1200 ± 800
$\langle F_{Na-O}^0 \rangle$ (amu·Å/fs ²)		24 ± 15	10 ± 10	16 ± 10	9 ± 8

$\langle \tau^0 \rangle$ (amu/fs ²)		14 ± 3	15 ± 3	16 ± 4	16 ± 4
$\langle E_{FC}^0 \rangle$ (kcal/mol)	30 ± 2	37 ± 5	46 ± 6	52 ± 7	56 ± 8

^aAverage properties over ensembles of configurations, along with standard deviations. ΔE_{FC} is the Franck-Condon energy gap, t_c is the time at which NaI reaches the curve-crossing region for the first time, $V_{1,lc}^C$ is the Coulombic interaction energy between the water molecule and ionic NaI at the curve-crossing point, R_c is the NaI internuclear separation at the curve-crossing point, T is the NaI vibrational period on the first excited state, F_{Na-O}^0 is the magnitude of the force acting on the water oxygen atom due to sodium upon excitation, τ^0 is the magnitude of the torque induced on the water molecule by NaI upon excitation, and E_{FC}^0 is the excess Franck-Condon energy upon excitation.

4.3.2 Nonadiabatic Dynamics

The excited-state population lifetimes resulting from the MDQT simulations are displayed in Fig. 4.5. For all cluster sizes, a sharp initial drop in the excited-state population occurs at *ca.* 200 fs, which roughly corresponds to the time at which the NaI system reaches the crossing region for the first time t_c , as supported by the average times at which NaI reaches the diabatic curve-crossing point for the first time $\langle t_c \rangle$ listed in Table 4.2. The drop in the excited-state population in the crossing region increases as a function of cluster size because the outer ionic portion of the excited-state curve is increasingly stabilized by the presence of water molecules. This is illustrated by the NaI–H₂O Coulombic interaction energies in the ionic state $\langle V_{1,lc}^C \rangle$ in the curve-crossing region, listed in Table 4.2, which increases in magnitude with cluster size. As a result, the average covalent/ionic curve-crossing points $\langle R_c \rangle$, also listed in Table 4.2, increases with cluster size, and since the NaI electronic coupling decreases exponentially with increasing internuclear distance, the excited- to ground-state transition probability

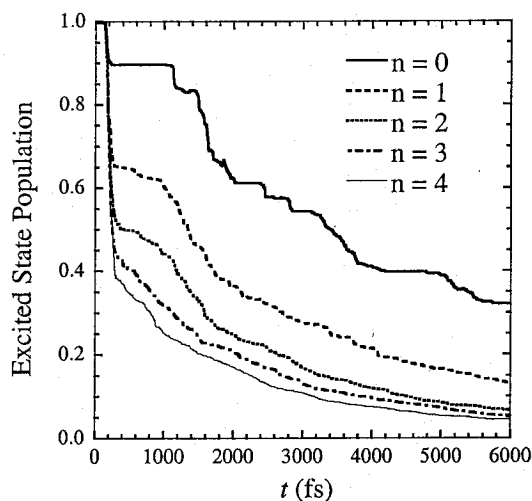


Figure 4.5 Excited-state population as a function of simulation time obtained from MDQT simulations of NaI(H₂O)_n clusters of size 0 (solid), 1 (dash), 2 (dot), 3 (dash-dot) or 4 (thin solid).

increases with cluster size, and the excited-state population decay also increases. Moreover, the excited-state population decay is enhanced by dynamical fluctuations in the relative position of the diabatic covalent and ionic states caused by the motion of the surrounding water molecules, which sometimes results in multiple nonadiabatic transitions during the first NaI oscillation period.

As was found previously for NaI(H₂O),¹²⁴ the NaI(H₂O)_n [n=1-4] excited-state population decay resembles that of bare NaI after reaching the curve-crossing region for the first time ($t > 200$ fs), as can be seen from Fig. 4.5. As will be discussed in more detail in the following Section, the initial repulsive force arising from the reversed NaI polarity causes the evaporation of 99% of the water molecules for NaI(H₂O) and 95% for NaI(H₂O)_n [n=2-4] by the time the NaI system reaches the curve-crossing region for the first time – the water evaporation time t_{evap} being defined as the time at the last inner

turning point in the Na–H₂O or I–H₂O bound motion. Nonetheless, the evaporated water molecules are at an average distance of only 5 ± 2 Å from NaI when it reaches the curve-crossing region for the first time (the average distance, which exhibits very little cluster size dependence, is evaluated over all configurations and cluster sizes). The water molecules are therefore still close enough to NaI to affect the excited-state dynamics in the crossing region, but solvation effects decline rapidly as the water molecules move further away from the solute, such that the NaI(H₂O)_n long-time excited-state dynamics are not significantly affected by the presence of water, and consequently resemble that of bare NaI.

The periodic features in the long-time excited-state decay observed for bare NaI disappear with increasing cluster size. Some periodicity in the excited-state population decay for the first NaI oscillation period is still apparent for cluster sizes 1 and 2, but it disappears completely for larger cluster sizes. The distributions of excited-state NaI vibrational periods $P(T)$ for the trajectories that remain in the excited state after reaching the curve-crossing region for the first time are shown in Fig. 4.6. The disappearance of the periodicity in the NaI vibrational motion with increasing cluster size is due to vibrational dephasing, as evidenced by the broadening of the $P(T)$ distributions with cluster size. Furthermore, the positions of the distribution peaks, and the corresponding average vibrational periods $\langle T \rangle$, listed in Table 4.2, decrease with cluster size, suggesting that NaI has increasingly less post-H₂O evaporation residual energy. We also note that, in the cluster case, the vibrational period can extend beyond that of gas-phase NaI, due to solvation of the ionic portion of the excited state when water remains bound to either the

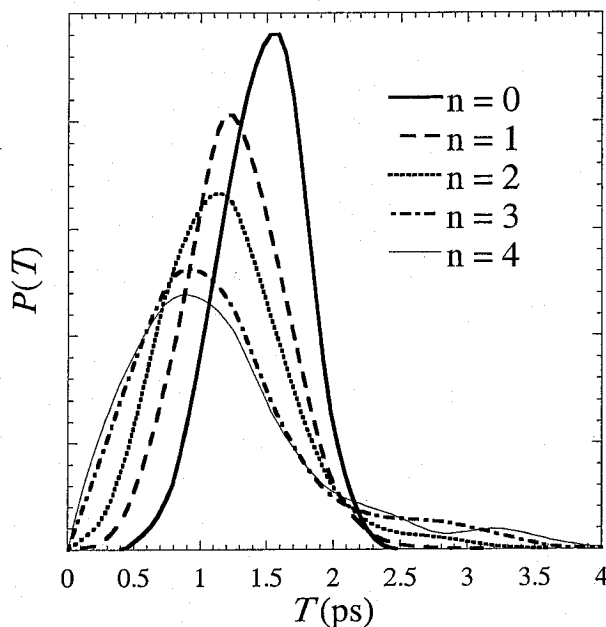


Figure 4.6 Distribution of excited-state NaI vibrational periods $P(T)$ for NaI(H₂O)_n clusters of size 0 (solid), 1 (dash), 2 (dot), 3 (dash-dot) and 4 (thin solid). The vibrational periods were evaluated over clusters that remain in the excited state. Data has been smoothed to remove slight numerical noise.

Na or I end of NaI after reaching the nonadiabatic transition region, as evidenced by the long tail in the $P(T)$ distributions for cluster sizes 2 to 4, shown in Fig. 4.6.

As seen in Fig. 4.5, the increased NaI nonadiabatic transition probability caused by the presence of surrounding solvent molecules results in a reduction of 18% to 28%, depending on cluster size, in the number of trajectories where NaI remains bound in the excited state over the simulation timescale, relative to bare NaI. For instance, 92% of the NaI(H₂O)₄ trajectories lead to dissociated ground-state atoms and 5% of the NaI population remains bound in the excited state after 6 ps, compared to 68% and 32%, respectively, for bare NaI. Interestingly, transitions to the ionic branch of the ground state occur during the simulation timescale for 3% of the NaI(H₂O)₄ population due to NaI–

H₂O energy transfer upon and prior to water evaporation, as will be discussed in more detail later.

4.3.3 Water Evaporation Dynamics

As mentioned in the previous Section, the long-time excited-state NaI(H₂O)_n [n=1-4] populations, *i.e.* for $t > 200$ fs, are similar to that of bare NaI due to rapid water evaporation after vertical excitation to the first excited state. In our previous NaI(H₂O) photodissociation dynamics study,¹²⁴ rapid water evaporation was found to be caused mainly by the reversed polarity of NaI in the Franck-Condon region of the first excited state. The average NaI dipole moment $\langle \mu \rangle$ and the average magnitude of the force exerted by NaI on the surrounding water molecules $\langle F_{\text{NaI-H}_2\text{O}} \rangle$ as a function of time and cluster size are displayed in Fig. 4.7. After approximately 100 fs, both the average NaI dipole moment and NaI-H₂O force vanish for all cluster sizes. Thus, water evaporation occurring before 100 fs is caused exclusively by the NaI-H₂O repulsive interactions induced by excitation of NaI to the predominantly covalent portion of the adiabatic excited state. Furthermore, the fact that most water molecules evaporate within 100 fs of excitation, where the evaporation time is defined as the time of the last turning point in the Na-H₂O or I-H₂O bound motion, suggests an extremely non-statistical evaporation process, since internal vibrational energy redistribution is unlikely to occur on such a short timescale.

In order to validate the present findings and the assumptions inherent in our QM/MM model, we compare the NaI-H₂O excited-state forces, after vertical excitation

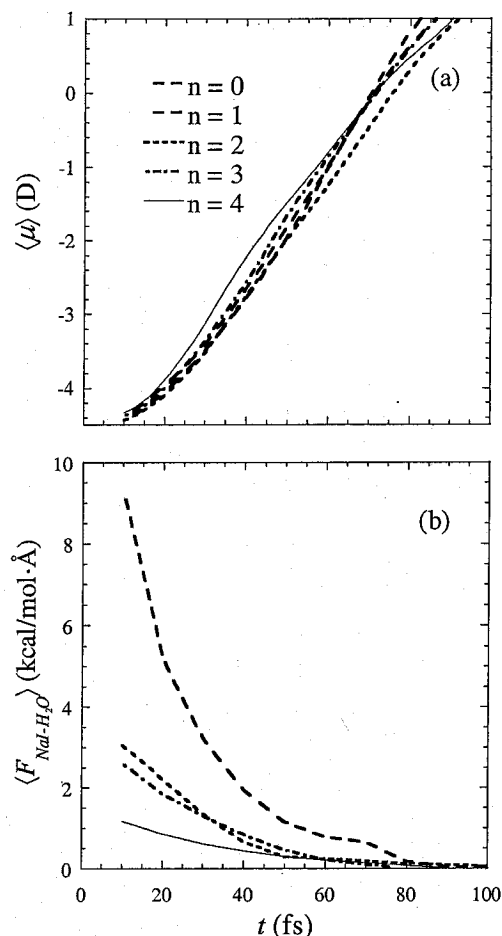


Figure 4.7 (a) Average NaI dipole moment $\langle \mu \rangle$ and (b) average force exerted by NaI on H₂O $\langle F_{NaI-H_2O} \rangle$ as a function of simulation time for NaI(H₂O)_n clusters of size 0 (solid), 1 (dash), 2 (dot), 3 (dash-dot) and 4 (thin solid).

from the ground-state minimum energy structure, with those obtained from MRCI/DZ calculations.¹⁹² As mentioned previously, NaI has a reversed polarity in the Franck-Condon region of the excited state, leading to repulsive NaI-H₂O forces. As a result, the negatively charged sodium atom will repel the oxygen atom, and thus the water molecule, while it will attract the lighter hydrogen atoms, inducing a torque on the water molecule.

In Table 4.3, we list the magnitude of the NaI repulsive force acting on the center of mass of the water $F_{\text{NaI-H}_2\text{O}}^0$, the angle between the NaI internuclear coordinate and the NaI-H₂O force θ , and the torque induced on the water τ in the excited state. Both the magnitude and the direction of the NaI-H₂O force obtained with the QM/MM potentials agree very well with the MRCI/DZ results. The QM/MM torque induced on the water molecule is also in relatively good agreement with its electronic structure theory counterpart, with a difference of 21%. We can therefore assume that the forces acting on the water molecules upon photoexcitation to the first NaI excited state yield relatively realistic water evaporation dynamics.

Table 4.3 Properties of the excited-state NaI-H₂O forces^a.

	QM/MM	MRCI/DZ
$F_{\text{NaI-H}_2\text{O}}^0$ (kcal/mol·Å)	14.8	14.2
θ^0 (deg.)	90	90
τ^0 (kcal/mol)	14.3	18.2

^aObtained from mixed semiempirical/classical potentials (QM/MM) and from high level electronic structure (MRCI/DZ) calculations [see ref. (192)] for the minimum energy ground state structure. $F_{\text{NaI-H}_2\text{O}}^0$ is the magnitude of the force exerted on the water center of mass by NaI, θ^0 is the angle between the NaI internuclear coordinate and the NaI-H₂O force, and τ^0 is the magnitude of the torque exerted on the water molecule.

As the system approaches the curve-crossing region, the NaI ionic character increases, and as such the average NaI dipole moment (*cf.* Fig. 4.7a) of the nascent NaI and the NaI-H₂O binding energy increase sharply (the binding energy of water to ionic NaI is 20 kcal/mol, whereas that to covalent is less than 1 kcal/mol, according to our QM/MM potentials). Therefore, if NaI remains in the excited state after reaching the

curve-crossing region, water molecules that lie near the sodium or the iodine end of NaI may become transiently or permanently bound. The average NaI ionic character $\langle C_{ionic}^2 \rangle$ is shown in Fig. 4.8 as a function of simulation time for both short-lived and long-lived NaI(H₂O)_n clusters. As might be expected, the ionic character of the long-lived clusters is much larger than that of short-lived clusters on the simulation timescale, thus supporting the fact that water molecules tend to stay bound to NaI with a predominantly ionic electronic structure. Furthermore, these relatively rare events occur when the excess Franck-Condon energy in the NaI internuclear coordinate, gained from pump excitation, is small to start with (averages listed in Table 4.2), or has already been depleted by the evaporation of neighboring water molecules, resulting in a smaller NaI vibrational period and slower NaI relative motion.

4.3.4 NaI-H₂O Energy Transfer and Mechanistic Aspects

As discussed in the previous Section, 99% of the water molecules for NaI(H₂O) and 95% for NaI(H₂O)_n [n=2-4] evaporate on a short timescale due to highly repulsive NaI-H₂O forces that arise from the reversed NaI polarity in the Franck-Condon region of the excited state. Upon excitation, the oxygen atom is repelled by the partial negative charge on the sodium atom, as evidenced by the average magnitude of the force exerted by Na^{-δ} on the water oxygen atom $\langle F_{Na-O}^0 \rangle$ upon excitation, and the post-evaporation average water translational energy $\langle E_{trans}(H_2O) \rangle$ (relative to the NaI center of mass) for short-lived clusters ($t_{evap} \leq 100$ fs), listed in Tables 4.2 and 4.4, respectively. Furthermore, the water hydrogen atoms are attracted towards the Na^{-δ}, and due to the light mass of the

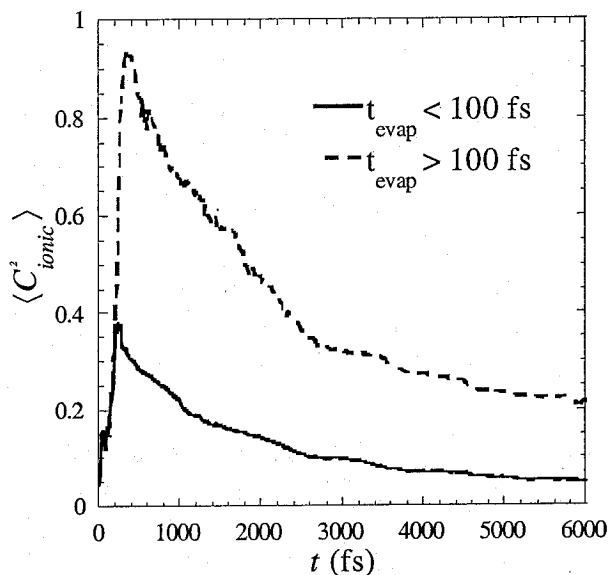


Figure 4.8 Average weight of the ionic state in the NaI electronic structure $\langle C_{ionic}^2 \rangle$ as a function of simulation time for short-lived ($t_{evap} \leq 100$ fs) and long-lived ($t_{evap} > 100$ fs) NaI(H₂O)_n clusters [$n=1-4$]. The ensemble average is evaluated over the full population of short-lived or long-lived clusters, regardless of parent cluster size.

hydrogen atoms, considerable torque is induced on the water upon excitation, as shown of the average magnitude of the torque $\langle \tau^0 \rangle$ in Table 4.2, resulting in significant rotational excitation. As found previously for NaI(H₂O),¹²⁴ the average water rotational energies are greater than the average translational energies for all cluster sizes, especially for short-lived clusters. The strong repulsive forces exerted on the water molecules upon NaI excitation thus induce non-statistical evaporation, and result in water molecules that are more rotationally hot than translationally hot.

For comparison, simulations of NaI excitation to the purely covalent (and repulsive) $\Omega=1$ state, rather than to the $\Omega=0^+$ state, were performed. As expected, 100%

of the water molecules evaporate within 100 fs following NaI excitation to the $\Omega=1$ state. Furthermore, the energy partitioning of the evaporated products for NaI(H₂O)_n is the same for the $\Omega=1$ state as that for the short-lived clusters excited to the $\Omega=0^+$ state. In NaI(H₂O)₄ clusters, for instance, 3 ± 3 kcal/mol is transferred to water relative translational energy and 7 ± 5 kcal/mol in rotational energy for excitation to the $\Omega=1$ state. Therefore, the translational and rotational NaI–H₂O energy transfer mechanisms in short-lived clusters excited to the $\Omega=0^+$ state is entirely governed by the initial repulsive dynamics and is not influenced whatsoever by curve-crossing dynamics.

We previously mentioned that 5% of the water molecules for NaI(H₂O)_n clusters [$n=2-4$] remain transiently or permanently bound mainly to the sodium end of NaI due to changes in the NaI electronic structure. From Table 4.4, NaI obviously has less average internal energy $\langle E_{\text{int}}(\text{NaI}) \rangle$ in long-lived clusters than in short-lived clusters and the average translational energy of the evaporated water molecules is slightly larger for long-lived clusters. Therefore, when water molecules remain bound, NaI primarily transfers energy to water translational motion, while the water molecules seem to retain the rotational energy gained due to the initial repulsive dynamics, resulting in a lower total average NaI internal energy for long-lived clusters.

4.3.5 Connection with Experiment

In this section, we explore various spectroscopic schemes to probe the NaI photodissociation dynamics in water clusters. As mentioned earlier, the photodissociation dynamics of NaI in water clusters has been previously studied by femtosecond pump-probe spectroscopy employing a 2×610 nm detection scheme, where photoexcitation to

the probe state occurs from the covalent branch of the excited state.⁶⁷ For an initial cluster size distribution between 1 and 7 water molecules, exponentially decaying Na⁺(H₂O)_p experimental probe signals, where p refers to the product cluster size post-water evaporation, were obtained with [p=1-3], and NaI⁺(H₂O)_p signals were presumably not detected. Our simulation results using the same two-photon detection scheme are shown in Figs. 4.9 and 4.10 for photoexcitation to the X and I probe states, respectively. To the best of our knowledge, experimental probe signals for bare NaI have not been reported. The simulated probe signals for bare NaI resulting from excitation of NaI at its ground-state equilibrium distance of 2.7 Å are shown in Figs. 4.9a and 4.10a, while those resulting from excitation of NaI with a distribution of room-temperature ground-state internuclear distances $P(R)$ (cf. Fig. 4.4a) are shown in Figs. 4.9b and 4.10b. Our results suggest that the I state is not energetically accessible with the two-photon probe scheme, and excitation occurs mainly to the NaI⁺ potential energy well of the X state. The NaI⁺ signal in Fig. 4.9a is oscillatory, reflecting the NaI transient trapping in the excited-state well, normally peaking at the inner turning point of the vibrational motion, and the signal decays over time due to nonadiabatic transitions to the ground state. The signal is broader in Fig. 4.9b and seems to decay more rapidly due to vibrational dephasing caused by the initial ground-state distribution of NaI internuclear distances.

The simulated Na⁺(H₂O)_p and NaI⁺(H₂O)_p signals as a function of pump-probe time delay are also shown in Fig. 4.9 for excitation to the X state, and Fig. 4.10 for excitation to the I state. Conversely to experimental results, exponentially decaying NaI⁺(H₂O)_p signals that are more intense than the Na⁺(H₂O)_p signals are detected for

excitation to both probe states. The simulated probe signals for bare NaI suggested that the two-photon probe pulse promotes the excited-state complex mainly to the potential energy well of the X state. It is therefore not surprising to obtain NaI⁺(H₂O)_p signals that are more intense than the Na⁺(H₂O)_p signals. Furthermore, the NaI⁺ probe states are stabilized by the presence of surrounding water molecules, relative to the covalent branch of the excited state, such that the I state becomes energetically accessible. In fact, the stabilization energy of the probe states ranges from 18 to 50 kcal/mol for n=1 to 4. Since photoionization occurs from the covalent branch of the excited state, the signals resulting from the two-photon probe scheme at short pump-probe time delays correspond to a multi-photon vertical excitation directly from the ground state to either the X or the I probe state. In the ground state, the waters are mainly located on the Na end of NaI (*cf.* Figs. 4.2 and 4.3). Therefore, upon rapid excitation to a given probe state, the water molecules, which have not moved more than 5 Å away from the NaI on the excited state, are attracted to the Na⁺ end of NaI⁺ very much like in the ground state, resulting in NaI⁺(H₂O)_p signals that correspond to the parent cluster size. On the other hand, Na⁺(H₂O)_p signals are only obtained for p=0,1 for parent cluster sizes 1 to 4. The Na⁺(H₂O)_p signals arise mainly when excitation occurs to the repulsive wall of the X or I probe states. Since the probe states are stabilized by the presence of water molecules, excitation occurs higher on the probe state repulsive wall than for bare NaI, and NaI therefore rapidly gains a large amount of kinetic energy after departing from the wall. The excess energy is also released through evaporation of water molecules on the

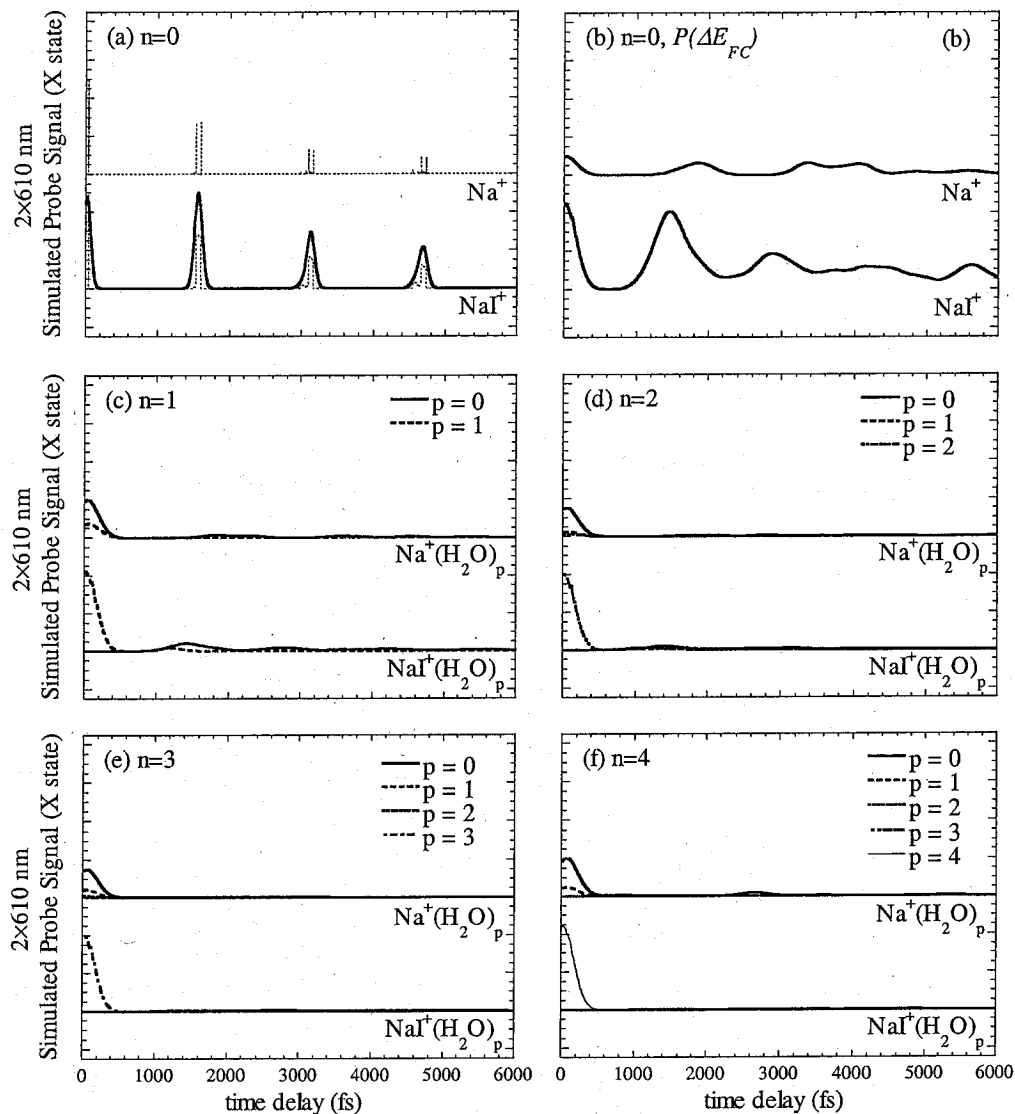


Figure 4.9 Probe signals for NaI(H₂O)_n photodissociation as a function of pump-probe time delay, generated using a 2x610 nm excitation from the covalent branch of the NaI first excited state to the X probe state. The product cluster size p is 0 (solid), 1 (dash), 2 (dot), 3 (dash-dot) and 4 (thin solid).

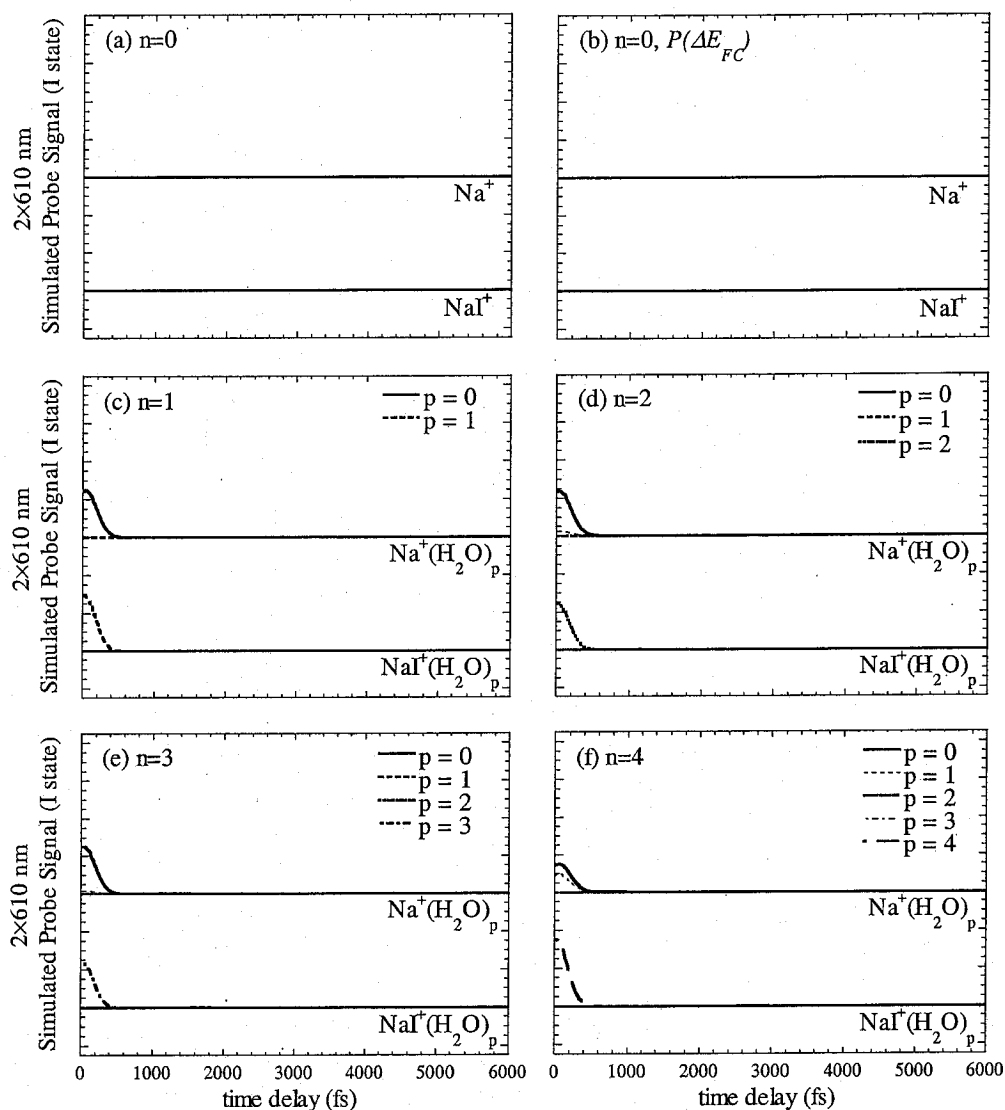


Figure 4.10 Probe signals for NaI(H₂O)_n photodissociation as a function of pump-probe time delay, generated using 2×610 nm excitation from the covalent branch of the NaI first excited state to the I probe state. The product cluster size p is (solid), 1 (dash), 2 (dot), 3 (dash-dot) and 4 (thin solid).

probe state, and thus, a strong bare Na⁺ probe signal with a residual Na⁺(H₂O)₄ [p=1] signal is observed. Finally, in agreement with experimental findings,⁶⁷ the probe signals decay exponentially over the first NaI excited-state vibrational period with very little evidence of long-time dynamics. In conclusion, the simulated probe signals obtained with the two-photon probe scheme are not revealing of the NaI photodissociation dynamics beyond the time NaI reaches the curve-crossing region for the first time, and therefore do not provide valuable information on the influence of water molecules on the NaI excited-state dynamics. However, our simulations suggest that the parent cluster size can be inferred from the NaI⁺(H₂O)_p signals, an issue that may deserve further experimental investigation.

We now turn our attention to the simulated probe signals resulting from the one-photon detection scheme, where probe excitation occurs from the ionic branch of the excited state, and which are displayed in Figs. 4.11 and 4.12 for excitation to the X and I states, respectively. For bare NaI, in agreement with experimental findings,^{64,171} we obtain a broad oscillatory Na⁺ signal, reflecting the NaI transient trapping in the excited-state well, that decays with increasing pump-probe time delay due to nonadiabatic transitions, as shown in panels a and b of Figs. 4.11 and 4.12. For excitation to the X state, the Na⁺ signal decreases as the NaI⁺ signal increases as the latter arises from excitation at the outer turning point in the excited-state NaI vibrational motion.^{64,171} At the outer turning point, NaI has very little or no kinetic energy, and since the X state is still slightly binding at this internuclear distance because of long-range interactions,²⁰⁰ NaI will not have enough residual kinetic energy after promotion to the X state to allow

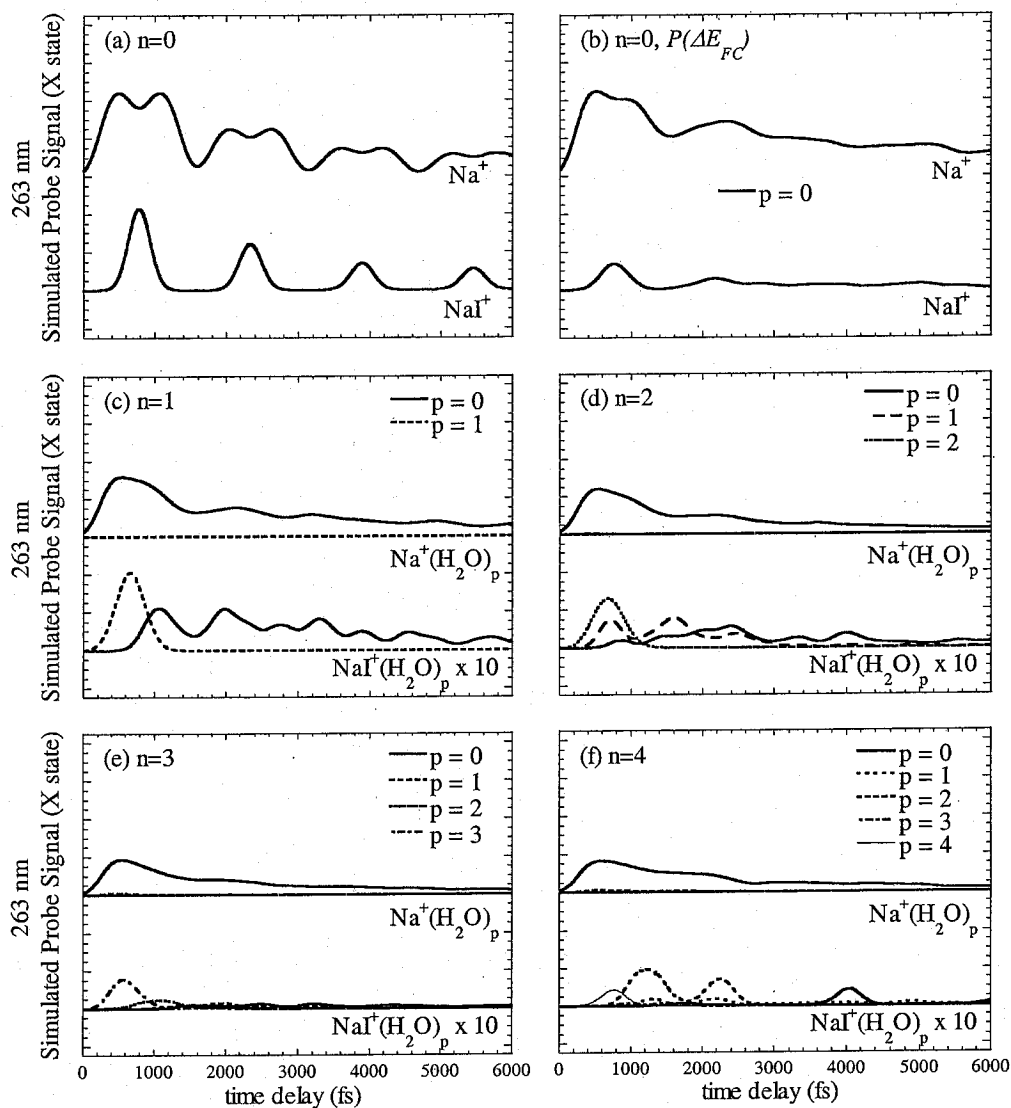


Figure 4.11 Probe signals for NaI(H₂O)_n photodissociation as a function of pump-probe time delay, generated using a 263 nm excitation from the ionic branch of the NaI first excited state to the X probe state. The product cluster size *p* is 0 (solid), 1 (dash), 2 (dot), 3 (dash-dot) and 4 (thin solid). The NaI⁺(H₂O)_p probe signals have been magnified by a factor of 10 relative to the Na⁺(H₂O)_p signals due to the low intensity of the signals.

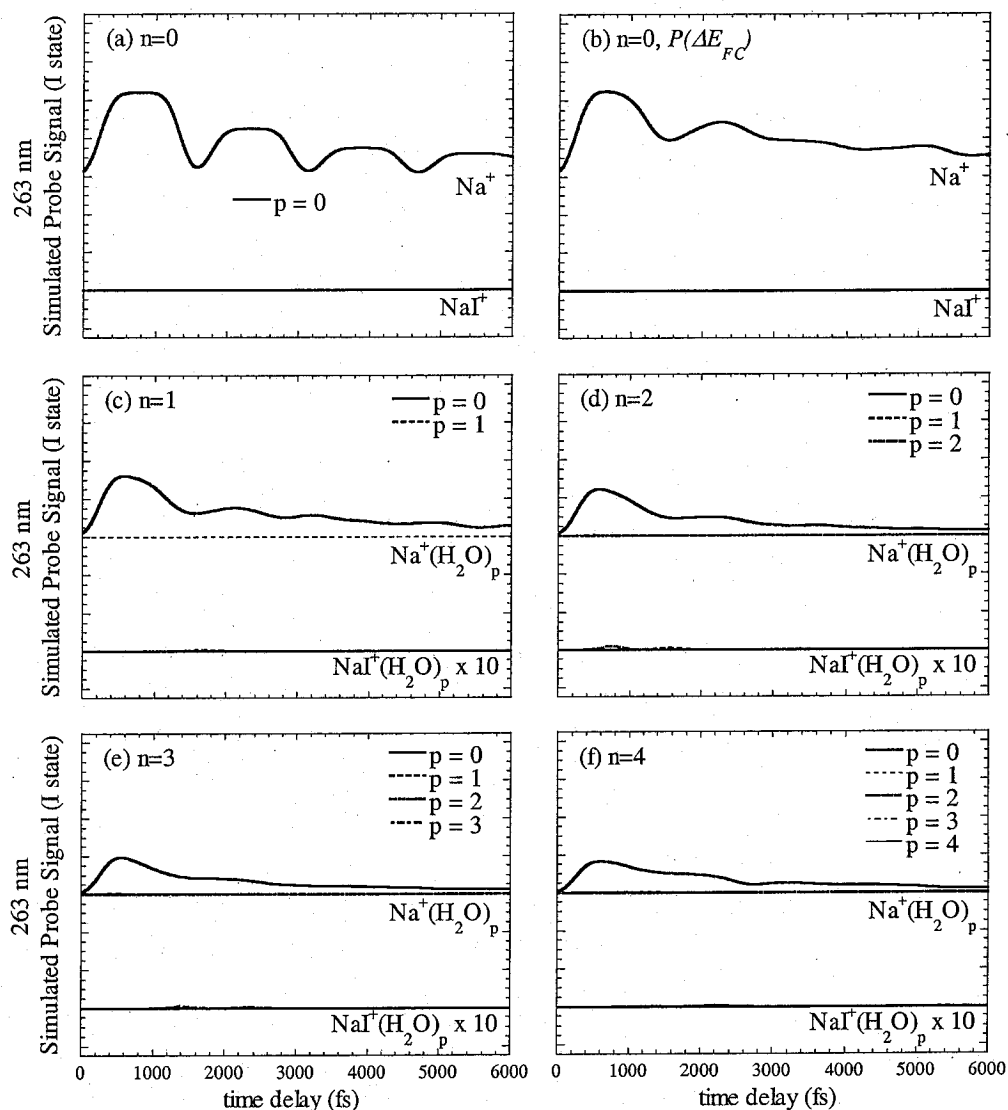


Figure 4.12 Probe signals for $\text{NaI}(\text{H}_2\text{O})_n$ photodissociation as a function of pump-probe time delay, generated using a 263 nm excitation from the ionic branch of the NaI first excited state to the I probe state. The product cluster size p is 0 (solid), 1 (dash), 2 (dot), 3 (dash-dot) and 4 (thin solid). The $\text{NaI}^+(\text{H}_2\text{O})_p$ probe signals have been magnified by a factor of 50 relative to the $\text{Na}^+(\text{H}_2\text{O})_p$ signals due to the low intensity of the signals.

for dissociation of the NaI⁺ complex. Consequently, we obtain a narrow NaI⁺ signal, which spans ~ 30 fs, as evidenced by the unconvoluted probe signals shown in Fig. 4.11a, and a corresponding decrease in the Na⁺ signal at the outer turning point in the NaI excited-state vibrational motion. As shown in Fig. 4.12a, excitation to the I state, however, does not produce a NaI⁺ signal because of a small barrier of ~ 0.1 kcal/mol in the I state at an internuclear distance of ~ 5 Å (the barrier is barely perceptible in Fig. 4.1), which prevents NaI⁺ complex formation, because of excitation to the product side of the barrier, with very little nuclear kinetic energy.²⁰⁰ Once again, the probe signals obtained for photoionization of NaI with a distribution of room-temperature ground-state internuclear distances are broader and the oscillatory features due to NaI transient trapping in the excited-state well are damped because of vibrational dephasing.

The simulated Na⁺(H₂O)_p and NaI⁺(H₂O)_p probe signals obtained from the one-photon probe scheme are also shown in Figs. 4.11 and 4.12 for photoexcitation to the X and I states, respectively. Bare Na⁺ signals that decay with increasing pump-probe time delay due to nonadiabatic transition are detected, and Na⁺(H₂O)_p signals are not observed due to further water evaporation on the probe state caused by excitation to the repulsive wall of the probe state, very much like in the two-photon probe situation. The signals are very similar for excitation to the X and I probe states, with an intensity that decreases slightly as a function of cluster size, reflecting the increase in the excited-state population decay (*cf.* Fig. 4.5) when NaI reaches the curve-crossing region for the first time, as mentioned earlier. On the other hand, faint NaI⁺(H₂O)_p signals are detected for excitation to the X state, and not to the I state due to the small barrier at ~ 5 Å mentioned earlier.

The first peak corresponds to the parent cluster size, because the water molecules do not move far enough from NaI prior to promotion to the X state, as was the case for the NaI⁺(H₂O)_p probe signals resulting from the two-photon probe scheme. The successive evaporation of water molecules at longer pump-probe time delays can also be observed from the NaI⁺(H₂O)_p signals. We can conclude that the probe signals resulting from the one-photon detection scheme show evidence of increased nonadiabatic transitions due to the stabilization of the ionic branch of the excited state. Moreover, the successive evaporation of water molecules due to the repulsive dynamics in the covalent region of the excited state can be monitored from the NaI⁺(H₂O)_p probe signals, given that the signals are sufficiently intense to be detected experimentally. The probe signals resulting from the one-photon probe scheme are thus much more revealing of the influence of water molecules on NaI photodissociation dynamics. Even though the two-photon probe scheme could be expected to be less sensitive to solvation because excitation occurs from the covalent branch of the NaI first excited state, our simulation results reveal that the one-photon scheme is even less sensitive to solvation in small clusters since the water molecules are bound mainly to the Na⁺ end of NaI on both the ionic branch of the excited state and the probe state, such that both states are stabilized to the same extent by the presence of water molecules. On the other hand, excitation energies from the covalent branch of the first excited state, as in the two-photon probe scheme, depend on the solvation of the sodium ion on the probe state.

Time-resolved photoelectron spectra obtained with the one-photon probe scheme are shown in Fig. 4.13. The photoelectron spectra obtained with the two-photon probe

scheme are not shown because very little information beyond the time at which NaI reaches the curve-crossing region for the first time can be inferred from the spectra. Furthermore, the spectra for excitation to the I state are not shown since they are very similar to those for excitation to the X state. For bare NaI, the NaI excited-state vibrational motion can be monitored, as well as the decay in the excited-state population due to nonadiabatic transitions from the decreasing gray intensity. For excitation of NaI with a room-temperature ground-state distribution of internuclear distances, large amplitude oscillations, with a period of ~ 4 ps, are observed. This large amplitude vibrational motion arises from excitation of NaI around the inner turning point of NaI motion on the ground-state potential, and results in promotion of NaI onto a highly repulsive point of the excited-state potential. For long-lived clusters, (*cf.* Figs. 4.13c to 4.13f) even larger amplitude vibrational motion is observed, because the ionic branch of the excited state is lower in energy, relative to the gas phase, when a water molecule remains bound to excited NaI, and the outer-turning point for NaI motion on the excited state extends further out, as illustrated by the long tail in the NaI vibrational period distributions shown in Fig. 4.6. The increase in the vibrational dephasing of NaI as a function of increasing cluster size is also quite obvious from the photoelectron spectra. Finally, the small amplitude vibrational motion caused by NaI energy transfer to evaporating water molecules in short-lived clusters, evidenced by the decrease in the average NaI vibrational period as a function of cluster size in Table 4.2, can also be observed in the photoelectron spectra. Therefore, the photoelectron spectra bring evidence of large amplitude NaI vibrational motion caused by the stabilization of the

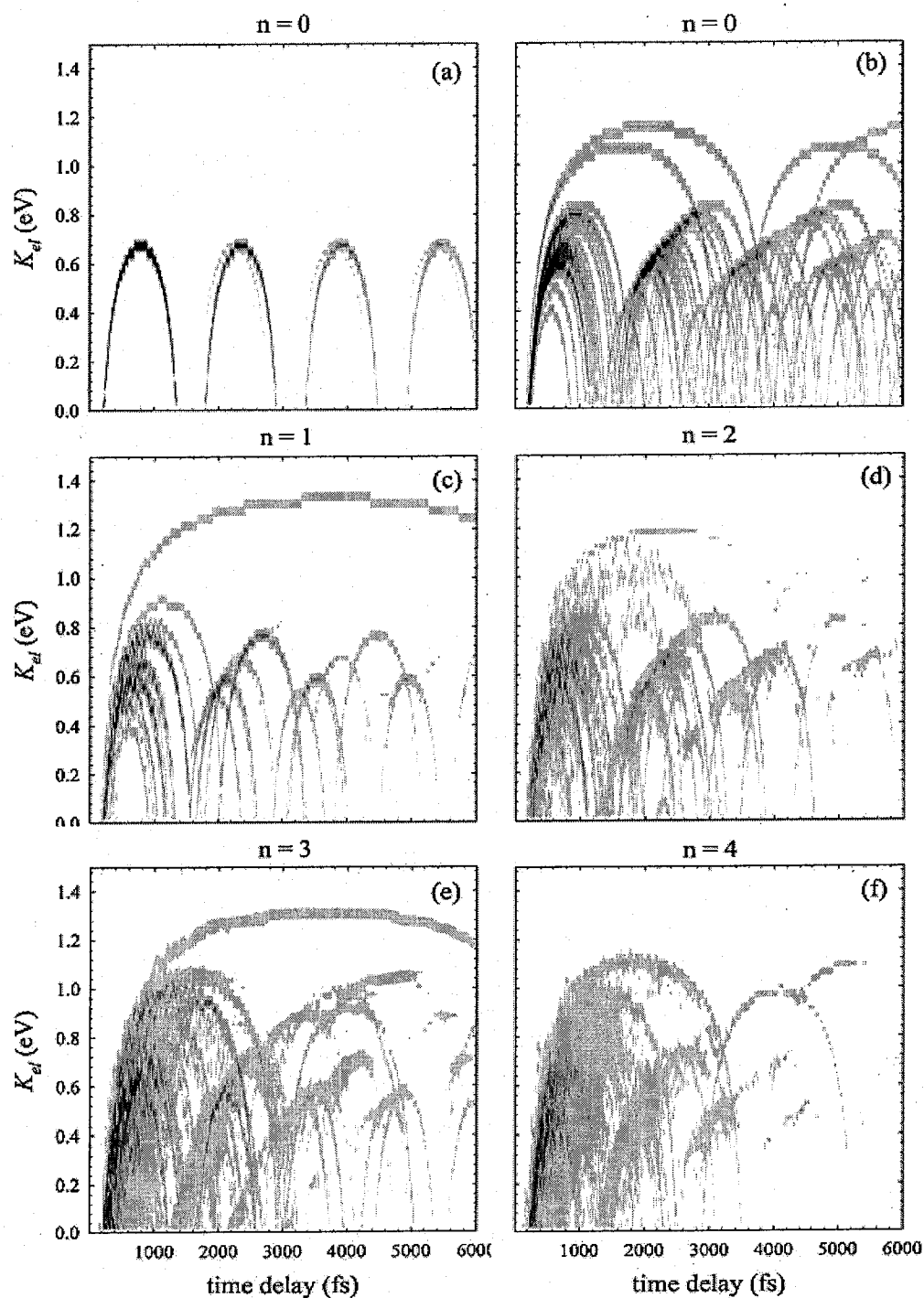


Figure 4.13 Time-resolved photoelectron spectra, produced with the one-photon detection scheme, as a function of pump-probe time delay. The gray scale is indicative of the NaI excited-state population, where the decreasing gray intensity corresponds to a decrease in the excited-state population.

ionic branch of the excited state, further evidence of the enhancement in the excited-state NaI vibrational dephasing caused by the presence of an increasing number of surrounding water molecules, and small amplitude NaI vibrational motion due to energy transfer between NaI and evaporating water molecules.

4.4 Concluding Remarks

We have investigated the photodissociation dynamics of NaI(H₂O)_n [n=1-4] clusters using a semiempirical valence-bond approach to describe the NaI electronic structure and classical solvent-solvent and solute-solvent interaction potentials, along with the molecular dynamics with quantum transitions method developed by Tully and co-workers.¹⁹³ Our simulations show that the excited-state population decay upon reaching the curve-crossing region increases with cluster size due to the increasing stabilization of the ionic branch of the NaI excited state by surrounding water molecules, and to multiple nonadiabatic transitions caused by dynamical fluctuations of the NaI internuclear separation at which the curve crossing occurs. After reaching the curve-crossing region for the first time, however, the excited-state population decay for all cluster sizes resembles that of bare NaI, although the periodicity of the NaI excited-state vibrational motion disappears in clusters due to vibrational dephasing. The excited-state population decay is no longer influenced by the water molecules beyond the first time NaI reaches the curve-crossing region because of rapid evaporation of 99% and 95% of the water population for NaI(H₂O) and NaI(H₂O)_n [n=2-4], respectively. The rapid water evaporation, which is governed by highly repulsive forces due to the reversed NaI polarity in the Franck-Condon region of the first excited state, takes place before internal

vibrational energy redistribution and is thus non-statistical. Furthermore, analysis of the post-evaporation water energy distributions revealed that the initial impulsive dynamics results in extensive rotational excitation, such that product water molecules are formed more rotationally than translationally hot, further supporting the highly non-statistical nature of the water evaporation process. Successful comparison of NaI(H₂O)_n excited-state forces predicted by our QM/MM model to those obtained from high-level electronic structure calculations confirms that our simulation methodology yields realistic dynamics and water evaporation is a real feature of NaI(H₂O)_n dynamics.

Our simulation results suggest that for 5% of the water population, in clusters containing 2 to 4 water molecules, solvent molecules remain transiently or permanently bound, mainly to the Na end of NaI. One or two water molecules may remain bound if NaI remains predominantly ionic (*i.e.* does not dissociate to atoms via a nonadiabatic transition) after reaching the curve-crossing region, and if the excess Franck-Condon energy in the NaI internuclear coordinate, gained from pump excitation, has already been depleted by the evaporation of neighboring water molecules. The vibrational period of NaI in the excited state may then extend beyond that of gas-phase NaI, due to stabilization of the ionic branch of the excited state, when water molecules remain bound to NaI after reaching the curve-crossing region. Finally, whereas water molecules retain the rotational energy gained from the initial repulsive dynamics, for long-lived clusters, energy is further transferred from NaI primarily to the water translational degrees of freedom.

High-level electronic structure calculations have shown that both the NaI⁺ X and I probe states are energetically accessible under the conditions employed in previous femtosecond pump-probe experiments.²⁰⁰ In this work, we have considered excitation to both of these states, and have simulated the Na⁺(H₂O)_p and NaI⁺(H₂O)_p probe signals resulting from two different schemes: a two-photon probe scheme used in previous femtosecond experiments of NaI photodissociation in water clusters,⁶⁷ where promotion to the probe state occurs from the covalent branch of the excited state, and a one photon-probe scheme employed in femtosecond studies of bare NaI,¹⁷¹ where excitation occurs from the ionic branch of the excited state. In agreement with experimental findings, the Na⁺(H₂O)_p two-photon probe signals decay exponentially over the first NaI excited-state vibrational period with very little evidence of long-time dynamics. However, a strong bare Na⁺ and a residual Na⁺(H₂O) signal are mostly obtained for all parent cluster sizes because excitation occurs to the repulsive wall of the probe state, causing further water evaporation. This clearly shows that experimentally observed signals arose from photodissociation of much larger parent clusters, because of the key role that water evaporation plays in the NaI(H₂O)_n dynamics. On the other hand, the NaI⁺(H₂O)_p signal, which was presumably not detected experimentally, is clearly reminiscent of the parent cluster size. At short pump-probe time delays, two-photon excitation from the covalent branch corresponds to an almost instantaneous multi-photon excitation from the ground state, and since the water molecules are mainly found on the Na⁺ end of NaI in the ground state, they remain bound to Na⁺ on the probe state. Nonetheless, the simulated probe signals obtained with the two-photon probe scheme are not revealing of the NaI

photodissociation dynamics beyond the time NaI reaches the curve-crossing region for the first time, and therefore do not provide valuable information on the influence of water molecules on NaI photodissociation dynamics.

The simulated probe signals resulting from the one-photon scheme, on the other hand, are much more revealing of the NaI photodissociation dynamics. Only a bare Na⁺ signal is obtained for all parent cluster sizes due to further water evaporation on the probe state. The intensity of the Na⁺ signal decreases with pump-probe time delay, due to nonadiabatic transitions, but the oscillatory motion evident in the signal for bare NaI disappears in water clusters due to NaI vibrational dephasing. Furthermore, the intensity of the Na⁺ signal decreases with increasing parent cluster size following the increasing stabilization of the ionic branch of the excited state, and the resulting increase of the nonadiabatic transition probability. Faint NaI⁺(H₂O)_p are also detected, where the first peak corresponds to the parent cluster size, as was the case for the two-photon detection scheme, and the successive evaporation of water molecules with increasing pump-probe delay can be monitored. Therefore, the one-photon probe scheme may allow monitoring of the effects of solvation on the nonadiabatic transition dynamics and successive evaporation of water molecules. We also note that the one-photon probe scheme is not very sensitive to solvation in small clusters, in that the differential solvation between the ionic branch of the NaI first excited state and the probe states is very small (as water molecules are located on the Na⁺ end of NaI in both cases) and probe excitation energies will remain the same over a range of cluster sizes. Time-resolved photoelectron spectra resulting from the ejection of an electron from sodium on the probe state were also

simulated. The information obtained from the spectra complements the $\text{NaI}^+(\text{H}_2\text{O})_p$ probe signals, in that the effects of solvation on the excited-state NaI vibrational motion can be monitored. These findings warrant further experimental investigation of $\text{NaI}(\text{H}_2\text{O})_n$ photodissociation dynamics. Finally, the possibility of observing inverted regime electron transfer behavior for NaI in these small clusters mentioned in the Introduction is obviously thwarted by the extensive evaporation observed. Nonetheless, this possibility remains open if this evaporation could be prevented by means of studying these small clusters in e.g. a matrix or a sufficiently dense buffer gas.

Theoretical Studies of Seeded Water Clusters: Structure,
Thermodynamics and Photochemistry

Chapter 5

Photodissociation Dynamics of NaI(H₂O)_n Clusters with a Polarizable Model

To be submitted:

Denise M. Koch and Gilles H. Peslherbe,
Journal of Physical Chemistry A (2006)

5.1 Introduction

The investigation of electron transfer reactions in simple chemical systems, such as ion pairs, has been the subject of numerous studies in recent years, due to the importance of charge transfer reactions in various chemical and biochemical processes. NaI has served as a paradigm molecule in the investigation of fundamental electron transfer processes, since the pioneering femtosecond photodissociation studies of Zewail and co-workers,⁶⁴ because the NaI electronic structure is characterized by a curve crossing between ionic and covalent states at small NaI internuclear separations where the electronic coupling between the states is large enough to allow the adiabatic potential to govern the NaI nuclear motion.¹⁵⁹ This curve crossing results in an avoided crossing in the adiabatic states, and a shallow well in the NaI first excited state, which gives rise to interesting, oscillatory dynamics as photoexcited NaI is transiently trapped in the well. Our main objective is to understand the effects of solvation on this elemental reaction process.

Since polar solvents preferentially stabilize charged species, the formation of ionic products may be favored over atomic products, as in the gas phase, when NaI photodissociation occurs in solution or in clusters. Further, the stabilization of the NaI ionic state in the presence of polar solvent molecules, relative to the covalent state, is expected to move the curve-crossing region towards larger internuclear separations and thus alter the NaI photodissociation process. A previous theoretical investigation of NaI

photodissociation in diethyl ether solution suggested that the formation of ionic photodissociation products could indeed occur by activated inverted electron transfer, but that radiative decay to the ground state occurs on a faster timescale. Extrapolation of the solution results to small clusters also suggested that inverted electron transfer could occur in small clusters.

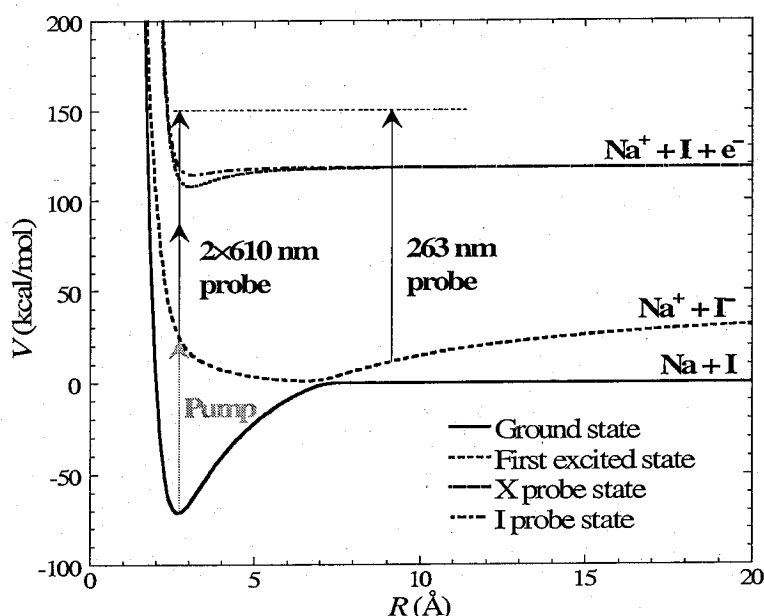


Figure 5.1 NaI potential energy curves for the ground and first excited adiabatic states, and the X and I probe states. Also illustrated are the one- photon (263 nm) and two-photon (2×610 nm) probe schemes.

The investigation of NaI photodissociation in solution was performed for a weakly polar solvent (diethyl ether), in which NaI charge separation is less likely.⁶⁵ It is well known that salts are fully ionized in solution of polar solvents such as water. In clusters however, NaI may exist as a contact ion pair (CIP) or a solvent separated ion pair (SSIP).⁶²

Photoexcitation was shown to occur only for CIP structures, since the presence of water molecules between sodium and iodide, inherent in the SSIP structure, may prevent the electron transfer process upon photoexcitation, and results in the reduction of the oscillator strength. The CIP structure in $\text{NaI}(\text{H}_2\text{O})_n$ was shown to survive up to quite large cluster sizes.⁹⁷ However, the SSIP structure becomes thermodynamically favored over the CIP structure around cluster size 32. Indeed, recent experiments have shown that photoexcitation occurs in $\text{NaI}(\text{H}_2\text{O})_n$ clusters containing up to 50 water molecules.²⁰⁴

Detailed investigations of $\text{NaI}(\text{H}_2\text{O})$ ¹²⁴ and $\text{NaI}(\text{H}_2\text{O})_n$ [$n=1-4$]²⁰⁵ photodissociation dynamics were reported earlier. The simulation results indicated that the $\text{NaI}(\text{H}_2\text{O})_n$ excited-state population decay upon reaching the NaI curve-crossing region increases with cluster size due to the stabilization of the ionic branch of the NaI excited state by the surrounding water molecules, and the resulting increase in nonadiabatic transition probability. After reaching the curve-crossing region for the first time, however, the excited-state population decay resembled that of bare NaI due to rapid evaporation of 99% and 95% of the water molecules for $\text{NaI}(\text{H}_2\text{O})$ and $\text{NaI}(\text{H}_2\text{O})_n$ [$n=2-4$], respectively. This extensive evaporation was attributed to the reversed NaI polarity in the Franck-Condon region of the NaI first excited state, which causes strong repulsive NaI- H_2O forces, and induces rapid non-statistical water evaporation, where product water molecules are formed more rotationally than translationally hot. In order to connect simulation results with experiment, femtosecond probe signals resulting from two-photon and one-photon excitation to the NaI^+ probe states, shown in Fig. 5.1, were also simulated. The simulated probe signals for the one-photon probe scheme were more

revealing of the $\text{NaI}(\text{H}_2\text{O})_n$ photodissociation dynamics than the two-photon probe signals, as they allowed monitoring of solvation effects on the NaI nonadiabatic dynamics and of the successive evaporation of water molecules. A key consequence of the rapid water evaporation is that experimentally observed signals must arise from the photodissociation of much larger $\text{NaI}(\text{H}_2\text{O})_n$ parent clusters.⁶⁷

Our previous simulations employed a molecular dynamics with quantum transitions method¹⁹³ and a quantum mechanics/molecular mechanics description of the intermolecular interactions in $\text{NaI}(\text{H}_2\text{O})_n$ clusters. The latter involves a semiempirical valence bond approach for the NaI electronic structure and a nonpolarizable model potential for solvent-solvent and solute-solvent interaction known as Optimized Parameters for Liquid Simulations (OPLS).^{86,99,100} However, simulation results with this model showed discrepancies with recent pump-probe experiments performed by Grégoire *et al.*⁶⁷ In these experiments, it was found that the maximum in absorption efficiency is blue-shifted by 1.1 eV for $\text{NaI}(\text{H}_2\text{O})_2$, relative to that of bare NaI, and by 1.3 eV for $\text{NaI}(\text{H}_2\text{O})_{16}$. High-level electronic structure calculations confirmed these findings, predicting excitation energies 1.1 eV and 1.2 eV larger than that for bare NaI for $\text{NaI}(\text{H}_2\text{O})_2$ and $\text{NaI}(\text{H}_2\text{O})_4$, respectively.²⁰⁵ The fact that addition of the first few water molecules causes a large increase in the excitation energy, but the shift becomes less pronounced as more water molecules are added, was attributed to the surface solvation observed in $\text{NaI}(\text{H}_2\text{O})_n$ clusters,⁶² where the addition of water molecules occurs further and further away from the surface at which NaI resides, and thereby will affect the NaI electronic structure less and less. Calculations with OPLS, on the other hand, predict a

linear increase in the excitation energy shift with cluster size, from by 0.8 eV for cluster size 1, relative to bare NaI, to 2.5 eV for cluster size 4. Due to the discrepancy between the OPLS excitation energies and the experimental and *ab initio* results, simulations of the $\text{NaI}(\text{H}_2\text{O})_n$ photodissociation dynamics were restricted to small cluster sizes, for which the discrepancy in the excitation energies is not too large.

Furthermore, the OPLS model potential does not allow electronic polarization of the solvent molecules by the solute (or by other solvent molecules). Significant differences were found in the ground-state structures of $\text{NaI}(\text{H}_2\text{O})_n$ clusters predicted by OPLS and a polarizable model known as Optimized Potentials for Cluster Simulations (OPCS), for cluster sizes larger than 4.⁹⁷ For instance, OPLS predicted the SSIP to become overwhelmingly predominant at much smaller cluster sizes than OPCS, which produced results consistent with experimental observations, as mentioned above. The polarization of water molecules could significantly affect the NaI electronic structure in both the ground and excited states. Indeed, the disagreement between the OPLS energy gaps between the ground and excited states and experimental data and high-level *ab initio* results suggests that polarization may be essential in properly describing NaI in clusters. The photodissociation dynamics of $\text{NaI}(\text{H}_2\text{O})_n$ clusters was then revisited with the polarizable OPCS water model, which, as we will see, also allows simulations of much larger cluster sizes than OPLS.

The outline of this Chapter is as follows. In Section 5.2, the various ingredients of the methodology employed for the simulations are presented. Simulation results are then

reported in Section 5.3, followed by a discussion of the results. We end with concluding remarks in Section 5.5.

5.2 Computational Procedure

5.2.1 QM/MM Potentials

A quantum mechanics-molecular mechanics model is adopted to describe intermolecular interactions in NaI(H₂O)_n clusters, in which the NaI solute electronic structure is obtained from semiempirical valence-bond theory, as described in great detail in previous work,²⁰⁵ and polarizable model potentials are employed to describe the solvent-solvent and solute-solvent interactions.

Briefly, a semiempirical valence bond (VB) approach is used to calculate the Hamiltonian matrix elements of the diabatic, constant-charge character, ionic Na⁺I⁻ and covalent NaI states. Only two electrons are treated explicitly, while the contribution due to the remaining electrons is embedded in a core-core potential. All electron integrals are evaluated under the point-charge, Pariser and Mulliken approximations,¹⁸⁰ resulting in analytical expressions for all diabatic matrix elements. Adiabatic ground and excited-state energies are then simply obtained by diagonalizing the Hamiltonian matrix in the VB state basis. The core-core potential parameters were adjusted separately for both VB states in order to reproduce experimental gas-phase NaI Franck-Condon (FC) energies and NaI potential curves predicted by high-level ab initio calculations.²⁰⁵

The solvent model, referred to in previous work as OPCS for Optimized Potentials for Cluster Simulations,⁶² employs a rigid water molecule with experimental gas-phase geometry, and its functional form includes Coulombic, many-body polarization and repulsion-dispersion terms. The model makes use of 4 charge sites, 2 of which are the hydrogen atoms (H) while the other 2 (oxygen) sites (M) are located on the bisector of the H-O-H angle off the water plane, in order to reproduce the gas-phase water dipole and quadrupole moments. The oxygen atom carries one polarizable site and one repulsion-dispersion (Lennard-Jones) site. The model potential also includes H-H repulsion terms of the Born-Mayer form. Some parameters were derived from available experimental data and the remaining (repulsion-dispersion) parameters were fitted to small pure and ionic water cluster data obtained from ab initio calculations.

Solute-solvent interactions are also described by model potentials. The electronic coupling between the ionic and covalent states is small in the range of diabatic curve crossing, which is indicative of the Born-Oppenheimer regime of solvation,⁶⁵ where the solvent electrons move much faster than the solute electrons. Accordingly, the solvent effectively “feels” charge-localized solute charge distributions, and the instantaneous solute-solvent energy for each solute VB state V_{ii} is computed and incorporated in the individual Hamiltonian matrix elements, before solving for adiabatic energies, as

$$H_{ii}(\mathbf{R}, \mathbf{r}) = H_{ii}^0(\mathbf{R}) + V_{ii}(\mathbf{R}, \mathbf{r}); \quad V_{ii} = V_{ii}^{\text{Coul}} + V_{ii}^{\text{pol}} + V_{ii}^{\text{rep-disp}} \quad (5.1)$$

where H_{ii}^0 is the isolated NaI diagonal Hamiltonian matrix element for state i (1=ionic, 2=covalent), \mathbf{R} represents the NaI solute coordinates and \mathbf{r} the solvent

coordinates, V_{ii}^{Coul} is the Coulombic interaction energy between the solute and solvent charge distributions, V_{ii}^{pol} is the solvent polarization energy and $V_{ii}^{rep-disp}$ is the solute-solvent repulsion-dispersion energy. The Coulombic energy V_{ii}^{Coul} is given by

$$V_{ii}^{Coul}(\mathbf{R}, \mathbf{r}) = \sum_{k=1}^n \sum_{S=H,M} \frac{q_{Na}^i \cdot q_S^k}{|\mathbf{R}_{Na} - \mathbf{r}_S^k|} + \frac{q_I^i \cdot q_S^k}{|\mathbf{R}_I - \mathbf{r}_S^k|} \quad (5.2)$$

where q_{Na}^i and q_I^i are the solute point charges associated with VB state i at position \mathbf{R}_{Na} and \mathbf{R}_I , respectively, and q_S^k are the point charges associated with sites \mathbf{r}_S^k of the k^{th} solvent molecule. The solvent polarization energy V_{ii}^{pol} (which includes both polarization by the solute charge distribution and by other solvent molecules) is obtained as

$$V_{ii}^{pol}(\mathbf{R}, \mathbf{r}) = -\frac{1}{2} \sum_{k=1}^n \boldsymbol{\mu}_k^i \cdot \mathbf{E}_k^{0,i} \quad (5.3)$$

where $\boldsymbol{\mu}_{i,k}$ represents the set of induced dipoles on each solvent molecule and $\mathbf{E}_{i,k}^0$ the electrostatic field due to all permanent charges, including those of the solute for VB state i , at the (oxygen atom) induced dipole site \mathbf{r}_O^k ,

$$\mathbf{E}_k^{0,i} = q_{Na}^i \frac{(\mathbf{r}_{Na} - \mathbf{r}_O^k)}{|\mathbf{r}_{Na} - \mathbf{r}_O^k|^3} + q_I^i \frac{(\mathbf{r}_I - \mathbf{r}_O^k)}{|\mathbf{r}_I - \mathbf{r}_O^k|^3} + \sum_{l \neq k}^n \sum_{S=H,M} q_S^l \frac{(\mathbf{r}_S^l - \mathbf{r}_O^k)}{|\mathbf{r}_S^l - \mathbf{r}_O^k|^3} \quad (5.4)$$

The induced dipoles $\boldsymbol{\mu}_k^i$ are evaluated as a linear response to the total electric field

$$\boldsymbol{\mu}_k^i = \alpha \cdot \mathbf{E}_k^i = \alpha \cdot [\mathbf{E}_k^{0,i} + \sum_{l \neq k}^n \mathbf{T}_{kl} \cdot \boldsymbol{\mu}_l^i] \quad (5.5)$$

where α is the solvent polarizability and \mathbf{T} the dipole tensor.¹²⁶ In practice, the self-consistent induced-dipole problem, Eq. (5.5), is solved in matrix form by LU decomposition and backsubstitution.¹²⁵ The solute-solvent repulsion-dispersion energy is modeled by a sum of standard Lennard-Jones potentials over all repulsion-dispersion sites (the ions/atoms and the water oxygen atoms)

$$V_{ii}^{\text{rep-displ}}(\mathbf{R}, \mathbf{r}) = \sum_{k=1}^n 4\epsilon_{O-Na}^i \left[\left(\frac{\sigma_{O-Na}^i}{|\mathbf{R}_{Na} - \mathbf{r}_O^k|} \right)^{12} - \left(\frac{\sigma_{O-Na}^i}{|\mathbf{R}_{Na} - \mathbf{r}_O^k|} \right)^6 \right] + \sum_{k=1}^n 4\epsilon_{O-I}^i \left[\left(\frac{\sigma_{O-I}^i}{|\mathbf{R}_I - \mathbf{r}_O^k|} \right)^{12} - \left(\frac{\sigma_{O-I}^i}{|\mathbf{R}_I - \mathbf{r}_O^k|} \right)^6 \right] \quad (5.6)$$

Finally, the solute-solvent contribution to the off-diagonal Hamiltonian matrix element is simply evaluated with the Mulliken approximation¹⁸³

$$H_{ij}(R, r) = H_{ij}^0(R) + \frac{S_{ij}}{2} \{ V_{ii}(R, r) + V_{jj}(R, r) \} \quad (5.7)$$

where S_{ij} is the off-diagonal element of the VB state overlap matrix.

Evaluation of the solute-solvent Coulombic and solvent polarization interaction energies requires solute partial point-charge distributions q_{Na}^i and q_I^i for both VB states. Accordingly, NaI *effective* VB point charges are extracted from high-level *ab initio* calculations of the gas-phase dipole moments for the first two NaI adiabatic states.¹⁶⁵ We note for future discussion that gas-phase excited-state NaI has a reversed polarity to that of the ground ionic Na^+I^- state in the Franck-Condon region and very quickly becomes nonpolar with increasing interatomic distance.

Table 5.1 Parameters of the OPCS model potentials^a

Water		
$r_{\text{O-H}} = 0.9572 \text{ \AA}^b$	$\theta_{\text{H-O-H}} = 104.52^\circ{}^b$	$q_{\text{H}}/e = 0.569$
$r_{\text{O-M}} = 0.342 \text{ \AA}$	$\theta_{\text{H}_2\text{O-M}} = \pm 43.4^\circ$	$q_{\text{M}}/e = -0.569$
	$\alpha_{\text{W}} = 1.45 \text{ \AA}^3{}^c$	
$\epsilon_{\text{O-O}} = 0.25 \text{ kcal/mol}$		$\sigma_{\text{O-O}} = 3.20 \text{ \AA}$
$A_{\text{H-H}} = 10^5 \text{ kcal/mol}$		$B_{\text{H-H}} = 5.5 \text{ \AA}^{-1}$
Na^+ (ground state)		
$q_{\text{Na}^+}/e = 1.0$		
$\epsilon_{\text{O-Na}^+} = 0.04 \text{ kcal/mol}$		$\sigma_{\text{O-Na}^+} = 3.11 \text{ \AA}$
Na (excited state)		
$q_{\text{Na}}/e = 0.0$		
$\epsilon_{\text{O-Na}} = 5.34 \text{ kcal/mol}$		$\sigma_{\text{O-Na}} = 2.17 \text{ \AA}$
I^- (ground state)		
$q_{\text{I}^-}/e = -1.0$		
$\epsilon_{\text{O-I}^-} = 0.85 \text{ kcal/mol}$		$\sigma_{\text{O-I}^-} = 3.81 \text{ \AA}$
I (excited state)		
$q_{\text{I}}/e = 0.0$		
$\epsilon_{\text{O-I}} = 0.92 \text{ kcal/mol}$		$\sigma_{\text{O-I}} = 3.61 \text{ \AA}$

^a r are interatomic distances, θ angles, q atomic charges, α polarizabilities, ϵ and σ the Lennard-Jones parameters and A and B the Born-Mayer potential parameters.

^bFrom reference 133. ^cFrom reference 126. ^dFrom reference 97.

With this choice of model potentials, the electronic polarizability of the solvent molecules is not kept frozen, in contrast to our previous work.²⁰⁵ Furthermore, not only are solvent molecules allowed to polarize each other, but the solute charge distribution (which enters the V_{ii}^{pol} term) is also allowed to polarize solvent molecules. In turn, solvent molecules also polarize the solute electronic structure by affecting the composition of the ground and excited adiabatic states in the VB state basis. Parameters for the solute-solvent (Lennard-Jones) interactions are derived from experimental data for

ion-water and atom-water binary complexes, supplemented by results of ab initio calculations. All model potential parameters are collected in Table 5.1.

5.2.2 Constant-Temperature MD Simulations and Free Energy Calculations

Our earlier work, based on a solvation dielectric continuum model, predicted an inverted-regime electron transfer process for NaI in small water clusters. In order to both test the validity of the prediction of the earlier model against our present, explicit, molecular description of the solvent and gain some insight into the electron transfer dynamics, diabatic free energy curves were generated as a function of a *collective* solvent coordinate around the NaI curve crossing point ($R_c = 7 \text{ \AA}$). Nosé-Hoover molecular dynamics (MD) simulations,^{141,142} thermostated at 200 K with a modified version of the velocity Verlet algorithm,¹⁴³ were used to that effect. The solvent coordinate, typically used in condensed-phase problems, is defined by the energy difference between the diabatic states^{65,124}

$$\Delta E = H_{22}(\mathbf{R}, \mathbf{r}) - H_{11}(\mathbf{R}, \mathbf{r}) \quad (5.8)$$

and basically gauges the relative energies of the two solute states for a given solvent configuration. The free energy curves $\Delta G_i(\Delta E)$ are computed as

$$\Delta G_i(\Delta E) = \Delta G_i^0(\Delta E) - k_B T \ln P_i(\Delta E)_i \quad (5.9)$$

where $P_i(\Delta E) = \delta[\Delta E - (H_{22} + H_{11})] \exp(-H_{ii}/k_B T)$ is the probability density of the diabatic state energy gap ΔE , which is directly evaluated during the simulation, and $\Delta G_i^0(\Delta E)$ is a reference free energy formally related to the ensemble configuration integral. Since equilibrium MD simulations typically sample a small region around the

minimum in the free energy, nonequilibrium umbrella sampling¹³⁵ was used to access regions of high free energy (where the solvent coordinate is far from equilibrium) while constraining the NaI interatomic distance R to the crossing point value R_c . Accordingly, MD simulations were performed with the umbrella potential

$$V_\lambda = H_{11}(\mathbf{R}, \mathbf{r}) + \lambda[H_{22}(\mathbf{R}, \mathbf{r}) - H_{11}(\mathbf{R}, \mathbf{r})] + \frac{1}{2}k(R - R_c)^2 \quad (5.10)$$

where the interpolation parameter λ was varied from 0 to 1 with increments $\Delta\lambda = 0.1$, and a force constant $k = 50 \text{ kcal/mol/\AA}^2$ was used. The weighted histogram analysis method (WHAM)¹³⁸ was used to remove the sampling bias introduced by the umbrella potential and to connect the probability densities evaluated separately for each sampling window. Finally, the relative position of the free energy curves was inferred from calculations of the equilibrium free energy difference between the diabatic states by statistical perturbation theory¹⁰¹

$$\begin{aligned} \Delta G_1^0 - \Delta G_2^0 &= -k_B T \ln \langle \exp(-[H_{11} - H_{22}]/k_B T) \rangle \\ &= \sum_{\lambda=0}^1 -k_B T \ln \langle \exp(-[V_{\lambda+\Delta\lambda} - V_\lambda]/k_B T) \rangle_\lambda \end{aligned} \quad (5.11)$$

where $\langle . \rangle_\lambda$ implies the standard ensemble average over configurations generated by the MD simulation with potential V_λ . The covalent state minimum free energy was used as the free energy reference ($\Delta G_2^0 = 0$) to allow a direct comparison with earlier solution work.⁶⁵

Constant-temperature MD simulations were also employed to generate canonical ensembles of $20 \times n$ ground-state $\text{NaI}(\text{H}_2\text{O})_n$ [$n=1-4, 8, 16$] structures, which will serve as

classical initial conditions for the nonadiabatic dynamics simulations discussed in the next section. Distributions of Franck-Condon energy gaps over 1,500 x n configurations were also evaluated with the same simulation technique for comparison with experimental data and other models.

5.2.3 Nonadiabatic Dynamics

Many methods have been developed to simulate nonadiabatic dynamics.⁸⁴ Following our previous work,²⁰⁵ we employ a “surface hopping” trajectory method known as the “molecular dynamics with quantum transitions” (MDQT) method, developed by Tully and coworkers,¹⁹³ to follow the dynamics in the excited electronic state and the decay to the ground state. In this method, the classical particles (nuclei) are constrained to evolve on an individual adiabatic (electronic) potential energy surface with the quantum (electronic) degrees of freedom propagated simultaneously, and, at each trajectory timestep, the quantum subsystem time evolution dictates the choice of which adiabatic potential energy surface the dynamics will be propagated on in the following timestep.

Typically, a time-dependent wavefunction expanded in terms of the electronic adiabatic states is propagated together with the classical nuclear motion and, at each trajectory time step, the probability to undergo a transition is calculated from the time-dependent wavefunction expansion coefficients. A stochastic “fewest switches” algorithm is then used to decide whether a hop to another adiabatic state should occur or not. If a switch between states is performed, the energy difference between the states is distributed among the various classical degrees of freedom along the nonadiabatic

coupling vector.¹⁹³ We note that very few *frustrated* hops, i.e. situations where the stochastic algorithm predicts a nonzero hopping probability to a higher-energy electronic state in regions where the nuclear momentum is insufficient to allow conservation of the total energy upon a surface switch, were encountered in our simulations, and therefore, we used Tully's original "fewest switches" algorithm without time-uncertainty adjustment.²⁰⁶ In general, the method has proven reliable to simulate nonadiabatic dynamics involving rapid transitions, as we will see shortly, is the case for $\text{NaI}(\text{H}_2\text{O})_n$ photodissociation.

In this work, the nonadiabatic coupling vector is most efficiently calculated numerically (along with the forces on the nuclei in the same step), because of the complexity of the potential. The nuclear motion is propagated classically with the "velocity" version of the Verlet algorithm,⁹⁸ and a stepsize of 0.2 fs, which ensures excellent energy conservation, while the propagation of the quantum degrees of freedom, a two-point boundary value problem, is performed with a second-order finite-difference-equation numerical scheme.¹²⁵ In the MDQT method, each trajectory is propagated completely coherently, i.e. values of the coefficients of the time-dependent wavefunction are retained throughout the propagation, so that memory of the coupling between quantum states is preserved at all times. In order to account for quantum decoherence, one needs to propagate a swarm of trajectories for a given classical initial condition. Test calculations showed that a swarm of 100 trajectories was sufficient to obtain converged results for the NaI curve crossing dynamics, and we shall use this swarm size thereafter.

5.2.4 Simulation of Probe Signals

We apply the same probe schemes as in previous work,²⁰⁵ and femtosecond probe signals and photoelectron spectra are generated by excitation to probe states which asymptotically correlate to $\text{Na}^+ + \text{I} + \text{e}$. The probe state potentials, as shown in Fig. 5.1, have been characterized by high-level ab initio calculations, which served as the basis for parameterizing accurate analytical potentials consisting of Born-Mayer repulsion terms and London dispersion terms for short-range interactions, and ion-induced dipole and ion-quadrupole terms for long-range interactions.^{200,205} Spin-orbit coupling of NaI^+ electronic states yields the X ($\Omega = 1/2$) state, with pure Π character, and the I ($\Omega = 3/2$) state, which is a mixture of $^2\Pi$ and $^2\Sigma$ states. Following selection rules for the photoionization of diatomic molecules proposed by Xie and Zare,²⁰¹ transition from the first excited NaI state to both the X and I NaI^+ states are allowed, and promotion to both of these states is considered in our simulations.

Two different detection schemes that were employed in previous experimental femtosecond studies of bare NaI and $\text{NaI}(\text{H}_2\text{O})_n$ clusters have been considered: a single-photon scheme involving 263 nm probe excitation from the ionic branch of the first excited state (as was used for studies of bare NaI) and a two-photon scheme involving 2 x 610 nm excitation from the covalent branch of the first excited state, as shown in Fig. 5.1. With both schemes, the excited-state NaI undergoes a vertical excitation from the appropriate branch of the excited state only, with an energy corresponding to the photon excitation, and if the total energy of the freshly excited species exceeds that of the X and/or I probe state, the species are promoted to the given NaI^+ probe state. Upon

promotion to the NaI^+ state, an electron is ejected with a kinetic energy corresponding to the excess energy of the ionizing probe photon energy relative to the probe state. The $\text{Na}^+(\text{H}_2\text{O})_p$ and the $\text{NaI}^+(\text{H}_2\text{O})_p$ probe signals, where p represents the detected product cluster size, were evaluated after propagating the $\text{NaI}^+(\text{H}_2\text{O})_n$ dynamics on the probe state for 4 ps to account for the long time delay between the probe pulse and detection by time-of-flight mass spectrometry. As done previously, the newly NaI^+ ionized species is considered dissociated if the internal energy exceeds the binding energy of 10.4 and 4.2 kcal/mol for the X state for the I state, respectively,²⁰⁰ and water molecules are considered evaporated from the cluster if their energy exceeds that of the $\text{Na}^+(\text{H}_2\text{O})$ or $\text{I}(\text{H}_2\text{O})$ binding energies. The resulting histogram distributions of various probe species are convoluted with a single Gaussian function, with variance 100 to 250 fs,¹⁷¹ in order to account for the presumably Gaussian experimental pump and probe pulse envelopes.²⁰⁷

5.3 Results and Discussion

5.3.1 Franck-Condon Energy Gaps

As mentioned earlier, the OPLS model potential employed in previous work predicts a continuous increase of the NaI excitation energy, or Franck-Condon (FC) energy gap ΔE_{FC} , with cluster size, while experimental and *ab initio* data suggest a convergence of the shift in excitation energies relative to that of bare NaI at cluster size ~ 4 .^{67,205} Due to this discrepancy,²⁰⁵ it was not possible to simulate $\text{NaI}(\text{H}_2\text{O})_n$ photodissociation dynamics for cluster sizes greater than 4 because the stabilization of the ground state relative to the excited state would be unrealistic at larger cluster sizes. It

should be noted, however, that neutral clusters produced by jet expansion in molecular beam experiments, such as $\text{NaI}(\text{H}_2\text{O})_n$, cannot be mass-selected prior to NaI photoexcitation, and therefore the predicted cluster sizes for which excitation energies are measured correspond to the mean of the cluster size distribution produced by jet expansion. However, Multi-Reference Configuration Interaction (MRCI) calculations do confirm that the shift in the Franck-Condon energy gaps relative to bare NaI converges rapidly with the addition of only a few water molecules.²⁰⁵

The distributions of Franck-Condon energy gaps $P(\Delta E_{FC})$ as a function of cluster size predicted by OPCS are shown in Fig. 5.2a. The peaks in the distribution move towards larger Franck-Condon energy gaps as a function of cluster size. The convergence of the ΔE_{FC} with increasing cluster size is not evident from the $P(\Delta E_{FC})$ distributions. The average shifts in the FC energy gaps relative to bare NaI $\Delta\Delta E_{FC}$ are then displayed in Fig. 5.2b, where they are compared to those obtained with OPLS, and where the standard deviations shown on the figure reflect the broadness of the $P(\Delta E_{FC})$ distributions. Obviously, the OPLS shifts in the FC energy gaps increase linearly with cluster size. The $\Delta\Delta E_{FC}$ obtained with OPCS, on the other hand, follow an exponential growth function of the form $\Delta\Delta E_{FC} = a[1 - \exp(b * n)]$, where $a = 1.832$ kcal/mol and $b = 0.268$ are fitted parameters, which converges towards an asymptotic limit at $n \sim 16$. The convergence of $\Delta\Delta E_{FC}$ with increasing cluster size for OPCS is in relatively good agreement with the experimental and MRCI predictions, in contrast to OPLS where a sharp linear increase is observed. Although experiment predicts a shift of 1.3 eV for $n = 16$, and OPCS a shift of

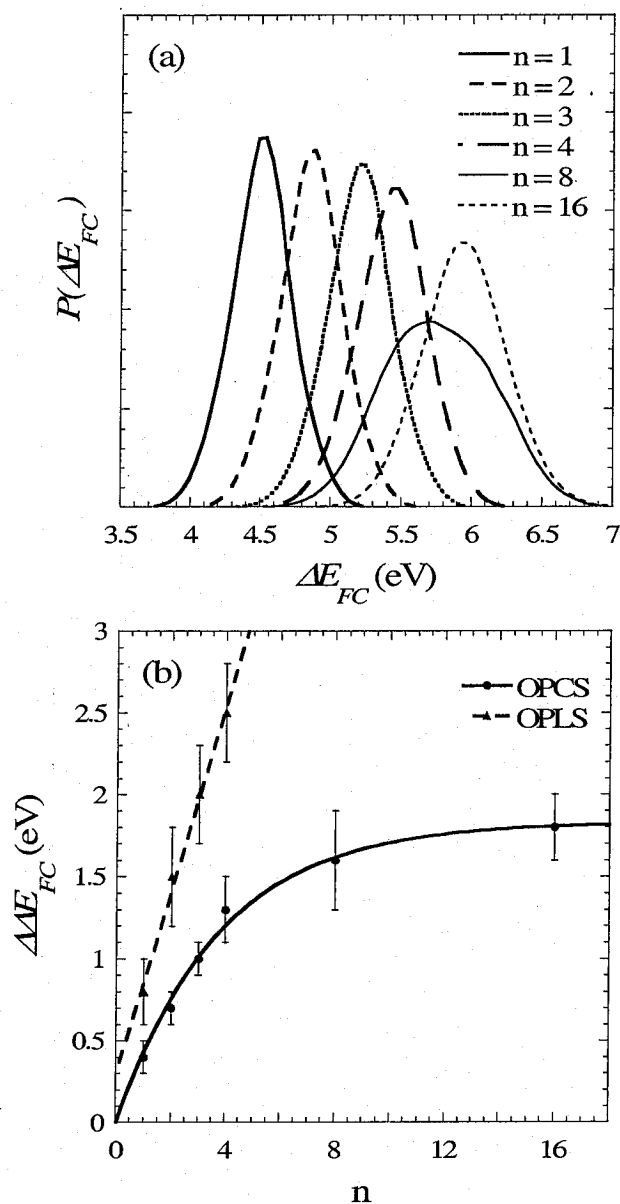


Figure 5.2 Probability distributions of the NaI ground to excited state Frank-Condon energy gaps $P(\Delta E_{FC})$ as a function of cluster size, Fig 5.2a, and average shifts in the Franck-Condon energy gaps $\Delta\Delta E_{FC}$ relative to bare NaI as a function of cluster size, Fig. 5.2b.

1.8 eV, this latter value is in reasonable agreement considering the large standard deviation in the $P(\Delta E_{FC})$ distributions, as shown in Fig. 5.2. Moreover, the average ΔE_{FC} for cluster size 4 obtained with OPCS is in excellent agreement with the results of MRCI calculations. It should be noted, however, that the OPCS data corresponds to the average Franck-Condon energy over a thermal distribution of structures at 200K, while the MRCI energy is that of the 0K minimum energy structure.

The reasons for the continuous increase of the Franck-Condon energy gaps predicted by OPLS as a function of cluster size can be traced to the continuously increasing stabilization of the (ionic) ground state upon addition of water molecules, accompanied by a continuously increasing destabilization of the (covalent) excited state with reversed NaI polarity. By allowing the NaI solute and solvent molecules to polarize each other in both the ground and first excited states with OPCS, the excited state is much less destabilized upon addition of water molecules, as the water molecules polarize to minimize the destabilization, and the differential solvation between the ground and excited states converges rapidly, which explains the rapidly converging Franck-Condon energy gaps observed. Therefore, we believe OPCS to describe the effects of solvation on the $\text{NaI}(\text{H}_2\text{O})_n$ electronic states more rigorously than OPLS, and thus, this more realistic model, which properly describes the Franck-Condon energy gaps as a function of cluster size, allows to extend simulations of $\text{NaI}(\text{H}_2\text{O})_n$ photodissociation dynamics to larger cluster sizes.

5.3.2 $\text{NaI}(\text{H}_2\text{O})_n$ Photodissociation Dynamics

The NaI excited-state population decay is displayed in Figure 5.3a as a function of simulation time and cluster size. In previous simulations with OPLS, the excited-state population decay after NaI reached the curve-crossing region for the first time resembled that of bare NaI due to evaporation of 99% to 95% of the water population within 100 fs after NaI photoexcitation, due to the reversal of the NaI polarity in the Franck-Condon region of the excited state. With OPCS, however, the excited-state population decays much more drastically with increasing cluster size. For cluster sizes 2 and larger, most of the excited state population is depleted within 1 ps after NaI photoexcitation, and for cluster size 1, the decay occurs over 1.6 ps, which happens to correspond to the vibrational period of bare NaI in the first excited state. As will be shown shortly, the differing behavior of the excited state population decay between OPLS and OPCS is due to differing water evaporation dynamics.

The excited-state population has been enlarged in Figure 5.3b, in order to better visualize the population decay over the first 1.2 ps for $n \geq 2$. It is clear that the excited-state population decay increases with cluster size, and at a cluster size 8, the full excited-state population is depleted when NaI reaches the curve-crossing region for the first time. The ionic state is increasingly stabilized relative to the covalent state as water molecules are added to the cluster, as is demonstrated by the change in FC energy gaps with cluster size, shown in Fig. 5.2. As a result, the curve-crossing region moves towards larger NaI internuclear separations. Since the nonadiabatic transition probability is inversely proportional to the NaI internuclear separation, the probability that NaI undergoes a

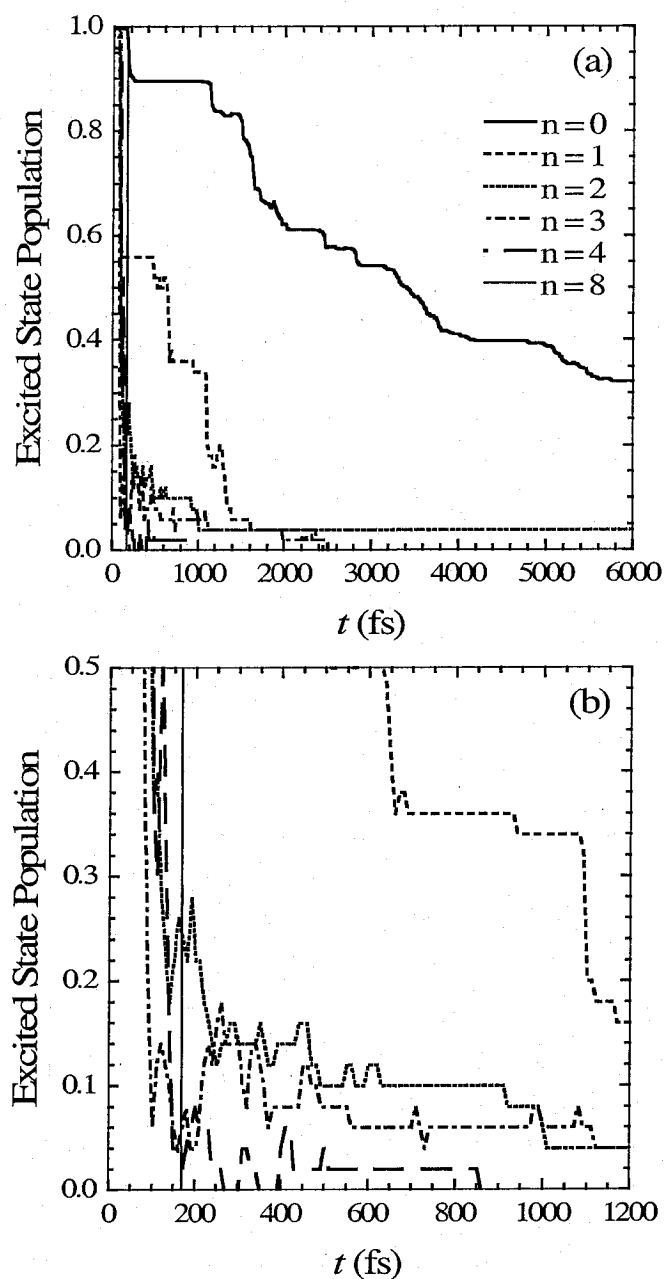


Figure 5.3 Excited-state population as a function of simulation time obtained from OPCS simulations of $\text{NaI}(\text{H}_2\text{O})_n$ clusters of size 0 (solid), 1 (dash), 2 (dot), 3 (dash-dot), 4 (large dash), and 8 (thin solid). Fig. 5.2b is an enlargement of Fig. 5.2a for shorter times

nonadiabatic transition upon reaching the curve-crossing region increases with cluster size. Moreover, the stabilization of the ionic state due to solvation can reach a point where the ionic state becomes lower in energy than the covalent state at all internuclear separations that is the ground state is entirely ionic and the first excited state entirely covalent for the full range of NaI internuclear separations. For cluster size 8, we will see in more detail later that the excited-state population decays completely to a pure, ionic ground state.

As mentioned earlier, the difference between the excited-state population decay obtained with OPLS and OPCS is due to differing water evaporation dynamics. The OPLS model accounts for solute-solvent and solvent-solvent interactions through Coulombic and repulsion-dispersion terms only. Consequently, the sudden reversal of the NaI charge distribution upon photoexcitation to the first excited state, where sodium adopts a small negative charge and iodine a small positive charge ($q_{Na} = -q_I = -0.3e$),²⁰⁵ causes strong Coulombic repulsions between NaI and the water molecules that were equilibrated to the NaI ground-state charge distribution. With OPCS, the mutual polarization of the water molecules and the NaI solute attenuates the NaI-H₂O repulsive interactions, as the induced dipole on the water molecules can adjust and reorient to the reversed NaI polarity upon photoexcitation. This is reflected in the variation of the Franck-Condon energy gaps with increasing cluster size, shown in Fig. 5.2, and discussed earlier. If the destabilization of the excited state in the Franck-Condon region, as well as the stabilization of the ground-state, are additive upon addition of solvent molecules with

OPLS, solvation effects with OPCS, on the other hand, are not additive due to the many-body polarization term.

The consequences of the additive Coulombic repulsions with OPLS were reflected in the excited-state population decay, which paralleled that of bare NaI after the system has reached the curve-crossing region for the first time, due to massive water evaporation (between 99% and 95% of the water population) occurring within 100 fs after NaI photoexcitation.²⁰⁵ In contrast, the excited-state population decay is much more pronounced with OPCS, and does not resemble that of bare NaI for any cluster size. The population of evaporated water molecules (%evap) that evaporated due to the repulsive NaI-H₂O interactions, are listed in Table 5.2. In previous work, the reversed polarity of NaI and the repulsive NaI-H₂O forces were found to subsist for 100 fs after NaI photoexcitation.²⁰⁵ The same trend is observed in the present simulations with OPCS, and the population of evaporated water molecules listed in Table 5.2 is thus evaluated over the first 100 fs after NaI photoexcitation, for direct comparison with previous work. Indeed, the population of evaporated water molecules decreases from 12% for $n = 1$, to 0% for $n = 8$, reflecting the fact that the polarization of the water molecules greatly reduces the repulsive NaI-H₂O interaction upon photoexcitation.

The distributions of water evaporation times t_{evap} are shown in Fig. 5.4 as a function of simulation time and cluster size. For comparison, the evaporation times for the small population of long-lived clusters for simulations performed with OPLS are also displayed. With OPLS, most long-lived clusters dissociate within 2 ps after NaI photoexcitation. In contrast, a significant population of NaI-bound water molecules

Table 5.2 Features of $\text{NaI}(\text{H}_2\text{O})_n$ photodissociation dynamics

	n				
	1	2	3	4	8
%evap ^a	12	9	10	7	0
$\langle E_{FC} \rangle$ (kcal/mol) ^b	33 ± 4	41 ± 4	47 ± 4	51 ± 5	48 ± 3
%bound ^c	6	22	34	53	46
$\langle E_{trans} \rangle$ (kcal/mol) ^d	5 ± 2	4 ± 3	4 ± 3	5 ± 4	4 ± 3
$\langle E_{rot} \rangle$ (kcal/mol) ^d	8 ± 3	8 ± 4	5 ± 4	5 ± 4	3 ± 3

^a Evaluated for the population of water molecules evaporating within 100 fs after NaI photoexcitation. ^b Average cluster excess Franck-Condon energy.

^c Population of trajectories where NaI remains bound over the simulation timescale. ^d Average translational $\langle E_{trans} \rangle$ and rotational $\langle E_{rot} \rangle$ energies.

subsists for ~ 3 ps after NaI photoexcitation for OPCS. Nonetheless, only a very small population of water molecules remain bound over the simulation timescale, because each time NaI passes through the covalent region of the excited state, the NaI- H_2O interactions decrease significantly, leading to further evaporation of water molecules.²⁰⁵

The average water rotational $\langle E_{rot} \rangle$ and translational energies $\langle E_{trans} \rangle$ post-evaporation are listed in Table 5. For $n \leq 4$, the water molecules evaporate more rotationally than translationally hot, suggesting a nonstatistical evaporation process. As was discussed thoroughly in our previous work (Chapter 4),²⁰⁵ rotational excitation of the water molecules arises because the light hydrogen atoms of the water molecules are attracted towards the negatively charged sodium atom in the Franck-Condon region of the first excited state, inducing a significant torque on the water molecules, while the water translational motion is mainly caused by the repulsion between the water oxygen atom and the negatively charged sodium atom. For cluster size 8, on the other hand, water

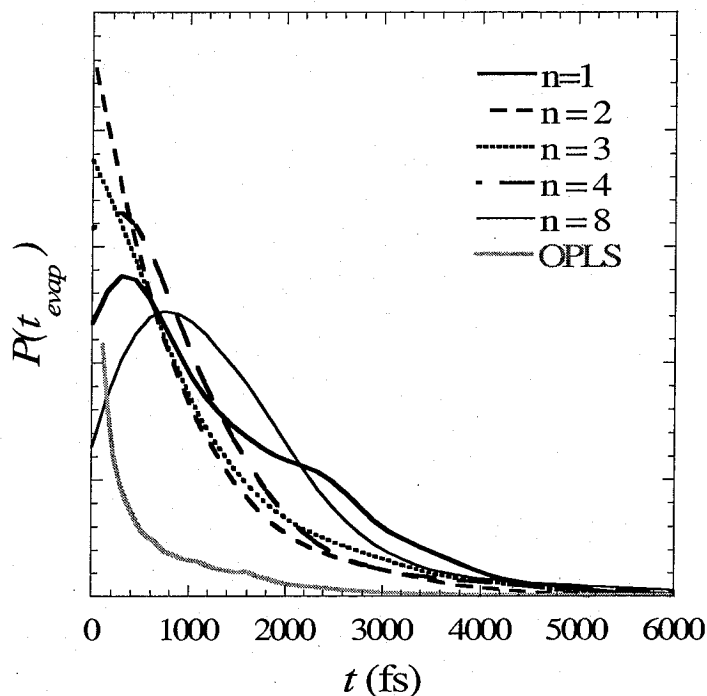


Figure 5.4 Comparison between OPCS and OPLS distributions of evaporation times $P(t_{\text{evap}})$ as a function of simulation time t for $\text{NaI}(\text{H}_2\text{O})_n$ clusters of size 1 (thick solid), 2 (dash), 3 (dash-dot), 4 (large dash), or 8 (thin solid). For OPLS (dark grey), the distribution is evaluated over all cluster sizes for the 5% population of water molecules that remain bound for more than 100 fs after NaI photoexcitation.

molecules evaporate with similar translational and rotational energies. Due to the large number of degrees of freedom in a cluster of this size, the NaI excess Franck-Condon energy after photoexcitation can be more efficiently redistributed throughout the cluster. Furthermore, there is a higher probability that energy transfer between water molecules

occurs. Thus, the water evaporation dynamics may become less impulsive and more statistical-like at large cluster sizes.

The population of NaI(H₂O)_n clusters where NaI remains bound in the excited state for long periods of time after photoexcitation is also significantly affected by solvation, as evident from the excited-state population decay in Fig. 5.3. However, the population of bound NaI (%bound) listed in Table 5.2 increases as a function of cluster size. Since the NaI internuclear separation at which curve crossing occurs increases with cluster size, one would expect that the population of clusters that undergo nonadiabatic transitions to form atomic products on the covalent branch of the ground state also increases with cluster size. However, if enough water molecules remain bound to NaI after photoexcitation, the stabilization of the ionic state is significant enough that the adiabatic states lose their mixed ionic/covalent character, and the excited state becomes purely covalent and the ground state purely ionic over the whole range of NaI internuclear separations, as mentioned earlier. For perspective, the asymptote of the ionic state is lower in energy than that of the covalent state, and thus the ionic products are more stable than the atomic products, if 2 water molecules solvate sodium or 4 water molecules solvate iodide. Obviously, more water molecules may be needed to stabilize the ionic state at intermediate NaI internuclear separations, since solvation of an ion pair is not as effective as that of ions and, for instance, for cluster size 8, the ionic state is on average 5 kcal/mol lower in energy than the covalent branch at an NaI internuclear separation of ~ 8.5 Å (the distance around which nonadiabatic transitions occur). The drastic stabilization of the ionic state for cluster size 8 then explains why the (covalent)

excited-state population decays to the ionic ground state very efficiently for this cluster size. Furthermore, the ground-state $\text{NaI}(\text{H}_2\text{O})_n$ cluster either dissociates to form ionic products, or remains bound in the ionic state well, which explains the population of bound NaI clusters. The formation of ionic products is observed for only 0.1% of the cluster population for cluster size 8, and the formation of ionic products occurs only when at least 5 water molecules are bound to NaI at the time of the excited-to-ground state transition.

To summarize, the excited-state population decay increases sharply with cluster size, and at cluster size 8, the stabilization from the water molecules causes the adiabatic ground and excited states to acquire pure ionic and covalent character, respectively, such that following transition back to ground state, NaI remains bound on the ground ionic state or the cluster dissociates to form ionic products. For smaller cluster sizes, the excited-state population decay resembles what was observed for small-cluster simulations with OPLS, that is increased enhancement with cluster size of nonadiabatic transitions to form atomic products, but the excited-state population decay is more rapid with OPCS, because of the lesser extent of water evaporation.

5.3.3 Connection with Experiment

Grégoire *et al.* performed a femtosecond pump-probe spectroscopy study of $\text{NaI}(\text{H}_2\text{O})_n$ clusters employing a two-photon (2×610 nm) detection scheme where photoexcitation to the probe state occurs from the covalent branch of the excited state.⁶⁷ For an initial cluster size distribution between 1 and 7 water molecules, exponentially

decaying $\text{Na}^+(\text{H}_2\text{O})_p$ experimental probe signals, where p refers to the post-evaporation product cluster size, were obtained for product cluster sizes 1 to 3, and $\text{NaI}^+(\text{H}_2\text{O})_p$ signals were not detected. In previous work (Chapter 4),²⁰⁵ our simulations resulted in a predominant bare Na^+ signal for parent cluster sizes 1 to 4, and more intense $\text{NaI}^+(\text{H}_2\text{O})_p$ signals corresponding to the parent cluster size were obtained with the two-photon probe scheme. The obtention of a bare Na^+ signal was attributed to photoexcitation to the repulsive wall of the probe state at small NaI internuclear separations, which resulted in water evaporation due to high NaI excess Franck-Condon energies. It was concluded that the $\text{Na}^+(\text{H}_2\text{O})_p$ [$p=1-3$] signals obtained experimentally resulted from photoexcitation of larger parent clusters. The $\text{NaI}^+(\text{H}_2\text{O})_p$ signals with $p=n$ were ascribed to excitation to the potential energy well of the NaI^+ probe states at short pump-probe time delays when photoexcitation and probe excitation occur almost vertically from the ground-state to the probe states. The minima of the probe state wells are ~ 10 and 4 kcal/mol deep for the X and I states, respectively.²⁰⁰ At short pump-probe time delays, the water molecules do not have time to travel far from NaI because of the reversed polarity of NaI in this region, such that upon reaching the probe state, the water molecules rapidly reequilibrate to the newly formed NaI^+ species, whose charge distribution appears relatively similar to that of ground-state ionic NaI for the majority of water molecules on the sodium end of NaI.

The simulated OPCS $\text{Na}^+(\text{H}_2\text{O})_p$ and $\text{NaI}^+(\text{H}_2\text{O})_p$ probe signals resulting from the two-photon probe scheme for photoexcitation to the X and I probe states are shown in Figs. 5.5 and 5.6, respectively. The $\text{NaI}^+(\text{H}_2\text{O})_p$ signals for photoexcitation to the X and I probe states are very similar, and are thus only shown in Fig. 5.5, in order to facilitate

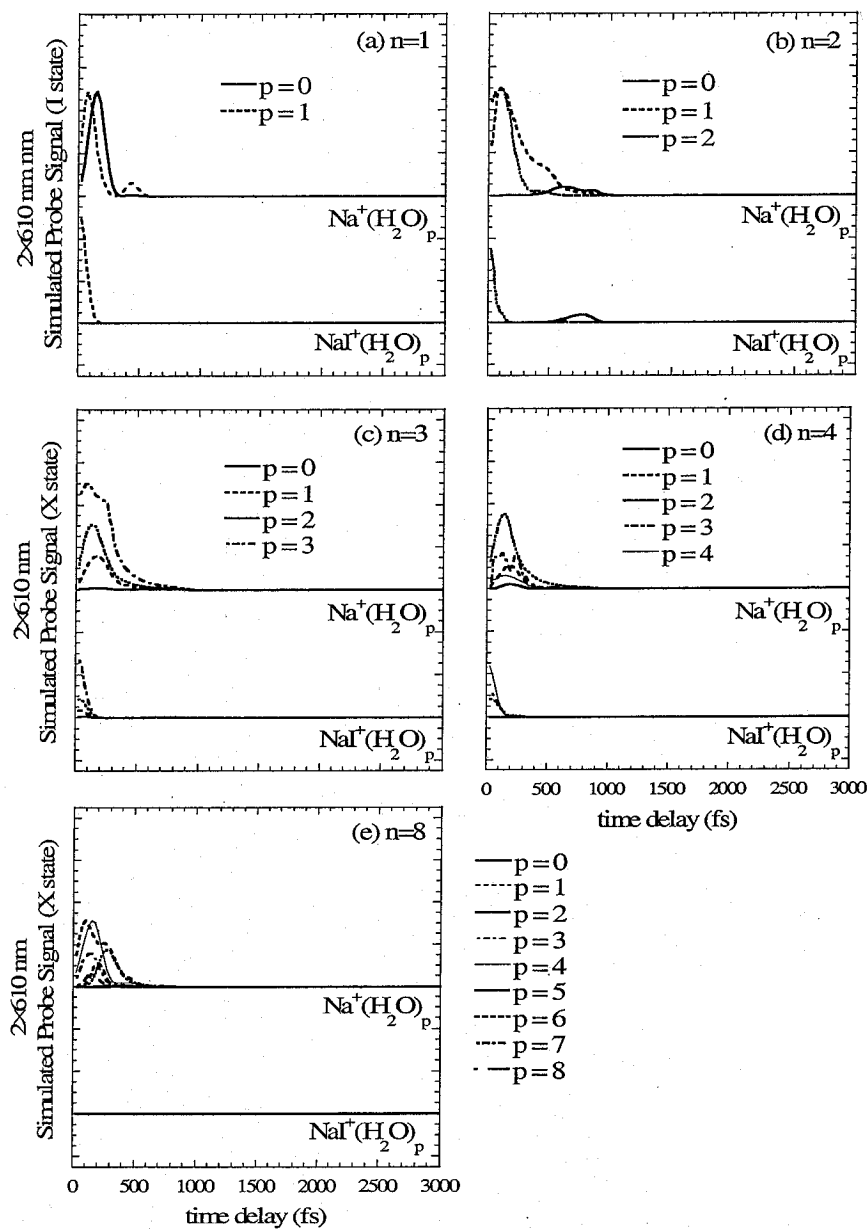


Figure 5.5 Probe signals for $\text{NaI}(\text{H}_2\text{O})_n$ photodissociation as a function of pump-probe time delay, generated using two-photon excitation from the covalent branch of the first excited state to the X probe state.

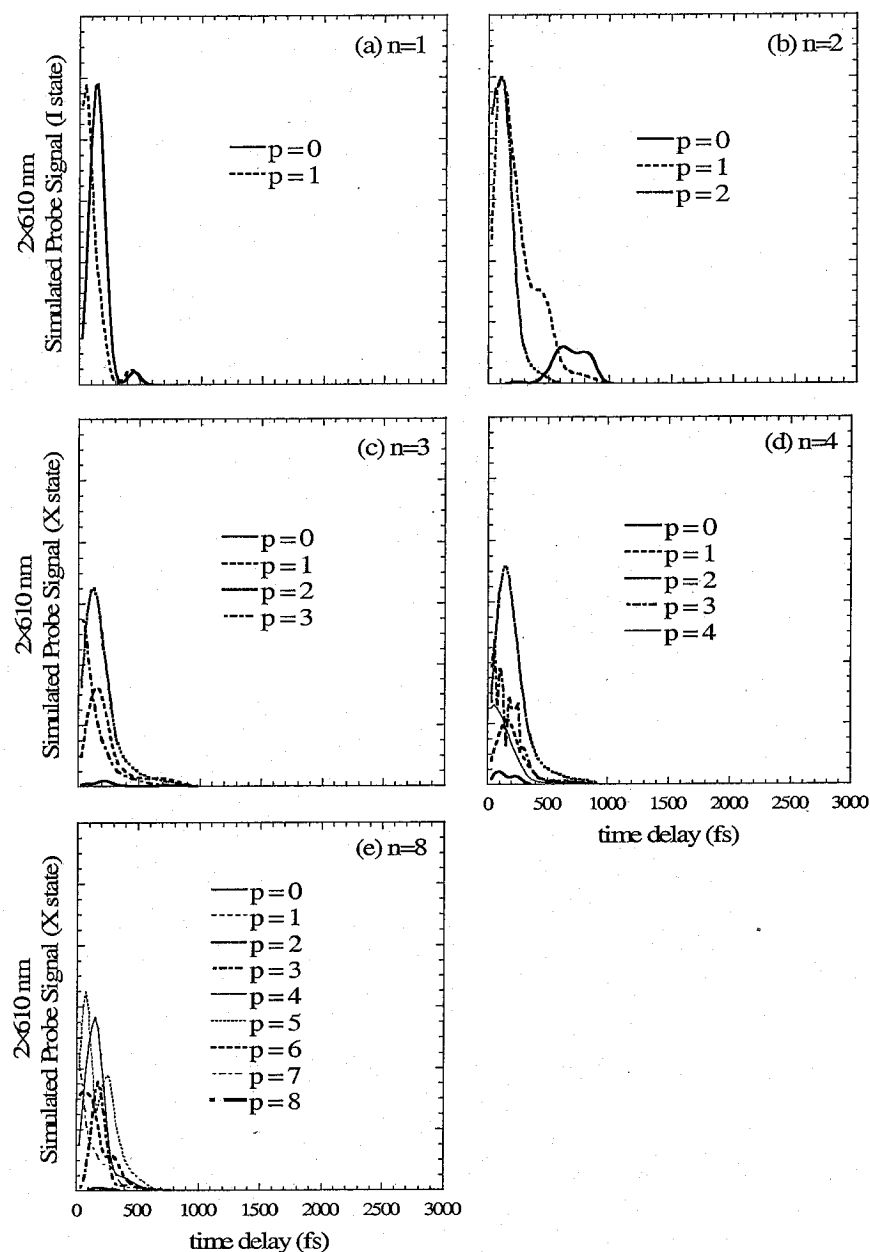


Figure 5.6 $\text{Na}^+(\text{H}_2\text{O})_p$ probe signals for $\text{NaI}(\text{H}_2\text{O})_n$ photodissociation as a function of pump-probe time delay, generated using two-photon excitation from the covalent branch of the first excited state to the I probe state.

visualization of the successive evaporation of water molecules apparent in the $\text{Na}^+(\text{H}_2\text{O})_p$ signals. In contrast to previous simulations with OPCS, significant $\text{Na}^+(\text{H}_2\text{O})_p$ signals are observed for all cluster sizes. Furthermore, the $\text{NaI}^+(\text{H}_2\text{O})_p$ signals are less intense than obtained previously with OPLS, and disappear completely for cluster size 8. From Fig. 5.2, it was clear that OPCS predicts lower Franck-Condon energy gaps. energy gaps between the NaI ground and excited states than OPLS, due to favorable rearrangement of the water induced-dipoles to the new NaI charge distribution in the excited state. Accordingly, the FC energy gap between the first NaI excited state and the X and I probe states is diminished relative to OPLS because the ground state and the probe states are similarly stabilized by the solvent molecules, and the water molecules are found mainly around the positively charge sodium in both states. Consequently, photoexcitation to the probe states with the 2×610 nm probe scheme occurs higher on the probe states with OPCS, and less bound NaI^+ is formed. In Table 5.3, we compare the average excess NaI FC energies after photoexcitation to the probe states with OPLS and OPCS, where the excess FC energy is evaluated relative to the asymptote of the probe

Obviously, NaI has more excess Franck-Condon energy after excitation to the probe states with OPCS than with OPLS. In fact, for OPLS and excitation to the X state, the average excess Franck-Condon energy relative to the asymptote is negative, indicating that excitation occurs mainly to the potential energy well of this state and that NaI^+ will remain bound. The average excess Franck-Condon energy for the I state is larger because of the higher population of clusters that are excited to the repulsive wall of the probe state, relative to the X state. With OPCS, on the other hand, the average excess

Franck-Condon energy is relatively similar for both X and I probe states, and approximately 10 kcal/mol above the probe state asymptotes. Thus, more intense $\text{Na}^+(\text{H}_2\text{O})_p$ signals arising in part from dissociation of NaI^+ species are obtained with OPCS.

Table 5.3 Average excess Franck-Condon energies (and standard deviation)^a

Two-photon probe scheme				
	OPLS		OPCS	
	X	I	X	I
1	-1 ± 6	10 ± 4	11 ± 9	14 ± 8
2	-3 ± 4	3 ± 4	8 ± 7	10 ± 6
3	-1 ± 4	5 ± 4	9 ± 7	11 ± 6
4	-1 ± 6	4 ± 5	8 ± 7	10 ± 7
8			7 ± 5	9 ± 6
One-photon probe scheme				
	OPLS		OPCS	
	X	I	X	I
1	3 ± 4	3 ± 4	5 ± 5	5 ± 5
2	1 ± 4	1 ± 4	3 ± 3	3 ± 3
3	2 ± 3	2 ± 3	4 ± 4	4 ± 4
4	2 ± 4	2 ± 4	3 ± 3	4 ± 4
8			2 ± 2	2 ± 2

^a in kcal/mol, relative to the asymptote of both probe states

In fact, the $\text{NaI}^+(\text{H}_2\text{O})_p$ signals obtained with OPCS, shown in Fig. 5.5, arise only for pump-probe time delays lower than 200 fs, when NaI can be found at short internuclear separations. At a pump-probe time delay of around 200 fs, when the $\text{Na}^+(\text{H}_2\text{O})_p$ signals appear, water molecules have started to evaporate on the first excited state due to the initial NaI- H_2O repulsive dynamics upon photoexcitation, and NaI has transferred a significant fraction of its excited-state excess Franck-Condon energy to the

surrounding water molecules, and the water molecules that have gained already a lot of kinetic energy on the excited state may continue to evaporate on the probe state. As can be seen clearly in Fig. 5.6., $\text{Na}^+(\text{H}_2\text{O})_p$ signals for $p < n$ arise at longer pump-probe time delays than the signals corresponding to the parent cluster size.

In agreement with experimentally-determined probe signals, the $\text{Na}^+(\text{H}_2\text{O})_p$ and $\text{NaI}^+(\text{H}_2\text{O})_p$ signals resulting from two-photon ionization decay exponentially after 200 fs, which is the time NaI reaches the curve-crossing region for the first time on the excited state, due to the increased nonadiabatic transition probability caused by solvation. Furthermore, the simulated OPCS signals, in contrast to the OPLS ones, demonstrate that the $\text{Na}^+(\text{H}_2\text{O})_p$ signals observed experimentally may arise from parent clusters close in size ($p \sim n$) and not necessarily from much larger parent clusters. For cluster sizes 1 to 4, $\text{Na}^+(\text{H}_2\text{O})_p$ signals are obtained for $p \leq 3$, but for cluster size 8, which was outside the experimental cluster size distribution, larger product signals are obtained. In contrast to experiment, however, $\text{NaI}^+(\text{H}_2\text{O})_p$ signals are also obtained for both OPLS and OPCS, even though the signals are much more pronounced with OPLS. The comparison between simulated probe signals obtained with OPLS and OPCS suggests that obtention of a $\text{NaI}^+(\text{H}_2\text{O})_p$ signal may depend on the model potential employed. Since OPCS predicts Franck-Condon energy gaps that are smaller than those predicted by OPLS, but are still larger than those found experimentally, it is conceivable that the $\text{NaI}^+(\text{H}_2\text{O})_p$ signals would disappear if more accurate potentials with the exact Franck-Condon energy gaps were employed to simulate $\text{NaI}(\text{H}_2\text{O})_n$ photodissociation dynamics. However, we note that the present QM/MM model is already fairly sophisticated, and performing

nonadiabatic dynamics simulations with intermolecular interactions derived from first-principles would be computationally prohibitive.

The simulated probe signals obtained with the one-photon (263 nm) probe scheme, where excitation occurs mainly from the ionic branch of the excited state, are shown in Fig. 5.7 for photoexcitation to the X state. The signals for photoexcitation to the I state are not shown because they do not differ from those shown for photoexcitation to the X state. As seen from Table 5.3, the average excess Franck-Condon energy is about the same for both states with this probe scheme, because photoexcitation occurs to the asymptotes of both states, which are equal in energy, resulting in equal signals for both states. It is clear from Fig. 5.7. that both the Na⁺(H₂O)_p and NaI⁺(H₂O)_p signals disappear by cluster size 3. As mentioned earlier, for large cluster sizes such as 4 or 8, almost all of the excited-state population undergoes a nonadiabatic transition upon reaching the NaI curve-crossing region for the first time. In previous OPLS simulations, the successive evaporation of the water molecules could be monitored from the NaI⁺(H₂O)_p signal. Since the NaI⁺(H₂O)_p signals arise only from excitation at the outer turning point of the NaI vibrational motion in the excited state, the signal is much less intense than the Na⁺(H₂O)_p signals, such that the signal is barely perceptible for cluster sizes larger than 1. Consequently, the probe signals resulting from one-photon ionization may reveal at which cluster size the ionic state is sufficiently stabilized, relative to the covalent state, to cause the depletion of the full excited-state population upon reaching the curve crossing point for the first time, but may not allow to probe much of the other aspects of the

photodissociation dynamics.

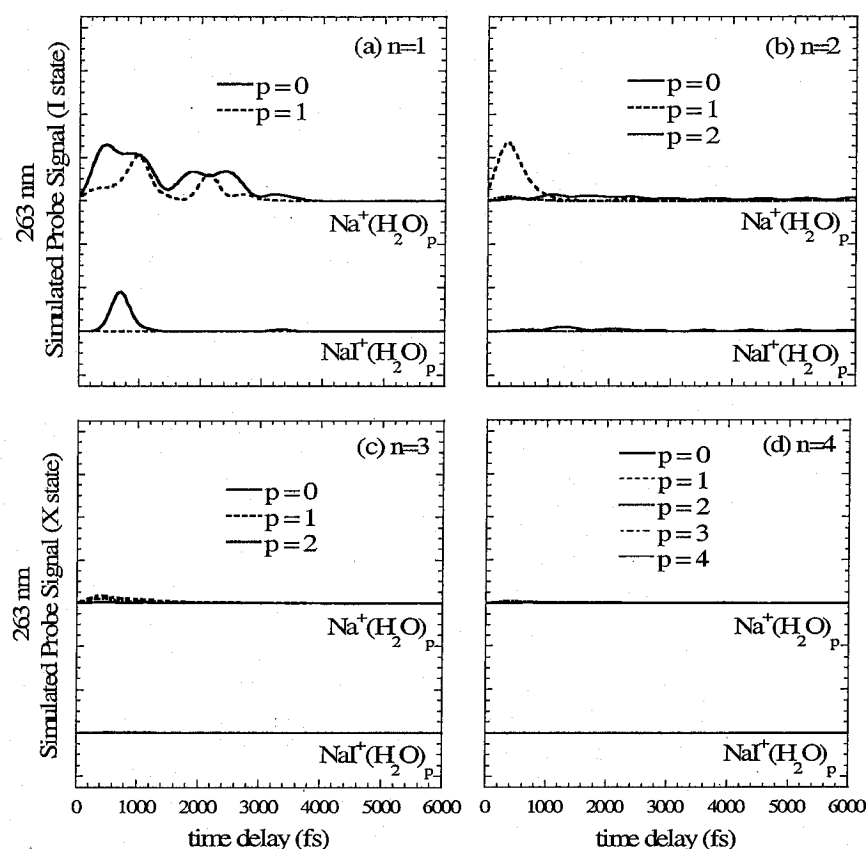


Figure 5.7 Probe signals for $\text{NaI}(\text{H}_2\text{O})_n$ photodissociation as a function of pump-probe time delay, generated using one-photon excitation from the ionic branch of the first excited state to the X probe state.

5.3.4 Electron Transfer Reaction in $\text{NaI}(\text{H}_2\text{O})_n$ Clusters

In previous work on NaI photodissociation in a solution of a weakly polar solvent, diethyl ether,⁶⁵ it was found that the solvent tremendously stabilizes the ionic state and formation of ionic products may proceed via inverted electron transfer. The inverted regime of electron transfer is characterized by a curve crossing between covalent and

ionic free energy surfaces at negative values of the solvent coordinate s , as shown in Fig. 5.8 (when the solvent coordinate reference is that of the covalent state at equilibrium). The solvent coordinate, in the solution case, is defined as the energy difference between the solute-solvent and solvent-solvent interactions of the covalent and ionic states. However, it was found that radiative decay to the ground state occurs over a shorter time scale than the possible inverted electron transfer reaction, and thus, ions are formed by radiative decay of excited NaI, followed by recombination of the ions on the ground state. Extrapolation of the solution results to small clusters suggested that inverted electron transfer could occur in small clusters, and we now attempt to connect the earlier predictions with the results of the present simulations.

The change in free energy for the NaI covalent and ionic states is shown in Fig. 5.9 as a function of the solvent coordinate for an NaI internuclear separation of 7\AA (the gas-phase crossing-point NaI separation). It should be noted that the definition of the solvent coordinate is slightly different in the present cluster work than in previous solution work. In solution, as mentioned above, the solvent coordinate is evaluated as the energy difference between the solute-solvent and solvent-solvent interaction energies of the ionic and covalent states, whereas for clusters, the solvent coordinate s also includes the difference in solute diabatic energies, *i.e.* it is the difference between the total cluster energy of the NaI covalent and ionic states. The coordinates, however, have approximately the same meaning at the NaI curve crossing point ($\sim 7\text{\AA}$) because the energy of the NaI solute is very similar for both ionic and covalent states, such that only

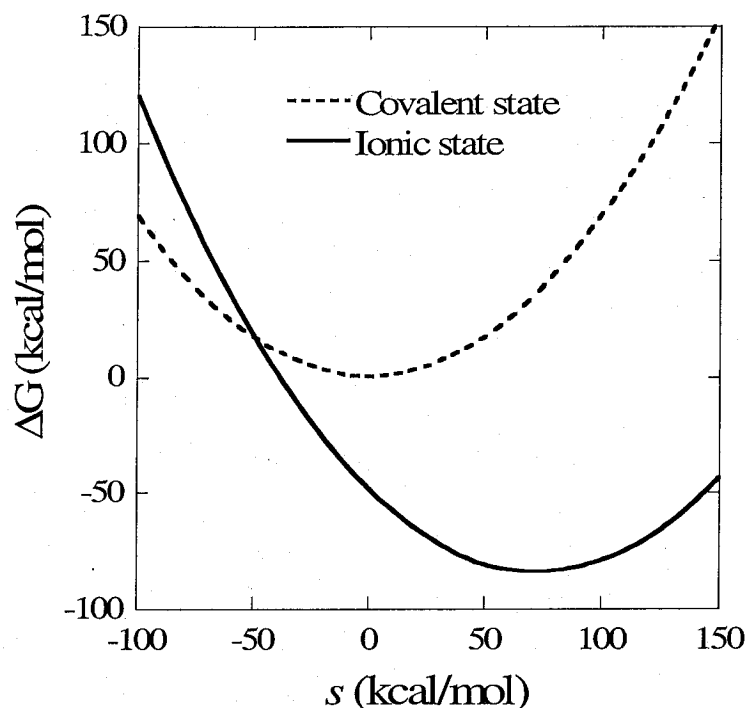


Figure 5.8 Change in free energy ΔG as a function of the solvent coordinate s , at an NaI internuclear separation of 7\AA . From reference 65.

the difference in solute-solvent and solvent-solvent interaction energies define the solvent coordinate in that region of NaI internuclear separation. It should also be noted that it is rather difficult to generate the free energy curves for clusters, shown in Fig. 5.9, over a wide range of solvent coordinates because the solvent coordinate is a large quantity, which dictates the use of many windows away from equilibrium in the umbrella sampling. Furthermore, due to the fluxional character of the clusters, large ensembles of configurations are required to obtain converged statistics. Consequently, the free energy curves shown in Fig. 5.10 were evaluated over a limited range of solvent coordinates.

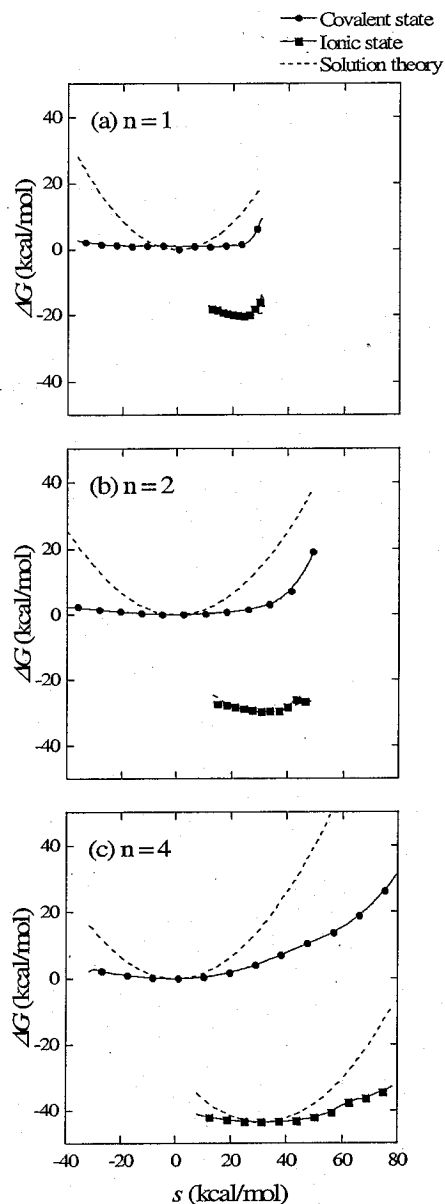


Figure 5.9 Change in free energy ΔG as a function of the solvent coordinate s , evaluated as the energy difference between the ionic and covalent states for cluster sizes 1 (Fig. 5.1a), 2 (Fig. 5.1b) and 4 (Fig. 5.1c). The dashed lines correspond to the free energy estimated from solution theory, the solid lines to the simulated data, where the squares correspond to the ionic state, and the dots to the covalent state.

The free energy curves of the NaI covalent and ionic states for NaI(H₂O)_n clusters, are fitted with a 2nd order polynomial, are shown in Fig. 5.10. Interestingly, the covalent free energy curve along the solvent coordinate is rather flat and independent of cluster size, while that of the ionic state exhibits a clear cluster size dependence, with the parabolic curves becoming increasingly broader with cluster size, consistent with extrapolation of solution theory to clusters. However, solution theory would predict parabola with the same curvature, related to the solvent effective force constant, for both states (and a given cluster size). This is due to the fact that the solvent force constant is not well defined in small clusters. In solution, the motion of the water molecules is rather collective, but in clusters, the solvent molecules can move freely around the solute without significantly affecting the free energy of the system, especially for the covalent state where the NaI-H₂O interaction energy is very low. Thus, it is evident that just a few water molecules moving around the nonpolar covalent solute is not sufficient to mimic the collective motion of solvent molecules in solution, such that the free energy curves for the covalent state are much flatter than that for the ionic state for very small clusters.

The fact that the covalent free energy surface is flat for small clusters suggests that electron transfer would proceed without an activation barrier along the solvent coordinate. In solution, the electron transfer process typically proceeds by the rearrangement of solvent molecules to reach the crossing point between free energy surfaces along the solvent coordinate. The extrapolated free energy curves reveal that the curve crossing between the NaI covalent and ionic states occurs at increasingly large negative values of the solvent coordinate, from $s = 0$ kcal/mol for cluster size 1, to $s \sim -20$

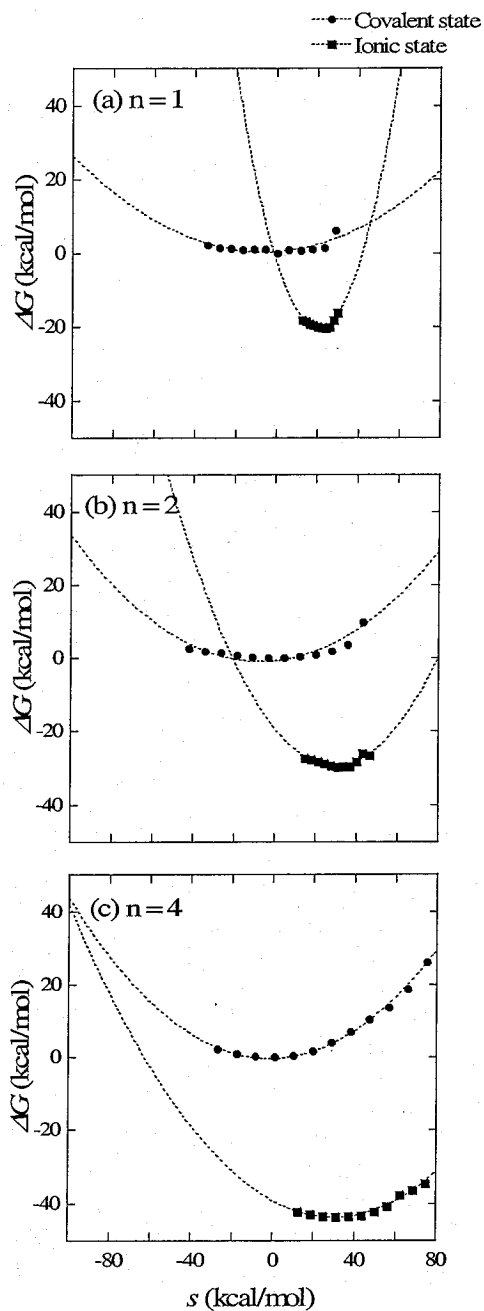


Figure 5.10 Change in free energy ΔG as a function of the solvent coordinate s , evaluated as the energy difference between the ionic and covalent states for cluster sizes 1 (Fig. 5.1a), 2 (Fig. 5.1b) and 4 (Fig. 5.1c). The dotted lines correspond to a fit to the curves with a 2nd order polynomial.

kcal/mol for $n = 2$, and to $s < -100$ kcal/mol for $n = 4$. The average value for the solvent coordinate at the curve crossing between the NaI covalent and ionic states in the MDQT simulations is 0 ± 2 kcal/mol for all cluster sizes, and thus, the transition from one state to the other does not proceed along the solvent coordinate, but along the NaI internuclear coordinate like in the gas phase. Furthermore, the fact that the solvent does not drive the electron transfer process like in solution arises from rapid solvent evaporation on the excited state. If the solvent remained close to NaI, it is clear from Fig. 5.10c that a nonadiabatic transition from the covalent to ionic states would be extremely unlikely at cluster size 4 (the free energy curves shown in Fig. 5.10 are generated from thermal ensembles of stable clusters of a given size, and thus do not account for water evaporation).

To summarize, the electron transfer process in clusters is not defined by the collective motion of the water molecules, as would be the case in solution, and it does not proceed along the solvent coordinate, but along the NaI internuclear separation coordinate like in the gas phase. Thus, in clusters, water molecules do not directly govern the electron transfer rate, they only influence the nonadiabatic transition dynamics by increasing the NaI internuclear separation at which the curve-crossing between the covalent and ionic states occurs.

5.4 Concluding Remarks

In our continuing effort to understand the effects of solvation on elementary electron transfer reactions, we extended our previous investigations of $\text{NaI}(\text{H}_2\text{O})_n$ cluster

photodissociation dynamics²⁰⁵ to larger cluster sizes, by implementing the polarizable OPCS model within the semiempirical valence bond approach employed to describe the NaI electronic structure, along with the molecular dynamics with quantum transitions method.¹⁹³ This new model alleviates the assumption of frozen electronic polarizability of the earlier model, and allows the solvent to polarize as a response to its environment in both the ground and excited states. The NaI ground to first excited state Frank-Condon energy gaps ΔE_{FC} predicted by the nonpolarizable OPLS model used earlier increase linearly with cluster size, in contrast to experimental⁶⁸ and high-level *ab initio* calculations²⁰⁵ results that suggest a convergence of ΔE_{FC} over the cluster size range 4-16. Due in part to this discrepancy, our previous simulations were limited to small cluster sizes. OPLS also predicted ground-state solvent-separated ion pairs to become overwhelmingly predominant at much smaller cluster sizes than OPCS, producing results less consistent with experimental observations. The OPCS model employed in the present investigation predicts a convergence of ΔE_{FC} at cluster size ~ 16 , in relatively good agreement with experiment and *ab initio* calculations. Exploration of solvation effects on the NaI electronic structure and photodissociation dynamics can thus be safely extended to larger cluster sizes with the present model.

The NaI excited-state dynamics appear to be quite sensitive to the model potential employed to simulate $\text{NaI}(\text{H}_2\text{O})_n$ cluster photodissociation dynamics. In contrast to our previous simulations with OPLS, where the NaI excited-state population decay resembled that of bare NaI after reaching the curve-crossing region for the first time, due to the rapid evaporation of up to 99% of the water population shortly after NaI photoexcitation,

the excited-state population decay with OPCS increases sharply with cluster size. For cluster sizes greater than 2, the full excited-state population decays within 800 fs after photoexcitation. Since the NaI solute and solvent molecules are allowed to polarize each other with OPCS, the NaI-H₂O repulsive forces caused by the NaI reversed polarity in the Franck-Condon region of the excited state upon photoexcitation are attenuated, relative to the OPLS case, and therefore, water evaporation is significantly reduced. In fact, our simulations predict that less than 10% of the water molecules have evaporated by the time NaI reaches the curve-crossing region for the first time, which leads to a more rapid excited-state population decay than OPLS. At cluster size 8, the stabilization of the ionic state by the water molecules causes the adiabatic ground and excited states to acquire pure ionic and covalent character, respectively. Therefore, following the transition back to the ground state after photoexcitation, NaI remains bound on the ground ionic state or the cluster dissociates to form ionic products. For smaller cluster sizes, on the other hand, the transition to the ground state leads to the formation of atomic photodissociation products.

Simulation of the femtosecond pump-probe signals resulting from two-photon (2×610 nm) ionization from the covalent branch of the excited state suggest that the Na⁺(H₂O)_p signals observed experimentally, where p refers to the post-evaporation product cluster size, may arise from parent clusters close in size ($p \sim n$), and not necessarily from much larger parent clusters as suggested by our earlier OPLS results. In contrast to experiment, NaI⁺(H₂O)_p signals are obtained for both OPLS and OPCS, but are less pronounced for the former, which suggests that obtention of a NaI⁺(H₂O)_p signal

depends on the model potential employed. However, performing nonadiabatic simulations with intermolecular interactions derived from first principles would be computationally prohibitive. The femtosecond pump-probe signals obtained with one-photon (263 nm) ionization from the ionic branch of the excited state, differ also from those obtained previously. Both $\text{Na}^+(\text{H}_2\text{O})_p$ and $\text{NaI}^+(\text{H}_2\text{O})_p$ signals are barely perceptible for cluster sizes larger than 1, due to the increased nonadiabatic transition probability caused by the presence of water molecules. The absence of signals with the one-photon probe scheme in the cluster case is consistent with experimental findings: this probe scheme, which was used earlier to probe the NaI gas-phase dynamics,¹⁷¹ was later abandoned in experimental studies of clusters⁶⁷ simply because no femtosecond signal could be detected.

Another important aspect of NaI photodissociation in clusters lies in the precise mechanism of electron transfer involved after photoexcitation upon increasing solvation. Free energy curves for both ionic and covalent states, analogous to those of solution theory, have been generated as a function of a collective solvent coordinate, defined as the energy difference between the two diabatic states, for this purpose. Inspection of the free energy curves reveals that the electron transfer process in clusters is not governed by the collective motion of the water molecules, as would be the case in solution, and it does not proceed along the solvent coordinate, but along the NaI internuclear separation coordinate, as in the gas phase. Therefore, solvation in small clusters mainly influences the nonadiabatic transition dynamics by increasing the NaI internuclear separation at which the curve crossing occurs, but does not directly govern the electron transfer

process as in solution. If the evaporation of water molecules could be prevented by embedding the NaI(H₂O)_n clusters in a matrix or a sufficiently dense buffer gas, the collective motion of the water molecules could become important and therefore govern electron transfer.

Theoretical Studies of Seeded Water Clusters: Structure,
Thermodynamics and Photochemistry

Chapter 6

On the Photoexcitation of NaI Ion Pairs in Water, Ammonia and Acetonitrile Clusters,

To be submitted:

Denise M. Koch, Tao-Nhan Nguyen and Gilles H. Peslherbe,
Chemical Physics Letters (2006)

6.1 Introduction

A good candidate system to investigate solvation phenomena is the NaI ion pair in polar solvent clusters. The NaI system has been a paradigm for femtosecond studies of photodissociation dynamics involving curve crossing of covalent and ionic states: photoexcitation of NaI results in bound oscillatory motion in the excited-state potential, modulated by electron transfer and predissociation to the ground state. This system has thus served as a prototype for cluster photochemistry,^{164,166} and has allowed exploration of solvent effects in the dynamics of fundamental processes such as electron transfer.²⁰⁸ Previous theoretical work on $\text{NaI}(\text{H}_2\text{O})_n$ clusters^{124,205} has shown that the presence of solvent greatly affects the NaI nonadiabatic photodissociation dynamics. Femtosecond photo-ionization experiments²⁰⁴ confirmed these findings by demonstrating the dramatic short-time increase of the atomic product population and the monotonic decay of the NaI excited-state population in the presence of water molecules, in contrast to the oscillatory motion observed for gas-phase NaI.

Multi-photon ionization experimental studies of NaI ion pairs in polar solvent clusters of water, acetonitrile and ammonia⁶⁸ show a very clear, solvent-selective, behavior in the distribution of the detected $\text{Na}^+(\text{solvent})_n$ product ions. More specifically, product clusters up to size 50 have been observed experimentally with water, but no clusters larger than size 9 and 6 have been observed with ammonia and acetonitrile, respectively, in multi-photon ionization experiments. The difference in experimental results for the various solvents was attributed to a varying degree of ground-state charge separation for the ion pair in the different cluster types.

In previous theoretical work,⁹⁷ NaI ion pairs were found to be stable with respect to ionic dissociation even in very large water clusters, but solvent-separated ion pair (SSIP) species become rapidly predominant over contact ion pair (CIP) species past cluster size 32. Interestingly, the structure of ion pairs in water clusters could be related to that of the individual ions in water clusters,⁶² and the “hydrophobic” nature of the iodide ion in aqueous clusters^{158,176,177} was shown to result in surface-solvated NaI ion pair structures at small cluster sizes.⁶² Model electronic structure calculations showed that the oscillator strength of CIPs remains about constant upon addition of solvent molecules, implying that the presence of solvent molecules perturbs the NaI CIP electronic structure only marginally.⁹⁷ SSIPs, however, have a much reduced oscillator strength and may not possess optically accessible excited states akin to that of gas-phase NaI.⁹⁷ A similar study of the NaCl ion pair in aqueous clusters also suggests that charge transfer to solvent (CTTS) may become increasingly important with cluster size increase, and may in fact compete with the ion-pair multi-photon ionization mechanism.^{97,209} This is consistent with the experimental observation⁶⁸ that multi-photon ionization produces $\text{Na}^+(\text{H}_2\text{O})_n$ cluster products of size no larger than $n \sim 50$, implying that large $\text{NaI}(\text{H}_2\text{O})_n$ clusters, which exist predominantly as SSIPs, are not photoexcitable. This also supports the assignment of the lack of large cluster products in multi-photon ionization experiments to ground-state charge separation.

Completely analogous investigations of $\text{NaI}(\text{CH}_3\text{CN})_n$ and $\text{NaI}(\text{NH}_3)_n$ clusters demonstrated that NaI CIPs are also stable for these types of clusters, but SSIPs do not appear before cluster size 32.^{78,79} Thus, ground-state charge separation seems to occur much earlier for water than for ammonia and acetonitrile clusters. Since model electronic

structure calculations showed that the NaI CIP surrounded by solvent molecules possesses optically accessible excited-states relatively similar to those of the isolated NaI molecule, in contrast to SSIPs, this suggests favorable conditions for multi-photon ionization experiments of large $\text{NaI}(\text{CH}_3\text{CN})_n$ and $\text{NaI}(\text{NH}_3)_n$. Yet only small clusters are observed as products of multi-photon ionization for these cluster types, in contrast to water clusters, which makes the ground-state charge separation argument questionable.

The lack of experimental product signal beyond cluster size 6 in $\text{NaI}(\text{CH}_3\text{CN})_n$ multi-photon ionization experiments could be rationalized by alternative photoexcitation mechanisms, involving for instance charge transfer to solvent (CTTS), which has been observed in ionic clusters and could be followed or not by electron photodetachment,^{27,52} or even direct ionization, resulting in different dynamics. As the molecular dipole moment of acetonitrile in the gas phase is about twice that of water, CTTS states can be expected to occur at smaller sizes in acetonitrile than in water clusters,²¹⁰ which would be consistent with experimental observations. Photoexcitation of $\text{NaI}(\text{H}_2\text{O})_n$ clusters was shown to induce massive solvent evaporation,²⁰⁵ and solvent evaporation dynamics on the ionized state may be even more significant for acetonitrile clusters. For instance, the NaI CIP is typically stretched to a smaller extent in acetonitrile clusters than in water clusters,⁷⁹ possibly resulting in larger Franck-Condon excess energies (due to excitation to the probe state repulsive wall), and in increased evaporation further reducing the size of acetonitrile product clusters. Furthermore, probe-state dissociation of $\text{NaI}(\text{CH}_3\text{CN})_n^+$ clusters with interior solvation structures may be more prone to reorganization than that of surface-structure $\text{NaI}(\text{H}_2\text{O})_n^+$ clusters, where iodine is essentially free to leave the

cluster without major solvent network disruption, possibly allowing large $\text{Na}^+(\text{H}_2\text{O})_n$ products to survive.

As for ammonia clusters, the small dipole moment of ammonia obviously precludes the possibility of CTTS in small clusters. Recent simulations⁷⁸ suggest that large $\text{NaI}(\text{NH}_3)_n$ clusters might not be formed under the conditions of the multi-photon ionization experiments. For instance, the maximum $\text{NaI}(\text{NH}_3)_n$ cluster size that can be produced at room temperature corresponds to 9 solvent molecules, which incidentally is the size at which the product signal vanishes in multi-photon ionization experiments. Room-temperature simulations also suggest that large ionic ammonia clusters containing more ammonia molecules than a single ion solvation shell readily undergo solvent evaporation at high temperatures. As a result, hot $\text{Na}^+(\text{NH}_3)_n$ products of photoexcitation might undergo further evaporation on the ionized state and very few cluster products containing more solvent molecules than a single ion solvation shell (coordination number of 5 for sodium) may be observed in multi-photon ionization experiments. Full-fledge nonadiabatic simulations of the photodissociation process of NaI in various solvent clusters analogous to our previous work on $\text{NaI}(\text{H}_2\text{O})_n$ clusters²⁰⁵ might be necessary to confirm or refute these hypotheses.

Asides from CTTS and massive solvent evaporation, which would require costly, convoluted simulations, and alternative explanation may lie in inhibition of the photoexcitation route because of tremendous differential solvation of the cluster states. The NaI ground ionic state is stabilized by polar solvent molecules to a much greater extent than the excited state in the Franck-Condon region, which is covalent. As the ion pair is increasingly solvated by solvent molecules, the NaI Franck-Condon energy gap

may increase to an extent that would render the laser wavelength inadequate for photoexcitation. This inhibition of photoexcitation might be less pronounced in water clusters, not only because of weaker ion-solvent interactions, but also because of their characteristic surface solvation structures. Addition of solvent molecules on one cluster side, remotely from the ion pair, could result in moderate additional stabilization of the ion pair and, in fact, very little change in the differential solvation energy of the ionic (ground) and covalent (excited) states (since water molecules tend to interact with each other rather than with NaI). Thus, in water clusters, it is conceivable that the excited state remains accessible for larger cluster sizes, consistent with the large product clusters observed in $\text{NaI}(\text{H}_2\text{O})_n$ multi-photon ionization experiments. Accordingly, we turn our attention to the photochemical properties of NaI ion pairs in water, acetonitrile and ammonia clusters.

The outline of this article is as follows. The computational methodology is presented in Section 6.2. Results are presented and discussed in Section 6.3. Concluding remarks follow in Section 6.4

6.2 Computational Methodology

6.2.1 QM/MM Molecular Dynamics Simulations

Distributions of Franck-Condon energy gaps are obtained for canonical ensembles of ground-state cluster structures generated by constant-temperature molecular dynamics (MD) simulations. Nosé-Hoover MD simulations,^{141,142} thermostated at 200 K with a modified version of the velocity Verlet algorithm,¹⁴³ were used to that effect. A quantum mechanics-molecular mechanics (QM/MM) model is adopted to describe intermolecular

interactions in $\text{NaI}(\text{H}_2\text{O})_n$ clusters, in which the NaI solute electronic structure is obtained from semiempirical valence-bond theory, as described in great detail in previous work,²⁰⁵ and polarizable model potentials are employed to describe the solvent-solvent and solute-solvent interactions, following our previous work for water,⁹⁷ ammonia⁷⁸ and acetonitrile⁷⁹ clusters.

Briefly, a semiempirical valence bond (VB) approach is used to calculate the Hamiltonian matrix elements of the diabatic, constant-charge character, ionic Na^+I^- and covalent NaI states. Only two electrons are treated explicitly, while the contribution due to the remaining electrons is embedded in a core-core potential, and the charge-localized VB states are expressed as the normalized Slater determinants $\Phi_1 = N_1 |\bar{X}X|$ and $\Phi_2 = N_2 (|\bar{M}X| - |MX\bar{M}|)$ for the ionic and covalent states, respectively, where the core electrons have been omitted, X represents the iodine valence p orbital lying along the bond axis, and M represents the sodium valence s orbital. All electron integrals are evaluated under the point-charge, Pariser and Mulliken approximations,¹⁸⁰ resulting in analytical expressions for all diabatic matrix elements:

$$H_{11}^0(R) = \langle \Phi_1 | \hat{H}^0 | \Phi_1 \rangle = H^{cc}(R) - IP(X) - EA(X) - \frac{2 \cdot e^2}{R} \quad (6.1)$$

$$H_{22}^0(R) = \langle \Phi_2 | \hat{H}^0 | \Phi_2 \rangle = \frac{1}{2[1 + S_{MX}^2(R)]} \left\{ H^{cc}(R) - 2IP(X) - 2IP(M) - \frac{2 \cdot e^2}{R} \right\} \\ - \frac{S_{MX}^2(R)}{1 + S_{MX}^2(R)} \{ 3IP(X) + 3IP(M) + EA(X) + EA(M) \\ + \frac{2 \cdot e^2}{R} + 2\rho(X) + 2\rho(M) \} \quad (6.2)$$

with the electronic coupling

$$\begin{aligned}
H_{12}^0(R) &= \langle \Phi_1 | \hat{H}^0 | \Phi_2 \rangle \\
&= \frac{S_{MX}(R)}{\sqrt{2[1 + S_{MX}^2(R)]}} \left\{ 2H^{cc}(R) - 2IP(X) - IP(M) - EA(X) \right. \\
&\quad \left. - \frac{2 \cdot e^2}{R} - \frac{1}{2}\rho(X) - \frac{1}{2}\rho(M) \right\} \quad (6.3)
\end{aligned}$$

while the diabatic state overlap is

$$S_{12}(R) = \langle \Phi_1 | \Phi_2 \rangle = \frac{S_{MX}(R)}{\sqrt{2[1 + S_{MX}^2(R)]}}, \quad (6.4)$$

where R is the NaI internuclear separation, IP and EA are the ionization potential and electron affinity, $\rho(\chi)$ is a one-electron integral of the form $\langle \chi | 1/r | \chi \rangle$ and S_{MX} is the overlap between the metal s and halogen p orbital. The 5p Slater orbital with exponent $\xi=1.9$ and the 3s Slater orbital with exponent $\xi=0.7333$ are used here for iodine and sodium, respectively.^{181,182} The ionization potentials for sodium and iodine are 5.14 and 10.45 eV, respectively, while the electron affinity of sodium and iodine is 0.55 and 3.06 eV, respectively.¹²⁶ The core-core potentials are chosen for both VB states to reproduce experimental gas-phase NaI Franck-Condon (FC) energies and NaI potential curves predicted by high-level ab initio calculations.²⁰⁵

$$H_{11}^{cc}(R) = IP(X) + IP(M) + \left[A_{ion} + \left(\frac{B_{ion}}{R} \right)^8 \right] e^{-R/R_{ion}} + \frac{e^2}{R} + E_{vdw/pol}(R) \quad (6.5)$$

where the van der Waals attraction and polarization energy term is expressed as

$$E_{vdw/pol}(R) = -\frac{C_{vdw}}{R^6} - \frac{(\alpha_{M^+} + \alpha_{X^-}) \cdot e^2}{2R^4} - \frac{(2\alpha_{M^+}\alpha_{X^-}) \cdot e^2}{R^7} \quad (6.6)$$

with $A_{ion} = 2760$ eV, $B_{ion} = 2.398$ eV^{1/8}Å, $R_{ion} = 0.3489$ Å, $C_{vdw} = 11.3$ eV·Å⁶, $\alpha_{M^+} = 0.408$ Å³ and $\alpha_{X^-} = 6.431$ Å³,^{162,185} and

$$H_{22}^{cc}(R) = IP(X) + IP(M) + A_{cov} e^{-B_{cov}(R-R_{cov})} \quad (6.7)$$

where $A_{cov} = 0.8$ eV, $B_{cov} = 2.5$ Å⁻¹ and $R_{cov} = 2.65$ Å. Adiabatic ground and excited-state energies are then simply obtained by diagonalizing the Hamiltonian matrix in the VB (diabatic) state basis.

Solute-solvent and solvent-solvent interactions are described by model potentials. Because of the large diabatic state energy gap, the ionic and covalent states are only weakly coupled in the Franck-Condon region, which is indicative of the Born-Oppenheimer regime of solvation,⁶⁵ where the solvent electrons move much faster than the solute electrons. Accordingly, the solvent effectively “feels” charge-localized solute charge distributions, and the instantaneous solute-solvent (and solvent-solvent) energy for each solute VB state V_{ii} is computed and incorporated in the individual Hamiltonian matrix elements, before solving for adiabatic energies

$$H_{ii}(\mathbf{R}, \mathbf{r}) = H_{ii}^0(\mathbf{R}) + V_{ii}(\mathbf{R}, \mathbf{r}); \quad V_{ii} = V_{ii}^{Coul} + V_{ii}^{pol} + V_{ii}^{rep-disp} \quad (6.8)$$

where H_{ii}^0 is the isolated NaI diagonal Hamiltonian matrix element for state i (1=ionic, 2=covalent), \mathbf{R} represents the NaI solute coordinates and \mathbf{r} the solvent coordinates, V_{ii}^{Coul} is the Coulombic interaction energy between the solute and solvent charge distributions, V_{ii}^{pol} is the solvent polarization energy and $V_{ii}^{rep-disp}$ is the solute-solvent (and solvent-solvent) repulsion-dispersion energy. For simplicity, the solvent-solvent interaction energy, which is the same for both VB states, is embedded into the solute-solvent interaction term. The Coulombic energy V_{ii}^{Coul} is then given by

$$V_{ii}^{Coul}(\mathbf{R}, \mathbf{r}) = \sum_{k=1}^n \sum_{S=H,M} \frac{q_{Na}^i \cdot q_S^k}{|\mathbf{R}_{Na} - \mathbf{r}_S^k|} + \frac{q_I^i \cdot q_S^k}{|\mathbf{R}_I - \mathbf{r}_S^k|} + \sum_{k < k'} \sum_{S, S'=H,M} \frac{q_S^k \cdot q_{S'}^{k'}}{|\mathbf{r}_S^k - \mathbf{r}_{S'}^{k'}|} \quad (6.9)$$

where q_{Na}^i and q_I^i are the solute point charges associated with VB state i at position and \mathbf{R}_{Na} and \mathbf{R}_I , respectively, and q_S^k are the point charges associated with sites \mathbf{r}_S^k of the k^{th} solvent molecule. The solvent polarization energy V_{ii}^{pol} (which includes both polarization by the solute charge distribution and by other solvent molecules) is obtained as

$$V_{ii}^{pol}(\mathbf{R}, \mathbf{r}) = -\frac{1}{2} \sum_k \boldsymbol{\mu}_k^i \cdot \mathbf{E}_k^{0,i} \quad (6.10)$$

where $\boldsymbol{\mu}_{i,k}$ represents the set of induced dipoles on each solvent molecule and $\mathbf{E}_{i,k}^0$ the electrostatic field due to all permanent charges, including those of the solute for VB state i , at the induced dipole site \mathbf{r}_α^k ,

$$\mathbf{E}_k^{0,i} = q_{Na}^i \frac{(\mathbf{r}_{Na} - \mathbf{r}_\alpha^k)}{|\mathbf{r}_{Na} - \mathbf{r}_\alpha^k|^3} + q_I^i \frac{(\mathbf{r}_I - \mathbf{r}_\alpha^k)}{|\mathbf{r}_I - \mathbf{r}_\alpha^k|^3} + \sum_{l \neq k} \sum_{S=H,M} q_S^l \frac{(\mathbf{r}_S^l - \mathbf{r}_\alpha^k)}{|\mathbf{r}_S^l - \mathbf{r}_\alpha^k|^3} \quad (6.11)$$

The induced dipoles $\boldsymbol{\mu}_k^i$ are evaluated as a linear response to the total electric field

$$\boldsymbol{\mu}_k^i = \alpha \cdot \mathbf{E}_k^i = \alpha \cdot [\mathbf{E}_k^{0,i} + \sum_{l \neq k} \mathbf{T}_{kl} \cdot \boldsymbol{\mu}_l^i] \quad (6.12)$$

where α is the solvent polarizability and \mathbf{T} the dipole tensor.¹²⁶ The self-consistent induced-dipole problem, Eq. (6.12), is solved in matrix form by LU decomposition and backsubstitution.¹²⁵ The short-range repulsion-dispersion interaction energy is modeled by a sum of modified, generalized Lennard-Jones potentials over all repulsion-dispersion sites (the ions/atoms and the solvent sites) separated by a distance r_{kl}

$$V_{ii}^{rep-disp} = \left(\sum_{k,l} \frac{A_{kl}^i}{r_{kl}^{12}} + \frac{B_{kl}^i}{r_{kl}^8} + \frac{C_{kl}^i}{r_{kl}^6} \right) (1 + D_{kl}^i \cos E_{kl}^i \varphi) \quad (6.13)$$

The last term in Eq. (6.13) adds directionality to the potential and was found in some cases necessary to account for hydrogen bonding between halide ions and solvent molecules; φ in Eq. (6.13) is the angle between an halide ion, a solvent hydrogen atom and a given solvent donor atom. Finally, the solute-solvent contribution to the off-diagonal Hamiltonian matrix element is simply evaluated with the Mulliken approximation¹⁸³

$$H_{ij}(R, r) = H_{ij}^0(R) + \frac{S_{ij}}{2} \{V_{ii}(R, r) + V_{jj}(R, r)\} \quad (6.14)$$

where S_{ij} is the off-diagonal element of the VB state overlap matrix.

The NaI partial point-charge distributions q_{Na}^i and q_I^i of both VB states, required to compute the solute-solvent interaction potential, are extracted from high-level *ab initio* calculations of the gas-phase dipole moments for the first two NaI adiabatic states.¹⁶⁵ We note for future discussion that gas-phase excited-state NaI has a reversed polarity to that of the ground ionic Na^+I^- state in the Franck-Condon region, and as a result, when polar solvent molecules stabilize the (ionic) NaI ground state, they tend to destabilize the NaI excited state (with reversed NaI polarity).

All solvent models, referred to in previous work as OPCS for optimized potentials for cluster simulations,⁶² employ a rigid water molecule with experimental gas-phase geometry. For water, both of the hydrogen atoms carry a fractional charge, while two M sites located on the bisector of the H-O-H angle but off the water plane carry a charge of opposite sign. The oxygen atom carries one polarizable site and one repulsion-dispersion

(Lennard-Jones) site. The model potential also includes H-H repulsion terms of the Born-Mayer form.²¹¹ The acetonitrile model employs point charges and repulsion-dispersion sites on all atoms, and a distributed molecular polarizability on the N, C, and methyl C (C_M) atoms. As for ammonia, the hydrogen atoms each bear a positive charge and the compensating negative charge is placed at a site M situated down the C_3 molecular axis from the nitrogen atom. The nitrogen atom carries a polarizable site and all atoms carry a repulsion-dispersion site. For all model potentials, some parameters were derived from available experimental data and the remaining (repulsion-dispersion) parameters were fitted to small pure solvent, ion-solvent and atom-solvent cluster data obtained from ab initio calculations. While extensive experimental and theoretical pure solvent and ionic cluster data has been reported earlier, little is known about atom-solvent complexes. The structure and binding energies of atom-solvent complexes, which serve as the basis for parameterization of the Lennard-Jones potentials, were then evaluated with MP2/6-311+G and are listed in Table 6.1. All model potential parameters are collected in Table 6.2.

We note that these model potentials allow the ion pair and solvent molecules to polarize each other in *both* the NaI ground and excited states. Not only are solvent molecules allowed to polarize each other, but the solute charge distribution (which enters the V_{ii}^{pol} term) is also allowed to polarize solvent molecules. In turn, solvent molecules also polarize the solute electronic structure by affecting the composition of the ground and excited adiabatic states in the VB state basis.

Table 6.1 Properties of atom-solvent binary complexes^a

	Geometry	D_0	
Na(H ₂ O)	C _{2v} ^b	5.3	$r_{\text{Na-O}} = 2.4 \text{ \AA}$
I(H ₂ O)	C _{2v} ^c	0.9	$R_{\text{I-O}} = 4.0 \text{ \AA}$
Na(NH ₃)	C _{3v} ^b	6.5	$r_{\text{Na-N}} = 2.5 \text{ \AA}$
I(NH ₃)	C _{3v} ^c	0.2	$R_{\text{I-N}} = 3.7 \text{ \AA}$
Na(CH ₃ CN)	C _{3v} ^b	4.0	$r_{\text{Na-N}} = 2.5 \text{ \AA}$
I(CH ₃ CN)	C _{3v} ^c	0.9	$R_{\text{I-C}_M} = 4.2 \text{ \AA}$

a. Obtained with MP2/aug-ccPVTZ. D_0 is the complex binding energies in kcal/mol.

b. The solvent most electronegative atom points towards the atom.

c. The solvent hydrogen atoms point to the atom.

6.2.2 Model Quantum Chemistry Calculations

The distributions of Franck-Condon energy gaps were also calculated for the ensembles of cluster structures generated by ground-state MD simulations with quantum chemistry. The size of the large clusters obviously precludes the straightforward use of high-level ab initio calculations for large ensembles of cluster structures. The solvent molecules are thus represented by a point-charge distribution in the electronic structure calculation. The point charge distribution for each solvent molecule is extracted from the total molecular dipole moment (i.e. the sum of the permanent and induced dipole moment) of the solvent molecule predicted by the model potentials for a given cluster configuration. For water and ammonia, a distribution of 4 charges (on the same sites as those of the model potentials) is calculated exactly from the three components of the molecular dipole moment vector under the constraint of overall charge neutrality, while for acetonitrile, the 6 charges on the atomic sites are evaluated by fitting the three

components of the molecular dipole moment vector with a nonlinear least-squares fit algorithm,¹²⁵ also under the constraint of overall charge neutrality.

We note that the calculation of the cluster electronic states with this approach only takes into account the ground-state polarization of the solvent molecules, and therefore neglects possible solvent electronic polarization in the excited state. However, this choice of model, where solvent effects are taken into account in the calculation of the NaI electronic states only via the electric field generated by the solvent molecules, precludes any charge-transfer-to-solvent process. This allows to unambiguously characterize the CIP Franck-Condon energy gaps for various cluster sizes and types, and thus, to completely untangle the roles of charge separation and differential solvation on the photochemical properties of NaI ion pairs in clusters. We also note that these model quantum chemistry calculations allow evaluation of the oscillator strength for the NaI electronic transition in the solvent environment. A weakness of the semiempirical VB theory approach outlined in the previous section lies in its inability to describe quantitatively the transition dipole because of the small, minimum basis set approximation.²¹²

The model chemistry employed is Configuration Interaction with Singles excitation (CIS) with a 6-31+G basis set for all the atoms for the electronic transition from the ground NaI state to the third Σ excited state, which is the first optically accessible excited state. The model was validated by comparing the results of gas-phase NaI calculations with available experimental data and small cluster calculated data (cf. Table 2)

Table 6.2 Model potential parameters^a

NaI						
	Na ⁺	I				
q _i	1.0	-1.0				
α _i	0.2	7.0				
H ₂ O						
	R _{O-H}	R _{O-M} ^b	θ _{H₂O-M} ^b	θ _{HOH}		
	0.957	0.342	± 43.4	104.52		
	H	M	O			
q _i	0.57	-0.57	-			
α _i	-	-	1.45			
	O-O	Na ⁺ -O	I-O			H-H ^c
A	1152920	137540	31811095	A'		100000
C	-1075	-150	-10400	B'		5.5
	Na-O		I-O			
A	226515		17907960			
C	-2200		-8120			
NH ₃						
	R _{N-H}	R _{H-H}	R _{N-M} ^b	θ _{HNH}		
	1.012	1.625	0.180	112.07		
	H	M	N			
q _i	0.56	-1.68	-			
α _i	-	-	2.22			
	N-N	Na ⁺ -N	Na ⁺ -H	I-N	I-H	
A	2676713	11200	40800	29126500	149750	
B	0	23000	-4100	63400	-1000	
C	-127	-1650	-50	-11800	-500	
	Na-N		I-N			
A	387810		1247130			
C	-3180		-990			
CH ₃ CN						
	r _{C_M-H}	r _{C_M-C}	r _{C-N}	θ _{H-C-H}		
	1.089	1.46	1.17	109.80		
	N	C	C _M	H		
q _i	-0.49	0.48	-0.56	0.19		
α _i	0.91	1.56	1.99			

	N-N	N-C	N-H	C-C	C-H	H-H
A	6410	1271400	72850	2100	37800	1
C	-35	-930	-160	-20	-115	-1
	Na ⁺ -N	Na ⁺ -C	Na ⁺ -H	I-N	I-C	I-H
A	73180	812500	39100	44536700	14432900	1085300
B	7700	-4800	660	76200	-56700	1450
C	-1050	-1425	-940	-10	-5	-460
D	0	0	0	0	0	0.60
E	0	0	0	0	0	2.01
	Na-N	I-C _M				
A	286170	23152940				
C	-2130	-9050				

a. Parameters not listed are zero. Distances are in Å, angles in degrees, point charges (q_i) in fractions of e , polarizabilities (α_i) in Å³, A in kcal.Å¹², B in kcal.Å⁸, C in kcal.Å⁶, and E in inverse degrees. D is unitless.

b. M is generally located along the molecular symmetry axis, towards the hydrogen atoms. For water, there are two M sites off the water plane by an angle $\theta_{\text{H}_2\text{O-M}}$.

c. Repulsive potential of the Born-Mayer form $A'e^{-B'r}$, with A' in kcal/mol and B' in Å⁻¹.

6.3 Results and Discussion

The OPCS distributions of Franck-Condon energy gaps are shown in Fig. 6.1 for all 3 solvents as a function of cluster size. Not surprisingly, the Franck-Condon energy gap distributions are shifted to larger values as a function of cluster size, as the ion pair ground state is increasingly stabilized by solvent molecules. The average shifts in the Franck-Condon energy gaps, shown in Fig. 6.2, relative to bare NaI are much more revealing. The average shifts in the Franck-Condon energies are larger for water than for ammonia at all cluster sizes, while those for acetonitrile tend to be much smaller and not to vary much with cluster size. We note, as observed earlier in Chapter 5, that the average OPCS Franck-Condon energy gaps for water are in reasonable agreement with experimental data.⁶⁸ In general, all average shifts of the Franck-Condon energy gaps

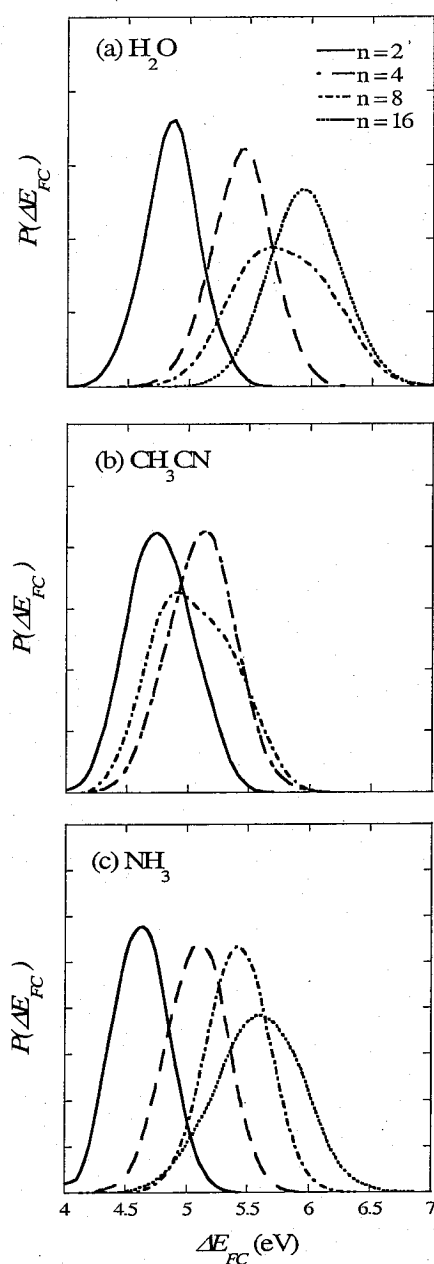


Figure 6.1 Franck-Condon energy gap distributions $P(\Delta E_{FC})$ as a function of cluster size (left panel) for (a) H_2O , (b) CH_3CN and (c) NH_3 , obtained with OPCS

seem to plateau around cluster size 16. Based on these results, the solvent-selective behavior of NaI multiphoton ionization can definitely not be ascribed to different extents of differential solvation which would render the laser wavelength

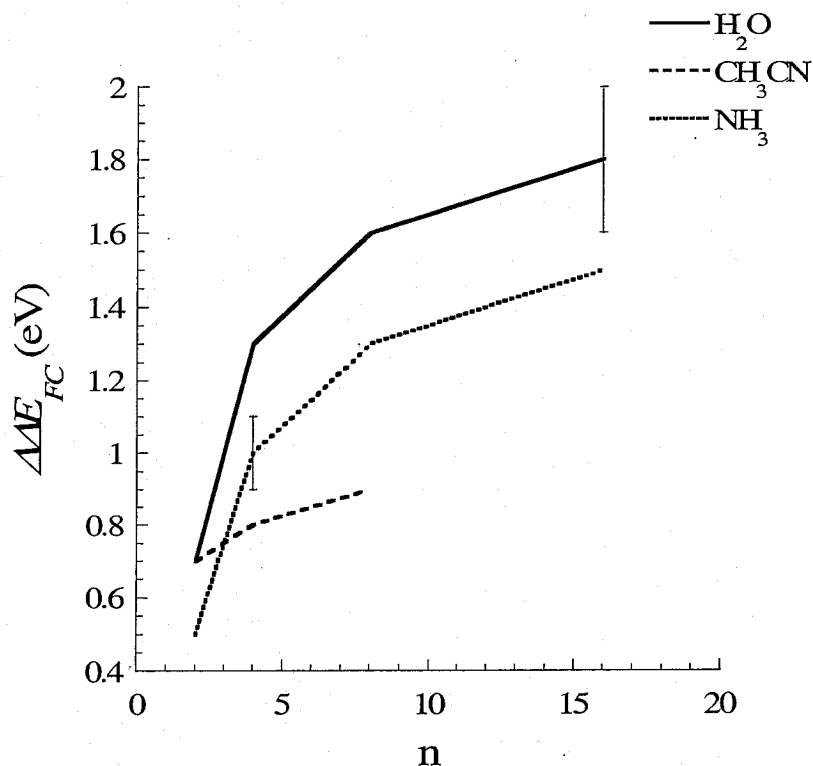


Figure 6.2 Shift in the average Franck-Condon energy gaps relative to bare NaI ΔE_{FC} as a function of cluster size, obtained with OPCS.

inadequate for photoexcitation, because, within the exact same methodology, water is predicted to possess the largest Franck-Condon energy gaps of all solvents, and yet it is the solvent for which the largest products of multi-photon ionization are observed.

We now turn our attention to the Franck-Condon energy gaps predicted by model quantum chemistry calculations, in which the solvent molecules are represented by frozen point charge distributions. One advantage of this approach is that it allows the calculation, not only of the Franck-Condon energy gaps, but also of oscillator strengths. Both distributions are displayed in Fig. 6.3 for all 3 solvents as a function of cluster size. Again, the average shifts of the Franck-Condon energy gaps and average oscillator

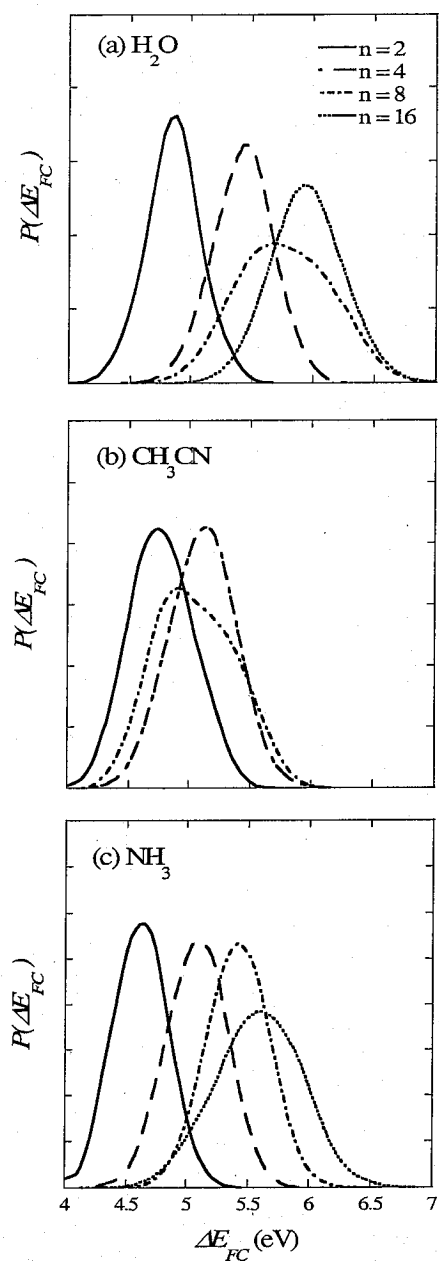


Figure 6.3 OPCS Franck-Condon energy gap distributions $P(\Delta E_{FC})$ as a function of cluster size (left panel) for (a) H_2O , (d) CH_3CN and (e) NH_3

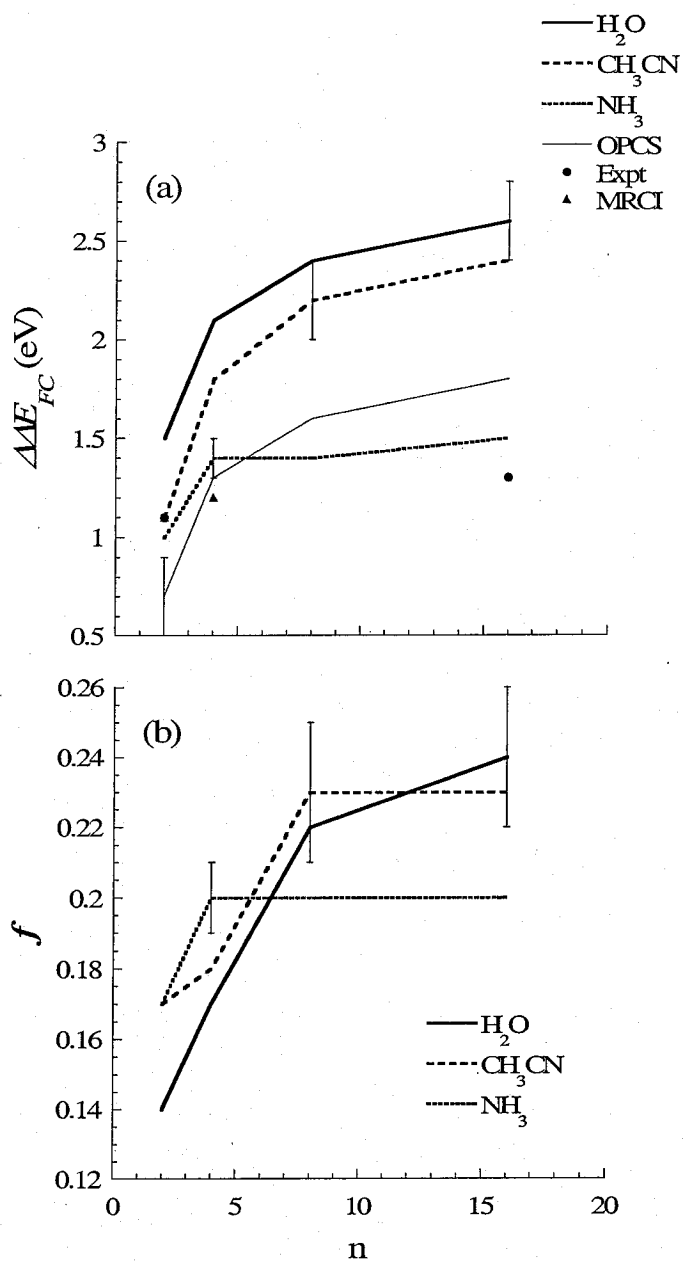


Figure 6.4 Shift in the average Franck-Condon energy gaps relative to bare NaI ΔE_{FC} as a function of cluster size (Fig. 6.2a), and variation of the oscillator strength f as a function of cluster size (Fig. 6.2b).

strengths, shown in Fig 6.4, are much more informative. The average shifts of the Franck-Condon gaps are still largest for water, but are closely paralleled by those for acetonitrile, while those for ammonia do not seem to vary after cluster size 4. All shifts seem to plateau around cluster size 16. The average oscillator strengths are similar for all 3 solvents and tend to increase as a function of cluster size, suggesting slightly more efficient absorption for large clusters.

The average Franck-Condon energy gaps predicted by model quantum chemistry calculations are significantly overestimated, compared to experimental data for water and compared to the OPCS data. This can be attributed to the frozen point charge distribution that is used to represent the solvent molecules. In contrast, with OPCS, the solvent molecules are allowed to polarize in response to the solvent environment, both in the ground and excited states. This generally results in smaller Franck-Condon energy gaps. For the model quantum chemistry calculations, very much like previous calculations with the nonpolarizable OPLS model, Franck-Condon energy gaps are much larger because of the combined stabilization of the (ionic) ground state and destabilization of the (covalent) excited state.

One could ascribe the fact that Franck-Condon energy gaps plateau rapidly for water clusters to the surface solvation structure of $\text{NaI}(\text{H}_2\text{O})_n$ clusters.⁶² Iodide adopts a surface solvation structure up to quite large cluster sizes, $n > 60$,¹²² and it was found that iodide drags sodium to the surface of the water cluster,⁶² such that the NaI molecule resides near the surface of the cluster. Therefore, the addition of water molecules occurs on the opposite side of the NaI moiety. As such, the addition of more water molecules, beyond a certain cluster size, will occur far away from NaI, such that its electronic

structure will no longer be affected. However, the fact that the Franck-Condon energy gaps seem to reach a plateau cannot really be ascribed to the peculiar surface solvation structure of ion pairs in water clusters, since this also happens for other solvents, for which ion pairs are known to adopt well-defined interior solvation structures.⁷⁹ Thus, apparently, regardless of the solvation structure, around cluster size 16, solvent molecules accumulate far from the ion pair, whether it is because of surface solvation for water, or completion of solvation shells for the other solvents, causing marginal changes in the differential solvation of the ground (ionic) and excited (covalent) states.

Overall, there seems to be no correlation between the average Franck-Condon energy gaps (and oscillator strengths) and solvent properties such as solvent polarity, dielectric constant, hydrogen-bonding strength, or preferential solvation structure. As mentioned earlier, water favors surface solvation structures and the other two solvent interior solvation structures. Water is much more polar than acetonitrile and ammonia. Acetonitrile has a much larger dipole moment than both ammonia and water, and tends to form much weaker hydrogen bonds than water and ammonia; as a matter of fact acetonitrile self-interactions are mainly dipole-dipole interactions, whereas water and ammonia typically form hydrogen bonded networks. Yet, ion pairs in all 3 solvents tend to have similar oscillator strengths.

The calculated Franck-Condon energies and similar oscillator strengths reported here cannot explain the solvent-selective behavior of NaI multiphoton ionization in clusters by different extents of differential solvation which would render the laser wavelength inadequate for photoexcitation for some solvents and not others. It should be noted that CIS calculations, and OPCS to a minor extent, predict Frank-Condon energy

shifts larger than those predicted by Multi-Reference Configuration Interaction calculations in which the solvent is considered explicitly in the quantum chemistry calculation.²⁰⁵ The high-level *ab initio* calculations predict a shift of 1.1 eV for NaI(H₂O)₂, and 1.3 eV for NaI(H₂O)₄, which agree well with experimental data.⁶⁸ This is due to the fact the solute-solvent and solvent-solvent polarization effects are not taken into account in our simple point charge representation of the solvent charge distribution in CIS calculations. Nonetheless, high-level *ab initio* calculations are hardly feasible for large ensemble of cluster structures and large cluster sizes, and the trends reported here for all 3 solvents can be used for relative comparison as they are obtained within the exact same computational approach.

6.4 Concluding Remarks

This Chapter focused on the photoexcitation of NaI in water, ammonia and acetonitrile clusters, in an attempt to explain the solvent-selective behavior of NaI multi-photon excitation in clusters observed experimentally. Franck-Condon energy gaps and oscillator strengths, calculated with two different methods for thermal ensembles of cluster structures, are similar for all seeded solvent clusters, suggesting very similar photochemical behavior. There is obviously much more to characterizing multi-photon ionization processes than simple inspection of ground to first excited state Franck-Condon energy gaps and oscillator strengths. For instance, multi-photon ionization involves resonant states and photon absorption depends on Franck-Condon factors, both features that are beyond straightforward computational reach and were not considered in this investigation. The Franck-Condon gaps from the excited to ionized state were not considered either, primarily because we believe that solvent effects will be more

pronounced for the first electronic transition. Overall, the zero-th order picture painted by the present simulations suggests similar features for photoexcitation of the ion pair in all solvent clusters.

To our knowledge, investigations of Franck-Condon energies or oscillator strengths are usually performed for ground-state minimum energy structures, and this is the first calculation of photochemical properties based on thermal ensembles of species. This approach is rendered necessary by the fluxional character of the clusters of interest, but precludes the use of high-level quantum chemistry methods to evaluate the ground and excited state properties of the clusters.

As mentioned earlier, ground-state charge separation within the cluster can be ruled out as possible explanations for the differences observed in the outcome of the multi-photon ionization experiments with different solvents, since ground-state charge separation occurs earlier for water than for the other two solvents. Since the present work also seems to rule out differential solvation arguments as a possible reason for the solvent-selective behavior, alternative explanations must be sought. The disappearance of the multi-photon ionization product signal at small cluster size, compared to water, could then be attributed to the predominance of photoexcitation to a charge-transfer-to-solvent (CTTS) state for acetonitrile clusters, and to the instability of large ground-state clusters with respect to evaporation for ammonia clusters.

As demonstrated for $\text{NaI}(\text{H}_2\text{O})_n$ clusters in Chapters 4 and 5, however, massive solvent evaporation could also occur on the excited states, and future work will involve simulations of the dynamics post-multi-photon ionization, i.e. on the ionized state to investigate possible differences in the solvent evaporation dynamics between water on

one hand, and ammonia and acetonitrile on the other. Again, because of the surface solvation structure of $\text{NaI}(\text{H}_2\text{O})_n$ clusters, it is conceivable that the ionized state dissociation to produce $\text{Na}^+(\text{H}_2\text{O})_p$ cluster products occurs more readily, with little solvent reorganization, because iodine sits at the surface of the cluster, therefore allowing larger cluster products to survive than in the case of acetonitrile and ammonia clusters, for which dissociation of interior ionized species may cause the whole cluster to blow up. This hypothesis will be explored further.

Theoretical Studies of Seeded Water Clusters: Structure,
Thermodynamics and Photochemistry

Chapter 7

Outlook and Future Directions

7.1 Solvation Thermodynamics from First Principles

7.1.1 Introduction

In our previous investigation of the structural properties and thermodynamics of halide-water clusters, two classical model potentials were employed, the Optimized Parameters for Liquid Simulations (OPLS) and the Optimized Potentials for Cluster Simulations (OPCS), to generate potentials of mean force (PMF) along the ion-water center-of-mass distance r_{cm} coordinate. Our simulations revealed that subtle polarization effects and the precise shape of the charge distribution of the water model significantly affect the solvation structure and thermodynamics of halide-water clusters. The entropic contribution to the free energy was concluded to govern the solvation thermodynamics, and therefore determine the most favored solvation structure adopted by the ions in the clusters. The induced polarization of water molecules, built in OPCS but not OPLS, was found essential in allowing for increased mobility and flexibility of the water molecules in the clusters. However, due to the simplicity of the model potentials and the discrepancies between the results with different models, it was concluded that a reliable and quantitative description of the solvation structure and thermodynamics of halide-water clusters would only be obtained by treating intermolecular interactions from first principles.

Various avenues were explored to obtain more accurate thermodynamics. Since the generation of PMFs requires evaluation of energies (and forces) for millions of structures, the use of “on the fly” *ab initio* quantum chemistry is prohibitively computationally expensive. Therefore, one must resort to employ approximate quantum chemistry methods “on the fly” to generate first-principles PMFs or design strategies that

greatly reduce the number of *ab initio* quantum chemistry calculations required to generate the PMFs. Accordingly, in the first part of this section, the use of semiempirical molecular orbital (MO) methods is explored to generate PMFs for halide-water clusters, while in the second part, methodologies are designed to allow refinement of PMFs generated from simulations with model potentials (or approximate quantum chemistry methods), making use of a limited number of high-level quantum chemistry calculations.

Semiempirical methods are readily applicable to large chemical systems at a relatively low computational cost, since they employ a series of approximations that greatly reduce the cost of solving the self-consistent field equations of MO theory. Semiempirical MO methods are based on three assumptions: (1) only valence electrons are treated explicitly, (2) minimum basis sets are used, and (3) some electron integrals are neglected while others are parameterized based on empirical data. Weak interactions such as hydrogen bonding, however, are often underestimated by semiempirical MO theory, due mainly to the small basis-set approach and the resulting lack of electronic polarization. Furthermore, halide-water clusters were not included in the training sets of molecules employed to parameterize the semiempirical Hamiltonians. For these reasons, various ways to improve available semiempirical MO methods for seeded water clusters in particular, and systems where weak interactions are essential in general, are also explored in the next section. Our efforts are concentrated on chloride-water clusters since chloride has an intermediate ionic radius and polarizability in the halide series.

7.1.2 PMFs Generated with Semiempirical Quantum Chemistry

7.1.2.1 Simulation Methodology

Semiempirical methods have been employed for theoretical studies of diverse problems due to their applicability to large chemical systems. The most frequently used methods, the Modified Neglect of Differential Overlap (MNDO), Austin Model 1 (AM1) and Parameter Model 3 (PM3) methods, are based on the Neglect of Differential Diatomic Overlap (NDDO) approximation. In a nutshell, the molecular wave function is expressed as a product of molecular orbitals constructed as a linear combination of atomic orbitals. Three- and four-center integrals are ignored, and the remaining one- and two-center terms depend on adjustable parameters. These parameters have been derived from experimental data such as bond lengths, heats of formation, and dipole moments for a set of small molecules. The $\text{Cl}^-(\text{H}_2\text{O})_n$ and $(\text{H}_2\text{O})_n$ 300K binding enthalpies from MNDO, AM1, PM3, high-level *ab initio* quantum chemistry calculations and experimental data are compared in Table 7.1. Obviously, the binding enthalpies obtained with MNDO are in gross disagreement with the results of high-level *ab initio* calculations,¹³⁰ which are found in excellent agreement with available experimental data, while those obtained with AM1 and PM3 are both in relatively good agreement with the *ab initio* data. Recently, Coe and co-workers have shown that AM1 does not predict the appropriate geometries for small water clusters.²¹³ As found in our previous investigations, properly describing the geometry of water clusters can be very important for determining the exact solvation structure of halides in water clusters, and PM3 was therefore selected to investigate the solvation thermodynamics and structural properties of halide-water clusters.

Table 7.1 $\text{Cl}^-(\text{H}_2\text{O})_n$ and $(\text{H}_2\text{O})_n$ 300K binding enthalpies (in kcal/mol) from MNDO, AM1, PM3, *ab initio* calculations and experimental data

	MNDO	AM1	PM3	<i>ab initio</i> ^a	Expt. ^b
$\text{Cl}^-(\text{H}_2\text{O})$	7.5	13.8	17.3	14.4	14.4
$\text{Cl}^-(\text{H}_2\text{O})_2$	14.8	28.1	32.0	27.4	25.8
$\text{Cl}^-(\text{H}_2\text{O})_3$	20.9	42.2	43.0	40.7	40.7
$(\text{H}_2\text{O})_2$	1.1	2.5	1.7	3.6	
$(\text{H}_2\text{O})_3$	22.2	10.2	8.7	9.4	

^a Halide-water cluster binding enthalpies obtained from Reference 130, and water cluster binding enthalpies from Reference 215. All *ab initio* enthalpies are calculated under the rigid rotor-harmonic oscillator approximation. ^b Average values from many experiments as available from the NIST Chemistry Webbook (<http://webbook.nist.gov/chemistry/>)

The Monte Carlo (MC) methodology with statistical perturbation theory that was employed in our investigation of iodide-water clusters (Chapter 3) was used here to generate PMFs for $\text{Cl}^-(\text{H}_2\text{O})_n$ clusters.²¹⁶ Semiempirical MO theory was also implemented within the molecular dynamics (MD) method employed in Chapter 4, but simulations with this approach are incomplete. The simulations explicitly include thermal effects within the canonical ensemble, and as such PM3 must be reparameterized so that it yields 0K binding enthalpies, rather than the 300K binding enthalpies normally obtained from semiempirical calculations. The semiempirical molecular orbital package Mopac7²¹⁷ was modified for this purpose, and a nonlinear least-squares fit algorithm¹²⁵ was used to reparameterize PM3 to reproduce the 0K binding enthalpies predicted by high-level *ab initio* calculations, and the minimum energy structures obtained from *ab initio* calculations performed with the Gaussian98²¹⁸ suite of programs using Moller-Plesset 2nd order perturbation theory with an augmented triple zeta correlation-consistent

basis set (MP2/aug-cc-pVTZ). The new set of parameters is referred to as PM3spc, for PM3 with specific parameters for classical simulations, as listed in Table 7.2. As shown in Table 7.3, the 0K binding enthalpies with PM3spc are in very good agreement with the results of high-level *ab initio* calculations. We have therefore employed PM3spc to generate the PMFs for $\text{Cl}^-(\text{H}_2\text{O})_{20}$ clusters, as now discussed.

Table 7.2 PM3 and PM3spc parameters

Atom	Parameter ^a	PM3	PM3spc
H	U_{ss}	-13.073	-13.076
H	β_s	-5.627	-5.624
H	ζ_s	0.968	0.968
H	α	3.356	3.356
H	G_{ss}	14.794	14.792
H	b_{11}	1.129	1.129
H	b_{12}	-1.060	-1.060
H	b_{21}	5.096	5.096
H	b_{22}	6.004	6.005
H	b_{31}	1.537	1.538
H	b_{32}	1.570	1.570
O	U_{ss}	-86.993	-86.994
O	U_{pp}	-71.880	-71.877
O	β_s	-45.203	-45.201
O	β_p	-24.753	-24.752
O	ζ_s	3.797	3.797
O	ζ_p	2.389	2.389
O	α	3.217	3.217
O	G_{ss}	15.756	15.758
O	G_{sp}	10.621	10.643
O	G_{pp}	13.654	13.656
O	G_{P2}	12.406	12.407
O	H_{sp}	0.594	0.607
O	b_{11}	-1.131	-1.134
O	b_{12}	1.138	1.136
O	b_{21}	6.002	6.003
O	b_{22}	5.951	5.950
O	b_{31}	1.607	1.607
O	b_{32}	1.598	1.598
CL	U_{ss}	-100.627	-101.743
CL	U_{pp}	-53.614	-53.613
CL	β_s	-27.529	-27.038
CL	β_p	-11.594	-11.379
CL	ζ_s	2.246	2.281
CL	ζ_p	2.151	2.161

CL	α	2.517	2.512
CL	G_{SS}	16.014	13.551
CL	G_{SP}	8.048	8.048
CL	G_{PP}	7.522	7.513
CL	G_{P2}	7.504	7.504
CL	H_{SP}	3.481	3.482
CL	b_{11}	-0.172	-0.172
CL	b_{12}	-0.013	-0.013
CL	b_{21}	6.001	6.649
CL	b_{22}	1.967	2.179
CL	b_{31}	1.088	1.010
CL	b_{32}	2.293	2.264

^a U_{ii} are the i th atomic orbital one-electron one center integrals, β_{ii} are i th atomic orbital one-electron two-center integrals, ζ_i are the i th-type Slater atomic orbital exponent, α is the atom core-core repulsion term, G_{ii} are the i th-type atomic orbital one-center two-electron repulsion integral, H_{sp} is the s-p atomic orbital one-center two-electron exchange integral and b_{na} are Gaussian exponent multipliers for the n th Gaussian of atom a .

Table 7.3 $\text{Cl}^-(\text{H}_2\text{O})_n$ and $(\text{H}_2\text{O})_n$ 0K binding enthalpies (in kcal/mol) from PM3spc and *ab initio* calculations

	PM3spc	Ab initio ^a
$\text{Cl}^-(\text{H}_2\text{O})$	13.8	13.6
$\text{Cl}^-(\text{H}_2\text{O})_2$	25.8	25.7
$\text{Cl}^-(\text{H}_2\text{O})_3$	39.3	38.1
$(\text{H}_2\text{O})_2$	3.6	3.3
$(\text{H}_2\text{O})_3$	9.8	9.4

^a Halide-water cluster binding enthalpies were obtained from Reference 130, and the water cluster binding enthalpies from Reference 215.

7.1.2.2 Preliminary Results

The ion-water center-of-mass distance probability distributions $P(r_{cm})$, which are just the Boltzmann factor of the PMFs, obtained with OPLS, OPCS and PM3spc are compared in Fig. 7.1. The peak in $P(r_{cm})$ occurs at approximately 2.6 Å with PM3spc. The distribution of angles between the water molecules, the ion and the water cluster center of mass were not suggestive of either a surface or an interior solvation structure at

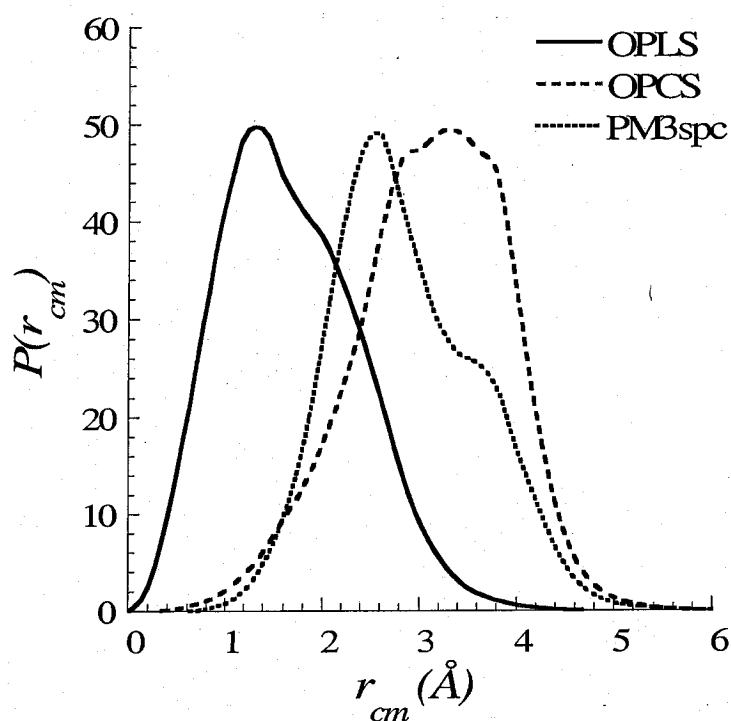


Figure 7.1 $\text{Cl}^-(\text{H}_2\text{O})_{20}$ ion-to-water center-of-mass distance probability distributions $P(r_{cm})$, generated with the OPLS (line) OPCS (dashed line) model potentials, and PM3spc (dotted line).

this r_{cm} value. Inspection of the configurations for that ensemble reveal that chloride is found just below the surface of the water cluster, as shown for a representative structure

in Fig. 7.2. The minimum energy structures for $\text{Cl}^-(\text{H}_2\text{O})_1$ and $\text{Cl}^-(\text{H}_2\text{O})_2$ generated with PM3spc predict a chloride-oxygen distance of 2.7 Å, which is 14% shorter than the distance of 3.1 Å obtained from high-level *ab initio* calculations.¹³⁰ Therefore, the water molecules tend to bind to the ion too closely, resulting in a solvation structure which is somewhat in between interior and surface solvation.

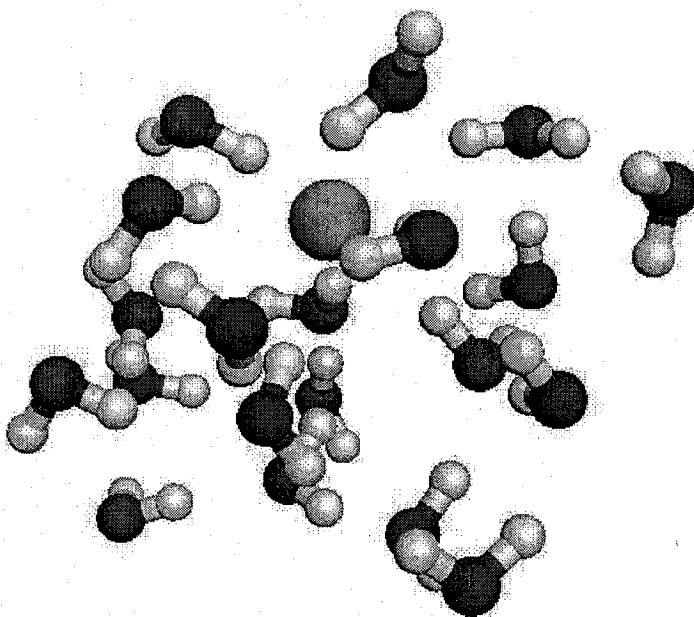


Figure 7.2 Representative $\text{Cl}^-(\text{H}_2\text{O})_{20}$ structure from the PM3spc ensemble of configurations at $r_{cm} = 2.6$ Å.

Due to this discrepancy of the chloride-oxygen distance predicted with PM3spc, PM3 does not seem to provide a good description of both the 0K binding enthalpies and the structure of small clusters, and thus does not produce reliable structural properties for larger halide-water clusters. It is well known that hydrogen bonding is not well described by NDDO methods,²¹⁹ because the nuclear-nuclear repulsion is represented by Gaussian functions which can lead to false minima along the internuclear distance coordinate.

Many functional forms have been proposed to improve the nuclear-nuclear repulsion of the NDDO methods,²¹⁹⁻²²² and we implemented many of these functional forms within Mopac7.²¹⁷ However, none of these proposed functional forms reproduce both the proper geometry and the 0K binding enthalpies for small chloride-water and water clusters. The nuclear-nuclear repulsion energy profile along the oxygen-chloride distance was generated with MP2/aug-cc-pTVZ calculations, and fit to an appropriate functional form. However, attempts to obtain a good set of parameters for the clusters failed, mostly due to the fact that a function could not be found that properly describes both the chloride-water and water-water interactions in larger clusters.

The difficulty in obtaining a proper description of the properties of chloride-water and water clusters is mainly due to the fact that semiempirical methods employ a minimal basis set, and the use of improved functional forms to model the nuclear-nuclear repulsion does not appear to be sufficient to describe subtle hydrogen bonding interactions. In another attempt, p-orbitals were added to the minimal 1s hydrogen basis set to better account for the electronic polarization involved in hydrogen bonding, but while this approach seemed to tremendously improve the description of water-water interactions, the description of the geometric features of chloride-water clusters deteriorated, presumably because of the resulting imbalance in the chloride and hydrogen basis sets and treatment of polarization. The next logical step to reduce this imbalance is to include d functions on the chloride and oxygen atoms in Mopac7, but this colossal task is left for future work. This will be worthwhile, given the renewed interest in semiempirical methods in the context of "on the fly" dynamics simulations, and the intense research in trying to improve semiempirical Hamiltonians for water clusters, and

systems involving weak interactions in general. At this point, however, semiempirical quantum chemistry methods in their present form are not accurate enough, due to the assumptions inherent in these methods, to properly describe hydrogen bonding, which is a key factor driving the solvation structure and thermodynamics of halide-water clusters.

7.1.3 *Ab initio* Refinements of Model Ion-Water Cluster PMFs

Other avenues to obtain a more quantitative and rigorous description of the solvation structure and thermodynamics of halide-water clusters were explored. In this section, we discuss a methodology where the PMFs generated with approximate models for describing intermolecular interactions are refined with more rigorous, but more computationally intensive, calculations of the interaction on a subset of structures using standard sampling techniques of statistical mechanics.^{135,223}

7.1.3.1 Simulation Methodology

A number of sampling techniques have been developed recently to refine PMFs generated with model potentials, making use of a limited number of single-point quantum chemistry calculations.²²⁴⁻²²⁹ Briefly, thermal ensembles of configurations are generated using either Monte Carlo (MC) or molecular dynamics (MD) simulations performed with model potentials V_m , and a first-principles PMF is calculated for a first-principles potential V_f from a sample of statistically independent configurations within the initial ensemble generated with the model potential. The model-based PMF can be refined with first-principles calculations by simple reweighting of the distribution of configurations.^{135,223} The ensemble average $\langle \rangle_f$ of any given property M of a given system, using a given (first-principles) potential V_f is

$$\langle M \rangle_f = \frac{\int M e^{-\beta V_f(X)} dX}{\int e^{-\beta V_f(X)} dX} \quad (7.1)$$

where $\beta = 1/k_B T$, k_B is the Boltzmann constant, T is the temperature, and X corresponds to the system coordinates. This ensemble average can be evaluated, based on an ensemble of configurations generated with another (model) potential V_m , by introducing $\Delta V = V_f - V_m$, so that

$$\langle M \rangle_f = \frac{\int M e^{-\beta \Delta V(X)} e^{-\beta V_m(X)} dX}{\int e^{-\beta \Delta V(X)} e^{-\beta V_m(X)} dX} \quad (7.2)$$

and the ensemble average becomes

$$\langle M \rangle_f = \frac{\langle M e^{-\beta \Delta V} \rangle_m}{\langle e^{-\beta \Delta V} \rangle_m} \quad (7.3)$$

where $\langle \rangle_m$ indicates an ensemble average from a simulation with V_m .

Different methods can be employed to evaluate the first-principles PMF, which mainly differ in the practical details of the implementation. Within the framework of statistical perturbation theory evaluation of free energy differences, described in Section 2.2, where M is the Boltzmann factor of energy differences between configuration at r_{cm} and $r_{cm} + \delta r_{cm}$, the first-principles PMF is

$$\Delta W_f(r_{cm}) = -k_B T \ln \frac{\langle e^{-\beta[V_f(r_{cm} + \delta r_{cm}) - V_f(r_{cm})]} e^{-\beta \Delta V} \rangle_m}{\langle e^{-\beta \Delta V} \rangle_m} \quad (7.4)$$

In practical terms, for every given point along the r_{cm} coordinate, a sample of the model-based ensemble of configurations is chosen and single-point quantum chemistry

calculations are performed in order to obtain first-principles $V_f(r_{cm} \pm \delta r_{cm})$ and $V_f(r_{cm})$, and ΔV for each configuration, and the average over the sample configurations is simply evaluated following Eq. (7.4). We note that this approach requires a model potential and a first-principles method that yield similar (or parallel) interaction energies in order to avoid convergence problems and numerical noise that may arise if ΔV is too large.

Doren and co-workers employed a slightly different scheme to adjust the model-based PMF based on similar arguments of statistical mechanics.²³⁰ In this method, the PMF is evaluated as

$$W_f(r_{cm}) = W_m(r_{cm}) - k_B T \ln \left\langle e^{-\beta \Delta V} \right\rangle_{r_{cm}} \quad (7.5)$$

such that the first-principles PMF is simply the refinement of the model PMF by a term involving the average of the Boltzmann-weighted energy difference between the model and the first-principles interaction energies over a sample of configurations. Again, this approach requires that the first-principles method and the model potential yield very similar interaction energies so that ΔV is small, very much like in standard free energy difference calculations.⁹⁸

More recently, Schofield and co-workers have developed a method where the first-principles PMF is evaluated as^{224,228}

$$\Delta W_f(r_{cm}) = -k_B T \ln \left\langle e^{-\beta [V_f(r_{cm} \pm \delta r_{cm}) - V_f(r_{cm})]} \right\rangle_f \quad (7.6)$$

which is the analog expression to that used to evaluate model-based PMFs, but the Metropolis algorithm is applied to a sample of model-based configurations on the first-principles potential energy surface. In other words, a model potential is used to drive the

generation of statistically very independent configurations, which are used as input for Monte Carlo Metropolis sampling with interaction energies calculated from first principles. Not surprisingly, it was shown that the more accurate the model potential, the faster the procedure converges, and the more efficient is the evaluation of the first-principles PMF.

7.1.3.2 Preliminary Results

We first benchmarked various quantum chemistry methods to obtain reliable chloride-water and water-water 0K binding enthalpies for small clusters. Since the first-principles refinement of the PMFs requires single-point energy calculations over hundreds of configurations, it is important to choose a combination of a level of theory and basis set that provides reliable energetics but is not too computationally intensive. Density functional theory (DFT) is usually appropriate for large systems or routine calculations, since it typically produces energetics comparable to high-level *ab initio* quantum chemistry methods, but at a much lower computational cost. The 0K binding energies calculated with the Gaussian 98 suite of programs²¹⁸ for small chloride-water and water clusters with a subset of the DFT functionals benchmarked are compared in Table 7.4. The water geometry was kept rigid in the geometry optimization since all structures generated with the model potentials involve rigid water molecules, fixed at the gas-phase geometry employed by the model potentials. Overall, the B3PW91/CEP-121+G* combination yields 0k binding enthalpies in very good agreement with those from high-level *ab initio* calculations, and is therefore employed to generate first-principles PMFs for chloride-water clusters.

Table 7.4 $\text{Cl}^-(\text{H}_2\text{O})_n$ and $(\text{H}_2\text{O})_n$ 0K binding enthalpies (in kcal/mol) from DFT and *ab initio* calculations^a

	B3LYP ^b	PBE0 ^c	B3PW91 ^d	<i>ab initio</i> ^e
$\text{Cl}-(\text{H}_2\text{O})$	13.7	14.6	13.6	13.6
$\text{Cl}-(\text{H}_2\text{O})_2$		27.8	25.3	25.8
$(\text{H}_2\text{O})_2$	3.7	4.2	3.2	3.6
$(\text{H}_2\text{O})_3$	12.1		10.1	9.4

^a Minimum energy structures with constrained O-H distances and H-O-H angle to the gas-phase water geometry. The Stephens/Basch/Krauss effective core potential triple-split basis, CEP-121+G*, was employed for all atoms. See Reference 231.

^b From Reference 232.

^c From Reference 233.

^d From Reference 234.

^e Halide-water cluster binding enthalpies were obtained from Reference 130, and the water cluster binding enthalpies from Reference 215.

The ion-to-water center-of-mass distance probability distributions for $\text{Cl}^-(\text{H}_2\text{O})_{12}$ are shown for OPLS, OPCS and B3PW91/CEP-121+G* in Fig. 7.3. A sample of 200 configurations was chosen from each ensemble of configurations along the r_{cm} coordinate generated with OPCS. Given our choice of model potential and first-principles method, we found that the first approach outlined in section 7.1.3.1. to evaluate first-principles PMFs was the most efficient, as the model seem to overestimate the interaction energy in large clusters, compared to first-principles calculations, but almost systematically, so that a constant energy difference can be removed in the calculation of ΔV . Accordingly, the first-principles PMFs were evaluated using eq. (7.4). We note that this approach simply implies application of statistical perturbation theory as in our model

simulations, but with a reweighting of the configurations to account for the fact that configurations were generated with an approximate model in the first place.

The DFT potential of mean force predicts interior solvation for $\text{Cl}^-(\text{H}_2\text{O})_{12}$, as obtained with OPLS. From the results discussed in Chapters 2 and 3, OPLS has a tendency to favor interior solvation over a wide range of cluster sizes where surface solvation would normally be expected. It is therefore surprising that the first-principles solvation would normally be expected. It is therefore surprising that the first-principles results also suggest interior solvation for chloride at such a small cluster size. This

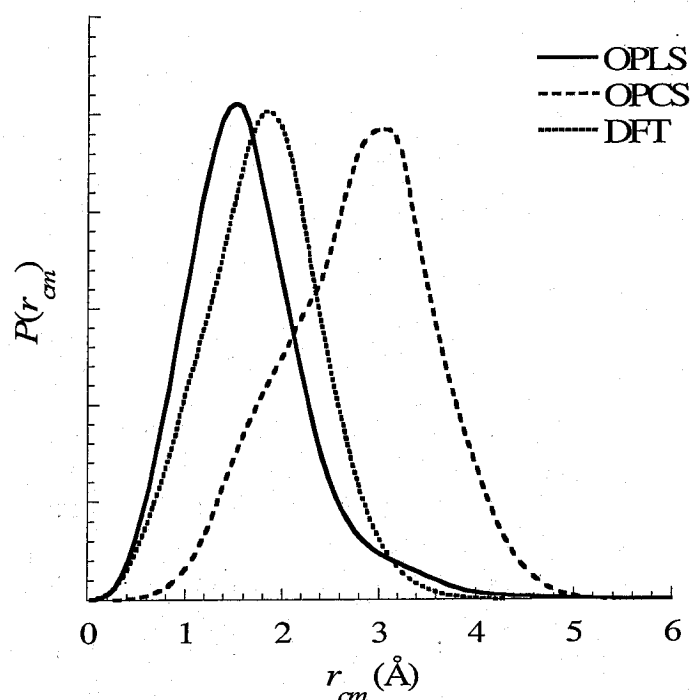


Figure 7.3 $\text{Cl}^-(\text{H}_2\text{O})_{12}$ ion-to-water center-of-mass distance probability distributions $P(r_{cm})$, generated with the OPLS (line) OPCS (dashed line) model potentials, and B3PW91/CEP-121+G* (dotted line). The first-principles PMF/distribution was evaluated from OPCS cluster configurations.

finding is even more surprising, considering that the PMF was evaluated from OPCS

configurations that predict a surface solvation structure. The chloride-oxygen internuclear distance predicted by OPCS is 3.23 Å, relative to 3.12 Å for B3PW91/CEP-121+G*. This implies that the DFT calculations are typically performed on structures where the water molecules are further away from the ion than what an actual DFT simulations would predict, and therefore hydrogen bonding to the ion will be underestimated. One would intuitively think that underestimating solute-solvent interactions would favor surface solvation structures, but the reweighting procedure apparently removes the bias. Since the competition between solute-solvent and solvent-solvent interactions plays a key role in the solvation structure of the ions, both the model potentials and first-principles methods chosen must reproduce the relative strengths of the interactions properly. Moreover, the present findings prove that a model that rigorously reproduces the first-principles cluster interaction energies and geometries is needed for consistency. It would therefore be more appropriate to evaluate first-principles PMFs, based on PMFs generated with improved semiempirical MO calculations "on the fly", which would allow for the flexibility of water molecules, and thus provide a more accurate representation of the chloride-water and water-water hydrogen bonding interactions.

7.1.3.3 Conclusions

Characterizing and describing the exact nature of hydrogen bonding in chemical systems involving water remains a formidable challenge for experimentalists and theoreticians alike. Our investigations of the structural properties and thermodynamics of halide-water clusters have revealed the importance of properly describing the subtle halide-water and water-water interactions. Our efforts so far in this endeavor have unequivocally demonstrated that a proper description of hydrogen bonding is essential for

predicting the solvation structure of halide-water clusters. For this reason, we have tried to reparameterize the semiempirical PM3 method to better reproduce the binding enthalpies and geometries of small halide-water and water clusters. The simple reparametrization of PM3, or the inclusion of functional forms to better describe the nuclear-nuclear repulsion within semiempirical MO theory were not sufficient to properly account for the subtle hydrogen-bonding interactions occurring in halide-water clusters. Increasing the minimal basis set employed in PM3 to include p-orbitals on the hydrogen atoms and d-orbitals on heavy atoms provides an avenue to account for the polarization involved in hydrogen bonds, and dispersion interactions could be introduced by 2nd order perturbation theory,⁶¹ but this colossal task is left for future work. We also showed that first-principles PMFs can be generated from model-based PMFs at a manageable computational cost. First-principles PMFs based on cluster configurations generated with model potentials produce unexpected, counter-intuitive, preliminary results, and the approach may fail when the model potentials and first-principles methods paint potential energy surfaces that are too different from one another. This brings further support for the development of a low-computational-cost semiempirical method geared towards a proper description of weak interactions.

7.2 Quantum effects in halide-water clusters

7.2.1 Introduction

It was previously believed that water molecules typically form four hydrogen bonds with neighboring water molecules in the bulk.¹⁵ However, recent experiments have revealed that the solvent molecules form only two hydrogen bonds due to the high degree

of fluctuations within the liquid.¹⁵ Previous theoretical studies employing techniques based on first-principles have found that quantum (nuclear) effects such as zero-point energy are paramount in determining the hydrogen-bonding structure of liquid water, due in part to the high frequency OH vibrations within the water molecules, which hinder the formation of directional hydrogen bonds with neighboring water molecules.¹⁵ This suggests that zero-point vibrational energy may be a very important issue to consider when describing the thermodynamics of interior vs. surface solvation of halides in water clusters. Since hydrogen bonds obviously involves hydrogen atoms, which are light and quantum-mechanical in nature, and auto-ionization of water could produce protons, whose quantum-mechanical nature is also notorious, it would not seem balanced to design a computationally intensive methodology that takes into account the subtle details of the system electronic structure, while neglecting quantum nuclear effects, which may be equally important for fully quantitative simulations of seeded water clusters. Therefore to provide a thorough investigation of the thermodynamics of solvation in seeded water clusters, it is important to investigate the importance of quantum effects within these clusters.

The Feynman path integral formulation of quantum statistics represents the Boltzmann statistics of a quantum atom as a set of replicated atoms, or “beads”, connected to each other in a cyclic chain, which can spread out, as a reflection of the Uncertainty Principle. As such, rather than solving a complex differential equation to describe the wave/particle duality of a quantum particle, as done in quantum mechanics, the quantum statistics of the chemical system is obtained by simulating a system

composed of many replicas, typically following classical methodologies such as Monte Carlo and molecular dynamics (MD) techniques.

We implemented a path integral molecular dynamics (PIMD) scheme within the umbrella sampling and weighted histogram analysis method described previously in order to assess the importance of zero-point vibrational energy and low temperature effects on the structure and thermodynamics of halides in water clusters.

7.2.2 Simulation Methodology

One of the fundamental principles of quantum mechanics is that the state of a system is completely specified by its wave function, and the probability for the system of being in a given quantum state is obtained as the square of the system wavefunction. The Feynman path integral formulation of quantum mechanics is an alternate method of describing the probabilistic nature of quantum particles, where it is stipulated that the probability for a system of being in a given quantum state can be obtained by summing the amplitudes of every possible path leading to that given quantum state. In the path integral formalism, the amplitude for a quantum particle to go from state a at time t_0 to state b at time t is given by

$$\psi = \langle r(t) | \dot{r}(t_0) \rangle = \sum_{\text{all paths}} \frac{1}{A} e^{\frac{i}{\hbar} S_{\text{path}}}, \quad (7.7)$$

where $r(t)$ are the atomic coordinates, A is the probability amplitude for a given path, \hbar is the Planck constant, and S_{path} is the path action, which is expressed as the integral over the Hamiltonian H , *i.e.*

$$S[r, \dot{r}, t_0, t] = \int_{t_0}^t H(r, \dot{r}) dt. \quad (7.8)$$

Typically, the Hamiltonian for chemical systems is expressed as a sum of kinetic K and potential V energies,

$$H(r, \dot{r}) = K(\dot{r}) + V(r) = \frac{1}{2} m \dot{r}^2 + V(r). \quad (7.9)$$

Any given mechanical property can be obtained through the evaluation of the partition function. To be directly applicable to constant-temperature MD or Monte Carlo simulations, the partition function for the canonical ensemble derived from statistical mechanics is applied to the path integral formalism. The partition function $Z(\beta)$ for the canonical ensemble is evaluated as

$$Z(\beta) = \int dr \langle r | e^{-\beta H} | r \rangle = \int dr \langle r | e^{-\beta(K+V)} | r \rangle \quad (7.10)$$

Generally speaking, the kinetic and potential energy operators do not commute, so that the exponential in eq. (7.10) cannot be evaluated directly. In these cases, the Trotter theorem can be applied,²³⁵ which yields the following partition function

$$Z(\beta) = \lim_{P \rightarrow \infty} \int dr \langle r | \Omega^P | r \rangle, \Omega = e^{-\frac{\beta}{2P}V} e^{-\frac{\beta}{P}K} e^{-\frac{\beta}{2P}V} \quad (7.11)$$

where eq. (7.11) involves a product of P factors of the operator Ω . Through a series of mathematical manipulations, the partition function becomes

$$Z(\beta) = \left(\frac{mP}{2\pi\beta\hbar^2} \right) \int dr_1 \cdots dr_P \exp \left\{ - \sum_{i=1}^P \left[\frac{mP}{2\beta\hbar^2} (r_{i+1} - r_i)^2 + \frac{\beta}{P} V(r) \right] \right\}_{r_{P+1}=r_1} \quad (7.12)$$

where m is the atomic mass, and $\hbar = h/2\pi$. To simplify this equation a chain frequency

$\omega_P = \frac{\sqrt{P}}{\beta\hbar}$ and an effective potential of the form

$$V_{eff}(r_1, \dots, r_P) = \sum_{i=1}^P \left[\frac{1}{2} m \omega_P^2 (r_{i+1} - r_i)^2 + \frac{1}{P} V(r) \right]_{r_{P+1}=r_1} \quad (7.13)$$

are introduced, such that the partition function becomes

$$Z_P(\beta) = \left(\frac{mP}{2\pi\beta\hbar^2} \right)^{P/2} \int dr_1 \cdots dr_P e^{-\beta V_{\text{eff}}} \quad (7.14)$$

Under this form, the partition function is a configurational partition function where each atom is represented as P particles, or beads, connected together in a cyclic chain. This form can be evaluated with MD or Monte Carlo simulations with a Hamiltonian of the form

$$H(p, r) = \sum_{i=1}^P \frac{p_i^2}{2m_i} + V_{\text{eff}} = \sum_{i=1}^P \left[\frac{p_i^2}{2m_i} + \frac{1}{2} m \omega_P^2 (r_{i+1} - r_i)^2 + \frac{1}{P} V(r) \right]_{r_{P+1}=r_1} \quad (7.15)$$

The main problem with this Hamiltonian is that the chain frequency ω_P increases linearly with P , whereas the potential energy term will be attenuated by a factor of $1/P$, such that the harmonic term will dominate. For this reason, the harmonic term and the potential term must be decoupled. Many possible ways have been proposed to accomplish this, we have chosen the staging transformation approach proposed by Ceperley and Pollock,²³⁶ which involves a simple change of variables of the form

$$\begin{aligned} u_1 &= r_1 \\ u_i &= r_i - r_i^*, \text{ where} \\ r_i^* &= \frac{(i-1)r_{i+1} + r_1}{i} \end{aligned} \quad (7.16)$$

The effective potential using the staging coordinates is expressed as

$$V_{\text{eff}}(u_1, \dots, u_P) = \sum_{i=1}^P \left[\frac{1}{2} m_i \omega_P^2 u_i^2 + \frac{1}{P} V(x_i(u_1, \dots, u_P)) \right] \quad (7.17)$$

The masses in this expression are called the staging masses, and are given by

$$\begin{aligned}
m_i^* &= 0 \\
m_i^* &= \frac{i}{i-1} m
\end{aligned}
\tag{7.18}$$

In eq. (7.17), the quadratic term is completely uncoupled in terms of the u variables from the interatomic potential term V . This uncoupled term represents the collective motion of the entire bead chain representing a given atom. The Hamiltonian equations of motion employed in molecular dynamics are evaluated as

$$\begin{aligned}
\dot{u}_i &= \frac{p_i}{m_i} \\
\dot{p}_i &= -\frac{\partial V_{\text{eff}}}{\partial u_i} = -m_i^* \omega_p^2 u_i - \frac{\partial V}{\partial u_i}
\end{aligned}
\tag{7.19}$$

where p refers to momenta. The forces are obtained by the chain rule as

$$\begin{aligned}
\frac{\partial V}{\partial u_i} &= \frac{1}{P} \sum_{i=1}^P \frac{\partial V}{\partial u_i} \\
\frac{\partial V}{\partial u_i} &= \frac{\partial V}{\partial r_i} - \frac{i-2}{i-1} \frac{\partial V}{\partial r_{i-1}}
\end{aligned}
\tag{7.20}$$

These equations of motion must be coupled to a thermostat to obtain a proper canonical ensemble with path integral molecular dynamics (PIMD). The Nosé-Hoover chain (NHC) method has been chosen for this purpose. In this approach, a set of M heat bath variables η_1, \dots, η_M is added along with a set of momenta $p_{\eta_1}, \dots, p_{\eta_P}$ to form an extended system. PIMD is governed by the harmonic motion due to the quadratic term in eq. (7.15), and as such, it was found important to couple at least one thermostat to each degree of freedom, that is to each Cartesian coordinate of all the beads comprising the system.²³⁷ The complete PIMD equations of motion, which include the Nosé-Hoover thermostats, become

$$\begin{aligned}
\dot{r} &= \frac{p}{m} \\
\dot{p} &= -\frac{\partial V}{\partial r} - \frac{p_{\eta_1}}{Q_1} p \\
\dot{\eta}_k &= \frac{p_{\eta_k}}{Q_k} \\
\dot{p}_{\eta_1} &= \frac{p^2}{m} - k_B T - \frac{p_{\eta_2}}{Q_2} p_{\eta_2} \\
\dot{p}_{\eta_k} &= \frac{p_{\eta_{k-1}}^2}{Q_{k-1}} - k_B T - \frac{p_{\eta_{k+1}}}{Q_{k+1}} p_{\eta_k} \\
\dot{p}_{\eta_M} &= \frac{p_{\eta_{M-1}}^2}{Q_{M-1}} - k_B T
\end{aligned} \tag{7.21}$$

and the total extended Hamiltonian is

$$H' = \sum_{i=1}^P \left\{ \frac{p_i^2}{2m_i} + \frac{1}{P} V(r_i) + \sum_{k=1}^M \left[\frac{p_{\eta_{k,i}}^2}{2Q_k} + k_B T \eta_{k,i} \right] \right\} \tag{7.22}$$

where Q_1, \dots, Q_M is a set of thermostat mass parameters that control the time scale of thermal equilibration, and are each assigned a values $Q_k = 1/\beta\omega_p^2$. The set of thermostat momenta are evolved using the Suzuki integrator-propagator algorithm,²³⁸ and the equations of motion for the beads are propagated with the velocity Verlet algorithm.¹⁹⁹ The Mopac7 semiempirical program²¹⁷ was incorporated within the PIMD simulation scheme to evaluate the interparticle interaction potentials and forces.

7.2.3 Preliminary results

The path integral molecular dynamics (PIMD) program developed to evaluate the importance of quantum effects such as zero-point energy motion of solvent molecules and the low temperature typical of experimental conditions for seeded clusters is still under development. In order to properly test the implementation of the PIMD program,

the PM3 semiempirical potential was reparameterized, following the same procedure discussed in Section 7.1.2.1, to the 0K binding energies (D_e , rather than the 0K binding enthalpies (D_0), and geometries of small chloride-water and water clusters, since zero-point energy is accounted for within the path integral formulation of quantum mechanics, as listed in Table 7.5. This reparameterized semiempirical potential is hereafter referred to as PM3spq, for PM3 with specific parameters for quantum simulations.

Table 7.5 PM3 and PM3spq parameters

Atom	Parameter ^a	PM3	PM3spc
H	U_{SS}	-13.073	-13.117
H	β_S	-5.627	-5.624
H	ζ_S	0.968	0.966
H	α	3.356	3.356
H	G_{SS}	14.794	14.918
H	b_{11}	1.129	1.129
H	b_{12}	-1.060	-1.060
H	b_{21}	5.096	5.099
H	b_{22}	6.004	6.001
H	b_{31}	1.537	1.537
H	b_{32}	1.570	1.570
O	U_{SS}	-86.993	-86.963
O	U_{PP}	-71.880	-71.887
O	β_S	-45.203	-45.270
O	β_P	-24.753	-24.727

O	ζ_S	3.797	3.794
O	ζ_p	2.389	2.390
O	α	3.217	3.220
O	G_{SS}	15.756	15.768
O	G_{SP}	10.621	10.449
O	G_{pp}	13.654	13.668
O	G_{P2}	12.406	12.402
O	H_{SP}	0.594	0.521
O	b_{11}	-1.131	-1.142
O	b_{12}	1.138	1.127
O	b_{21}	6.002	6.003
O	b_{22}	5.951	5.988
O	b_{31}	1.607	1.608
O	b_{32}	1.598	1.598
CL	U_{SS}	-100.627	-110.459
CL	U_{pp}	-53.614	-53.613
CL	β_S	-27.529	-26.678
CL	β_p	-11.594	-11.587
CL	ζ_S	2.246	2.234
CL	ζ_p	2.151	2.140
CL	α	2.517	2.508
CL	G_{SS}	16.014	11.720
CL	G_{SP}	8.048	8.039

CL	G_{pp}	7.522	7.508
CL	G_{P2}	7.504	7.500
CL	H_{SP}	3.481	3.441
CL	b_{11}	-0.172	-0.172
CL	b_{12}	-0.013	-0.013
CL	b_{21}	6.001	6.992
CL	b_{22}	1.967	1.955
CL	b_{31}	1.088	0.926
CL	b_{32}	2.293	2.309

^a U_{ii} are the i th atomic orbital one-electron one center integrals, β_{ii} are i th atomic orbital one-electron two-center integrals, ζ_i are the i th-type Slater atomic orbital exponent, α is the atom core-core repulsion term, G_{ii} are the i th-type atomic orbital one-center two-electron repulsion integral, H_{sp} is the s-p atomic orbital one-center two-electron exchange integral and b_{na} are Gaussian exponent multipliers for the n th Gaussian of atom a .

The 0 K and 300 K binding enthalpies obtained with the PIMD/PM3spq method employing 5 beads for each atom, an integration step size of 0.1 fs, and 3 Nosé-Hoover thermostat chains on each degree of freedom, are compared to available experimental data in Table 7.6. The PM3spq binding enthalpies were evaluated as an ensemble average over 1000 configurations collected at intervals of 500 fs along a 500 ps trajectory for each cluster. As seen from Table 7.6, the calculated binding enthalpies overestimate their experimental counterpart by no more than ~5 %. These preliminary results are very promising since both the zero-point energy motion, as reflected in D_0 , and the thermal

Table 7.6 $\text{Cl}^-(\text{H}_2\text{O})_n$ and $(\text{H}_2\text{O})_n$ binding energies and enthalpies (in kcal/mol) from PIMD simulations, ab initio calculations and experiment.

			0 K		300 K	
	PM3spq	D_e^a	PM3spq	D_0^a	PM3spq	$\Delta H^{300\text{ a}}$
$(\text{H}_2\text{O})_2$	5.1	5.0	4.0	3.6		
$\text{Cl}^-(\text{H}_2\text{O})$	14.1	14.8	14.2	13.6	14.9	14.4
$\text{Cl}^-(\text{H}_2\text{O})_2$	28.6	29.4	28.2	25.8	28.8	27.4

^a The water dimer binding energies and enthalpies were obtained from Reference 127 and the small chloride-water cluster binding energies and enthalpies from Reference 21.

motion of the clusters, as reflected in ΔH^{300} , are well reproduced with the PIMD method. Simulations are currently being performed to generate PMFs for $\text{Cl}^-(\text{H}_2\text{O})_{20}$ for comparison with the OPLS, OPCS and PM3spc $P(r_{cm})$ probability distributions discussed earlier. As mentioned previously, the simple reparameterization of PM3 produces chloride-water cluster geometries which are too tight to provide accurate thermodynamics in larger clusters. Similar geometries were naturally obtained for the parameterization of PM3spq. The underestimation of the chloride-water distance obtained with PM3 may have less drastic effects on the solvation structure of large halide-water clusters for simulations performed with PIMD, than those performed with the Monte Carlo procedure described in Section 7.1.2. The water molecules are kept rigid in Monte Carlo simulations with PM3spc, but not in PIMD simulations with PM3spql. Because of the stretching and bending vibrational motions of the water molecules, the rigidity of the chloride-water interaction might be reduced. Simulations employing the molecular dynamics method described in Chapter 3 and PM3spc, where the water geometry is allowed to fluctuate,

may be useful for comparison, both of the role of flexible water molecules and of the importance of quantum effects, but employing flexible water molecules may lead to artificial zero-point energy flow in the simulations, an issue that may deserve some attention. As mentioned earlier, truly quantitative simulations of the structural and thermodynamic properties of halide-water clusters will require an appropriate method to describe the intermolecular interactions in the cluster properly.

7.2.4 Conclusion

Our efforts so far have demonstrated that an accurate description of hydrogen-bonding in these clusters is crucial to obtain a quantitative assessment of the thermodynamics of surface vs. interior solvation in halide-water clusters. As such, the quantum nature of the hydrogen bond may have significant effects on the structural properties of the clusters. The path integral formulation of quantum mechanics has been incorporated within a molecular dynamics methodology (PIMD) in order to assess the importance of quantum effects in these clusters. A semiempirical PM3 Hamiltonian, PM3spq, reparameterized to reproduce small chloride-water and water cluster 0K binding energies and geometries is employed for the calculation of interatomic interactions. The developed PIMD methodology is still in the testing phase, but preliminary results so far are very promising. Indeed, the 0K and 300K binding enthalpies for small chloride-water and water clusters generated with PIMD/PM3spq are in good agreement with experimentally-determined values, which indicates that the zero-point vibrational motion of the water molecules is well represented with PIMD. Simulations of the structural and thermodynamic properties of $\text{Cl}^-(\text{H}_2\text{O})_{20}$ are currently being performed for comparison with our previous (classical) findings.

The use of model potentials with PIMD has also been considered for the simulation of very large clusters. Flexible models usually employ simple harmonic force fields to describe the vibrational motion within the water molecules. The use of flexible water molecules with high-frequency (O-H) modes is known to cause artificial zero-point energy flow, that may lead to water dissociation, in classical simulations, and very likely in PIMD simulations as well. For this reason, rigid waters would preferentially need to be employed in order to apply the PIMD methodology with model potentials, and maybe even semiempirical methods. This is not a trivial task within the PIMD framework, however, since the bead representation of the atoms precludes the use of rigid interactions and requires a reformulation of the PIMD method, a task which is left for future work.

Finally, we note that most applications of PIMD have dealt with condensed-phase problems, where Newton equations are typically solved with some flavor of the Verlet algorithm. While we implemented the same methodology for cluster simulations, resulting in a very convoluted code of over 5,000 lines, it is conceivable to borrow more of the traditional gas-phase classical trajectory approach for cluster simulations. Accordingly, it would be worthwhile to explore solving PIMD Hamilton's equations of motion, eq. (7.21), directly, as typically done for gas-phase trajectory calculations.²³⁹ However, because of the multiple timescale associated with the beads motion and the thermostats, simple, traditional predictor-corrector integration algorithms are likely to fail and the use of adaptive stepsize methods for stiff equations could be explored. We note that Manolopoulos recently employed a similar practical approach to PIMD in a very different context.¹²³ Furthermore, following his interpretation of the beads momenta, we

propose to employ PIMD simulations as a means to generate truly quantum-mechanical initial conditions for trajectory studies of chemical reactions.

7.3 Vibrational excitation/relaxation of ion pairs in clusters and solvation control of reactivity

As briefly discussed in Chapters 4 and 5, previous studies have shown that vibrational excitation/relaxation of ion pairs in both the ground and excited states can significantly affect their photodissociation dynamics. It is evident from distributions of ground-state NaI internuclear distances that the presence of water molecules broadens the range of internuclear distances accessed by NaI in the ground-state. As a result, one can expect ground-state NaI with short internuclear separations to access very high vibrational levels of the excited state. Our preliminary NaI(H₂O)_n cluster results have also underlined the importance of solute-solvent energy transfer in photodissociation reactions. It is therefore important to study solute-solvent energy transfer mechanisms in more detail.

In an effort to better understand these mechanisms, the energy transfer mechanisms between NaI and surrounding water molecules after vibrational excitation in the ground state were investigated using standard MD simulations with the same mixed semiempirical/OPLS classical model potentials as in Chapter 4. Preliminary results, shown in Fig. 7.4 for NaI(H₂O)₄, suggest that excess energy in the NaI vibrational coordinate is mainly transferred to the rotational degrees of freedom of surrounding water molecules, as was found in the analysis of the energetics of the water evaporation process in excited state NaI.^{124,205}

Another important aspect of the vibrational excitation/relaxation dynamics of ion pairs in water clusters lies in the possibility of CIP to SSIP solvation state interconversion following ground-state vibrational excitation, and possible caging of the solute, by surrounding water molecules, in the SSIP state. Due to advances in technology, high-power infrared lasers could be used to prepare molecules in specific vibrational states. Accordingly, vibrational excitation of the ground-state CIP, and subsequent vibrational relaxation at larger internuclear distances could lead to the trapping of the ion pair in the SSIP solvation state. Interconversion of the CIP to the SSIP was actually observed in MD simulations of $\text{NaI}(\text{H}_2\text{O})_{16}$ with an initial excess vibrational energy of 30 kcal/mol in the NaI coordinate, over a 2 ps timescale. Since it is believed that photoexcitation from the

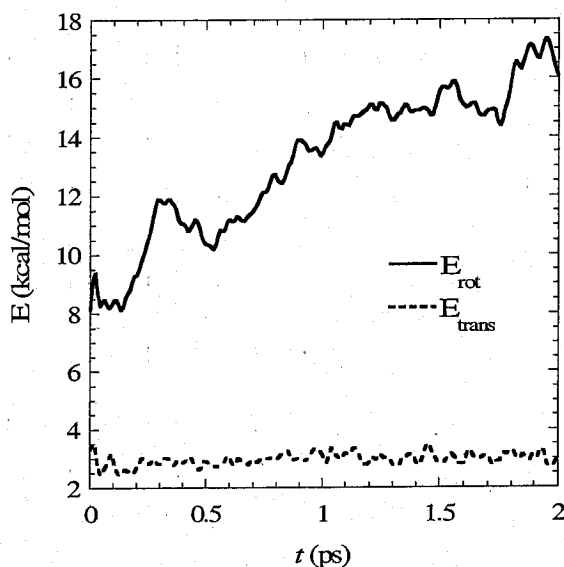


Figure 7.4 Average rotational E_{rot} and translational E_{trans} energies as a function of simulation time t for vibrational excitation of $\text{NaI}(\text{H}_2\text{O})_n$ with 20 kcal/mol of kinetic energy along the NaI internuclear distance coordinate.

SSIP state leads to charge-transfer-to-solvent (CTTS) excited states, control of CTTS to NaI excited state product ratio through ground state NaI vibrational excitation could be possible, providing an avenue for solvation/laser control of cluster photochemistry, and this deserves further investigation.

7.4 Photodissociation Dynamics of $\text{NaI}(\text{H}_2\text{O})_n$ Clusters in a Matrix

7.4.1 Introduction

Our investigations of the $\text{NaI}(\text{H}_2\text{O})_n$ photodissociation dynamics, discussed in Chapters 4 and 5, revealed that solvent molecules influence the electron transfer process, but rapid solvent evaporation precludes the observation of an activated inverted electron transfer process akin to that in solution. By embedding these clusters in a rare gas matrix, solvent evaporation could be greatly reduced, and therefore the gradual effects of solvation on NaI photodissociation dynamics, as a function of increasing cluster size, could be observed more readily. In this Section, preliminary results of the photodissociation dynamics in $\text{NaI}(\text{H}_2\text{O})_n \cdot \text{Ar}_m$ clusters are presented.

7.4.2 Simulation Methodology

The same semiempirical valence-bond approach to describe the NaI electronic structure and both Optimized Parameters for Liquid Simulations (OPLS) and Optimized Parameters for Cluster Simulations (OPCS) solvent-solvent and solute-solvent interaction potentials, along with the molecular dynamics with quantum transitions method developed by Tully and co-workers was employed,¹⁹³ as described in Chapters 4 and 5. The argon-solute and argon-solvent interactions were modeled by Lennard-Jones

potentials, with parameters derived from high-level *ab initio* calculations performed with the Gaussian98 suite of programs.²¹⁸ The parameters were calculated from a non-linear least squares fit¹²⁵ of the 0K binding enthalpies and minimum-energy geometries obtained from calculations employing Möller-Plesset 2nd order perturbation theory with augmented correlation-consistent double-zeta aug-cc-pVDZ basis sets for hydrogen, oxygen and argon,^{240,241} a correlation-consistent core/valence polarized double-zeta cc-pCVDZ basis set for sodium,²⁴² and the ECP46MDF large-core pseudopotential and basis set²⁴³ for iodine. The resulting parameters, employed for both OPLS and OPCS, are listed in Table 7.7. An argon matrix containing approximately 1500 argon atoms was employed for all NaI(H₂O)_n cluster sizes.

Table 7.7 Argon-solute and argon-solvent Lennard-Jones parameters.

	σ (kcal/mol)	ϵ (Å)
Ar-Ar	0.2755	3.738
Ar-O	0.0584	3.060
Ar-H	0.1391	3.090
Ar-Na ^a	3.6772	2.771
Ar-I ^a	0.9726	3.912

^a The argon-NaI interactions were considered to be the same for the NaI ground and excited states.

7.4.3 Preliminary Results

The caging effects provided by the embedding of NaI(H₂O)_n clusters in an argon matrix are different for OPLS and OPCS. As discussed earlier, the repulsive forces caused by the reversed polarity of NaI in the Franck-Condon region of the excited state

are more pronounced with OPLS, relative to OPCS. Preliminary results for the simulation of the photodissociation dynamics in $\text{NaI}(\text{H}_2\text{O})_n \bullet \text{Ar}_m$ clusters reveal that $\sim 45\%$ of the water molecules in $\text{NaI}(\text{H}_2\text{O})_n$ clusters, $[n = 1 - 4]$, are repelled to $\sim 10 \text{ \AA}$ away from NaI within the argon matrix, due to the repulsive NaI- H_2O interactions after photoexcitation with OPLS. With OPCS, on the other hand, the full population of water molecules remains bound to NaI, i.e. at NaI- H_2O distances smaller than 5 \AA , after photoexcitation.

In Chapter 5, it was concluded that solvent evaporation precludes the observation of an inverted electron transfer regime in $\text{NaI}(\text{H}_2\text{O})_n$ clusters. The surface solvation structure of iodide in $\text{NaI}(\text{H}_2\text{O})_n$ clusters may also facilitate NaI large-amplitude motion that results in efficient electron transfer via nonadiabatic transitions along the NaI internuclear coordinate. The argon matrix can hinder this process, as shown in Fig. 7.5 from the NaI internuclear distances along the simulation timescale. In fact, the NaI large-amplitude motion is quenched by the argon matrix, and since the curve-crossing region along the NaI internuclear coordinate is hardly reached, electron transfer must proceed along the solvent coordinate, as in solution. On average, NaI vibrational relaxation occurs within $\sim 800 \text{ ps}$ of photoexcitation for both model potentials for cluster size 4. Whether vibrational relaxation occurs in the ground or excited states, on the other hand, depends on the number of water molecules that remain bound following the initial NaI- H_2O repulsive dynamics. Preliminary results suggest that when two water molecules remain bound to sodium, the full excited-state population decays to the ground state, independently of the parent cluster size or model potential, in agreement with the almost

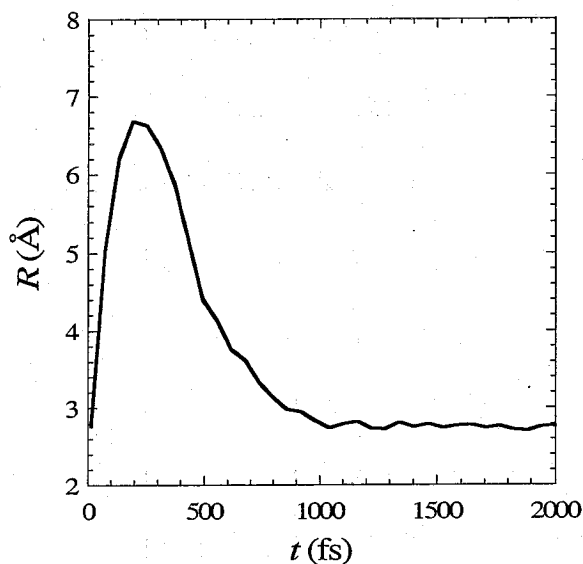


Figure 7.5 Average NaI internuclear distance R as a function of simulation time for $\text{NaI}(\text{H}_2\text{O})$.

barrierless electron transfer along the solvent coordinate inferred from the diabatic free energy curves for $\text{NaI}(\text{H}_2\text{O})_2$ clusters in Fig4. 5.10, and in contrast to our previous simulations where ground-state ionic recombination was only observed for free $\text{NaI}(\text{H}_2\text{O})_8$ with OPCS. These preliminary results therefore suggest a very interesting electron transfer process analogous to the solution-phase problem, possibly in the activated inverted regime for larger clusters, in $\text{NaI}(\text{H}_2\text{O})_n$ clusters embedded in an argon matrix.

7.4.4 Conclusions

Previous investigations of the $\text{NaI}(\text{H}_2\text{O})_n$ photodissociation dynamics showed that solvent molecules influence the electron transfer process, but rapid solvent evaporation precludes the observation of an activated inverted electron transfer process akin to that in

solution. The present simulations of the photodissociation dynamics of $\text{NaI}(\text{H}_2\text{O})_n$ cluster embedded in an argon matrix reveal that the solvent evaporation is entirely prevented by the matrix with OPCS, while only $\sim 45\%$ of the water population diffuses into the argon matrix after NaI photoexcitation, due to the stronger NaI- H_2O repulsive forces in the Franck-Condon region of the excited state, with OPLS. In contrast to previous findings for free $\text{NaI}(\text{H}_2\text{O})_n$ clusters, NaI large-amplitude motion is quenched by the matrix, resulting in rapid vibrational relaxation, and electron transfer must proceed along the solvent coordinate, without a barrier for small clusters. Embedding the clusters in an argon matrix may then result in activationless electron transfer, and activated inverted electron transfer in larger clusters as suggested by the free energy curves evaluated in Chapter 5, analogously to the solution process, and in contrast to the photodissociation of free $\text{NaI}(\text{H}_2\text{O})_n$ clusters.

7.5 Concluding Remarks

In this Chapter, future research avenues that arose in the context of this Thesis were briefly discussed. Strategies were designed for fully quantitative simulations of the solvation structure and thermodynamics of seeded water clusters, in which potentials of mean force are evaluated from first-principles, and include quantum nuclear effects via path integral molecular dynamics (PIMD) simulations. Much more work remains to be performed in the area, in particular to develop computationally efficient semiempirical quantum chemistry methods that properly describe weak interactions, and to exploit the full potential of PIMD simulations, by including constraints or designing simplified strategies to solve the equations of motion. The use of PIMD simulations as a general approach to generate fully quantum-mechanical initial conditions for trajectory

simulations should also be explored. Attention was also paid to the ground-state vibrational excitation of ion pairs in water clusters, as a promising potential route for solvation and laser control of cluster photochemistry. Finally, in the long-standing search for inverted electron transfer in clusters, embedding $\text{NaI}(\text{H}_2\text{O})_n$ clusters in a matrix appears to quench the NaI large-amplitude motion that resulted in electron transfer along the NaI internuclear coordinate in free clusters and the gas phase, favoring activationless (or activated inverted) electron transfer along the solvent coordinate analogously to the solution-phase process. All these avenues will be explored further.

Theoretical Studies of Seeded Water Clusters: Structure,
Thermodynamics and Photochemistry

Chapter 8

General Conclusions

The primary objective of this thesis was to understand how the solvation structure of paradigm solutes in solvent clusters affects their reactivity. In this endeavor, the elementary electron transfer reaction occurring upon photoexcitation of NaI is chosen as a model system to advance our knowledge of solvation effects on reaction dynamics, mainly because photodissociation of the gas-phase ion pair has been well characterized.⁷⁷ The surface solvation state adopted by large halide ions in water clusters can have profound effects on the cluster photochemistry. A portion of this thesis was therefore dedicated to providing a detailed investigation of the solvation states adopted by halides in water clusters, before turning our attention to the effects of solvation on the photochemical behavior of NaI seeded solvent clusters.

In Chapters 2 and 3, a rigorous and quantitative investigation of the solvation structure and thermodynamics of halide-water clusters was conducted, in order to characterize the nature of the ion interior and surface solvation states, and to establish which properties govern the solvation structure of the ions in water clusters. Chapter 2 was devoted to iodide-water clusters because iodide was the first ion for which the existence of a surface solvation state was proposed. We evaluated the free energy change as a function of the distance between the ion and the solvent center of mass r_{cm} for $\text{I}^-(\text{H}_2\text{O})_n$ clusters ($n=32$ and 64) by means of constrained Monte Carlo simulations, using both a nonpolarizable OPLS model developed for liquid simulations and a polarizable OPCS model developed for small cluster simulations. The results indicate that iodide preferentially adopts an interior solvation structure for $\text{I}^-(\text{H}_2\text{O})_{32}$ clusters, and an

equilibrium between surface and interior solvation exists for $\text{I}^-(\text{H}_2\text{O})_{64}$ clusters, where the interior state is preferred over the surface state.

In Chapter 3, this study was extended to the full halide series. Once again, the free energy change as a function of the distance between the ion and the solvent center of mass r_{cm} in halide-water clusters was evaluated, but by a different theoretical approach: Nosé-Hoover molecular dynamics simulations thermostated at 200 K with umbrella sampling, together with the weighted histogram analysis method, using both OPLS and OPCS model potentials were employed. The resulting potentials of mean force (PMF) and r_{cm} probability distributions $P(r_{cm})$ indicate that interior solvation is thermodynamically favored with OPLS for all cluster sizes investigated and for the whole halide series, except for iodide, for which the surface solvation state is predominant at cluster size 32 and 64. With OPCS, on the other hand, our results indicate that fluoride favors interior solvation at cluster size 20, and, according to the interior-to-surface equilibrium constants, the interior and surface solvation states are nearly equally populated for chloride, bromide and iodide at cluster size 64, with the surface state becoming increasingly more favored as the ionic radii and polarizabilities increase down the halide series. These findings are consistent with the variation in ionic properties, such as polarizability and ion-water binding enthalpy, along the halide series. Fluoride is much less polarizable, and the ion-water binding energy much larger than that of the other halides. It is therefore expected that fluoride will favor interior solvation at a lower cluster size than other halides. Chloride and bromide have very similar polarizabilities and ion-water binding enthalpies, and not surprisingly, our results demonstrate very similar solvation behaviors as a function of increasing cluster size for the ions.

Overall, polarization and entropy seem to mostly govern the solvation structure of the ions in water clusters. The discrepancy between the predictions of OPLS and OPCS has been attributed to the fact that OPLS does not account for ion-water and water-water polarization, which has proven to be an essential factor in determining the solvation structure of ions in water clusters. Simulations of $\text{Cl}^-(\text{H}_2\text{O})_{20}$ clusters with varying ion-water binding enthalpies and polarizabilities reveal that the polarizability alone drives the ion to the surface or towards the interior of the cluster, and as such, the OPLS model cannot provide reliable thermodynamics of ionic solvation. The discrepancy between model potentials reveals that subtle polarization effects and the precise shape of the charge distribution of water significantly affects the cluster entropy and, thus, the solvation structure of ions in water clusters. Hence, methodologies based on first-principles intermolecular interactions are explored in Chapter 7 in order to eventually obtain a quantitative and definitive description of the transition from surface to interior solvation in halide-water clusters.

In Chapter 4, the photodissociation dynamics of $\text{NaI}(\text{H}_2\text{O})_n$ [$n=1-4$] clusters is investigated using the molecular dynamics with quantum transitions method and a quantum mechanics/molecular mechanics description of $\text{NaI}(\text{H}_2\text{O})_n$, which involves a semiempirical valence-bond approach to describe the NaI electronic structure and model OPLS interaction potentials. Our simulation results show that the $\text{NaI}(\text{H}_2\text{O})_n$ excited-state population decay upon reaching the NaI curve-crossing region increases with cluster size, due to the stabilization of the ionic branch of the NaI excited state by the surrounding water molecules, and to the resulting increase in the nonadiabatic transition probability. After reaching the curve-crossing region for the first time, however, the excited-state

population decay resembles that of bare NaI because of rapid evaporation of 99% and 95% of the water molecules for NaI(H₂O) and NaI(H₂O)_n [n=2-4], respectively. This extensive evaporation is due to the reversed NaI polarity in the Franck-Condon region of the NaI first excited state, which causes strong repulsive NaI-H₂O forces, and induces rapid non-statistical water evaporation, where product water molecules are formed more rotationally than translationally hot. A few water molecules (5% or less) remain transiently or permanently bound to NaI forming long-lived clusters, when NaI remains predominantly ionic, *i.e.* remains in the excited state, after reaching the curve-crossing region.

In order to connect simulation results with experiment, femtosecond probe signals resulting from two-photon and one-photon excitation to the X and I NaI⁺ probe states were simulated. In agreement with experimental findings, the probe signals resulting from the two-photon probe scheme, where excitation occurs from the covalent branch of the excited state, decay exponentially over the NaI first excited-state vibrational period, with very little evidence of long-time dynamics. The one-photon probe scheme (not used for experimental cluster studies) is shown to be less sensitive to solvation, in that excitation energies will remain similar over a range of cluster sizes, as the ionic branch of the excited state and the NaI⁺ probe states are stabilized to the same extent by the presence of water molecules. The resulting probe signals also seem to be more revealing of the NaI(H₂O)_n photodissociation dynamics than the two-photon probe signals, as they may allow monitoring of solvation effects on the NaI nonadiabatic dynamics and of successive evaporation of water molecules. Time-resolved photoelectron spectra provide limited additional information regarding the NaI(H₂O)_n photodissociation dynamics. A

key consequence of the rapid water evaporation demonstrated in Chapter 4 with hybrid QM/OPLS simulations is that experimentally observed signals most likely arise from the photodissociation of much larger $\text{NaI}(\text{H}_2\text{O})_n$ parent clusters.

In Chapter 5, we extended the previous investigations of $\text{NaI}(\text{H}_2\text{O})_n$ cluster photodissociation dynamics²⁰⁵ to larger cluster sizes, by implementing the polarizable OPCS model within the semiempirical valence bond approach employed to describe the NaI electronic structure, along with the molecular dynamics with quantum transitions method.¹⁹³ This new, hybrid QM/OPCS model alleviates the assumption of frozen electronic polarizability of QM/OPLS, and allows the solvent to polarize as a response to its environment in both the ground and excited states. The NaI ground to first excited state Frank-Condon energy gaps predicted by the nonpolarizable QM/OPLS model used earlier increase linearly with cluster size, in contrast to experimental and high-level *ab initio* calculations results that suggest a convergence of the gaps over the cluster size range 4-16. Due in part to this discrepancy, our previous QM/OPLS simulations were limited to small cluster sizes. On the other hand, the QM/OPCS model predicts a convergence of the Franck-Condon energy gaps at cluster size ~ 16 , in relatively good agreement with experiment and *ab initio* calculations, therefore demonstrating once again the importance of solvent polarization, and allowing us to safely extend the range of cluster sizes to be simulated.

The excited-state population decay with QM/OPCS, in contrast to the simulations with QM/OPLS, increases sharply with cluster size. For cluster sizes greater than 2, the full excited-state population decays within 800 fs of photoexcitation. Since the NaI solute and solvent molecules are allowed to polarize each other with QM/OPCS, the NaI- H_2O

repulsive forces caused by the NaI reversed polarity in the Franck-Condon region of the excited state upon photoexcitation are attenuated, relative to the QM/OPLS case, and therefore, water evaporation is significantly reduced. In fact, our simulations predict that less than 10% of the water molecules have evaporated by the time NaI reaches the curve-crossing region for the first time, which leads to a more rapid excited-state population decay than QM/OPLS. At cluster size 8, the stabilization of the ionic state by the water molecules causes the adiabatic ground and excited states to acquire pure ionic and covalent character, respectively. Therefore, following the transition back to the ground state after photoexcitation, NaI remains bound on the ground ionic state or the cluster dissociates to form ionic products. For smaller cluster sizes, on the other hand, the transition to the ground state leads to the formation of atomic photodissociation products as observed earlier.

Simulation of the femtosecond pump-probe signals resulting from two-photon (2×610 nm) ionization from the covalent branch of the excited state suggest that the $\text{Na}^+(\text{H}_2\text{O})_p$ signals observed experimentally, where p refers to the post-evaporation product cluster size, may arise from parent clusters close in size ($p \sim n$), and not necessarily from much larger parent clusters as suggested by our earlier QM/OPLS results. In contrast to experiment, $\text{NaI}^+(\text{H}_2\text{O})_p$ signals are obtained for both QM/OPLS and QM/OPCS, but are less pronounced for the former, which suggests that obtaining a $\text{NaI}^+(\text{H}_2\text{O})_p$ signal depends on the model potential employed. However, performing nonadiabatic simulations with intermolecular interactions derived from first principles would be computationally prohibitive. The femtosecond pump-probe signals obtained with one-photon (263 nm) excitation from the ionic branch of the excited state, differ also

from those obtained previously. Both $\text{Na}^+(\text{H}_2\text{O})_p$ and $\text{NaI}^+(\text{H}_2\text{O})_p$ signals are barely perceptible for cluster sizes larger than 1, due to the increased nonadiabatic transition probability caused by the presence of water molecules. The absence of signals with the one-photon probe scheme in the cluster case is consistent with experimental findings: this probe scheme, which was used earlier to probe the NaI gas-phase dynamics,¹⁷¹ was later abandoned in experimental studies of clusters⁶⁷ simply because no femtosecond signal could be detected.

The precise electron transfer mechanism following photoexcitation was also investigated. Free energy curves for both ionic and covalent states, analogous to those of solution theory, were generated as a function of a collective solvent coordinate, defined as the energy difference between the two diabatic states, for this purpose. Inspection of the free energy curves reveals that the electron transfer process in clusters is not governed by the collective motion of the water molecules, as would be the case in solution, and it does not proceed along the solvent coordinate, but along the NaI internuclear separation coordinate, as in the gas phase. Therefore, solvation in small clusters mainly influences the nonadiabatic transition dynamics by increasing the NaI internuclear separation at which the curve crossing occurs, but does not directly govern the electron transfer process as in solution. If the evaporation of water molecules could be prevented by embedding the $\text{NaI}(\text{H}_2\text{O})_n$ clusters in a matrix or a sufficiently dense buffer gas, the collective motion of the water molecules could become important and therefore govern electron transfer. As a matter of fact, this issue is investigated in Chapter 7.

In Chapter 6, a different aspect of NaI photodissociation was explored. Multiphoton ionization experimental studies of NaI ion pairs in polar solvent clusters of water,

acetonitrile and ammonia⁶⁸ have shown a very clear, solvent-selective, behavior in the distribution of the detected $\text{Na}^+(\text{solvent})_n$ product ions. More specifically, product clusters up to size 50 have been observed experimentally with water, but no clusters larger than size 9 and 6 have been observed with ammonia and acetonitrile, respectively, in multi-photon ionization experiments. Ground-state charge separation within the cluster and resulting loss of absorption of solvent-separated ion pairs, can be ruled out as a possible explanation for the solvent-selective behavior of multi-photon ionization, since ground-state charge separation occurs earlier for water than for the other two solvents. Chapter 6 then focused on the photoexcitation of NaI in water, ammonia and acetonitrile clusters, in an attempt to find an alternative explanation. Photochemical properties based on thermal ensembles of species, and not for a single ground-state minimum energy structure as usually done, both with the hybrid QM/OPCS model (extended to ammonia and acetonitrile) and model (configuration interaction with single excitations) quantum chemistry calculations, indicate that Franck-Condon energy gaps and oscillator strengths are similar for all seeded solvent clusters, suggesting very similar photochemical behavior.

The disappearance of the multi-photon ionization product signal at small cluster size, compared to water, could then be attributed to the predominance of photoexcitation to a charge-transfer-to-solvent (CTTS) state for acetonitrile clusters, and to the instability of large ground-state clusters with respect to evaporation for ammonia clusters. As demonstrated for $\text{NaI}(\text{H}_2\text{O})_n$ clusters in Chapters 4 and 5, however, massive solvent evaporation typically occurs on the excited states, and future work will involve simulations of the dynamics post-multi-photon excitation to probe possible differences in

the ionized-state solvent evaporation dynamics with different solvents. It is conceivable that the ionized state dissociation to produce $\text{Na}^+(\text{H}_2\text{O})_p$ cluster products occurs more readily, with little solvent reorganization for surface-solvated $\text{NaI}(\text{H}_2\text{O})_n$ clusters, because iodine sits at the surface of the cluster, therefore allowing larger cluster products to survive than in the case of acetonitrile and ammonia clusters, for which dissociation of interior ionized species may cause the whole cluster to blow up upon multi-photon excitation.

Chapter 7 is devoted to future research avenues that arose in the context of this thesis. Strategies for fully quantitative simulations of the solvation structure and thermodynamics of seeded water clusters have been designed, in which potentials of mean force are evaluated from first-principles and include quantum nuclear effects via path integral molecular dynamics (PIMD) simulations. Much more work remains to be performed in the area, in particular to develop computationally efficient semiempirical quantum chemistry methods that properly describe weak interactions, and to exploit the full potential of PIMD simulations. The use of PIMD simulations as a general approach to generate fully quantum-mechanical initial conditions for trajectory simulations is also pointed out. The ground-state vibrational excitation of ion pairs in water clusters was also explored as a promising route for solvation and laser control of cluster photochemistry. Finally, simulations of the photodissociation dynamics of $\text{NaI}(\text{H}_2\text{O})_n$ clusters embedded in a matrix suggest quenching of the NaI large-amplitude motion that resulted in electron transfer along the NaI internuclear coordinate in free clusters and the gas phase, favoring activationless (or activated inverted) electron transfer along the solvent coordinate analogously to the solution-phase process. All these avenues deserve further exploration.

quantum chemistry methods that properly describe weak interactions, and to exploit the full potential of PIMD simulations. The use of PIMD simulations as a general approach to generate fully quantum-mechanical initial conditions for trajectory simulations is also pointed out. The ground-state vibrational excitation of ion pairs in water clusters was also explored as a promising route for solvation and laser control of cluster photochemistry. Finally, simulations of the photodissociation dynamics of $\text{NaI}(\text{H}_2\text{O})_n$ clusters embedded in a matrix suggest quenching of the NaI large-amplitude motion that resulted in electron transfer along the NaI internuclear coordinate in free clusters and the gas phase, favoring activationless (or activated inverted) electron transfer along the solvent coordinate analogously to the solution-phase process. All these avenues deserve further exploration.

To summarize, this thesis presented an array of simulation methodologies that were developed to investigate various aspects of the structure, thermodynamics and photochemistry of seeded water clusters. Valuable insight was obtained into the solvation structure of ions in water clusters and solvation effects on the elementary electron transfer reaction occurring upon photoexcitation of paradigm NaI ion pairs. We hope that the simulation methodologies developed and the newly gained knowledge for simple, prototypical systems can be applied to better understand other chemical processes in more complex molecular systems.

Bibliography

- ¹ K. A. Dill; *Biochem* 29, 7133 (1990).
- ² J. Rupley and G. Careri; *Adv. Protein Chem.* 41, 37 (1991).
- ³ T. V. Chalikian, J. Volker, E. Plum and K. Breslauer; *Proc. Natl. Acad. Sci. U.S.A* 96, 7853 (1999).
- ⁴ P. C. Jordan; *Biophys. J.* 58, 1133 (1990).
- ⁵ B. Katz; *Nerve, Muscle, and Synapse* (Mc Graw-Hill, London, 1966).
- ⁶ K. D. Collins and M. W. Washabaugh; *Q. Rev. Biophys.* 18, 323 (1985).
- ⁷ M. G. Cacace, E. M. Landau and J. J. Ramsden; 30, 241 (1997).
- ⁸ M. Maroncelli, J. MacInnins and G. R. Fleming; *Science* 243, 1674 (1989).
- ⁹ M. F. Kropman and H. J. Bakker; *Science* 291, 2118 (2001).
- ¹⁰ S. Habuchi, H. B. Kim and N. Kitamura; *Anal. Chem.* 73, 366 (2001).
- ¹¹ A. R. Ravishankara; *Science* 276, 1056 (1997).
- ¹² E. M. Knipping, M. J. Lakin, K. L. Foster, P. Jungwirth, D. J. Tobias, R. B. Gerber, B. Dabub and B. J. Finlayson-Pitts; *Science* 288, 301 (2000).
- ¹³ J. T. Snodgrass, J. V. Coe, C. B. Freidhoff, K. M. McHugh, S. T. Arnold and K. H. Bowen; *J. Phys. Chem. A* 99, 9675 (1995).
- ¹⁴ B. Plastringe, M. H. Cohen, K. A. Cowen, D. A. Wood and J. V. Coe; *J. Phys. Chem. A* 99, 118 (1995).
- ¹⁵ D. Kennedy; *Science* 306, 2013 (2004).
- ¹⁶ B. Hribar, N. T. Southall, V. Vlachy and K. A. Dill; *J. Am. Chem. Soc.* 124, 12302 (2002).
- ¹⁷ P. Kebarle; *Ann. Rev. Phys. Chem.* 28, 445 (1977).
- ¹⁸ A. W. Castleman and R. G. Keese; *Chem. Rev.* 86, 589 (1986).
- ¹⁹ T. D. Mark and A. W. Castleman; *Adv. At. Mol. Phys.* 20, 65 (1985).
- ²⁰ A. W. Castleman, Jr. and R. G. Keese; *Chem. Rev.* 86, 589 (1986).
- ²¹ K. Hiraoka, S. Mizuse and S. Yamabe; *J. Phys. Chem.* 92, 3943 (1988).
- ²² K. Hiraoka, S. Fujimaki, K. Aruga and S. Yamabe; *Chem. Phys. Lett.* 208, 491 (1993).
- ²³ M. Meot-ner; *J. Amer. Chem. Soc.* 106, 1265 (1984).
- ²⁴ G. Markovich, L. Perera, M. L. Berkowitz and O. Cheshnovsky; *J. Chem. Phys.* 105, 2675 (1996).
- ²⁵ D. W. Arnold, S. E. Bradforth, E. H. Kim and D. M. Neumark; *J. Chem. Phys.* 97, 9468 (1992).
- ²⁶ D. W. Arnold, S. E. Bradforth, E. H. Kim and D. M. Neumark; *J. Chem. Phys.* 102, 3510 (1995).
- ²⁷ C. E. H. Dessent, C. G. Bailey and M. A. Johnson; *J. Chem. Phys.* 103, 2006 (1995).

- ²⁸ G. Markovich, R. Giniger, M. Levin and O. Cheshnovsky; *Z. Phys. D* 20, 69 (1991).
- ²⁹ G. Markovich, S. Pollack, R. Giniger and O. Cheshnovsky; *J. Chem. Phys.* 101, 9344 (1994).
- ³⁰ J. V. Coe, G. H. Lee, J. G. Baton, S. T. Arnold, H. W. Sarkas, K. H. Bowen, C. Ludewigt, H. Haberland and D. R. Worsnop; *J. Chem. Phys.* 92, 3980 (1990).
- ³¹ G. H. Lee, S. T. Arnold, J. G. Eaton, H. W. Sarkas, K. H. Bowen, C. Ludewigt and H. Haberland; *Z. Phys. D* 20, 9 (1991).
- ³² F. Misaizu, K. Tsukamoto, M. Sanekata and K. Fuke; *Chem. Phys. Lett.* 188, 241 (1992).
- ³³ D. G. Leopold, J. Ho and W. C. Lineberger; *J. Chem. Phys.* 86, 175 (1987).
- ³⁴ J. Ho, K. M. Ervin and W. C. Lineberger; *J. Chem. Phys.* 93, 6987 (1991).
- ³⁵ G. Gantefor, K. H. Meiwes-Broer and H. Lutz; *Phys. Rev. A* 37, 2716 (1988).
- ³⁶ G. Gantefor, M. Gauss, K. H. Meiwes-Broer and H. Lutz; *Faraday Discuss.* 88, 16 (1988).
- ³⁷ O. Cheshnovsky, K. J. Taylor, J. Conceicao and R. E. Smalley; *Phys. Rev. Lett.* 64, 1785 (1990).
- ³⁸ M. J. Deluca, B. Niu and M. A. Johnson; *J. Chem. Phys.* 88, 5857 (1988).
- ³⁹ M. J. Deluca, C. C. Han and M. A. Johnson; *J. Chem. Phys.* 93, 268 (1990).
- ⁴⁰ G. Markovich, R. Giiger, M. Levin and O. Cheshnovsky; *J. Chem. Phys.* 95, 9416 (1991).
- ⁴¹ O. Cheshnovsky, R. Giniger, G. Markovich, G. Makov, A. Nitzan and J. Jortner; *J. Chim. Phys. Phys.-Chim. Biol.* 92, 397 (1995).
- ⁴² O. M. Cabarcos, C. J. Weinheimer, J. M. Lisy and S. S. Xantheas; *J. Chem. Phys.* 110, 5 (1999).
- ⁴³ O. M. Cabarcos, C. J. Weinheimer, T. J. Martinez and J. M. Lisy; *J. Chem. Phys.* 110, 9516 (1999).
- ⁴⁴ C. G. Bailey, J. Kim and M. A. Johnson; *J. Phys. Chem.* 100, 16782 (1996).
- ⁴⁵ M. S. Johnson, K. T. Kuwata, C.-K. Wong and M. Okumura; *Chem. Phys. Lett.* 260, 551 (1996).
- ⁴⁶ J. H. Choi, K. T. Kuwata, Y. B. Cao and M. Okumura; *J. Phys. Chem. A* 102, 503 (1998).
- ⁴⁷ D. A. Wild, Z. M. Loh, R. L. Wilson and E. J. Bieske; *J. Chem. Phys.* 117, 3256 (2002).
- ⁴⁸ D. A. Wild, R. L. Wilson, P. S. Weiser and E. J. Bieske; *J. Chem. Phys.* 113, 10154 (2000).
- ⁴⁹ D. A. Wild, P. J. Milley, Z. M. Loh, P. P. Wolyneec, P. S. Weiser and E. J. Bieske; *J. Chem. Phys.* 113, 1075 (2000).
- ⁵⁰ D. A. Wild, Z. M. Loh, P. P. Wolyneec, P. S. Weiser and E. J. Bieske; *Chem. Phys. Lett.* 332, 531 (2000).
- ⁵¹ P. Ayotte, C. G. Bailey, G. H. Weddle and M. A. Johnson; *J. Phys. Chem. A* 102, 3067 (1998).

- ⁵² P. Ayotte, G. H. Weddle, J. Kim and M. A. Johnson; *Chem. Phys. Lett.* 239, 485 (1998).
- ⁵³ P. Ayotte, S. B. Nielsen, G. H. Weddle, J. Kim, M. A. Johnson and S. S. Xantheas; *J. Phys. Chem. A* 103, 10665 (1999).
- ⁵⁴ P. Ayotte, G. H. Weddle and M. A. Johnson; *J. Chem. Phys.* 110, 7129 (1999).
- ⁵⁵ J. M. Weber, J. A. Kelley, W. H. Robertson and M. A. Johnson; *J. Chem. Phys.* 114, 2698 (2001).
- ⁵⁶ P. Ayotte, J. A. Kelley, S. B. Nielsen and M. A. Johnson; *Chem. Phys. Lett.* 316, 455 (2000).
- ⁵⁷ C. J. Tsai and K. D. Jordan; *Chem. Phys. Lett.* 213, 181 (1993).
- ⁵⁸ S. S. Xantheas; *J. Phys. Chem.* 100, 9703 (1996).
- ⁵⁹ G. W. Neilson and J. E. Enderby; *Ann. Rep. Prog. Chem., Sect. C* 76, 185 (1979).
- ⁶⁰ D. Liu, G. Ma, L. M. Levering and H. C. Allen; *J. Phys. Chem. B* 108, 2252 (2004).
- ⁶¹ B. C. Garrett; *Science* 303, 1146 (2004).
- ⁶² G. H. Peslherbe, B. M. Ladanyi and J. T. Hynes; *Chem. Phys.* 258, 201 (2000).
- ⁶³ T. S. Rose, M. J. Rosker and A. H. Zewail; *J. Chem. Phys.*, 91, 7415 (1989). P. Cong, G. Roberts, J. L. Herek, A. Mohktari and A. H. Zewail; *J. Chem. Phys.*, 100, 7832 (1996).
- ⁶⁴ M. J. Rosker, T. S. Rose and A. H. Zewail; *Chem. Phys. Lett.* 146, 175 (1988). T. S. Rose, M. J. Rosker and A. H. Zewail; *J. Chem. Phys.* 88, 6672 (1988). A. H. Zewail; *J. Chem. Soc. Faraday Trans.* 85, 1221 (1989). P. Cong, A. Mohktari and A. H. Zewail; *Chem. Phys. Lett.* 172, 109 (1990). A. Mohktari, P. Cong, J. L. Herek and A. H. Zewail; *Nature* 348, 225 (1990). A. H. Zewail; *Faraday Trans. Chem. Soc.* 91, 207 (1991). A. H. Zewail; *Femtochemistry - Ultrafast Dynamics of the Chemical Bond*; World Scientific: Singapore, 1994. A. H. Zewail; In *Femtosecond Chemistry*; Manz J.; Wöste L., Eds.; VCH: New York, 1994; Vol. 1, p.15.
- ⁶⁵ G. H. Peslherbe, R. Bianco, J. T. Hynes and B. M. Ladanyi; *J. Chem. Soc., Faraday Trans.* 93, 977 (1997).
- ⁶⁶ G. Grégoire, M. Mons, I. Dimicoli, C. Dedonder-Lardeux, C. Juvet, S. Martrenchard and D. Solgadi; *J. Chem. Phys.* 110, 1521 (1999).
- ⁶⁷ G. Grégoire, C. Dedonder-Lardeux, I. Dimicoli, C. Juvet, M. S. and D. Solgadi; *J. Chem. Phys.* 112, 8794 (2000).
- ⁶⁸ G. Grégoire, E. Charron, M. Mons, I. Dimicoli, C. Juvet, S. Martrenchard, F. Piuze, D. Solgadi, C. Dedonder-Lardeux and A. Suzor-Weiner; *Eur. Phys. J. D* 1, 187 (1998).
- ⁶⁹ D. Serxner, C. E. H. Dessent and M. A. Johnson; *J. Chem. Phys.* 105, 7231 (1996).
- ⁷⁰ A. E. Johnson, N. E. Levinger and P. F. Barbara; *J. Phys. Chem.* 96, 7841 (1992).
- ⁷¹ D. A. V. Klinner, J. C. Alfano and P. F. Barbara; *J. Chem. Phys.* 98, 5375 (1993).
- ⁷² M. Li, J. Owrutsky, M. Sarisky, J. P. Culver, A. Yodh and R. M. Hochstrasser; *J. Chem. Phys.* 98, 5499 (1993).
- ⁷³ H. Rabitz, R. de Vivie-Riedle, M. Motzkus and K. Kompa; *Science* 288, 824 (2000).

- ⁷⁴ A. Assion, T. Baumert, M. Bergt, T. Brixner, B. Kiefer, V. Seyfried, M. Strehle and G. Gerber; *Science* 282, 919 (1998).
- ⁷⁵ H. Rabitz, G. M. Menkir and R. J. Levis; *Science* 292, 709 (2001).
- ⁷⁶ E. Charron and A. Suzor-Weiner; *J. Chem. Phys.* 108, 3922 (1998).
- ⁷⁷ A. H. Zewail; *Femtochemistry* (World Scientific, Singapore, 1994, Vol. 1 and 2).
- ⁷⁸ T.-N. V. Nguyen, M. Harpham, B. M. Ladanyi and G. H. Peslherbe; *J. Phys. Chem. A* to be submitted (2006).
- ⁷⁹ T.-N. V. Nguyen, S. R. Hughes and G. H. Peslherbe; *J. Phys. Chem. A* to be submitted (2006).
- ⁸⁰ Y. Marcus; *Ion Solvation* (Wiley, New York, 1985).
- ⁸¹ G. W. Robinson, S.-B. Zhu, S. Singh and M. W. Evans; *Water in Biology, Chemistry and Physics: Experimental Overview and Computational Methodologies* (World Scientific, Singapore, 1996).
- ⁸² B. J. Mason; *The Physics of Clouds*, 2nd ed. (Oxford University Press, London, 1971).
- ⁸³ E. R. Bernstein, ed.; *Chemical Reactions in Clusters* (Oxford University Press, New York, 1996).
- ⁸⁴ P. Jayaweera, A. T. Blades, M. G. Ikononou and P. Kebarle; *J. Am. Chem. Soc.* 112, 2452 (1990).
- ⁸⁵ P. Ayotte, G. H. Weddle, J. Kim, J. A. Kelley and M. A. Johnson; *J. Phys. Chem. A* 103, 443 (1999).
- ⁸⁶ W. L. Jorgensen and D. L. Severance; *Journal of Chemical Physics* 99, 4233-4235 (1993).
- ⁸⁷ L. S. Sremaniak, L. Perera and M. L. Berkowitz; *Chem. Phys. Lett.* 218, 377 (1994).
- ⁸⁸ H. D. Gai, G. K. Schenter, L. X. Dang and B. C. Garrett; *J. Chem. Phys.* 105, 8835 (1996).
- ⁸⁹ T. N. Truong and E. V. Stefanovich; *Chem. Phys.* 218, 31 (1997).
- ⁹⁰ J. E. Combariza, N. R. Kestner and J. Jortner; *J. Chem. Phys.* 100, 2851 (1994).
- ⁹¹ M. Arshadi, R. Yamaguchi and P. Kebarle; *J. Phys. Chem.* 74, 1475 (1970).
- ⁹² R. G. Keesee and A. W. Castleman, Jr.; *Chem. Phys. Lett.* 74, 139 (1980).
- ⁹³ K. Liu, J. D. Cruzan and R. J. Saykally; *Science* 271, 929-933 (1996).
- ⁹⁴ J. D. Cruzan, L. B. Braly, K. Liu, G. Brown, J. G. Loeser and R. J. Saykally; *Science* 271, 59 (1996).
- ⁹⁵ J. V. Coe; *J. Phys. Chem. A* 101, 2055 (1997).
- ⁹⁶ D. S. Lu and S. J. Singer; *Chem. Phys.* 105, 3700 (1996).
- ⁹⁷ G. H. Peslherbe, B. M. Ladanyi and J. T. Hynes; *J. Phys. Chem. A* 104, 4533 (2000).
- ⁹⁸ M. P. Allen and D. J. Tildesley; *Computer Simulation of Liquids* (Oxford University Press, New York, 1989).
- ⁹⁹ W. L. Jorgensen, J. Chandrasekhar, J. D. Madura, R. W. Impey and M. L. Klein; *Journal of Chemical Physics* 79, 926-935 (1983).

- ¹⁰⁰ J. Chandrasekhar, D. C. Spellmeyer and W. L. Jorgensen; *J. Am. Chem. Soc.* 106, 903-910 (1984).
- ¹⁰¹ J. K. Buckner and W. L. Jorgensen; *J. Am. Chem. Soc.* 111, 2507 (1989).
- ¹⁰² C. H. Bennett; *J. Comp. Phys.* 22, 245-268 (1976).
- ¹⁰³ S. J. Stuart and B. J. Berne; *J. Phys. Chem.* 100, 11934 (1996).
- ¹⁰⁴ D. M. Koch and G. H. Peslherbe, manuscript in preparation.
- ¹⁰⁵ It is important to note that the cluster $P(r_{HL})$ distributions vary from the liquid radial distribution functions by a factor of $4\pi r^2$, and the probabilities are normalized such that the integral distributions equal the number of solvent molecules in the cluster.
- ¹⁰⁶ S. H. Lin and P. C. Jordan; *J. Chem. Phys.* 89, 7492 (1988).
- ¹⁰⁷ S. McLaughlin; *Annu. Rev. Biophys. Biophys. Chem.* 18, 113 (1989).
- ¹⁰⁸ M. Sprik, J. Hutter and M. Parrinello; *J. Chem. Phys.* 105, 1142 (1996).
- ¹⁰⁹ P. Jungwirth and D. J. Tobias; *J. Phys. Chem. B* 105, 10468 (2001).
- ¹¹⁰ P. Jungwirth and D. J. Tobias; *J. Phys. Chem. B* 106, 6361 (2002).
- ¹¹¹ K. L. Foster, M. A. Tolbert and S. M. George; *J. Phys. Chem. A* 101, 4979 (1997).
- ¹¹² K. W. Oum, M. J. Lakin, D. O. DeHaan, T. Brauer and B. J. Finlayson-Pitts; *Science* 279, 74 (1998).
- ¹¹³ D. K. Perovich and J. A. Richer-Menge; *J. Geophys. Res.* 99, 16341 (1994).
- ¹¹⁴ J. H. Hu, Q. Shi, P. Davidovits, D. R. Worsnop, M. S. Zahniser and C. E. Kolb; *J. Phys. Chem.* 99, 8768 (1995).
- ¹¹⁵ S. Martin, Y. Yu and R. Drucker; *J. Geophys. Res.* 101, 12111 (1996).
- ¹¹⁶ A. Richter, F. Wittrock, M. Eisinger and J. P. Burrows; *Geophys. Res. Lett.* 25, 2863 (1998).
- ¹¹⁷ C. T. McElroy, C. A. McLinden and J. C. McConnell; *Nature* 397, 338 (1999).
- ¹¹⁸ K. L. Foster, R. A. Plastringe, J. W. Bottenheim, A. G. Gallant, K. A. Brice, P. B. Shepson and B. J. Finlayson-Pitts; *Science* 291, 471 (2001).
- ¹¹⁹ H. Cho, P. B. Shepson, L. A. Barrie, J. P. Cowin and R. J. Zaveri; *Phys. Chem. B* 106, 11226 (2002).
- ¹²⁰
- ¹²¹ W. H. Robertson and M. A. Johnson; *Annu. Rev. Phys. Chem.* 54, 173 (2003).
- ¹²² D. M. Koch and G. H. Peslherbe; *Chem. Phys. Lett.* 359, 381 (2002).
- ¹²³ D. H. Hecce, L. Perera, T. A. Darden and C. Sagui; *J. Chem. Phys.* 122, 024513 (2005).
- ¹²⁴ G. H. Peslherbe, B. M. Ladanyi and J. T. Hynes; *J. Phys. Chem. A* 102, 4100 (1998).
- ¹²⁵ W. H. Press, S. A. Teukolsky, W. T. Vetterling and B. P. Flannery; *Numerical Recipes, the Art of Scientific Computing, Second Edition* (Cambridge University Press, Cambridge, England, 1992).
- ¹²⁶ D. R. Lide; *CRC Handbook of Chemistry and Physics, 77th Edition* (CRC, Boca Raton, FL, 1996).
- ¹²⁷ L. A. Curtiss, D. L. Frurips and M. Blander; *J. Chem. Phys.* 71, 2703 (1979).

- ¹²⁸ J. Baik, J. Kim, D. Majumdar and K. S. Kim; *J. Chem. Phys.* 110, 9116 (1999).
¹²⁹ D. Majumdar, J. Kim and K. S. Kim; *J. Chem. Phys.* 112, 101 (2000).
¹³⁰ J. Kim, H. M. Lee, S. B. Suh, D. Majumdar and K. S. Kim; *J. Chem. Phys.* 113, 5259 (2000).
¹³¹ H. M. Lee, D. Kim and K. S. Kim; *J. Chem. Phys.* 116, 5509 (2002).
¹³² H. M. Lee and K. S. Kim; *J. Chem. Phys.* 114, 4461 (2001).
¹³³ W. S. Benedict, N. Gailar and E. K. Plyler; *J. Chem. Phys.* 24, 1139 (1956).
¹³⁴ T. P. Lybrand, I. Ghosh and J. A. McCammon; *J. Am. Chem. Soc.* 107, 7793 (1985).
¹³⁵ G. M. Torrie and J. P. Valleau; *Chem. Phys. Lett.* 28, 578 (1974).
¹³⁶ M. Souaille and B. Roux; *Comp. Phys. Comm.* 135, 40 (2001).
¹³⁷ B. Roux; *Comp. Phys. Comm.* 91, 275 (1995).
¹³⁸ S. Kumar, D. Bouzida, R. H. Swendsen, P. A. Kollman and J. M. Rosenberg; *J. Comput. Chem.* 13, 1011 (1992).
¹³⁹ B. Roux, H.-A. Yu and M. Karplus; *J. Phys. Chem.* 94, 4683 (1990).
¹⁴⁰ W. L. Jorgensen and J. Tirado-Rives; *J. Phys. Chem.* 100, 14508-14513 (1996).
¹⁴¹ S. Nose; *J. Chem. Phys.* 81, 511 (1984).
¹⁴² G. H. Hoover; *Phys. Rev. A* 31, 1695 (1985).
¹⁴³ G. Ciccotti and J. P. Ryckaert; *Comp. Phys. Rep.* 4, 345-392 (1986).
¹⁴⁴ R. A. Bryce, M. A. Vincent, N. O. J. Malcolm, I. H. Hillier and N. A. Burton; *J. Chem. Phys.* 109, 3077 (1998).
¹⁴⁵ L. Perera and M. L. Berkowitz; *J. Chem. Phys.* 100, 3085 (1994).
¹⁴⁶ J. E. Combariza, N. R. Kestner and J. Jortner; *Chem. Phys. Lett.* 203, 423 (1993).
¹⁴⁷ S. S. Xantheas and L. X. Dang; *J. Phys. Chem.* 100, 3989 (1996).
¹⁴⁸ R. J. Beuhler and L. Friedman; *J. Chem. Phys.* 78, 4669 (1988).
¹⁴⁹ D. Dreyfus and H. Y. Wachman; *J. Chem. Phys.* 61, 5282 (1974).
¹⁵⁰ S. Yoo, Y. A. Lei and X. C. Zeng; *J. Chem. Phys.* 119, 6083 (2003).
¹⁵¹ L. Perera and M. L. Berkowitz; *J. Chem. Phys.* 99, 4222 (1993).
¹⁵² L. Perera and M. L. Berkowitz; *J. Chem. Phys.* 96, 8288 (1992).
¹⁵³ L. Perera and F. G. Amar; *J. Chem. Phys.* 90, 7354-7368 (1989).
¹⁵⁴ P. L. Silvestrelli and M. Parrinello; *Phys. Rev. Lett.* 82, 3308 (1999).
¹⁵⁵ A. C. Shepard, Y. Beers, G. P. Klein and L. S. Rothman; *J. Chem. Phys.* 59, 2254 (1973).
¹⁵⁶ B. T. Gowda and S. W. Benson; *J. Comp. Chem.* 4, 283 (1983).
¹⁵⁷ I. Rips and J. Jortner; *J. Chem. Phys.* 97, 536 (1992).
¹⁵⁸ D. J. Tobias, P. Jungwirth and M. Parrinello; *J. Chem. Phys.* 114, 7036 (2001).
¹⁵⁹ R. S. Berry; *Optical spectra of the alkali halide molecules*; P. Davidovits and D. L. McFadden, Ed.; Academic: New York, 1979.
¹⁶⁰ F. J. Lovas and E. Tiemann; *J. Phys. Chem. Ref. Data* 3, 609 (1974).
¹⁶¹ K. D. Jordan; *Structure of alkali halides: theoretical methods*; P. Davidovits and D. L. McFadden, Ed.; Academic: New York, 1979.

- ¹⁶² M. B. Faist, B. R. Johnson and R. D. Levine; *Chem. Phys. Lett.*, 32, 1 (1975). M. B. Faist and R. D. Levine; *J. Chem. Phys.*, 64, 2953 (1976).
- ¹⁶³ V. Engel, H. Metiu, R. Almeida, R. A. Marcus and A. H. Zewail; *Chem. Phys. Lett.*, 152, 1 (1988). V. Engel and H. Metiu; *J. Chem. Phys.*, 90, 6116 (1989).
- ¹⁶⁴ V. Engel and H. Metiu; *Chem. Phys. Lett.* 155, 77 (1985). M. Braun, C. Meier and V. Engel; *J. Chem. Phys.* 105, 530 (1996).
- ¹⁶⁵ Y. Sakai, E. Miyoshi and T. Anno; *Can. J. Chem.* 70, 309 (1992).
- ¹⁶⁶ T. J. Martinez and R. D. Levine, *Chem. Phys. Lett.*, 259, 252 (1996). *J. Chem. Phys.*, 105, 6334 (1996).
- ¹⁶⁷ A. B. Alekseyev, H. P. Liebermann, R. J. Buenker, N. Balakrishnan, H. R. Sadeghpour, S. T. Cornett and M. J. Cavagnero; *J. Chem. Phys.* 113, 1514 (2000).
- ¹⁶⁸ R. Grice and D. R. Herschbach; *Molecular Physics* 27, 159 (1974).
- ¹⁶⁹ J. Tomasi and M. Persico; *Chem. Rev.* 94, 2027 (1994).
- ¹⁷⁰ N. J. A. V. Veen, M. S. D. Vries, J. D. Sokol, T. Baller and A. E. D. Vries; *Chemical Physics* 56, 81 (1981).
- ¹⁷¹ C. Jouvét, S. Martrenchard, D. Solgadi, C. Dedonder-Lardeux, M. Mons, G. Grégoire, I. Dimicoli, F. Piuze, J. P. Visticot, J. M. Mestdagh, P. D'Oliveira, P. Meynadier and M. Perdrix; *J. Phys. Chem. A* 101, 2555 (1997).
- ¹⁷² R. Bianco and J. T. Hynes; *J. Chem. Phys.*, 102, 7864 (1995). *ibid.*, 104, 7885 (1995). For a review, see R. Bianco and J. T. Hynes; in *Solvent Effects and Chemical Reactivity*, ed. O. Tapia and J. Bertrán, Kluwer, Dordrecht, 1996, p. 259.
- ¹⁷³ See e.g. J. T. Hynes; *J. Phys. Chem.*, 90, 3701 (1986), and references therein.
- ¹⁷⁴ R. A. Marcus; *J. Chem. Phys.*, 24, 966 (1956). *J. Chem. Soc. Faraday Trans.*, 29, 21 (1960).
- ¹⁷⁵ G. Grégoire, M. Mons, C. Jouvét and C. Dedonder-Lardeux; *Eur. Phys. J. D* 1, 5 (1998).
- ¹⁷⁶ L. Perera and M. L. Berkowitz; *J. Chem. Phys.* 95, 4236 (1991). *ibid.* 99, 4236 (1993). *ibid.* 99, 4222 (1993). L. Dang and B. C. Garrett; *J. Chem. Phys.* 99, 2972 (1993). L. X. Dang and D. E. Smith; *J. Chem. Phys.* 99, 6950 (1993).
- ¹⁷⁷ D. Serxner, C. E. H. Dessent and M. A. Johnson; *J. Chem. Phys.* 105, 7231 (1996). P. Ayotte, C. G. Bailey, G. H. Weddle and M. A. Johnson; *J. Phys. Chem. A* 102, 3067 (1998).
- ¹⁷⁸ Y. Zeiri, M. Shapiro; *Chem. Phys.*, 31, 217 (1978). M. Shapiro, Y. Zeiri; *J. Chem. Phys.*, 70, 5264 (1979). Y. Zeiri, M. Shapiro; *ibid.*, 75, 1170 (1981).
- ¹⁷⁹ Y. Zeiri and G. G. Balint-Kurti; *J. Mol. Spectrosc.* 99, 1 (1983).
- ¹⁸⁰ R. S. Mulliken; *J. Chim. Phys.*, 46, 497, (1949). R. Pariser; *J. Chem. Phys.*, 21, 568 (1953); H. A. Pohl, R. Rein and K. Appel; *J. Chem. Phys.*, 41, 3383 (1964).
- ¹⁸¹ P. W. Atkins; *Molecular Quantum Mechanics* (Clarendon, Oxford, 1970).
- ¹⁸² S. P. McGlynn, L. G. Vanquickenborne, M. Kinoshita and D. G. Carroll; *Introduction to Applied Quantum Chemistry* (Holt, Rinehart and Winston, New York, 1972).

- ¹⁸³ R. S. Mulliken, C. A. Rieke, D. Orloff and H. Orloff; *Journal of Chemical Physics* 17, 1248 (1949).
- ¹⁸⁴ E. S. Rittner; *Journal of Chemical Physics* 19, 1030 (1951).
- ¹⁸⁵ G. A. L. Delvigne and J. Los; *Physica* 67, 166 (1973).
- ¹⁸⁶ S. H. Schaefer, D. Bender and E. Tiemann; *Chem. Phys. Lett.*, 92, 273 (1982). S. H. Schaefer, D. Bender and E. Tiemann; *Chem. Phys.*, 89, 65 (1984).
- ¹⁸⁷ H. G. Hanson; *J. Chem. Phys.*, 23, 1391 (1955). J. R. Barker and R. E. Weston; *ibid.*, 65, 1427 (1976). W. R. Anderson, B. M. Wilson and T. L. Rose; *Chem. Phys. Lett.*, 48, 284 (1977). R. D. Bower, P. Chevrier, P. Das, H. J. Foth, J. C. Polanyi, M. G. Prisant and J. P. Visticot; *J. Chem. Phys.*, 89, 4478 (1988). H. Blum, J. Lindner and E. Tiemann; *ibid.*, 93, 4556 (1990).
- ¹⁸⁸ T.-M. R. Su and S. J. Riley; *Journal of Chemical Physics* 71, 3194 (1979).
- ¹⁸⁹ J. Wang, A. J. Blake, D. G. McCoy and L. Torop; *Chemical Physics Letters* 175, 225 (1990).
- ¹⁹⁰ See also D. A. Zichi, G. Ciccotti, R. Kapral and J. T. Hynes; *J. Phys. Chem.* 93, 6261 (1989). I. Benjamin, P. F. Barbara, B. J. Gertner and J. T. Hynes; *J. Phys. Chem.* 99, 7557 (1999).
- ¹⁹¹ L. X. Dang and B. M. Pettit; *J. Chem. Phys.* 86, 6560 (1987).
- ¹⁹² Calculations using the Multi-Reference singly and doubly excited Configuration Interaction method with a double-zeta basis set (MRCI/DZ), see ref. (48), and a relaxed water geometry were performed with the MOLPRO package. MOLPRO, is a package of ab initio programs written by H.-J. Werner and P. J. Knowles, version 2002.6, with contributions from R. D. Amos, A. Bernhardsson, A. Berning, P. Celani, D. L. Cooper, M. J. O. Deegan, A. J. Dobbyn, F. Eckert, C. Hampel, G. Hetzer, T. Korona, R. Lindh, A. W. Lloyd, S. J. McNicholas, F. R. Manby, W. Meyer, M. E. Mura, A. Nicklass, P. Palmieri, R. Pitzer, G. Rauhut, M. Schatz, H. Stoll, A. J. Stone, R. Tarroni, and T. Thorsteinsson.
- ¹⁹³ J. C. Tully; *J. Chem. Phys.* 93, 1061 (1990). J. C. Tully; *Int. J. Quantum Chem., Quantum Chem. Symp.* 25, 299 (1991). S. Hammes-Schiffer, J. C. Tully; *J. Chem. Phys.* 101, 4657 (1994).
- ¹⁹⁴ Alternative methods have been reported to estimate the quantum decoherence time of a system, so that quantum amplitudes along a trajectory can be reset at decoherence time intervals, avoiding the need for propagating swarms of trajectories [see e.g. B. J. Schwartz, E. R. Bittner, O. V. Prezhdo and P. J. Rossky; *J. Chem. Phys.* 104, 5942 (1996), and references therein]. While the latter method is particularly economical for condensed-phase simulations, we employ the original trajectory swarm methodology, in the present work, for simplicity.
- ¹⁹⁵ See e.g. P. Bala, P. Grochowski, B. Lesyng and J. A. McCammon; *J. Phys. Chem.* 100, 2535 (1996). B. J. Schwartz, E. R. Bittner, O. V. Prezhdo and P. J. Rossky; *J. Chem. Phys.* 104, 5942 (1996). D. F. Coker; In *Computer Simulation in Chemical Physics*; M. P. Allen and D. J. Tildesley, Eds.; Kluwer Academic Publishers: The Netherlands, 1993; p. 315.

- ¹⁹⁶ For a discussion of the Hellmann-Feynman forces in *first-principles* or mixed quantum/classical MD simulations, see e.g. K. Bolton, W. L. Hase and G. H. Peslherbe; In *Multidimensional Molecular Dynamics Methods*; D. L. Thompson, Ed.; World Scientific: 1998.
- ¹⁹⁷ J. Hellmann; *Einführung in die Quantenchemie*, Deuticke & Co.: Leipzig, 1937.
- ¹⁹⁸ R. P. Feynman; *Phys. Rev.* 56, 340 (1939).
- ¹⁹⁹ W. C. Swope, H. C. Andersen, P. H. Berens and K. R. Wilson; *Journal of Chemical Physics* 76, 637-649 (1982).
- ²⁰⁰ L. Verlet; *Phys. Rev.* 159, 98-103 (1967).
- ²⁰¹ Q. K. Timerghazin, D. M. Koch and G. H. Peslherbe; *J. Chem. Phys.* accepted for publication, Dec. 2005 (DOI:10.1063/1.2137691) (2005).
- ²⁰² J. Xie and R. N. Zare; *Journal of Chemical Physics* 97, 2891 (1992).
- ²⁰³ S. Nosé; *Molecular Physics* 52, 255-268 (1984).
- ²⁰⁴ J. Dzidic and P. Kebarle; *J. Phys. Chem.* 74, 1466 (1970).
- ²⁰⁵ G. Gregoire, M. Mons, I. Dimicoli, C. Dedonder-Lardeux, C. Jouvet, S. Martrenchard and D. Solgadi; *Eur. Phys. J. D* 11, 227 (2000).
- ²⁰⁶ D. M. Koch, Q. T. Timerghazin, G. H. Peslherbe, B. M. Ladanyi and J. T. Hynes; *J. Phys. Chem. A* accepted for publication, November (2005).
- ²⁰⁷ A. W. Jasper, C. Zhu, S. Nangia and D. G. Truhlar; *Faraday Discussions* 127, 1 (2004).
- ²⁰⁸ S.-Y. Lee, W. T. Pollard and R. A. Mathies; *J. Chem. Phys.* 90, 6146-6150 (1989).
- ²⁰⁹ V. Balzani; *Electron Transfer Reactions*, V. Balzani (VCH Press, 2001, Vol. 1).
- ²¹⁰ S. S. M. C. Godinho, d. Couto, P. Cabral and B. J. C. Cabral; *Chem. Phys. Lett.* 399, 206 (2004).
- ²¹¹ Q. K. Timerghazin and G. H. Peslherbe; *Chem. Phys. Lett.* 354, 31 (2002).
- ²¹² M. Born; *Z. Phys.* 1, 45 (1920).
- ²¹³ D. Y. C. Chan, D. J. Mitchell and B. W. Ninham; *J. Chem. Phys.* 70, 2946 (1979).
- ²¹⁴ M. D. Tissandier, S. J. Singer and J. V. Coe; *J. Phys. Chem. A* 104, 752 (1000).
- ²¹⁵ H. J. Kim and J. T. Hynes; *J. Chem. Phys.*, 93, 5194 (1990). *ibid.*, 96, 5088 (1992). R. Bianco, J. Juanos, I. Timoneda and J. T. Hynes; *J. Phys. Chem.*, 98, 12103 (1994). J. Juanos, I. Timoneda and J. T. Hynes; *J. Phys. Chem.*, 95, 10431 (1991). T. Fonseca, H. J. Kim and J. T. Hynes; *J. Mol. Liq.*, 60, 161 (1994).
- ²¹⁶ S. S. Xantheas, C. J. Burnham and R. J. Harrison; *J. Chem. Phys.* 116, 1493 (2002).
- ²¹⁷ D. M. Koch and G. H. Peslherbe; *manuscript in preparation* (2005).
- ²¹⁸ D. M. Koch and Gilles H. Peslherbe, Modified Mopac7 (IBMWS/PVM3) by J.J.P. Stewart et. al, Quantum Chemistry Program Exchange, Indiana University, Bloomington, IN, 1994.
- ²¹⁹ M. J. Frisch, G. W. Trucks, H. B. Schlegel, G. E. Scuseria, M. A. Robb, J. R. Cheeseman, V. G. Zakrzewski, J. A. Montgomery, R. E. Stratmann, J. C. Burant, S. Dapprich, J. M. Millam, A. D. Daniels, K. N. Kudin, M. C. Strain, O. Farkas, J. Tomasi, V. Barone, M. Cossi, R. Cammi, B. Mennucci, C. Pomelli, C. Adamo, S.

- Clifford, J. Ochterski, G. A. Petersson, P. Y. Ayala, Q. Cui, K. Morokuma, D. K. Malick, A. D. Rabuck, K. Raghavachari, J. B. Foresman, J. Cioslowski, J. V. Ortiz, B. B. Stefanov, G. Liu, A. Liashenko, P. Piskorz, I. Komaromi, R. Gomperts, R. L. Martin, D. J. Fox, T. Keith, M. A. Al-Laham, C. Y. Peng, A. Nanayakkara, C. Gonzalez, M. Challacombe, P. M. W. Gill, B. G. Johnson, W. Chen, M. W. Wong, J. L. Andres, M. Head-Gordon, E. S. Replogle and J. A. Pople; *Gaussian 98 (Revision A.1)* (Gaussian, Inc., Pittsburgh, PA, 1998).
- ²¹⁹ M. I. Bernal-Uruchurtu, M. T. C. Martins-Costa, C. Millot and M. F. Ruiz-Lopez; *J. Comp. Chem.* 21, 572 (2000).
- ²²⁰ K. Y. Burstein and A. N. Isaev; *Theor. Chim. Acta* 64, (1984).
- ²²¹ M. J. S. Dewar, E. G. Zoebisch, E. F. Healy and J. J. P. Stewart; *J. Am. Chem. Soc.* 107, 3902-3909 (1985).
- ²²² M. P. Repasky, J. Chandrasekhar and W. L. Jorgensen; *J. Comp. Chem.* 23, 1601 (2002).
- ²²³ G. M. Torrie and J. P. Valleau; *J. Comput. Phys.* 23, 187 (1977).
- ²²⁴ R. Iftimie, D. Salahub and J. Schofield; *J. Chem. Phys.* 119, 11285 (2003).
- ²²⁵ E. A. Carter, G. Ciccotti, J. T. Hynes and R. Kapral; *Chem. Phys. Lett.* 156, 472 (1989).
- ²²⁶ S. Melchionna; *Phys. Rev. E* 62, 8762 (2000).
- ²²⁷ Z. Zhu, M. E. Tuckerman and G. J. Martyna; *Phys. Rev. Lett.* 88, 100201 (2002).
- ²²⁸ R. Iftimie, D. Salahub, D. Wei and J. Schofield; *J. Chem. Phys.* 113, 4852 (2000).
- ²²⁹ J. V. d. Vondele and U. Rothlisberger; *J. Chem. Phys.* 113, 4863 (2000).
- ²³⁰ D. J. Doren, R. W. Wood, C. Tong, G. Lai and Y. Ming; *submitted to Chem. Phys. Lett.* (2004).
- ²³¹ W. Stevens, H. Basch and J. Krauss; *J. Chem. Phys.* 81, 6026 (1984).
- ²³² A. D. Becke; *J. Chem. Phys.* 98, 5648 (1993).
- ²³³ J. P. Perdew, K. Burke and M. Ernzerhof; *Phys. Rev. Lett.* 77, 3865 (1996).
- ²³⁴ J. P. Perdew, K. Burke and Y. Wang; *Phys. Rev. B* 54, 16533 (1996).
- ²³⁵ L. Shulman; *Techniques and Application of Path Integration* (John Wiley & Sons, New York, 1981).
- ²³⁶ E. L. Pollock and D. M. Ceperley; *Phys. Rev. B* 30, 2555 (1984).
- ²³⁷ X. G. Zhao, A. Gonzalez-Lafont, D. G. Truhlar and R. Steckler; *J. Chem. Phys.* 94, 5544 (1991).
- ²³⁸ M. Suzuki; *J. Math. Phys.* 32, 400 (1991).
- ²³⁹ F. Sobott, A. Wattenberg, K.-D. Barth and B. Brutschy; *Int. J. Mass Spect.* 185, 271 (1999).
- ²⁴⁰ T. H. D. Jr.; *J. Chem. Phys.* 90, 1007 (1989).
- ²⁴¹ R. A. Kendall, T. H. D. Jr. and R. J. Harrison; *J. Chem. Phys.* 96, 6796 (1992).
- ²⁴² D. E. Woon and T. H. D. Jr.; *J. Chem. Phys.* 103, 4572 (1998).
- ²⁴³ H. Stoll, B. Metz and M. Dolg; *J. Comp. Chem.* 23, 767 (2002).